Doctoral Programme in Electrochemistry, Science and Technology

Autonoma University of Madrid

DOCTORAL THESIS

Graphene-Based Hybrid Materials with Metal Compounds and their Application in Electrochemical Energy Storage Devices

---

Materiales Híbridos Basados en Grafeno con Compuestos Metálicos y su Aplicación en Dispositivos Electroquímicos de Almacenamiento de Energía

A thesis submitted to Autonoma University of Madrid in fulfillments of the requirements for the degree of Doctor of Philosophy

by:

Jaime Sánchez Sánchez

Supervisors:

Dr. Rebeca Marcilla García

Dr. Afshin Pendashteh

Electrochemical Processes Unit-IMDEA Energy Institute

Academic Tutor:

Dr. Pilar Ocón Esteban

Autonoma University of Madrid

Madrid, 2019

"*Utopia* is on the horizon.
I move two steps down;
It moves two steps further away.
I walk another ten steps
and the horizon runs ten steps further away.
As much as I may walk, I'll never reach it.
So what's the point of *Utopia*?
The point is this: to keep walking"

Eduardo Hughes Galeano

TO MY FAMILY

AND FUTURE WIFE

Acknowledgements

PhD is an exciting journey filled with lessons, hardships, moments of experimental desperation and also some celebrations that ultimately lead me to complete a new stage in my life. The road was not always smooth. In fact, throughout the whole travel, I encountered many challenges, and luckily I have learned and gained a lot from them, basically thanks to many people. At the moment, it is the time to say goodbye to this wonderful journey and it is the time to say thanks to everyone who have helped me during the last four years. Considering all the people who are involved, plenty of them Spanish speakers, I will continue in my native language.

"Cuatro años de felicidad intercalada", comienza la letra de la canción Siete vidas de Antonio González Flores. Pues no hay mejor manera de describir lo que es para mí la realización de un doctorado, un viaje tipo montaña rusa de emociones en el que pasas rapidamente de la euforia a la desesperación, principalmente por esos momentos de desesperación me gustaría agradecer su actitud y apoyo a mucha gente:

En primer lugar, me gustaría agradecer la oportunidad brindada a mis directores *Dra. Rebeca Marcilla* y *Dr. Afshin Pendashteh*. Ha sido un verdadero placer trabajar a vuestro lado, personal y profesionalmente habéis sido la combinación perfecta para el correcto desarrollo de la tesis. Gracias por todos los consejos, el conocimiento transmitido, la paciencia y el tiempo invertidos, sin lugar a dudas he llegado hasta aquí gracias a vuestro apoyo. La consecución de este doctorado es en gran parte gracias a vosotros. Muchas gracias de corazón. En particular, me gustaría destacar la labor de Afshin, has sido todo un ejemplo para mí, el espejo donde mirarme cada día, desde el minuto uno que empezamos a trabajar juntos sentí esa conexión contigo en la que yo mismo me exigía un nivel "TOP", un nivel de auto-exigencia y dedicación que me ha llevado a vivir con pasión y dedicación todo aquello en lo que hemos estado trabajando, porque hemos sido un equipo, un equipazo, "yo a este tío no puedo fallarle" decía cuando las cosas no salían. Eres un verdadero profesional, pero sobre todo una excelente persona, me llevo un amigo, un hermano mayor para toda la vida…esas cosas que te da un doctorado y que no aparecen en los papeles. Gracias por todo Bro.

A su vez, me gustaría agradecer la labor del *Dr. Jesús Palma* y el *Prof. Marc Anderson*. Gracias por las charlas personales y científicas, gracias por brindarme la oportunidad de pertenecer a esta

unidad, nunca olvidaré aquella entrevista personal contigo Jesús ya hace cuatro años, habías sido mi profesor en la universidad y tus clases habían sido inspiradoras, yo después de trabajar un periodo corto en industria buscaba algo más estimulante… sinceramente, no tenía ni idea de que aquello se podía traducir en un Doctorado en Electroquímica y Materiales. A ti Marc, gracias sobre todo por el afecto, la cercanía y el apoyo incondicional, eres un ejemplo para mí, ojalá yo con tu edad pueda llegar a ser una cuarta parte de lo que tú hoy en día simbolizas. Siempre dije que eres el "Glue" que aportas esa cohesión única en la unidad, ese buen ambiente que transmites incluso desde la distancia.

Quiero agradecer también a mi tutora en la UAM, la *Dra. Pilar Ocón* por su disponibilidad para ayudarme en lo que he necesitado para los trámites relativos a la Universidad. También me gustaría agradecer al departamento de química inorgánica y su grupo de estructura electrónica en el instituto de investigación "Fritz-Haber-Institut der Max-Planck-Gesellschaft" (Berlín) por acogerme durante mi estancia en Alemania y en especial al *Prof. Robert Schlögl*, *Dr. Axel Knop-Gericke*, *Dr. Juan José Velasco Vélez* y *Dr. Detre Teschner* por ayudarme y enseñarme temas relativos a la radiación en Sincrotrón durante dicho periodo.

No tengo palabras para agradecer a los miembros de la unidad de procesos electroquímicos de IMDEA Energía. Han sido mi familia durante los últimos cuatro años y sin lugar a dudas voy a echar de menos trabajar en una unidad tan especial. Quiero agradecer al *Dr. Enrique García-Quismondo* por todos aquellos "buenos momentos" vividos hablando de catástrofes aéreas, por ese ejemplo de constancia en el trabajo y por sus buenos días cada mañana, da gusto trabajar con personas así. Agradecer al *Dr. Edgar Ventosa* por su trato personal y profesional, siempre aportando ideas "out of the box", un electroquímico 10. Gracias al *Dr. Julio Lado* por todas las conversaciones mantenidas y todos esos ratos futbolísticos, ha sido un placer. Gracias al *Dr. Nagaraj Patil*, al *Dr. Andreas Mavrantonakis* y al *Dr. Nicola Boaretto* por todas sus charlas científicas o personales, os deseo lo mejor en el futuro. Gracias al *Dr. Girum Tiruye* y al *Dr. Evgeny Senokos*, una sonrisa y una energía única todas las mañanas, un placer haber sido vuestro compañero. Como me voy a olvidar de mis dos compañeras y amigas ya doctoras, *Dra. Cleis Santos* Y *Dra. Paula Navalpotro*, gracias por acogerme desde el minuto uno, sois únicas y brilláis con luz propia haya donde vais. Esos momentos de Alex Ubago y la Mordidita en el laboratorio y durante el cleaning serán recordados para la eternidad. Realmente los echo de menos. Gracias chicas. Gracias *David*, mi compañero inseparable durante todo este viaje, eres un 12 como persona, gracias por todas los momentos

vividos en la máquina de café, en los webbers, por todas aquellas confesiones, vamos crack! Ya casi lo tenemos. A *Mayte* por ser mi hermanita desde el minuto uno y protegernos mutuamente del malvado y villano quien tú ya sabes! A *Diana, Antonio, Dani, Carlos, Iciar, Bea y Sabrina* por los buenos momentos vividos, os deseo lo mejor, sois grandes chicos. A los mejores técnicos-ingenieros-lo que ellos quieran ser- del mundo, *Guzmán y Nacho*, sois especiales humana y profesionalmente hablando.

También quiero emplear unas líneas en agradecer a los Imdeanos míticos de otras unidades, que hicieron de Imdea un ambiente especial y realmente único durante mi periodo de doctorado. Gracias a mis amigos de toda la vida, *Rodri, Carlitos, Rafa* sois únicos, aquellos hermanos de vida que uno tiene la posibilidad de elegir. Dar las gracias a mis "abuelitos" mostoleños *Jesús y Pepi*, por escucharme, por apoyarme siempre en mis decisiones por muy raras o locas que parecieran. Especialmente quiero dar las gracias a mi compañera de vida, *Melisa*, la que será mi futura esposa el próximo mes de Septiembre, porque este 2019 viene cargado de emociones fuertes. Gracias cariño por el apoyo diario, por buscar siempre mi felicidad, por ser mi complemento perfecto, por hacerme sentirme especial y sobre todo, por hacer de este sueño una realidad que empezó a más de 12000 km de distancia hace ya casi 10 años, y los que nos quedan…

Por último, me gustaría agradecer a mi gran familia (ni más ni menos que alrededor de 50 miembros entre prim@s, ti@s...) todos con una relación magnífica y de los que estoy muy orgulloso de formar parte, somos Sánchez y haya donde vamos se nos nota que somos Sánchez! Una semilla de un pasado humilde en un par de pueblitos del norte de Extremadura, en el que unos abuel@s que por desgracia ya no están, dejaron huella y unos valores imborrables. Mención especial merece mi hermana, *Ana*, gracias por empujarme siempre hacia adelante y apoyarme en todas mis decisiones, eres la mejor hermana del mundo y nunca podré devolverte todo el cariño que me has dado. Siempre me vas a tener a tu lado. Finalmente quiero dar las gracias a mis padres, *Zacarías* y *Loli* los cuales me han inculcado los valores del esfuerzo diario y del sacrificio desde pequeñito, han apoyado todas y cada una de mis decisiones de manera incondicional, "tu hijo positivo siempre para adelante que todo sale", uno no puede ni imaginar lo afortunado que soy al teneros como hijo. Mis valores como persona son vuestras respectivas victorias como padres. Esta tesis va por todos y cada uno de los esfuerzos que habéis destinado a que mi vida fuera siempre especial. Por último, me gustaría terminar con una reflexión que escuche hace poco:

"Trabaja duro en silencio, que el éxito sea tu ruido"

TABLE OF CONTENT

Abstract

Without shadow of a doubt, achieving secure and sustainable energy is one of the greatest challenges of our nowadays life. To this end, efficient storing energy of renewable sources (e.g. wind or solar) in order to deliver it on demand and the vast implementation of the electric vehicle in the automotive market truly highlights the importance of development of cost-effective, safe and high-performance energy storage systems. Over the past decade, exploring and developing hybrid systems benefitting from merits of both batteries and capacitors attracted great attention as a solution for ever-increasing energy demand in new rising markets (e.g. electric vehicles). In this regard, development of novel hybrid materials combining faradaic with capacitive processes capable of providing both high energy and power densities are of great importance.

In spite of recent scientific progresses, many challenges yet need to be overcome to achieve applicable high-performance materials for energy storage (such as simple and low-cost synthesis, easy scalability, benignity, and etc).

In the course of this PhD thesis, development of some novel graphene-based hybrids with transition metal compounds (e.g. metal oxides or sulfides) have been followed with an eye on the ease of synthesis route. The microstructural properties of the materials were tuned by alteration the morphology or particle-sizes in order to enhance their electrochemical signal with the aim of enhancing their storage or electrocatalytic features. The thesis consists of five sections: Introduction and literature overview (chapter 1), objectives (chapter 2), experimental and methodology (chapter 3), chapters devoting to the obtained results (chapters 4-9), and conclusion and future perspectives (chapter 10). Hence, the current thesis is organized in 10 chapters which are outlined as follows:

Chapter 1 introduces the background and terminology of energy storage systems (including batteries, supercapacitors and their hybrid systems) as well as a brief literature survey to make a comparison of the here obtained results with the state-of-the-art. Moreover, the advantages of using graphene-based materials and their hybridization with transition metal compounds (e.g. oxide or sulfides) for energy applications have been described. **Chapter 2** provides research objectives of the present thesis. In **Chapter 3**, experimental methods employed in the present thesis are provided. This includes detailed synthesis procedures, physicochemical and

electrochemical characterizations and the utilized instruments. **Chapter 4** describes an easy method to boost the electrochemical energy storage properties of commercial Fe_3O_4 nanoparticles in hybridization with rGO nanosheets. The as-prepared Fe_3O_4-rGO hybrids were evaluated as high power negative electrodes for aqueous batteries. In **Chapter 5**, ilmenite nickel manganese oxides were hydrothermally anchored on rGO nanosheets ($NiMnO_3$-rGO) and the hybridization effect on energy storage properties were explained. In **Chapter 6,** the hydrothermal synthesis of porous nickel cobalt manganese ternary metal oxide nanosheets supported on rGO layers (NiCoMnO-rGO) is presented. The effect of various synthesis conditions, such as oxide/carbon ratio and hydrothermal reaction time, was examined and at last the optimum hybrid material was evaluated as a positive electrode for high performance hybrid energy storage devices. In **Chapter 7**, Co_3O_4 Nanorods (NRs) were anchored on N-doped graphene nanosheets via a simple electrostatic coagulation method. The optimized oxide was hybridized with graphene (Co_3O_4/N-rGO) and the resulting hybrid was examined as a bifunctional (ORR/OER) electrocatalyst, and was compared with the state-of-the-art noble-metal catalyst (e.g. PtRuC) in Zn-air rechargeable batteries. **Chapter 8** is focused on understanding charge storage mechanism of directly growth mixed metal sulfide ($NiCoMnS_2$) arrays on Ni foam. To this end, various post-mortem and operando analyses have been carried out and explained in the chapter. In **Chapter 9**, the ternary metal Ni-Co-Mn sulfide (with a different phase than in Chapter 8) was anchored on N-doped graphene nanosheets and the obtained hybrid ($NiCoMnS_4$/NrGO) was evaluated as bifunctional electrocatalysts for rechargeable Zn-air batteries. Various electrochemical characterizations were conducted and the results were compared with previous works reported in literature. In addition, the results were also compared with a previous work of the group on similar phase but metal oxide to sketch the activity differences between oxide and sulfide analogues. Finally, **Chapter 10** summarizes main conclusions of the conducted research in the thesis, and outlines suggestions for future work to further evaluate and benefit from the hybridization of graphene derivatives with metal compounds for electrochemical energy storage.

Resumen

Desarrollar un plan energético seguro y sostenible es, sin lugar a dudas uno de los mayores desafíos de nuestros días. Para ello, el almacenamiento eficiente de energía mediante fuentes renovables (por ejemplo, eólica o solar) con el fin de entregar dicha energía bajo demanda, junto a la gran implementación del vehículo eléctrico en el mercado automotriz, realza aún más si cabe la importancia del desarrollo de sistemas energéticos seguros, a un precio competitivo y con un elevado rendimiento. Sin embargo, ha sido durante la última década, cuando se ha comenzado a fomentar la investigación, desarrollo e implementación de nuevos sistemas híbridos que pueden llegar a beneficiarse de las ventajas que ofrecen tanto baterías como condensadores, atrayendo una enorme expectación como posible solución para la creciente demanda de nuevos mercados en alza (por ejemplo, el vehículo eléctrico). En este sentido, la síntesis y el desarrollo de nuevos materiales híbridos capaces de combinar procesos faradaicos con capacitivos, logrando a su vez proporcionar altas densidades de energía y potencia ha pasado a ser un aspecto de elevado interés para la comunidad científica.

A pesar de los innumerables avances científicos en lo relativo a la ciencia de materiales, aún quedan infinidad de desafíos por afrontar a la hora de sintetizar nuevos materiales potencialmente aplicables en el almacenamiento eficiente de energía, que puedan mostrar un alto rendimiento electroquímico en comparación a los ya actuales (empleando métodos de síntesis simples, rentables desde el punto de vista económico, de fácil escalabilidad y a su vez procurando ser benévolos con el medio ambiente, etc.)

Durante el transcurso de la presente tesis doctoral, se ha considerado de vital importancia el empleo de métodos de síntesis fácilmente reproducibles para el desarrollo de nuevos materiales híbridos basados en grafeno y compuestos de metales de transición (por ejemplo, óxidos metálicos o sulfuros metálicos). Las propiedades microestructurales de los materiales sintetizados se optimizaron mediante la alteración en su morfología, composición o tamaño de partícula, con el fin de mejorar su respuesta electroquímica y con el objetivo final de mejorar sus propiedades de almacenamiento electroquímico o sus características electrocatalíticas. La tesis consta de cinco secciones: Introducción y revisión del estado del arte (capítulo 1), objetivos de la presente tesis doctoral (capítulo 2), parte experimental y de metodología (capítulo 3), capítulos dedicados a los

resultados obtenidos (capítulos 4-9) y capítulo de conclusiones finales y perspectivas futuras (capítulo 10). Por lo tanto, la presente tesis doctoral está organizada en 10 capítulos que se resumen a continuación:

El **Capítulo 1** presenta los antecedentes, estructura y situación actual de los distintos sistemas de almacenamiento de energía (incluidas las baterías, los supercondensadores y sus sistemas híbridos), así como una breve comparativa bibliográfica de los resultados obtenidos en la presente tesis con el estado del arte. Además, se han descrito las ventajas de usar materiales basados en grafeno y su hibridación con compuestos de metales de transición (por ejemplo, óxido o sulfuros) para aplicaciones energéticas. El **Capítulo 2** enumera los objetivos perseguidos durante la presente tesis doctoral. En el **Capítulo 3**, se detallan los métodos experimentales y la metodología empleada. Esto incluye procedimientos de síntesis detallados, caracterizaciones fisicoquímicas y electroquímicas, así como todos los instrumentos utilizados. El **Capítulo 4**, como primer capítulo de resultados, describe el empleo de un método fácil para la hibridación de nanopartículas de Fe_3O_4 comerciales con nanoláminas de óxido de grafeno reducido (rGO), con la finalidad de aumentar las propiedades de almacenamiento de energía características del óxido puro. Se prepararon distintas composiciones del material híbrido (Fe_3O_4-rGO), cuyas propiedades electroquímicas de almacenamiento fueron comparadas, empleando finalmente el material optimizado (Fe_3O_4-rGO 60:40) como electrodo negativo en baterías acuosas de alta potencia. En el **Capítulo 5**, óxidos de níquel-manganeso en fase ilmenita fueron anclados mediante un método hidrotermal en nanoláminas de rGO ($NiMnO_3$-rGO), explicando el efecto de su hibridación en las propiedades de almacenamiento de energía. En el **Capítulo 6**, un óxido ternario de niquel cobalto y manganeso se ancla mediante un método hidrotermal en nanoláminas de rGO (NiCoMnO-rGO). Se examinó el efecto de varias condiciones de síntesis, como la relación óxido/carbono y el tiempo empleado en la reacción hidrotermal, finalmente se evaluó el material híbrido optimizado como electrodo positivo para dispositivos híbridos de almacenamiento de energía. En el **Capítulo 7**, Co_3O_4 nanorods (NR) fueron anclados en nanoláminas de grafeno dopadas con nitrógeno mediante un simple método de coagulación electrostática. El óxido optimizado se hibridó con grafeno (Co_3O_4/N-rGO) y el híbrido resultante se examinó como electrocatalizador bifuncional (ORR/OER), siendo comparado con uno de los catalizador bifuncionales de metales nobles más empleado (PtRuC) en baterías recargables de Zn-aire. El **Capítulo 8** se centra en comprender el mecanismo de almacenamiento de carga perteneciente a un sulfuro metálico mixto sintetizado

sobre espuma de niquel ($NiCoMnS_2$). Con esta finalidad, varios análisis post mortem y operando se han llevado a cabo y se han explicado en detalle en el capítulo. En el **Capítulo 9**, se detalla la síntesis de un sulfuro ternario de Ni-Co-Mn (con una fase diferente que en el Capítulo 8) en nanoláminas de grafeno dopado con nitrógeno. El material híbrido ($NiCoMnS_4$/NrGO) sintetizado, se evaluó como electrocatalizador bifuncional para baterías recargables de Zn-aire. Se llevaron a cabo varias caracterizaciones electroquímicas y los resultados se compararon con anteriores trabajos ya publicados en la literatura. Además, los resultados también se compararon con un trabajo previo del grupo en una fase similar pero empleando un óxido metálico ternario, para aclarar y comparar las diferencias en la actividad catalítica entre óxidos y sulfuros análogos. Finalmente, el **Capítulo 10** resume las principales conclusiones de la investigación realizada en la presente tesis doctoral y presenta sugerencias para futuros trabajos de investigación a la hora de evaluar y beneficiarse de la hibridación de los compuestos derivados del grafeno con distintos compuestos metálicos para su aplicación en el almacenamiento electroquímico de energía.

CHAPTER 1

Introduction and Literature Overview

1.1 Energy Demands and Challenges

Energy is considered the driving force of Human civilization and development. Achieving a secure, affordable and sustainable energy system has been a cornerstone of the world's increasing prosperity and economic growth since the beginning of the twenty-first century. Every year, the mankind paves its path through more than 500 million Tera joules of energy which is roughly equivalent to the energy released from the Hiroshima nuclear bomb every four seconds. Beyond a shadow of a doubt, energy consumption, production and storage are probably the greatest technical, environmental and social challenges the world are facing nowadays.[1–5] Moreover, electric vehicles (EV) have also grown in popularity because of the increasing concern for the environmental impact that CO_2 emissions cause ("Car Emissions and Global Warming"). However, electric motors have been an interest of many inventors since the 19th century, although fully electric vehicles were not appear until 2008 when Tesla Motors released the Roadster.[6]

Generally speaking, energy sources could be divided into two main categories based on their nature: renewable and non-renewable sources. Renewable energies are inexhaustible and could be generated repeatedly when required, such as wind, solar, tide, geothermal and biomass. Non-renewable energies including fossil fuels such as oil, natural gas and coal, are available in limited quantity on the planet and could not be regenerated within a short span of time. It is projected by the International Energy Agency that the global electricity demand will grow from 22 000 TeraWatt hour (TWh) to 36 0000 TWh in 2040, a 80% increase between 2018 and 2040 (***Figure 1.1***),[7] being China and India by far the fastest-growing regions due to the exponential population-industrialization growth.

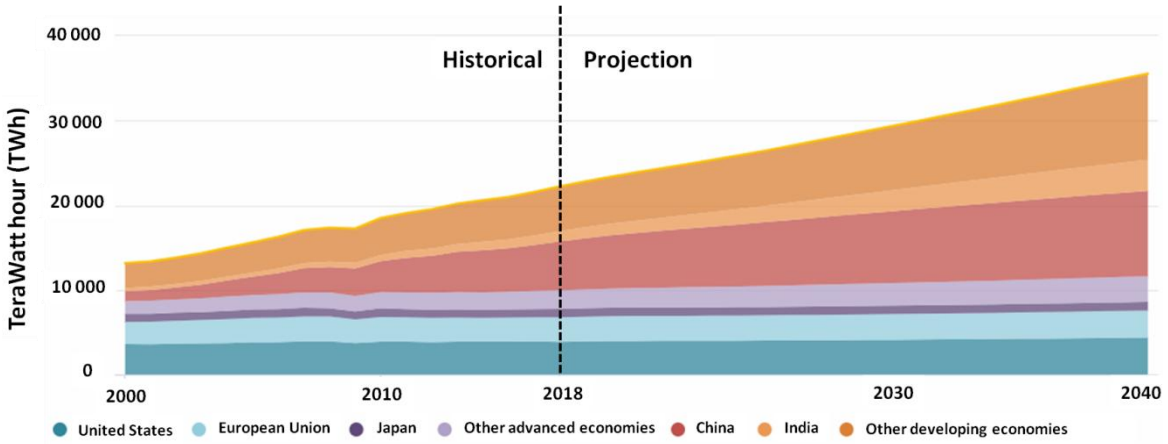

Figure 1.1 Global electricity demand by region (adapted from [7])

With rapidly increasing energy demand and recent concerns over energy security and global pollution, it is highly desirable to explore renewable and sustainable energy sources. It is anticipated by the U.S. Energy Information Administration that the share of renewable energies in primary energy consumption would rise from 13% in 2018 to 18% in 2040 (***Figure 1.2***), resulting from rapidly growing demand for modern renewable society to produce heat, generate power and make transport fuels. As the potential sources of biomass, hydro, or geothermal energy are still limited in many countries, wind power and solar photovoltaic (PV) will play a dominant role. As an example, Germany often considered as one of the European countries in the front-line of renewable energy practices, is planning to raise-up the percentage of renewable energy employed as electricity consumption to 80% by 2050, compared to 36% in 2017 and only around 3% in the beginning of the 90s.[8]

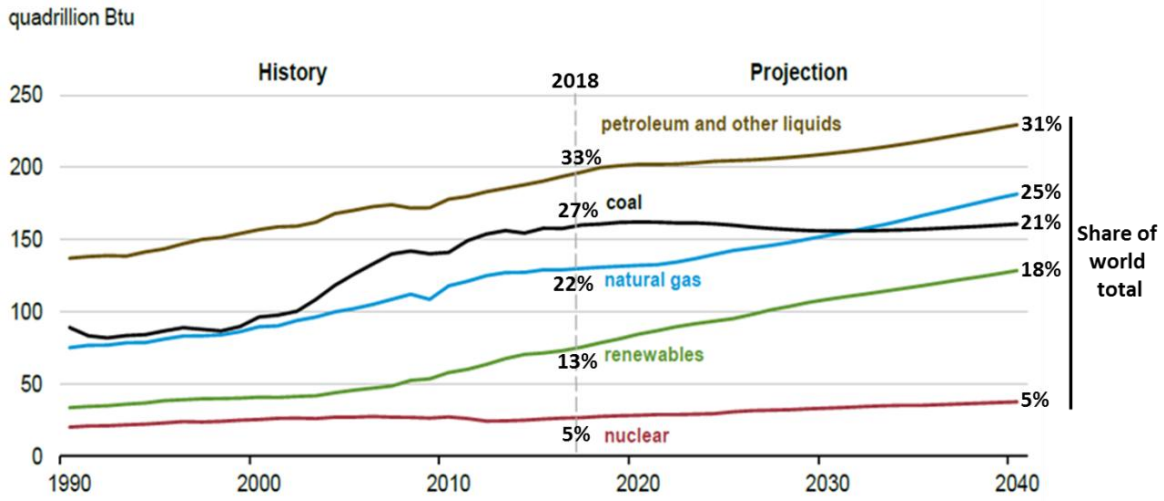

Figure 1.2 World Energy consumption by energy source (adapted from [7])

Solar photovoltaic (PV) and wind power are the world's fastest-growing renewable energies. Solar and wind energies would account for about 19% of global installed power capacity, and they will reach almost 35% of that of the European Union in 2035 according to the International Energy Agency.[7] However, unlike dispatchable power generation technologies (fossil fuel-fired, hydropower with reservoir, geothermal, and bio-energy), which may be ramped up or down to match the fluctuating energy demand, the output from wind power and solar PV is only intermittently available and is highly dependent on the availability of the sources including the weather, time, season and location, while the demands and consumption of electric energy are relatively constant.[9,10] At this stage, the potential temporal mismatch of supply and demand raises

two fundamental questions: How to deal with variable renewable energy at times when there is too much supply? How to serve demand at times when supply is scarce?

1.2 Electrochemical Energy Storage Systems

Evidently, large-scale stationary Energy Storage Technologies (ESTs) connected to renewable power plants can provide an answer to the questions above, for instance, in the form of battery cell stacks, or pumped-hydroelectricity storage plants, allowing to shift energy over time.[11] To be highly competent and flexible, ESTs are required to be adapted for various applications. ESTs could be categorized into four types based on the mechanism through which the process takes place; mechanical, electrical, chemical and electrochemical (highlighted in different colors in ***Figure 1.3***).[3]

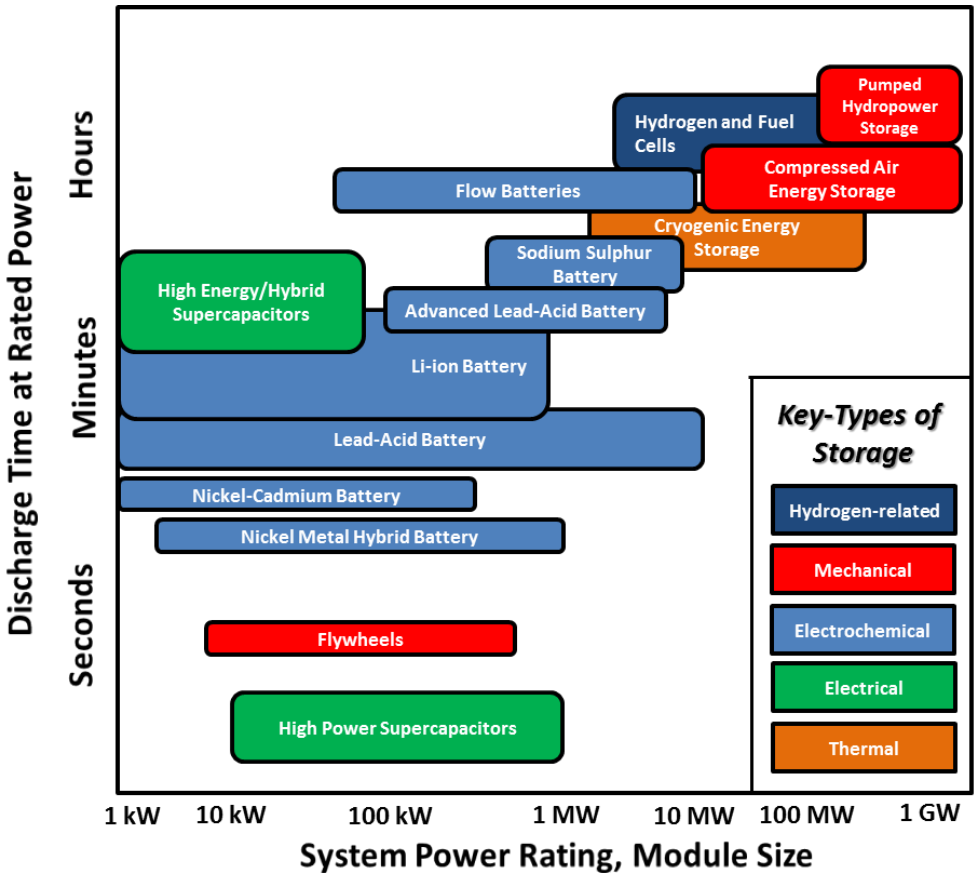

Figure 1.3 Applicable power ranges and discharge power duration of different ESTs (adapted from [12])

Figure 1.3 shows the relationship between the different ESTs based on their system power rating and discharged time responses. Although existing energy storage technologies is dominated by pumped hydropower, there is the recognition that electrochemical energy storage in the form of

supercapacitors (SCs) and batteries; with system power ratings in the range of kW to MW and discharged times between seconds and hours, has by far found their wide application in powering portable electronics ***(Figure 1.4***) and electrification of the transportation sector because of their desirable characteristic such as high round-trip efficiency, controllable power and energy, long cycle life, environmental-friendly feature and low costs.[3]

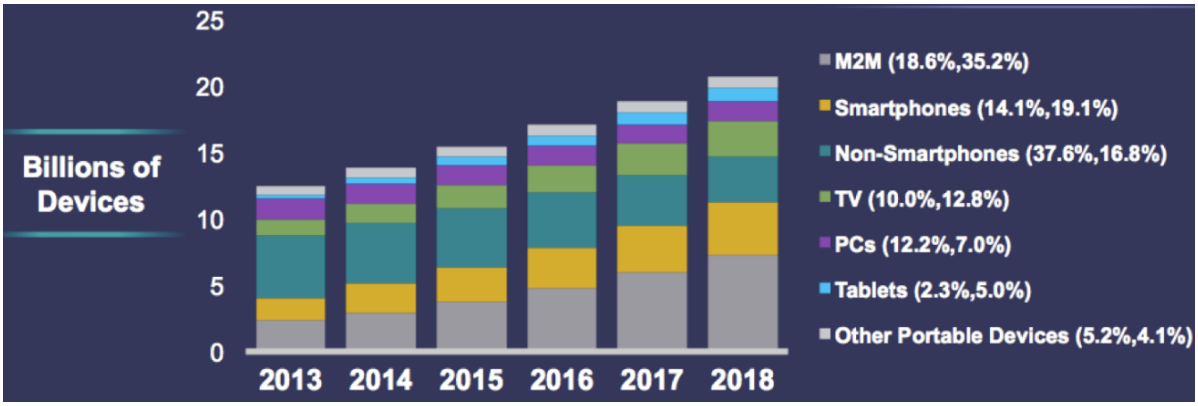

Figure 1.4 Global connected devices growth by type (Source: Cisco VNI Global IP Traffic Forecast, 2013-2018)

The vast majority of these devices mostly rely on batteries for an extended energy contribution, however, SCs for certain peak-power demands could reduce the stress of the battery, extending its life-time. These characteristics are directly connected to the energy storage mechanism that govern their processes, in general terms while batteries rely on a chemical storage through redox reactions or intercalation/deintercalation processes, SCs is governed by physical electrostatic phenomena. Other important parameters are the excellent cycle-life of SCs and the temperature operation where SCs have demonstrated great performances at low temperatures below -20 ^{o}C.[13] The main features of batteries and SCs are gathered in ***Table 1.1***.

Table 1.1 General comparison between batteries and SCs.[14]

Parameter	Battery (Li-ion)	Supercapacitor (EDLC)
Storage Mechanism	Chemical	Physical
Specific Energy (Wh·kg$^{-1}_{anodo+cathode}$)	Very High <400	Low <12
Specific Power (kW·kg^{-1})	Low<1	High 0.5-10
Charge/Discharge time	0.3-10 hours	s to min
Operating Temperature (°C)	-20 to 65	-40 to 85
Cycle-Life (cycles)	<10 000	>1 000 000
Efficiency (%)	70-99	99.9

In addition, both devices possess similar configuration consisting of two electrode materials (current collector + active material) separating by an ion-permeable membrane (separator) and

ionically connecting by an electrolyte. The two electrodes are insulated by the membrane separator, impregnated with the electrolyte. The current collectors are usually metals with high stability in the selected electrolyte and good electric contact with the electrode active material. The membrane separator only permits the ion mobility but prevents electric contact.[15] Different types of electrolytes can be distinguished depending on their chemical nature: aqueous, organic, polymer electrolytes and ionic liquids. Aqueous electrolytes have usually limited cell voltage restricted by water decomposition at 1.23 V, whereas cells based on organic electrolytes can reach voltages of 2.7 V while having lower ionic conductivities than aqueous electrolytes. Aqueous electrolytes also feature such important assets as low cost and ease in handling.[16] On the other hand, Ionic liquids are resistant to the reduction and the oxidation in a wide voltage potential window, which depends on the counter ion, providing a cell voltage of around 4.5 V, with some of them being able to reach 6 V.[17]

1.2.1 Metal-Air Batteries

To date, lithium-ion battery technology is the most developed and widely distributed energy storage system for the already mentioned applications due to their many advantages over other older technologies such as lead-acid, nickel-cadmium (Ni-Cd) and nickel-metal hydride (Ni-MH) batteries.[18–20] However, one major drawback of lithium ion batteries is that the energy density depends on the amount of active material that can be placed inside the battery due to the nature of the intercalation and de-intercalation battery chemistry.[21] The “limitation” in the energy density of lithium ion batteries, particular for EV applications, causes “range anxiety” in the buyers even though the driving range has been significantly improved over the past few years.[6]

In parallel, researchers have recently put significant research efforts in developing electrically rechargeable metal-air batteries that have theoretical energy density higher than Li-ion technology. In particular, lithium-air and Zn-air batteries have gained tremendous attention as they boost much higher energy densities compared to that of lithium-ion batteries, and are still electrically rechargeable.[22,23] Metal-air batteries consume atmospheric oxygen as cathodic active material and they become of great importance due to their singular open structure, making them more compact and less expensive than other on-going technologies. Particularly, Zn-air batteries have re-gained research attention since their initial appearance in the 1970s [25] due to recent

development of electrocatalysts make it possible to electrochemically recharge the battery and their remarkable high gravimetric and volumetric energy density, as shown in ***Figure 1.5.***

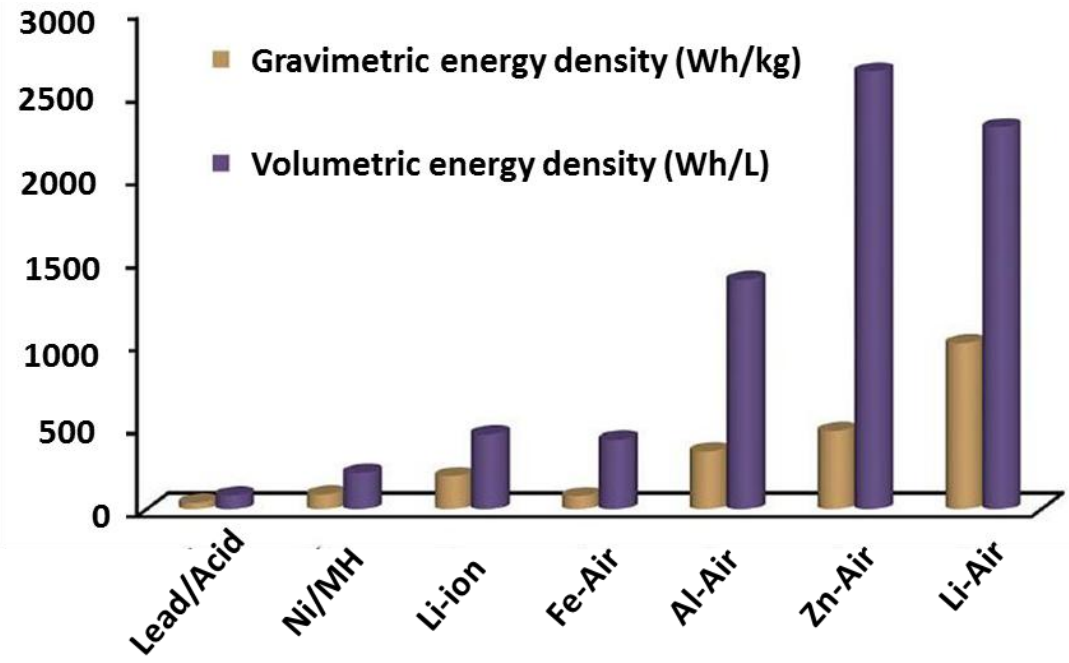

Figure 1.5 Practical gravimetric specific energy and volumetric energy density of various types of rechargeable and metal–air batteries (adapted from [24])

However, despite their promising energy storage capabilities and recent advances, low charge/discharge energy efficiencies and limited cycle stability have yet hampered their commercialization and wide spread in the market. This mainly originates from the sluggish kinetics of oxygen reduction/evolution reactions (ORR and OER), occurring during battery discharge and battery charge respectively, which is considered one of the bottlenecks of the technology. Therefore, development of efficient oxygen electrodes to speed up the kinetics and yet maintain the low-cost is certainly a key factor in success of rechargeable zinc-air technology.[26]

The use of zinc metal as the anode, which is one of Earth's most abundant elements and the water-based (aqueous) solutions as the electrolyte (as opposed to organic ones) make the rechargeable zinc-air battery development, ecofriendly attractive, safe to operate and seemingly easy to scale-up even compared to lithium/aluminum-air and commercial lithium-ion, and lead acid batteries. In addition, the oxygen drawn from atmospheric air is virtually unlimited in quantity, making zinc-air batteries extremely cost-effective. Moreover, a techno-economic analysis has predicted the price of rechargeable zinc-air batteries to be approximately a half of the current

lithium-ion battery price. As lately reported in New York Times, NantEnergy a company based in US, announced development of a rechargeable zinc-air battery technology able to store energy with less cost than commercial lithium-ion technologies. As claimed, it is possible to take commercial orders with at less $100/kWh of capacity, which is one-half to one-fifth the cost of available lithium-ion grid storage.[27,28]

Addressing the fabrication and manufacturing of zinc-air batteries, this can be done under ambient conditions due to the possibility of use aqueous electrolytes, while metals such as lithium and sodium require an inert atmosphere (organic electrolytes) for handling and fabricating the devices. A rechargeable zinc-air battery operates by combining these half reactions as shown in the schematic illustration above (***Figure 1.6***). Particularly, during discharge, electrons generated at the metallic zinc anode travel through an external connection and then reach the air cathode, forming zincates ions (i.e. $Zn(OH)_4^{2-}$) at the anode which are released into the electrolyte [Eq 1.1].

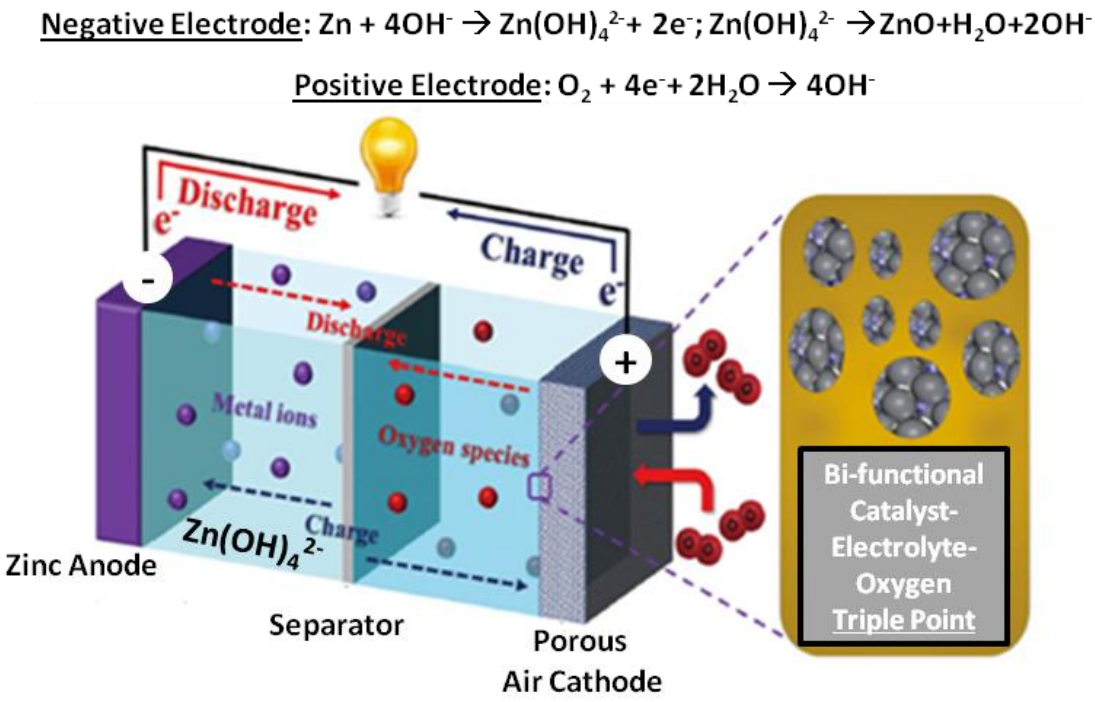

Figure 1.6 Schematic illustration of a rechargeable zinc–air battery and its operating principle based on the electrochemical oxygen reactions occurring on a bi-functionally active catalyst (adapted from [24])

Discharge usually proceeds until the electrolyte is supersaturated of $Zn(OH)_4^{2-}$ ions,[23] after which the zincates ions decompose to insoluble zinc oxide as shown by [Eq 1.2].

$$Negative\ Electrode:\ Zn + 4OH^- \rightarrow Zn(OH)_4{}^{2-} + 2e^- \quad [\text{Eq. } 1.1]$$

$$; Zn(OH)_4{}^{2-} \rightarrow ZnO + H_2O + 2OH^- \quad [\text{Eq. } 1.2]$$

$$Positive\ electrode: O_2 + 4e^- + 2H_2O \rightarrow 4OH^- \quad [\text{Eq. } 1.3]$$

$$Overall\ reaction: 2Zn + O_2 \rightarrow 2ZnO \quad [\text{Eq. } 1.4]$$

$$Parasitic\ reaction: Zn + 2H_2O \rightarrow Zn(OH)_2 + H_2 \quad [\text{Eq. } 1.5]$$

In parallel with the oxidation reaction at the negative electrode, an undesirable parasitic reaction between zinc and water can occur resulting in hydrogen gas generation [Eq 1.5]. This causes a gradual self-corrosion of the zinc metal anode, decreasing the active material utilization. At the air cathode, atmospheric oxygen enters through the pores by diffusion where it is electrochemically reduced, releasing hydroxide ions into the electrolyte [Eq 1.3]. In particular, the reduction of oxygen takes place at the triple point site where liquid(electrolyte), gas (oxygen) and solid (electrocatalyst) meet, as shown in ***Figure 1.6.***[23] Therefore, the design and optimization of air-cathode electrode play an important role in the overall performance of the zinc-air batteries, being undoubtedly one of the main objectives to be tackled in this thesis.

To further clarify the ORR/OER electrocatalyst mechanism in a Zn-air battery, the following paragraph discusses the mechanisms of ORR and OER in detail:

There are two types of classical oxygen catalysts for ORR: metals and metal oxides. For metal catalysts, such as platinum, a four-electron pathway or a two-electron pathway may proceed for the ORR, depending on the type of oxygen adsorption.[29] For metal oxide catalysts, such as spinel Co_3O_4, the ORR reaction pathways at the surface follow the same principle, but with a different charge distribution due to the surface cations of stoichiometric oxides that are not fully coordinated with oxygen atoms. These oxides or their hybrids with graphene, preferently catalyze the reaction in alkaline aqueous solutions from O_2 to H_2O in a direct 4*e* pathway, producing hydroxyl groups with a small formation of peroxide during ORR, as schematically illustrated in ***Figure 1.7.*** In aqueous electrolytes, anion coordination is completed by the oxygen of a water molecule. Consequently, the reduction of a surface cation by an electron from the external circuit is charge-compensated by protonation of a surface oxygen ligand.[30] The reaction pathway of ORR on a metal oxide surface is generally, as follow:[31]

$$2M^{m+} - O^{2-} + 2H_2O + 2e^- \rightarrow 2M^{(m-1)+}{-}OH^- + 2OH^- \text{ [Eq 1.6]}$$

$$O_2 + e^- \rightarrow O_{2\,ads-} \text{ [Eq 1.7]}$$

$$2M^{(m-1)+}{-}OH^- + O_{2\,ads-} + e^- \rightarrow 2M^{m+} - O^{2-} + 2OH^- \text{[Eq 1.8]}$$

The ORR pathways and mechanisms may vary depending on the catalyst used and its electronic structure. For instance, the degree of σ* orbital and the metal-oxygen covalency has influence on the competition between $O2^{2-}$/OH^- displacement and OH^- regeneration on the surface of transition metal ions as the rate-determining steps of the ORR. Hence, correctly tuning the electronic structure of metal oxide catalysts by optimization of the composition is crucial for obtaining high performance catalyst.[32]

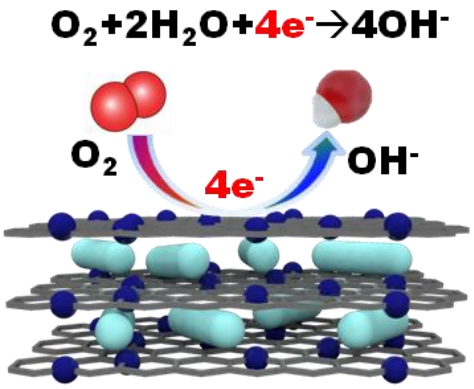

Figure 1.7 Schematic illustration of a NrGO/Co_3O_4 hybrid material catalyzing the ORR from a 4e pathway

On the other hand, the OER pathways and mechanisms are relatively complex. Generally, oxygen is evolved from an oxide phase, rather than a bare metal,[33] which means the mechanisms may vary depending on the catalyst having different site geometry of metal cations. The multi-valence characteristic of transition metal ions is important for OER because the reaction is induced by the interaction between the metal ions and oxygen intermediates which leads to the formation of a bond by changing in the valence state. The site geometry of metal cations changes the adsorption energy of the oxygen species, which determines the kinetics of OER. For a transition metal oxide catalyst, the OER in alkaline electrolyte proceeds as follows:

$$M^{m+} - O^{2-} + OH^- \rightarrow M^{(m-1)+}{-}O{-}OH^- + e^- \text{ [Eq 1.9]}$$

$$M^{(m-1)+}{-}O{-}OH^- + OH^- \rightarrow M^{m+}{-}O{-}O^{2-} + H_2O + e^- \text{[Eq 1.10]}$$

$$2M^{m+}-O-O^{2-} \rightarrow 2M^{m+}-O^{2-} + O_2 \text{ [Eq 1.11]}$$

As it is mentioned earlier, electrically rechargeable zinc–air batteries rely significantly on air (oxygen) electrodes that are bifunctionally active and durable, such that they withstand the harsh conditions during repetitive discharge and charge cycles. The development of a highly bifunctional active air electrode is quite challenging because both ORR and OER occur at high overpotentials, and thereby relies on a stable electrocatalyst. To address this, tremendous effort has been made in scientific community to explore highly active and stable bi-functional electrocatalysts. Non-precious metal alternatives commonly demonstrate high OER activity but moderate ORR catalytic properties.[34] Among them, earth-abundant transition metal oxides/sulfides, have been widely explored as promising alternatives to noble-metal nanocatalysts.[35] However, inferior electrical conductivity and tendency to form large particles/agglomerations during electrocatalytic processes limit their activity. On the other hand, carbonaceous nanomaterials (e.g. CNTs, porous carbons, graphene, rGO) when doped with heteroatoms (N, O, P, S, etc.) are proven to be effective catalysts for ORR, however they are susceptible to certain instability under OER conditions. Therefore, during the last years researchers have developed different strategies to hybridize these two families of materials forming a hybrid bi-functional electrocatalyst, which commonly demonstrate synergistically enhanced ORR and OER performance and improved durability. Typically, the carbon counterpart either acts as active component of the hybrid improving the ORR catalytic activity or as the support due to its notable electronic conductivity and high surface area. In both cases, graphene can be considered as a suitable candidate. In the former, as the building block of the carbon family, it is considered intrinsically inert, but possesses electrocatalytic activity by chemical modification or doping. In the latter, as a highly conductive support with relatively large surface area, graphene is considered an ideal substrate to anchor the metal-based catalysts on.

The integration of metal-based catalysts with graphene materials stimulates a synergistic effect arisen from: (i) new rapid electron transfer paths through the electronic interaction between the two components[36] (ii) the fact that graphene can initially facilitate the reduction of water to peroxide where metal species subsequently catalyze the reduction of peroxide to hydroxide, resulting in the overall four electron reduction process.

1.2.2 Supercapacitors (SCs)

The prosperity of portable electronics together with the exponential growth of hybrid electric vehicles in the automotive market, has promoted increasing demand for high-performance SCs. These devices, also called electrochemical capacitors (ECs) or ultracapacitors store energy using either physical ion adsorption (electrochemical double-layer capacitors (EDLCs)) or fast surface chemical redox reactions (pseudo-capacitors (PSCs). Moreover, due to similar configuration with batteries as we already tackled above, a third category could be constructed, the so-called hybrid SCs or hybrid energy storage systems. This classification, along with typical materials employed in each SCs type is schematically represented in ***Figure 1.8.***

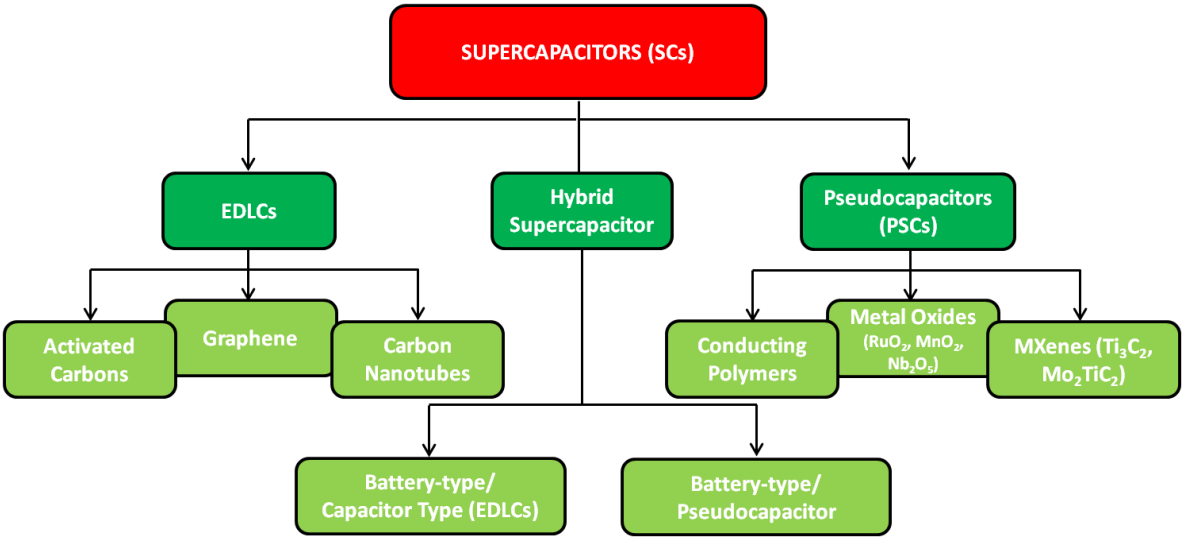

Figure 1.8 Classification of Supercapacitors (adapted from [17])

Lately, SCs have had an important role in complementing or replacing batteries in the energy storage field, when high power delivery or uptake is needed. As shown in **Figure *1.9***, SCs are prime candidates to fill the gap on the energy versus power spectrum between the high specific power provided by conventional capacitors and the high specific energy provided by batteries.[37,38] As can be seen, SCs supply a higher energy density than conventional capacitors, albeit with slightly lower values of power density. Recently, hybrid energy storage devices that strive to advance along the diagonal of a so-called simplified Ragone plot **(Figure *1.9)***, by combining the high energy content of rechargeable batteries with the high power characteristics of SCs, have been extensively explored.[14]

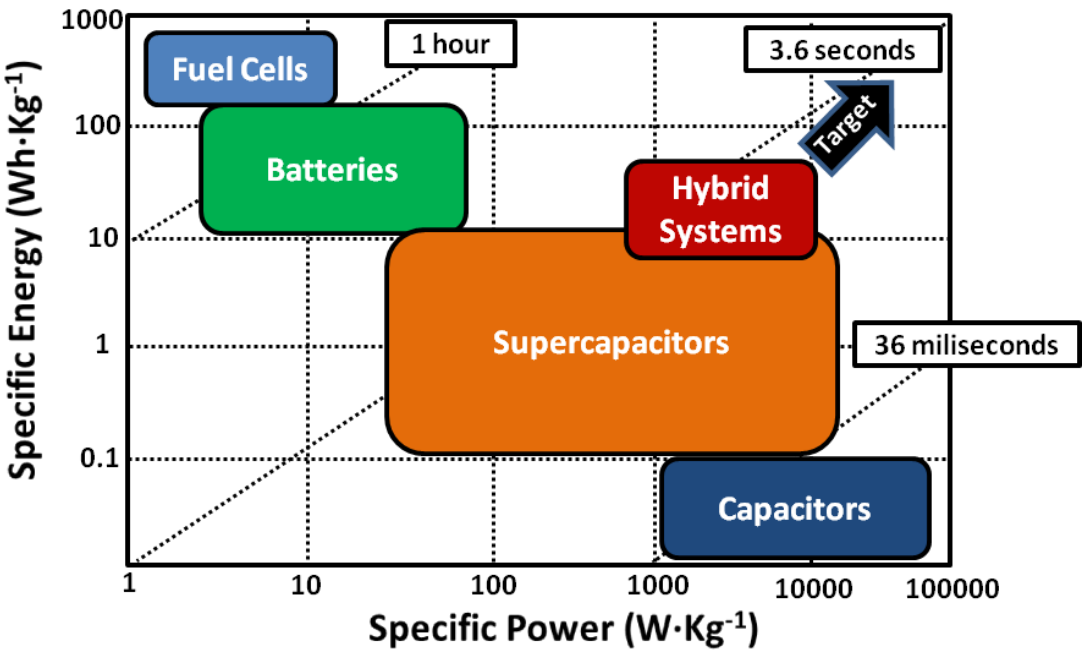

Figure 1.9 Simplified Ragone plot comparisons between different electrochemical energy conversion and storage systems

Nevertheless, the realization of high performance electrochemical energy storage devices is strongly dependent on the achievements of multidisciplinary sciences, including chemistry, physics and material sciences. In the following sections, a deep description of the different types of SCs, their components and the mechanism involved are presented.

1.2.2.1 Electrochemical Double Layer Capacitors (EDLCs)

In conventional capacitors, the electrodes are metallic plates that are separated by a dielectric material and store energy in a static electric field, while in the case of EDLCs the dielectric material is substituted by an electrolyte storing energy by the electrostatic accumulation of charges in the Helmholtz electric double layer, upon the application of a voltage near the electrode/electrolyte interface, as shown in ***Figure 1.10***.[39] This charge buildup leads to the diffusion of opposite charges across the separator, leading to the fast-creation (10^{-8} s) of a double layer on each electrode. The presence of this double layer, along with high surface area electrodes and small thickness of electrostatic double layer, enables EDLCs to have higher capacitance and therefore larger energy densities than conventional capacitors. The electrode materials for EDLCs are generally capacitor-type materials, such as activated carbon (AC), mesoporous carbon, carbon nanotubes, graphene, etc.

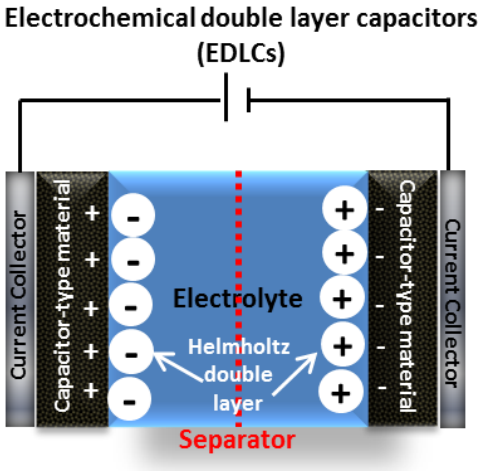

Figure 1.10 Scheme of EDLCs with capacitor-type materials as positive and negative electrodes

The electric double-layer (EDL) capacitance of an electrode, which can be calculated using the following equation, is closely dependent on the surface area of the active material:

$$C_{electrode} = \frac{\varepsilon_r \varepsilon_O}{d} A \quad [\text{Eq } 1.12]$$

where ε_r and ε_O are the relative permittivity and the dielectric constant of vacuum, respectively, *A* is the specific surface area of the electrode accessible to the electrolyte ions, and *d* is the effective thickness of the EDL. Moreover, the equation which correlated the C of each electrode ($C_{electrode}$) with the total C of the final EDLC system is calculated according to the following equation:

$$\frac{1}{C} = \frac{1}{C_{electrode1}} + \frac{1}{C_{electrode2}} \quad [\text{Eq } 1.13]$$

The energy and power densities are other important parameters related to the performance of EDLCs. Energy density is the ability to store energy and it determines how long the EDLCs can act as a power source, maximum energy density is represented by equation below:

$$E = \frac{1}{2} C V^2 \ [\text{Eq } 1.14]$$

where C represents the capacitance of the final device and V is the operation voltage window. On the other hand, power density determines how fast the energy could be released. The maximum power achievable by EDLC is given in the equation below:

$$P = \frac{V^2}{4ESR} \text{ [Eq 1.15]}$$

where V represents the voltage and ESR is the equivalent series resistance. Because of the non-faradaic nature of energy storage mechanism of EDLCs, charges are not transferred between the electrode materials and the electrolyte. Consequently, there is no compositional and phase changes on the electrodes materials during consecutive charge and discharged cycles. Thus, the EDLCs have good cycling stability, but do not exhibit a high enough energy density to meet the ever-growing need for peak-power assistance in EV.

Particularly research on graphene-based materials as electrodes for EDLCs is a rapidly advancing field.[40] Probably, the first and the most important factor to justify the employment of pure graphene in EDLCs is the theoretical specific surface area of the material, which determines the capacitance and, by extension, the SCs performance, according to [Eq 1.12]. Although, graphene has a large theoretical surface area (2600 $m^2 \cdot g^{-1}$), this area will not result in high EDLC performance if it is not accessible to electrolyte ions. On the other hand, graphene derivatives as reduced graphene oxide (rGO) formed by the reduction of graphene oxide (GO) has a specific surface area between 150 and 600 $m^2 \cdot g^{-1}$ depending on the quality of graphite employed as a raw material and the number of defects,[41] which is much less than the aforementioned theoretical value of graphene, resulting in moderate EDLCs performance. As reported by Ruoff and coworwers,[42] a symmetric EDLC based on rGO electrodes in both, positive and negative electrodes exhibited specific capacitances of 135 and 100 $F \cdot g^{-1}$ in aqueous and organic electrolytes, respectively. These moderate values of capacitance are explained since rGO generally suffers from serious agglomeration and restacking during the drying process due to the van der Waals interaction between the rGO layers. Doping with heteroatoms, such as N-doped reduced graphene oxide (N-rGO), increases the electrical conductivity, the pseudocapacitive effects[43] and thus improves the overall electrochemical performance,[44] however N-rGO still has a low specific surface area, similar to rGO. A performance comparison of various carbonaceous electrode materials for EDLCs was presented in ***Table 1.2***. As can be seen, different carbonaceous materials like Graphene or functionalized porous carbons shows superior or comparable capacitance values than the ones presented by commercial activated carbons. However, common benchmark materials will only be replaced when mass-produced and price of the aforementioned materials has the same

outstanding performance as the best activated carbons obtained in research laboratories around the globe.

Table 1.2 A comparison of various carbon electrode materials for EDLCs (adapted from [45])

Carbonaceous Material	Theoretical Specific Surface Area ($m^2 \cdot g^{-1}$)	Electrical conductivity ($S \cdot cm^{-1}$)	Cost	Aqueous electrolyte		Organic electrolyte	
				$F \cdot g^{-1}$	$F \cdot cm^{-3}$	$F \cdot g^{-1}$	$F \cdot cm^{-3}$
CNTs	120-500	10^4-10^{10}	High	50-100	<60	<60	<30
Graphene	2630	10^6	High	100-205	>100-205	80-110	>80-110
Activated Carbons	1000-3500	0.1-1	Low	<200	<80	<100	<50
Template porous carbons	500-3000	0.3-10	High	120-350	<200	60-140	<100
Functionalized porous carbons	300-2200	>300	Medium	150-300	<180	100-150	>90
Carbon aerogels	400-1000	1-10	Low	100-125	<80	<80	<40

Thus, the current challenge in the EDLCs devices is to develop carbon materials, preferably graphene-based materials with a single layer or a few layers combined with less agglomeration, large accessible specific surface area, better electrolyte affinity, a tailored pore-size distribution and high electrical conductivity to optimize the whole EDLC performance.

1.2.2.2 Pseudo-capacitors (PSCs)

In contrast to EDLCs which store energy through physical adsorption, pseudo-capacitors (PSCs) store charge through faradaic processes, which involves fast an reversible redox reactions between the electrolyte and the electroactive materials on the electrode surface, but without any bulk phase transformation as shown in ***Figure 1.11***.[46] As a result, the charge and discharge curves of these devices look like those of a typical capacitor, exhibiting a linear dependence of the charge stored with the width of the potential window. Therefore, pseudocapacitive processes differ from the ideal Nernstian processes involved in a battery-type material where faradaic reactions occur at a constant potential. There are several faradaic processes that can result in pseudocapacitance according to Conway, (i) under-potential deposition (UPD), (ii) surface redox system, and (iii) intercalation system,[47] however we will not get too bogged down in some of the details here due to the topic is not crucial for the guideline of the present thesis. Owing to its faradaic mechanism

of charge storage (faradaic in nature although the "pseudo"capacitive response) these PSCs in general display higher capacitances and specific energies than their EDLC counterparts.

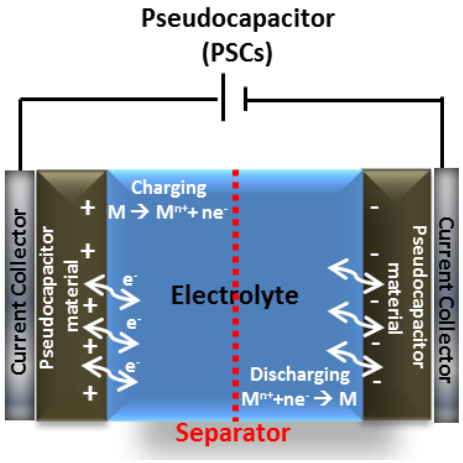

Figure 1.11 Scheme of a symmetric Pseudocapacitor

As reported by Conway and coworkers, the capacitance of pseudocapacitor materials can be 10-100 times higher than that of capacitor-type materials,[48] still holding the promise of achieving battery-level energy density combined with the cycle life and power density of capacitor-type materials. In essence, the electroactive materials, which possess various oxidation/valence states, have pseudo charge storage abilities. In this fashion, pseudocapacitor materials include certain metal oxides (e.g. MnO_2, RuO_2), conducting polymers (e.g. PANI, PPy), carbide derived carbons (e.g. Ti_3C_2) and materials possessing nitrogen and oxygen containing surface functional groups.[49] ***Figure 1.12*** compares the widely studied and most representative electrode materials for EDLCs and PSCs, including both capacitor-type electrodes and pseudocapacitor electrodes. Ruthenium oxide, has been the focus of research attention for the past few decades in PSCs technology as it has three distinct oxidation states below 1.2 V and provides very high specific capacitance (1358 $F \cdot g^{-1}$) in acidic solutions.[50] However, the high cost and low potential window render RuO_2 useless in practical terms. Many less expensive transition metal oxides, e.g. MnO_2, [51,52] have been investigated as replacements for RuO_2 but they never reach as high specific capacitance as RuO_2 does. On the other hand, although carbonaceous materials are well known to be classical capacitor-type materials for EDLCs, they also possess certain degree of pseudocapacitance. In fact, capacitor-type materials have been estimated to possess about 5-10 of their total capacitance arising from pseudocapacitance.[50] For example, functionalized CNTs or GO are known to possess faradaic functional groups on the surface that contribute to the overall capacitance of the

electrodes. In contrary, about 2-5% of total capacitance of PSCs has been reported to arise from EDLCs. Regarding the device configuration, PSCs can be symmetric (two pseudocapacitive electrode materials, ***Figure 1.11***) or asymmetric (one capacitor-type electrode material and a pseudocapacitor electrode material).

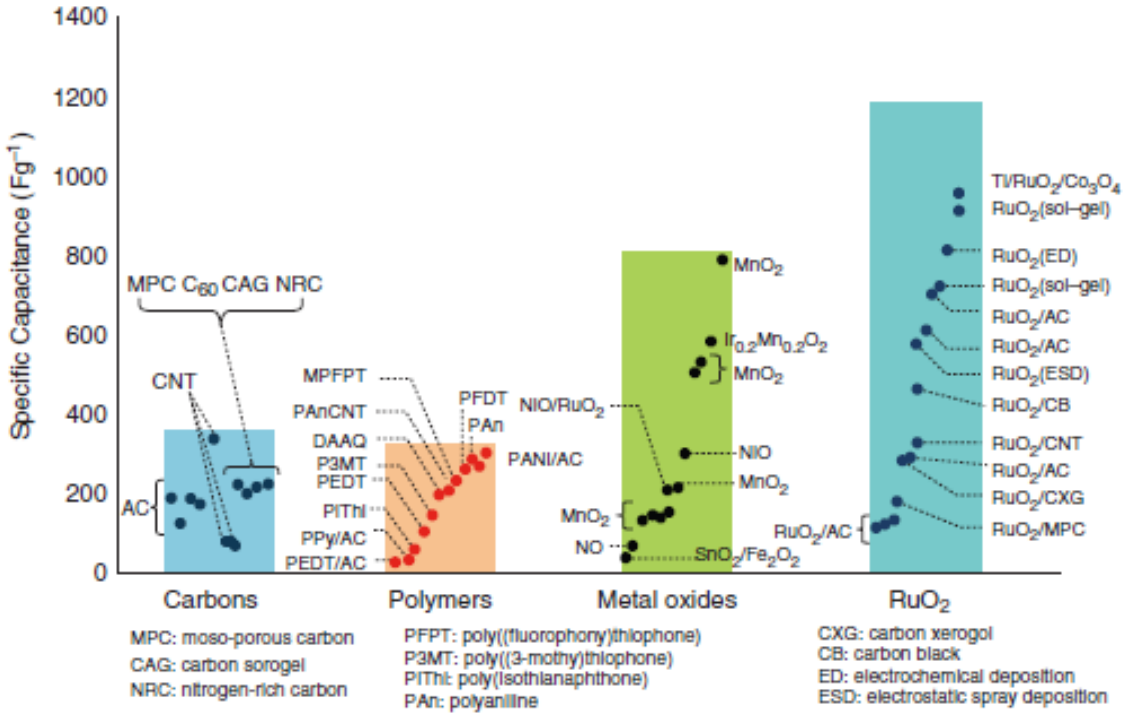

Figure 1.12 Capacitance performance for both capacitor-type electrodes and pseudocapacitor electrodes for EDLCs and PSCs, respectively (including transition metal oxides and conducting polymers) (reproduced with permission [53])

Asymmetric PSCs are used to boost the operating voltage range (and hence its energy and power density following equation 1.14 and 1.15) operating in the whole electrochemical stability window of the electrolyte. With that purpose, the negative and positive electrodes are mass balanced to compensate their different specific capacitances.

1.2.3 Hybrid Devices

One common mistake founded in literature is the indistinct use of the terms “asymmetric device” and “hybrid device”. Asymmetric SCs covers a wider range of electrode combinations because it can be used for SCs using electrodes of the same nature (i.e. capacitor-type/capacitor type) but with different mass loadings, or two electrodes with different nature (capacitor-

type/pseudocapacitor) but with capacitive electrochemical response. Brousse and coworkers suggested that the term "asymmetric" should be used only when capacitive or pseudocapacitive electrodes are involved (such as activated carbon//MnO_2)[37,54] in order to avoid confusion with the "true" hybrid devices (always a battery-type electrode involved). It has been recently well-established that the term hybrid SCs should be used when pairing two electrodes with different charge storage behavior, i.e., one capacitor-type and one battery-type (***Figure 1.13***), and the resulting electrochemical response in the device is in between a battery and a SCs (***Figure 1.14***).

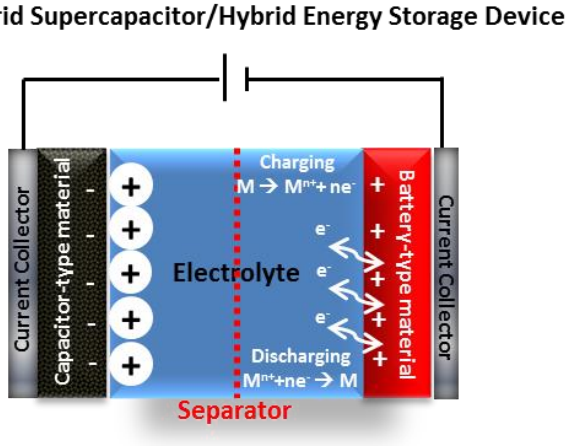

Figure 1.13 Scheme of Hybrid Supercapacitor or Hybrid Energy Storage Device

Since two different electrodes with different charge storage mechanisms are employed in a hybrid supercapacitor, these two electrodes possess different values of intrinsic capacitance/capacity.

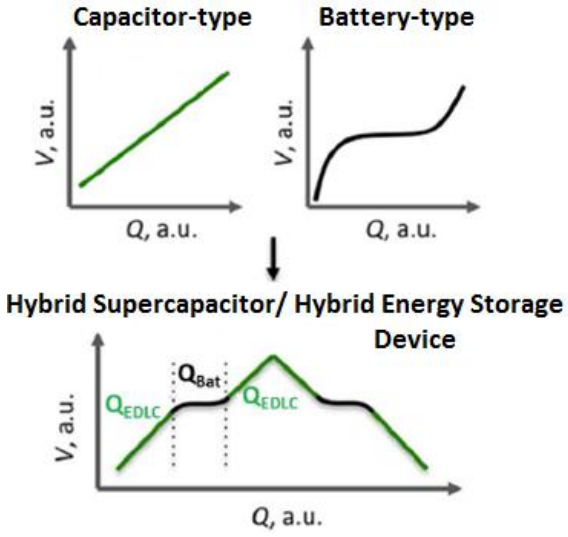

Figure 1.14 Voltage vs. capacity profiles for typical capacitor-type and battery-type materials as well as for traditional hybridization (adapted from [55])

In general, the faradaic electrode (usually in the positive side) has a much larger ability to store electrical charge than its capacitor-type counterpart (often in the negative side), and therefore the overall capacity exhibited by the device is usually limited by the capacitor-type material. Therefore, it is a key point in these devices to compensate the charge contributions of the different electrodes, in order to have a proper charge balance in the final cell. Accordingly, the negative and positive electrodes are mass balanced to compensate their different charge contributions. In addition, both electrodes should be chosen such that their potentials are either at the high or low end of the operating cell voltage (***Figure 1.15***) in order to maximize the operational voltage of the cell (second strategy to increase energy density). Based on the equation 1.14, energy increase as potential squared so, the wider the voltage window, the more is the enhancement in energy.

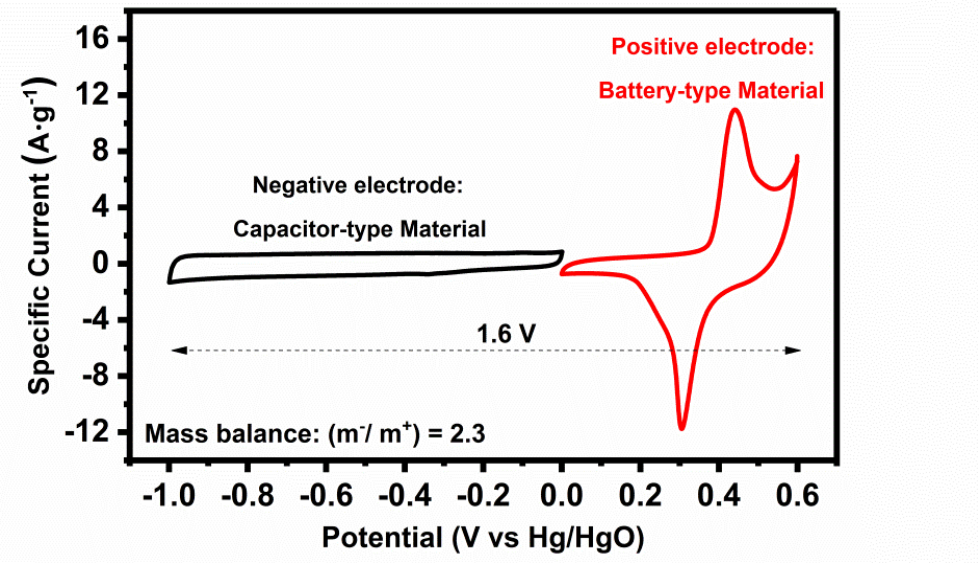

Figure 1.15 Cyclic voltammograms of electrodes in a hybrid device: capacitor-type carbon electrode/ battery-type electrode. Aqueous electrolyte (3M KOH)

The technological issues lie in the cyclability of the faradaic electrode, which is much less than that of the capacitor-type electrode. Particularly, the design of electroactive hybrid materials, combining electroactive and conducting components in a single hybrid electrode (i.e. graphene-based hybrid materials), is one way to lessen the aforementioned cycle-life concerns. But it also provides the opportunity to get all-in-one faradaic and capacitive activities displayed in parallel in a single electrode. This has led to widespread efforts in laboratories around the world to explore a

large variety of hybrid combinations in nanostructured electrode materials for different applications in novel energy storage devices.[56,57]

1.3 Materials for Electrochemical Energy Storage

In general, electrode materials can be classified according to their charge storage mechanism in three different categories: capacitor-type materials, pseudocapacitive materials and battery-type materials. However, most active electrode materials (e.g., transition−metal oxides, hydroxides, sulfides, carbides, nitrides, conducting polymers, hybrid materials, etc.) cannot be classified just by purely capacitive or faradaic contributions. Understanding the mechanism of energy storage for these materials is extremely important, not only from a fundamental point of view, but also because knowledge of charge storage and transport mechanisms builds a strong basic for the development of devices (SCs, batteries and hybrid systems) and their resulting electrochemical response. One of the first questions a researcher should answer when performing electrochemical data analysis on a new electrode material is whether the material is capacitor-type or battery-type. The introduction of the pseudocapacitive category of materials has contributed to blur the distinctions between two main fundamentally different energy-storage modalities (capacitive storage and redox/faradaic storage), leading to confusion for both readers and authors.[49,58,59]

Figure 1.16 illustrates the characteristic behavior of these electrochemical energy storage materials and summarizes the features that distinguish them from each other. In this regard, four key features are: shape of the Cyclic Voltammetry (CV), shape of the Galvanostatic Charge-Discharge (GCD), phase transformation and intrinsic kinetics, as outlined below. Any material with CV showing intense and clearly separated oxidative and reductive peaks (***Figure 1.16e***) or obvious plateaus in GCD curves (***Figure 1.16f***) should be categorized as a battery-type electrode. On the other end of the analysis, capacitor-type materials will show rectangular or nearly rectangular CV (***Figure 1.16a***) and linear voltage responses during constant-current discharging (***Figure 1.16b***). Analyzing the intrinsic kinetics of the mechanism, the peak current (i) response of a battery-type electrode material will be proportional to the square root of the scan rate ($i \sim v^{1/2}$), whereas a capacitor-type material will show linear current response dependency with the scan rate ($i \sim v$). With these concepts in mind, it should be clear what a battery-type electrode material and a capacitor-type material is when one observes their corresponding electrochemical responses. On the other hand, pseudocapacitive materials (i.e. RuO_2, MnO_2, NbO_5, conducting polymers, MXnes)

with an electrochemical signature similar to a capacitive electrode *(**Figure 1.16 c,d***) undergo fast and highly reversible redox reactions near to the surface, making them able to store more energy than typical capacitor-type materials. Basically, the term “pseudo” (by definition: not actually but having the appearance of) capacitor material was created in order to describe the properties of an electrode that behaves like a capacitor in its electrochemical signature while rapid and reversible faradaic processes involved. However, since the charge storage is governed by faradaic processes, these materials suffer from moderate cycling and relatively shorter cycle longevity as compared to capacitive materials.

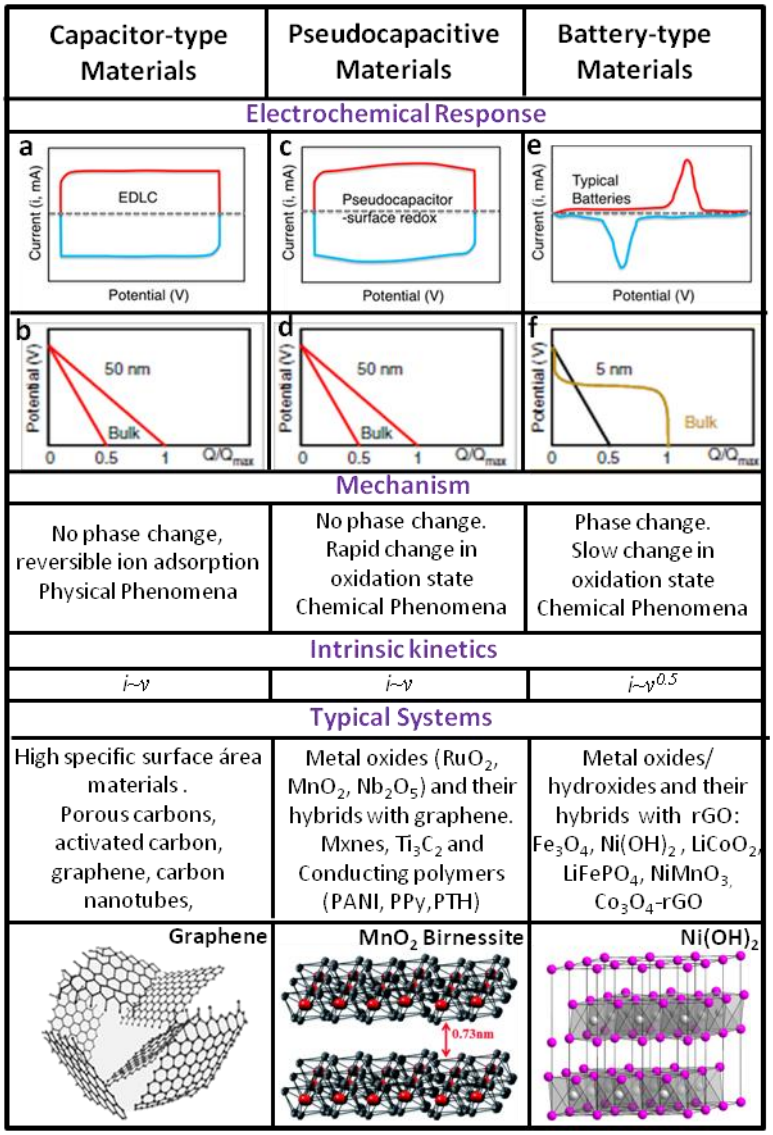

Figure 1.16 Summary of the characteristic metrics such as CV, GCD, key mechanism descriptions and typical systems that are known to classified the mentioned charge storage mechanism (adapted from [58])

A possible alternative to enhance the cyclability and longer lifespans of pseudocapacitive materials is hybridization with capacitive materials like graphene.[60–62]In view of the above classification and considering the possible hybridization of capacitor-type and pseudocapacitive/battery-type materials, the ability to deconvolute total current into contributions of different electrode materials is critically important to understand charge-storage mechanism in a hybrid device.[63]

Once electrode materials have been categorized by their energy storage mechanism, researchers should quantify the total charge (Q) stored by the material itself. This quantification has brought even more confusion for both readers and authors trying to elucidate when it is appropriate the use of the terms Capacity or Capacitance depending on the electrochemical responses. In the form of the latter, capacitance is the ability of a body to store an electrical charge. This capacitance is constant over a given voltage window and can be used to calculate the charge stored if the electrode material falls into the capacitor-type or pseudocapacitive category, using the equation below: [49]

$$\Delta Q = C \times \Delta V \quad [\text{Eq } 1.16]$$

where ΔQ (expressed in coulombs, C or mAh) is the differential charge stored, C (expressed in farads, F) is the capacitance, and ΔV(V) is the width of the voltage window. However, for a battery-type material the definition of capacitance does not apply due to the presence of voltage plateaus in charge/discharge profiles, exhibiting a non-linear dependence of the stored charge with the width of the potential window ***(Figure 1.16f)***. Here, only the capacity (ΔQ/3.6) in mAh or Coulombs (C) provides a consistent metric with which one can make a comparison against other materials. This misunderstanding resulted in appearance of many previously reported articles employing capacitance ($F \cdot g^{-1}$) for battery-type electrodes. In order to make a fair comparison with the results published in the present thesis, capacity values were calculated using the provided information in the already mentioned articles and here reported based on $mAh \cdot g^{-1}$.

Moreover, regardless of the nature of the material in question, the values reported should be normalized to the mass, area, or volume of the electrode.[64] In this regard, it should be mentioned that in some of the reported works, low mass loadings of the active materials (<1 to 2 $mg \cdot cm^{-2}$) resulted in unrealistic storage capabilities for a practical device.[65] Therefore, it is still a huge challenge to develop active materials capable of retaining high capacity at high mass loadings at a competitive cost. Summarizing, reliable material performance metrics; which often do not fit

simple “battery” or “capacitor” definitions, is a vital necessity for the research community to correctly address the description of the electrode materials. The combination of different energy storage mechanism described above in the same electrochemical energy storage system lead to improved rate performance and the ability to store larger amounts of energy over extended periods of time. However, we should be aware about the classifications depending on the charge storage mechanism, avoiding general confusions in the final response of our energy storage device.

On the other hand, about possible materials as bifunctional electrocatalysts for ORR and OER in Zn-Air Batteries, the best known are carbon supported precious metals like platinum (Pt/C) and Ru (or Ir)-based, respectively. However the use of these scarce and expensive metals based catalysts for large scale applications like EV or energy storage systems is not considered a good business for a vast commercialization. Additionally, the poor durability of these electrocatalysts make them non-appropriate for long-term usage under normal device operating conditions.[24] Even more importantly, these metal-based electrocatalyst have been usually optimized for being very active towards only one of the two oxygen reactions, triggered by the research on fuel cells (ORR) and electrolyzers (OER). However, an ideal electrocatalyst for a reversible metal-air battery must not be only non-precious (inexpensive), but also be bifunctional, capable of catalyzing both ORR (during discharge) and OER (during charge). Currently, the research on bifunctional oxygen electrocatalysts is directed towards development of non-precious metal (e.g. carbides, nitrides, oxides, hydroxides, sulfides)[66–68] and/or carbon-based (or metal-free) catalysts.[69] Within this framework, researchers attempt to utilize transition metal ions and nitrogen doped disordered carbon to fabricate advanced bifunctional electrocatalysts.[70]

Once we addressed the possible confusions in the classification of the different electrode materials and the possible candidates as electrocatalyst materials for zinc-air batteries, we will focus on justifying the different families of materials employed in the present thesis.

1.3.1 Metal Oxides

There are several challenges in the development of high performing electrochemical energy storage devices that are rooted primarily in finding electrochemically active materials that are better at both storing and delivering large amounts of energy. These functions would ideally be performed by abundant, low-cost and non-toxic materials where, for example some transition

metal oxides (TMOs) appear as an attractive solution either in the negative or positive electrode, mainly due to their fast and reversible redox reactions.[71] In recent years, different TMOs were introduced and studied as electrode materials through nanostructuring and materials engineering. Having high surface areas, porous accessible channels, and small ion diffusion paths in these nanostructures, faradaic reactions can be facilitated and taken place in faster discharge regimes. Accordingly, plenty of TMOs with various chemistries (i. e. simple or mixed metal oxides, nanostructures, hybrid materials, composites, etc.) such as NiO, Co_3O_4,CoO,Mn_3O_4, MnO_2, Fe_3O_4, Fe_2O_3, RuO_2, $NiCo_2O_4$ and so on, have been explored as high performance electrode materials for SCs, Li-ion batteries and also as electrocatalyst materials for Metal-Air Batteries or Fuel Cells.[35,72–74] Interestingly, the optimal combination of several simple TMOs leads to formation of mixed transition metal oxides (MTMOs) with two or three different metal cations, rather than mixtures of two binary or single metal oxides. These MTMOs are emerging as promising electrode materials for both Li-Ion Batteries and SCs (mostly pseudocapacitors and hybrid devices), as shown in ***Figure 1.17***, due to their high electrochemical activities owing to the complex chemical compositions and possible synergistic effects between distinct metal cations contributing to the exceptional high specific capacity/capacitance typically superior than those of the carbon-based electrode materials.[75,76] More significantly, these MTMOs usually exhibit higher electrical conductivity than simple TMOs owing to the relatively low activation energy for electron transfer between cations.[77] Moreover, the presence of multiple valence states is helpful to obtain the desirable electrochemical behavior of the as-synthesized electrocatalysts towards the ORR and OER for high-performance Metal-Air Batteries and fuel cells by providing donor–acceptor chemisorption sites for the reversible adsorption of oxygen.[24,78]

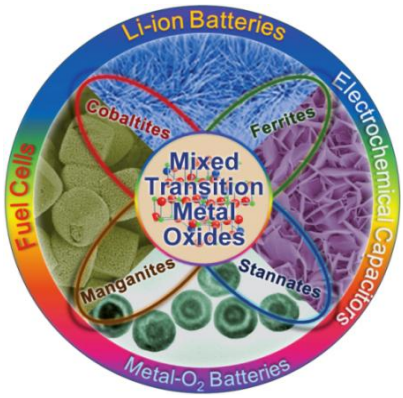

Figure 1.17 Illustrative scheme of mixed transition metal oxides and their potential applications (reproduced with permission of [76])

1.3.2 Metal Sulfides

Although more studies have been focused on the use of single or mixed metal oxides to enhance the electrochemical performance of energy storage systems (***Figure 1.18)***, recently metal sulfides (MSs) have been demonstrated to exhibit better electrical conductivity, thermal and mechanical stability and therefore higher electrochemical activity than their corresponding metal oxide counterparts, ascribed to their lower band-gap energy.[79,80]

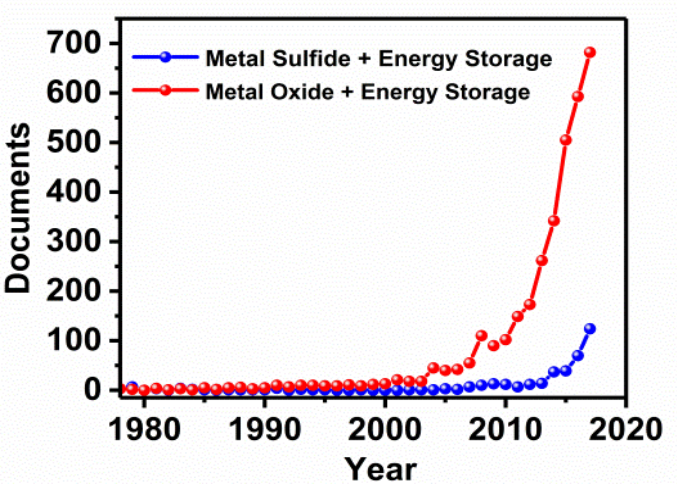

Figure 1.18 Published documents per year according to Scopus with "Metal Sulfide", "Metal Oxide" and "Energy Storage" as searching keywords

Since MSs commonly exist in nature as minerals, such as pyrite (FeS_2), chalcocite (Cu_2S), heazlewoodite (Ni_3S_2), molybdenite (MoS_2), tungstenite (WS_2) and so on; they are also considered abundant and cheap which is beneficial for exploiting large-scale facilities.[81] Moreover, their rich redox chemistry, similar to the one in metal oxides, contributes to their high specific capacity/capacitance, make them stand out from other electrode materials like carbon-based electrodes. However, the sluggish diffusivity of Li-ion in metal sulfides and the low surface area of the bulk electrodes limit their power and energy contributions, respectively. Therefore, tremendous efforts has been made in nanoestructuring electrode materials with increased surface area and improved diffusion pathways to enhance their power density for Li-ion batteries and energy density for SCs.[80]

As it happened previously with metal oxides; compared to the monometal sulfides, mixed metal sulfides (MMSs) shows richer redox chemistry and higher electronic conductivity, resulting in

significant improvement of the electrochemical performances.[82,83] As an example, $NiCo_2S_4$ displays much higher specific capacity than the corresponding monometal sulfides (Ni*S*x and Co*S*x) and exhibits an electric conductivity about 100 times that of $NiCo_2O_4$.[84] Benefiting from characteristic previously addressed and synergistic effect from two-three metal ions, MMSs have emerged as promising electrode materials for Li-Ion, Na-Ion, SCs and hybrid devices as well as great potential as bifunctional electrocatalyst for Metal-Air batteries and water splitting, as shown in ***Figure 1.19***.

Figure 1.19 Illustrative scheme of mixed metal sulfides and their potential applications (reproduced with permission of [85])

1.3.3 Graphene

Graphene, a single atom-thick layer of sp^2-bonded carbon atoms in a closely packed honeycomb lattice, has sparked unprecedented interest owing to its intrinsic properties, being considered as the basic building block for all other carbon allotropes (***Figure 1.20***).[86,87]

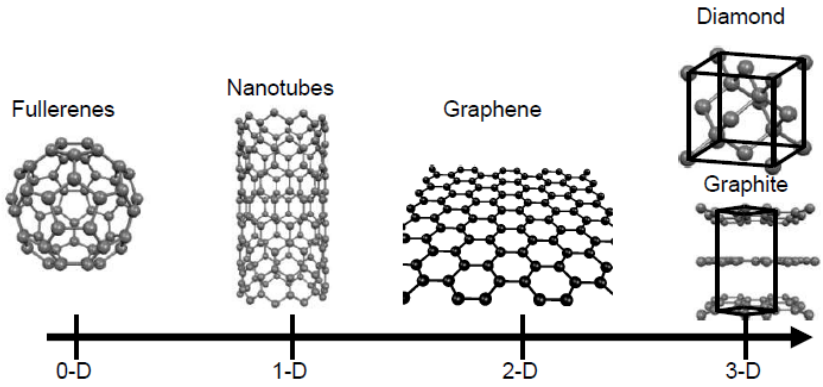

Figure 1.20 Carbon allotropes and their dimensionalities (adapted from [88])

Although the discovery of the carbon allotropes family (fullerene, nanotubes and graphene), has occurred in a recent and relatively short period of time (1985-2004) (***Figure 1.21***), these materials had been discovered and described much earlier. However, their intrinsic potential had not been appreciated in the first place. In fact, graphene was already employed in the early ´40s, in the course of studying theoretical calculations about graphite electrical properties.[89] Later, in the 1960s it was discovered that graphite intercalation compounds could be superconducting and attempts were made to prepare thin layers of graphite.[90] The term graphene was proposed for the first time in 1986 to define each of graphite layers,[91] however until 2004 scientists thought that it was a thermodynamically unstable material, when K. Novoselov and A. Geim broke the molds and could isolate graphene at the University of Manchester.[92] In fact, these scientists received the Nobel Prize in Physics in 2010 in recognition of their breakthrough.

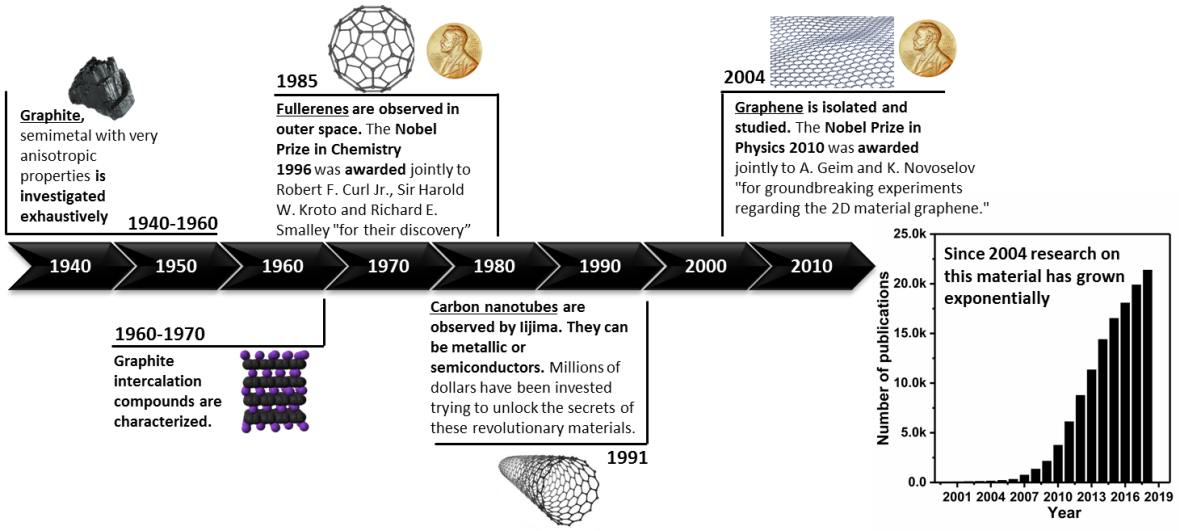

Figure 1.21 Timeline related to research carbon compounds. Number of publications per year with the keyword Graphene in the scientific search "Scopus" (adapted from [93])

Over the last years after the first isolation, descriptions such as graphite layers, carbon layers or carbon sheets have been employed for the term graphene, however the IUPAC commission has established that: "it is not correct to use, for a single layer, a term that includes graphite which implies a 3D structure. But how many layers are needed before the structure is regarded as 3D? For the case of graphene, the situation has recently become reasonably clear. In this sense, graphene has been defined as a polycyclic aromatic hydrocarbon infinitely alternating rings of only

6 carbon atoms employed as long as the number of layers is <10, with different properties of monolayer, bi-layer and multi-layer graphene. [91,94]

Since its first isolation in 2004, graphene has become one of the hottest topics in the field of materials science, and its highly appealing properties have led to a plethora of scientific papers (***Figure 1.21***). Moreover, Europe's biggest ever research-industry initiative called Graphene Flagship with a budget of €1 billion was launched in 2013 to commercialize graphene technologies within 10 years. But, why graphene awakes such a tremendous interest? Graphene is the thinnest 2D crystal material in nature, what provides it some of its extraordinary properties. It exhibits excellent mechanical,[95] electrical,[96] thermal,[97] and optical properties,[98] and is particularly suitable for the implementation in electrochemical applications because of extraordinary electrical conductivity (64 $mS \cdot cm^{-1}$)[99] large specific surface area (theoretical surface area ~2630 $m^2 \cdot g^{-1}$),[100,101] unique heterogeneous electron transfer and charge carrier rates, and good electrochemical stability.[102] Graphene and its derivatives have been used as effective counter electrodes for dye-sensitized solar cells,[103] photo-catalysts for water splitting,[104] electrocatalysts for oxygen reduction/hydrogen evolution in fuel cells,[105] high-performance electrodes in SCs,[45] ion-intercalated (Li^+, Na^+, Al^{3+}, etc.) batteries, lithium-sulfur batteries[106] and lithium-O_2 batteries,[107] as shown in ***Figure 1.22***. The synthesis of graphene in both high quality and quantity in a green and economical way is therefore highly desirable.[108,109]

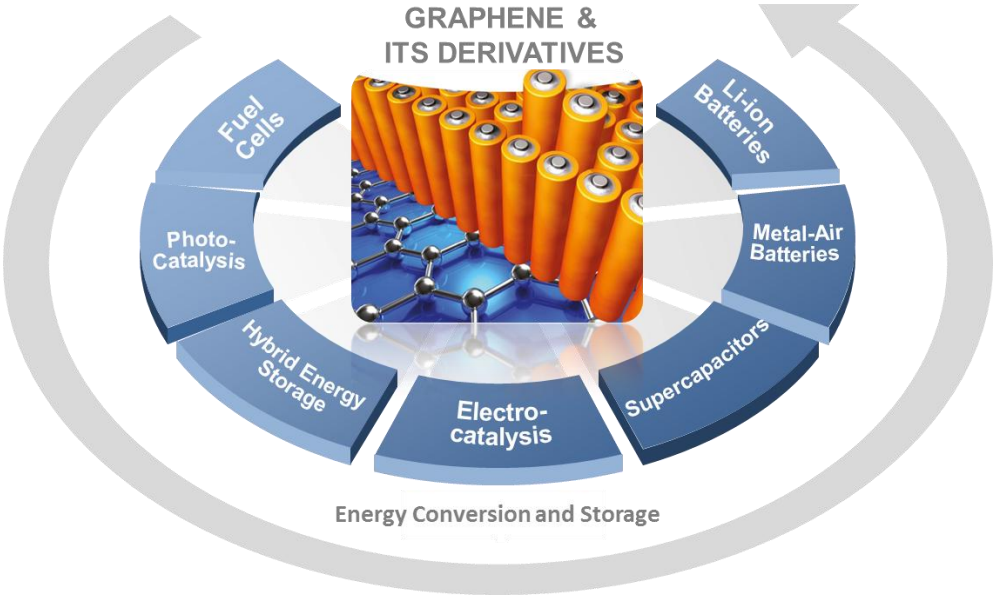

Figure 1.22 Graphene & its derivatives and their application in both energy conversion and storage devices

Since the first fabrication of single-layer graphene through micromechanical exfoliation of bulk graphite in 2004,[92] a number of methods have been proposed for producing graphene depending on the desired final application, which can be accomplished by two different approaches: bottom-up approach and top-down approach (***Figure 1.23***).[110] Bottom-up approaches, based on the catalytic decomposition of hydrocarbon gases, can provide large sized graphene with high crystal nature via epitaxial growth[111] or Chemical Vapor Deposition (CVD).[112] Top-down approaches, consisting of the intercalation of additional elements between graphite layers to form graphite intercalation compound (GIC), and then followed by the exfoliation of GIC either by physical, chemical or electrochemical methods, have received intense interest due to their scalability and low production cost.[113–116]

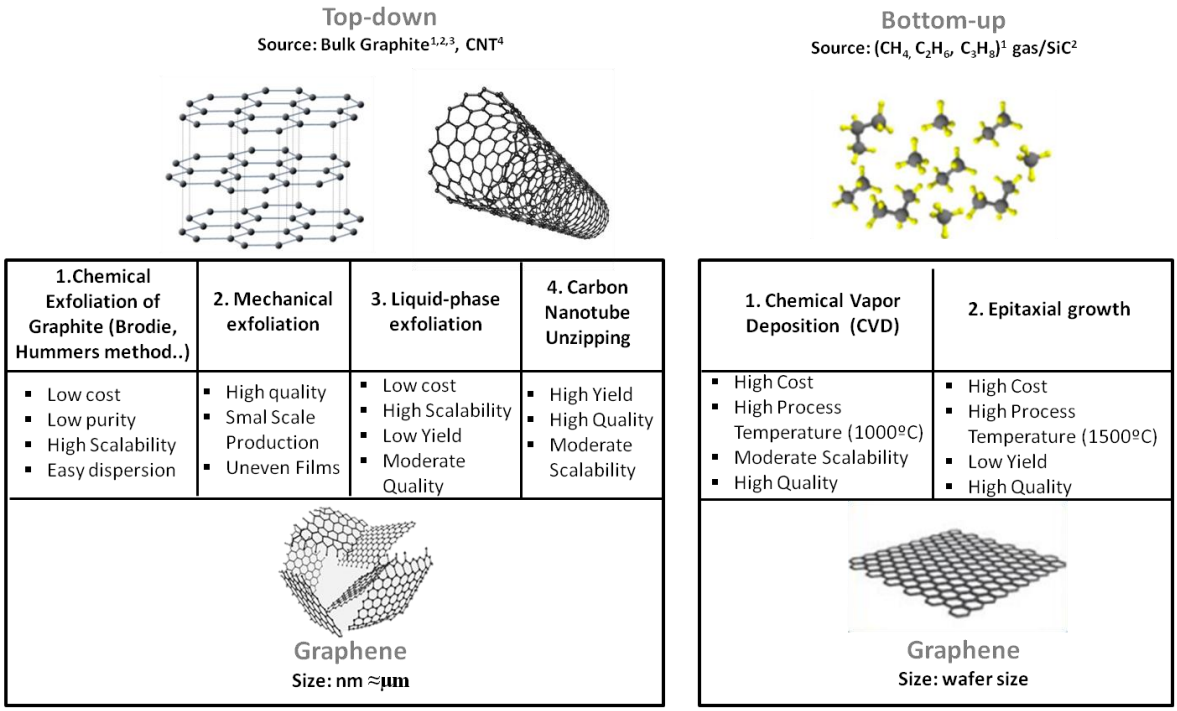

Figure 1.23 Schematic illustration of top-down and bottom-up approaches for graphene synthesis (adapted from [117])

Chemical exfoliation of graphite based on Brodie, Staudenmaier and Hummers methods, which involves the oxidation of graphite with strong acids and oxidants forming graphene oxide (GO), and subsequent chemical or thermal reduction forming reduced graphene oxide (rGO), is particularly favorable due to easy-processing and scalability.[113] Unfortunately, the use of strong acids and oxidants severely damages the sp2-covalent bonds of graphene and deteriorates its

performance in various applications even though these damages could be recovered partially by subsequent reduction process, decreasing the number of oxygen functional groups, as shown in ***Figure 1.24.***[118] The reduced graphene oxide became less hydrophilic due to the removal of oxygen atoms. The reason of re-establishment of the conjugated graphene network could be attributed to the reaction pathway proposed by Stankovich et al.[41]

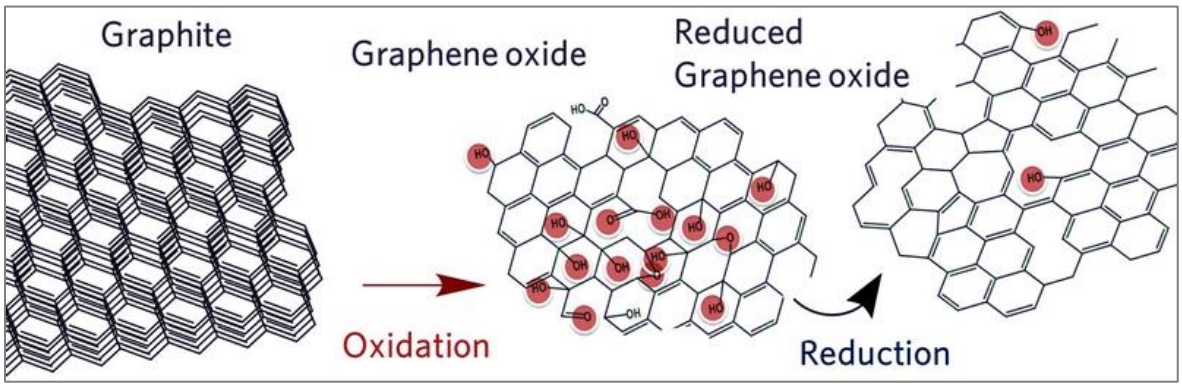

Figure 1.24 Illustration of oxidation of graphite to graphene oxide and its subsequent reduction to reduced graphene oxide (adapted from [119])

Interestingly, the mechanical exfoliation of graphite, method winner of a Nobel prize in physics in 2010, was first reported by Seibert, Kurz and coworkers in 1990,[120] and subsequently developed by Novoselov, Geim and coworkers in 2004,[92] the method is based on peeling off successively layers of graphite using a scotch tape until obtaining a single layer of graphene. The method is suitable for producing high quality graphene for laboratory research because of the few graphene processing steps required, however it is unsuitable for large-scale production because of the slow and labor-intensive nature of the process. Similar to mechanical exfoliation, graphite can be exfoliated into graphene via liquid-phase exfoliation.[114,116] However, the success of ultrasonic liquid-phase exfoliation is strongly dependent on the proper choice of solvents and surfactants as well as the sonication frequency amplitude and time, which thus impedes its practical applications. On the other hand, graphene sheets can also be produced by unzipping carbon nanotubes (CNTs) via simultaneous intercalation of NH_3-solvated Li^+ into interlayer space of MWCNTs,[121] or use strong oxidizing agents $KMnO_4$ to cut MWCNTs along the longitudinal direction.[122] Microwave-assisted heating method was also employed to treat GO, pyrolytic graphene oxide (PGO) and hydrogen-reduced pyrolytic graphene oxide (HPGO) due to the strong microwave absorption ability of graphitic materials.[123]

Although graphene can be exfoliated from graphite via the "top down" approaches as described above, these approaches are not suitable for producing large-area, high quality graphene films. Therefore, for determined applications like sensors or electronic devices "bottom up" approaches including CVD and epitaxial growth are desirable. In CVD method, hydrocarbon compounds are pyrolized on the surface of a metal catalyst at high temperatures.[124] High quality, large-area graphene was successfully obtained by these methods, however it is extremely challenging to control the manufacturing process, consequently increasing the manufacturing cost. Additionally, the as-prepared graphene film cannot be easily manipulated.

Beyond all the methods already described, the chemical exfoliation method is thought to be an efficient route for synthesizing graphene on a large scale and at low cost, although it is difficult to obtain single-layer high quality graphene because of the defect creation during exfoliation.[113]

1.3.4 Why Graphene-Based Hybrid Materials?

Among the many affected areas of materials science, the rise of graphene has influenced particularly the world of electrochemical energy storage devices as we highlighted in previous sections, mainly due to the high electrical conductivity and relatively large specific surface area of graphene.[101] However, most of the research studies have not used graphene in its pure form (pristine graphene) due to its limited yield from the preparation point of view. In this fashion, graphene derivatives such as GO and rGO with a potential high scalability have become more attractive as active electrode material or conductive support for certain applications such as electrochemical energy storage devices. Different from CVD graphene, GO and rGO have usually more layers and many functional groups (carboxylic acid groups at the edges, epoxy and hydroxyl groups on the basal plane) and defects on surface. Therefore, the surface and electrical properties of GO and rGO are very different to those superior properties ascribed to CVD graphene.[125] Nevertheless, these functional groups (***Figure 1.25***) play a significant role as initial nucleation sites to grow/anchor other nanomaterials by hydrothermal or electrostatic processes and vapor depositions via covalent bonding; hence, GO is more used for synthesis of graphene-based hybrid nanostructures. Moreover, forming hybrid materials with pristine graphene sheet has known to be difficult, because it is chemically stable and non-active.[126–128] Hybrid nanostructures synthesized with graphene derivatives could be divided into two categories depending on the nature of the

integrated compounds: graphene-based inorganic materials and graphene-based organic materials.

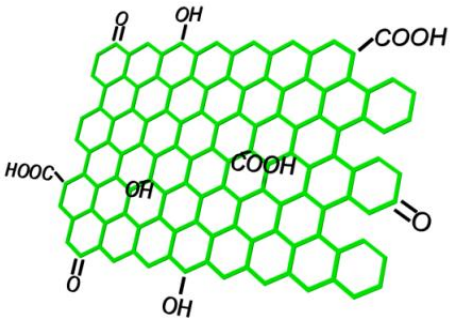

Figure 1.25 Schematic illustration of GO layer

There has been considerable research on how graphene could be integrated with carbon materials, transition single or mixed metal oxides, sulfides, hydroxides, conducting polymers, metal organic frameworks (MOFs) and biomolecules to produce hybrids with excellent electrochemical properties, as shown in ***Figure 1.26.***[118,129] In the present thesis, we will focus on different graphene-based inorganic structures, especially graphene hybridized with different metal oxide/sulfide nanostructures.

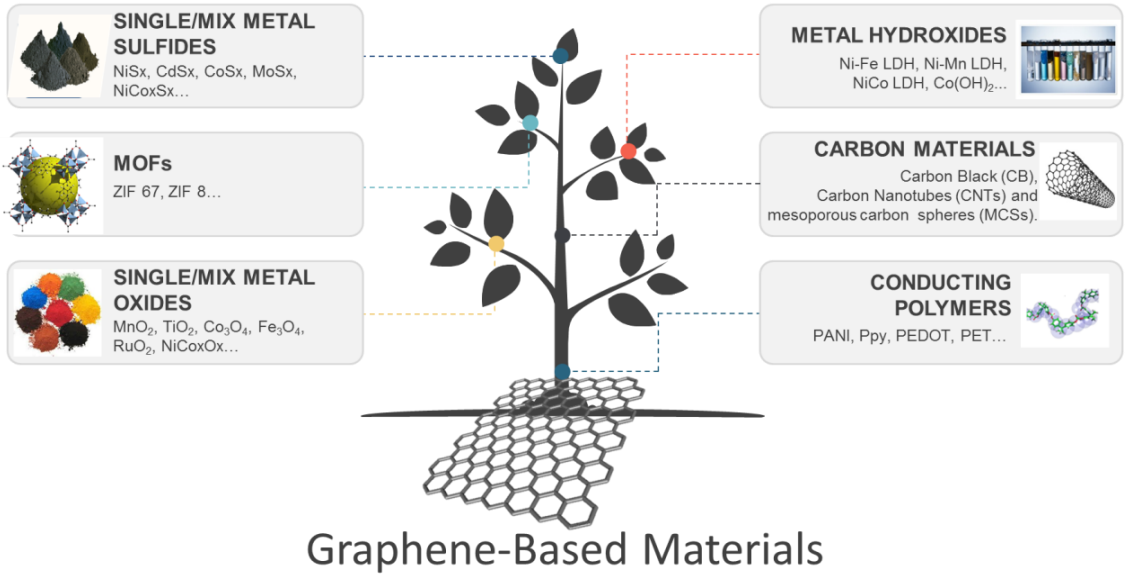

Figure 1.26 Schematic illustration of the different Graphene-Based Materials

Although, graphene is predicted to have a large specific surface area, the electrochemical performance of rGO is strongly affected by the inevitable aggregation or restacking of individual graphene sheets as a result of the interlayer π-π interaction, decreasing the electrolyte ion accessible surface area.[42,130,131] In order to inhibit or prevent the restacking of single-layer graphene sheets, different strategies have been developed.[132–134] Intercalating "stabilizers" or "spacers" such as metal, polymers or carbon nanotubes with different morphologies between the graphene layers has proved to be an easy way and effective method to avoid partially the restacking.[135–137] On the other hand, heteroatom-doping via the introduction of heteroatoms (e.g., nitrogen, boron, phosphorus) into graphene structure, increase the electrical conductivity arising from the doping-assisted network restoration particularly useful for energy storage and conversion.[138,139]

Many approaches have been reported to load single or mixed transition metal oxides on graphene sheets with the aim of enhancing the effective surface area (suppressing the restacking and helping the particle decoration) and introducing additional redox/faradaic capacity, as shown in ***Figure 1.27.***[140,141] Moreover, it has been already realized in the case of oxides/sulphides that presence of multi-valence transition metals (forming mixed transition metal oxides/sulphides) empowers them to achieve superior performance compared to their single counterparts.[85,142] In this regard, different structures, such as those of ruthenium, manganese, cobalt, nickel, copper, iron, and vanadium, synthesized with different morphologies (nanoparticles, nanorods, nanosheets…) have been incorporated in their simple or mixed state into graphene and their electrochemical properties have been studied intensively as electrode materials for SCs or bifunctional electrocatalyst materials for rechargeable metal-air batteries.[24,127,143–145]

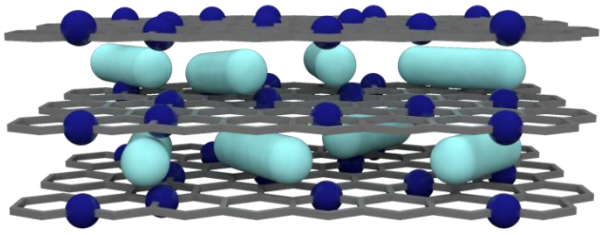

Figure 1.27 Schematic illustration of metal nanorods intercalated between N-rGO layers

To definitively understand why we selected the synthesis of different graphene-based hybrid materials as a key point of the present thesis in the fabrication of various electrochemical energy conversion and storage devices, the paragraphs above can be summarized as follows:

1) Some of the transition metal compounds (e.g. oxides and sulfide) suffer from poor electrical conductivity and hence can benefit from the excellent conductivity of graphene.
2) rGO, although having a large specific surface area, has a high tendency of agglomeration and restacking; the transition metal compounds, on the other hand, can suppress this restacking by acting as “spacers” or “stabilizers” between the graphene sheets.
3) Oxygen functional groups creating during GO synthesis help the decoration and homogeneously distribution of different transition metal compounds on the surface of graphene.

Although significant process has been made until now, the exploring of graphene-based hybrid materials for their practical applications in energy storage devices including high power energy storage devices and rechargeable batteries is highly-desirable and meaningful. These issues and challenges will be addressed to some extent in this thesis.

1.4 References

1 J. M. Cullen, J. M. Allwood and E. H. Borgstein, *Environ. Sci. Technol.*, 2011, **45**, 1711–1718.

2 I. Hadjipaschalis, A. Poullikkas and V. Efthimiou, *Renew. Sustain. Energy Rev.*, 2009, **13**, 1513–1522.

3 B. Dunn, H. Kamath and J. M. Tarascon, *Science (80-.).*, 2011, **334**, 928–935.

4 S. Sorrell, *Renew. Sustain. Energy Rev.*, 2015, **47**, 74–82.

5 D. Cahen and I. Lubomirsky, *Mater. Today*, 2008, **11**, 16–20.

6 A. Schmid, *An Anal. Environ. Impact Electr. Veh. Missouri S&T's Peer to Peer*, 2017, **1**, 1–9.

7 I. E. Agency, *World Energy Outlook 2018 (WEO 2018)*, 2018.

8 A. Zerrahn, W. P. Schill and C. Kemfert, *Eur. Econ. Rev.*, 2018, **108**, 259–279.

9 P. E. Bett and H. E. Thornton, *Renew. Energy*, 2016, **87**, 96–110.

10 K. Engeland, M. Borga, J. D. Creutin, B. François, M. H. Ramos and J. P. Vidal, *Renew. Sustain. Energy Rev.*, 2017, **79**, 600–617.

11 T. W. Brown, T. Bischof-Niemz, K. Blok, C. Breyer, H. Lund and B. V. Mathiesen, *Renew. Sustain. Energy Rev.*, 2018, **92**, 834–847.

12 D. Sprake, Y. Vagapov, S. Lupin and A. Anuchin, in *Internet Technologies and Applications (ITA) Conference*, 2017, pp. 137–142.

13 T. A. Smith, J. P. Mars and G. A. Turner, in *IEEE 33rd Annual IEEE Power Electronics Specialists Conference*, 2002, pp. 124–128.

14 A. Noori, M. F. El-Kady, M. S. Rahmanifar, R. B. Kaner and M. F. Mousavi, *Chem. Soc. Rev.*, 2019, **48**, 1272–1341.

15 L. Zhang, X. Hu, Z. Wang, F. Sun and D. G. Dorrel, *Renew. Sustain. energy Rev.*, 2018, **81**, 1868–1878.

16 F. Béguin, V. Presser, A. Balducci and E. Frackowiak, *Adv. Mater.*, 2014, **26**, 2219–2251.

17 A. González, E. Goikolea, J. A. Barrena and R. Mysyk, *Renew. Sustain. Energy Rev.*, 2016, **58**, 1189–1206.

18 C. Julien, A. Mauger, A. Vijh and K. Zaghib, in *Lithium Batteries: Science and Technology*, 2015, pp. 1–619.

19 H. C. Hesse, M. Schimpe, D. Kucevic and A. Jossen, *Energies*, 2017, **10**, 1–42.

20 G. Pistoia, *Batteries for portable devices*, Elsevier, 2005.

21 A. Rahman, X. Wang and C. Wen, *J. Electrochem. Soc.*, 2013, **160**, 1759–1771.

22 J. Fu, Z. P. Cano, M. G. Park, A. Yu, M. Fowler and Z. Chen, *Adv. Mater.*, 2017, **29**, 1604685–1604719.

23 J. S. Lee, S. T. Kim, R. Cao, N. S. Choi, M. Liu, K. T. Lee and J. Cho, *Adv. Energy Mater.*, 2011, **1**, 34–50.

24 D. U. Lee, P. Xu, Z. P. Cano, A. G. Kashkooli, M. G. Park and Z. Chen, *J. Mater. Chem. A*, 2016, **4**, 7107–7134.

25 C. Chakkaravarthy, C. Electrochemical, A. K. A. Waheed and H. V. K. Udupa, *J. Power Sources*, 1981, **6**, 203–228.

26 V. Neburchilov, H. Wang, J. J. Martin and W. Qu, *J. Power Sources*, 2010, **195**, 1271–1291.

27 NantEnergy U.S., https://nantenergy.com/zinc-air/.

28 Y. Li and H. Dai, *Chem Soc Rev*, 2014, **43**, 5257–5275.

29 J. S. Spendelow and A. Wieckowski, *Phys. Chem. Chem. Phys.*, 2007, **9**, 2654–2675.

30 W. Reitz, *Handbook of Fuel Cells: Fundamentals, Technology, and Applications*, Wiley, 2007.

31 F. Cheng and J. Chen, *Chem. Soc. Rev.*, 2012, **41**, 2172–2192.

32 J. Suntivich, H. A. Gasteiger, N. Yabuuchi, H. Nakanishi, J. B. Goodenough and Y. Shao-Horn, *Nat. Chem.*, 2011, **3**, 546–550.

33 L. Jörissen, *J. Power Sources*, 2006, **155**, 23–32.

34 F. Lu, M. Zhou, Y. Zhou and X. Zeng, *Small*, 2017, **13**, 1701931–1701949.

35 F. Song, L. Bai, S. Lee, C. Hu, L. Liardet, X. Hu, F. Song, L. Bai, A. Moysiadou, S. Lee, C. Hu and L. Liardet, *J Am Chem Soc*, 2018, **25**, 7748–7759.

36 Y. Liang, H. Wang, J. Zhou, Y. Li, J. Wang, T. Regier and H. Dai, *J. Am. Chem. Soc.*, 2012, **134**, 3517–3523.

37 J. W. Long, D. Bélanger, T. Brousse, W. Sugimoto, M. B. Sassin and O. Crosnier, *MRS Bull.*, 2011, **36**, 513–522.

38 G. Yu, X. Xie, L. Pan, Z. Bao and Y. Cui, *Nano Energy*, 2013, **2**, 213–234.

39 J. Xie, P. Yang, Y. Wang, T. Qi, Y. Lei and C. M. Li, *J. Power Sources*, 2018, **401**, 213–223.

40 Q. Ke and J. Wang, *J. Mater.*, 2016, **2**, 37–54.

41 S. Stankovich, D. a. Dikin, R. D. Piner, K. a. Kohlhaas, A. Kleinhammes, Y. Jia, Y. Wu, S. T. Nguyen and R. S. Ruoff, *Carbon N. Y.*, 2007, **45**, 1558–1565.

42 M. D. Stoller, S. Park, Y. Zhu, J. An and R. S. Ruoff, *Nano Lett.*, 2008, **8**, 3498–3502.

43 X. Wang, X. Li, L. Zhang, Y. Yoon, P. K. Weber, H. Wang, J. Guo and H. Dai, *Science (80-.).*, 2009, **324**, 768–771.

44 Y. Qiu, X. Zhang and S. Yang, *Phys. Chem. Chem. Phys.*, 2011, **13**, 12554–12558.

45 L. L. Zhang, R. Zhou and X. S. Zhao, *J. Mater. Chem.*, 2010, **20**, 5983–5992.

46 C. Costentin, T. R. Porter and J. M. Savéant, *ACS Appl. Mater. Interfaces*, 2017, **9**, 8649–8658.

47 B. E. Conway and W. G. Pell, *J. Solid State Electrochem.*, 2003, **7**, 637–644.

48 B. E. Conway, V. Birss and J. Wojtowicz, *J. Power Sources*, 1997, **66**, 1–14.

49 T. Brousse, D. Belanger and J. W. Long, *J. Electrochem. Soc.*, 2015, **162**, 5185–5189.

50 B. E. Conway, *Electrochemical Supercapacitors, Scientific Fundamentals and Technological Applications,* Kluwer Acadamic/Plenum, 1999.

51 O. Ghodbane, J. L. Pascal and F. Favier, *ACS Appl. Mater. Interfaces*, 2009, **1**, 1130–1139.

52 I. Ryu, G. Kim, H. Yoon, S. J. Ahn and S. Yim, *RSC Adv.*, 2016, **6**, 102814–102820.

53 K. Naoi and P. Simon, *Electrochem. Soc. Interface*, 2008, **17**, 34–37.

54 T. Brousse, P. L. Taberna, O. Crosnier, R. Dugas, P. Guillemet, Y. Scudeller, Y. Zhou, F. Favier, D. Bélanger and P. Simon, *J. Power Sources*, 2007, **173**, 633–641.

55 A. Vlad, N. Singh, J. Rolland, S. Melinte, P. M. Ajayan and J.-F. Gohy, *Sci. Rep.*, 2014, **4**, 4315–4322.

56 Q. Shi, Y. Cha, Y. Song, J. I. Lee, C. Zhu, X. Li, M. K. Song, D. Du and Y. Lin, *Nanoscale*, 2016, **8**, 15414–15447.

57 B. Zhao, D. Chen, X. Xiong, B. Song, R. Hu, Q. Zhang, B. H. Rainwater, G. H. Waller, D. Zhen, Y. Ding, Y. Chen, C. Qu, D. Dang, C. P. Wong and M. Liu, *Energy Storage Mater.*, 2017, **7**, 32–39.

58 M. R. Lukatskaya, B. Dunn and Y. Gogotsi, *Nat. Commun.*, 2016, **7**, 12647–12660.

59 Y. Gogotsi and R. M. Penner, *ACS Nano*, 2018, **12**, 2081–2083.

60 A. A. El-Moneim, *Mater. Today Energy*, 2017, **3**, 24–31.

61 S. Kong, K. Cheng, T. Ouyang, Y. Gao, K. Ye, G. Wang and D. Cao, *Electrochim. Acta*, 2017, **246**, 433–442.

62 J. Shen, T. Li, W. Huang, Y. Long, N. Li and M. Ye, *Electrochim. Acta*, 2013, **95**, 155–161.

63 M. Forghani and S. W. Donne, *J. Electrochem. Soc.*, 2018, **165**, 664–673.

64 Y. Gogotsi and P. Simon, *Science (80-.).*, 2011, **334**, 917–918.

65 X. Li, J. Shen, W. Sun, R. Wang, X. Hong, X. Zhao and X. Yan, *J. Mater. Chem. A*, 2015, **3**, 13244–13253.

66 Y. N. Regmi, G. R. Waetzig, K. D. Duffee, S. M. Schmuecker, J. M. Thode and B. M. Leonard, *J. Mater. Chem. A*, 2015, **3**, 10085–10091.

67 Q. Wang, L. Shang, R. Shi, X. Zhang, Y. Zhao, G. I. N. Waterhouse, L. Z. Wu, C. H. Tung and T. Zhang, *Adv. Energy Mater.*, 2017, **7**, 1700467–1700474.

68 H. F. Wang, C. Tang, B. Wang, B. Q. Li and Q. Zhang, *Adv. Mater.*, 2017, **29**, 1702327–170336.

69 X. Liu and L. Dai, *Nat. Rev. Mater.*, 2016, **1**, 16064–16076.

70 T. Liu, F. Yang, G. Cheng and W. Luo, *Small*, 2018, **14**, 1703748–1703757.

71 V. Augustyn, P. Simon and B. Dunn, *Energy Environ. Sci.*, 2014, **7**, 1597–1614.

72 D. Wang and D. Astruc, *Chem. Soc. Rev.*, 2017, **46**, 816–854.

73 W. Zhang, F. Liu, Q. Li, Q. Shou, J. Cheng, L. Zhang, B. J. Nelson and X. Zhang, *Phys. Chem. Chem. Phys.*, 2012, **14**, 16331–16337.

74 J. Zhang and A. Yu, *Sci. Bull.*, 2015, **60**, 823–838.

75 S. Tajik, D. P. Dubal and P. Gomez-romero, *Int. J. Hydrogen Energy*, 2017, **42**, 12384–12395.

76 Y. Xie, X. W. Lou, C. Yuan, H. Bin Wu, Y. Xie, X. Wen and D. Lou, *Angew. Chem. Int.*, 2014, **53**, 1488–1504.

77 L. Hu, L. Wu, M. Liao, X. Hu and X. Fang, *Adv. Funct. Mater.*, 2012, **22**, 998–1004.

78 F. Cheng, J. Shen, B. Peng, Y. Pan, Z. Tao and J. Chen, *Nat. Chem.*, 2011, **3**, 79–84.

79 Y. Zhang, Q. Zhou, J. Zhu, Q. Yan, S. X. Dou and W. Sun, *Adv. Funct. Mater.*, 2017, **27**, 1702317–1702351.

80 X. Rui, H. Tan and Q. Yan, *Nanoscale*, 2014, **6**, 9889–9924.

81 Y. Liu, Y. Li, H. Kang, T. Jin and L. Jiao, *Mater. Horizons*, 2016, **3**, 402–421.

82 J. Staszak-Jirkovský, C. D. Malliakas, P. P. Lopes, N. Danilovic, S. S. Kota, K. C. Chang, B. Genorio, D. Strmcnik, V. R. Stamenkovic, M. G. Kanatzidis and N. M. Markovic, *Nat. Mater.*, 2016, **15**, 197–203.

83 L. Shen, L. Yu, H. Bin Wu, X. Y. Yu, X. Zhang and X. W. Lou, *Nat. Commun.*, 2015, **6**, 6694–6702.

84 H. Chen, J. Jiang, L. Zhang, H. Wan, T. Qi and D. Xia, *Nanoscale*, 2013, **5**, 8879–8883.

85 X. Y. Yu and X. W. Lou, *Adv. Energy Mater.*, 2017, **8**, 1701592–1701629.

86 A. Hirsch, *Nat. Mater.*, 2010, **9**, 868–871.

87 A. K. Geim, *Science (80-.).*, 2014, **1530**, 1530–1534.

88 A. Al-Jumaili, S. Alancherry, K. Bazaka and M. V. Jacob, *Materials (Basel).*, 2017, **10**, 1–26.

89 C. Soldano, A. Mahmood and E. Dujardin, *Carbon N. Y.*, 2010, **48**, 2127–2150.

90 C. Roscoe and J. M. Thomas, *Proc. R. Soc. A Math. Phys. Eng. Sci.*, 1967, **297**, 397–407.

91 V. Singh, D. Joung, L. Zhai, S. Das, S. I. Khondaker and S. Seal, *Prog. Mater. Sci.*, 2011, **56**, 1178–1271.

92 K. S. Novoselov, A. K. Geim, S. V Morozov, D. Jiang, Y. Zhang, S. V Dubonos, I. V Grigorieva and A. A. Firsov, *Science (80-.).*, 2004, **306**, 666–669.

93 J. G. Carmona, M. A. H. Vozmediano and F. Guinea, *Investig. Cienc.*, 2010, **408**, 42–48.

94 A. K. Geim and K. S. Novoselov, *Nat. Mater.*, 2007, **6**, 183–191.

95 C. Lee, X. Wei, J. W. Kysar and J. Hone, *Science (80-.).*, 2008, **321**, 385–388.

96 K. I. Bolotin, K. J. Sikes, Z. Jiang, M. Klima, G. Fudenberg, J. Hone, P. Kim and H. L. Stormer, *Solid State Commun.*, 2008, **146**, 351–355.

97 A. A. Balandin, S. Ghosh, W. Bao, I. Calizo, D. Teweldebrhan, F. Miao and C. N. Lau, *Nano Lett.*, 2008, **8**, 902–907.

98 S. Bae, H. Kim, Y. Lee, X. Xu, J.-S. Park, Y. Zheng, J. Balakrishnan, T. Lei, H. Ri Kim, Y. Il Song, Y.-J. Kim, K. S. Kim, B. Özyilmaz, J.-H. Ahn, B. H. Hong and S. Iijima, *Nat. Nanotechnol.*, 2010, **5**, 574–578.

99 X. Wang, L. Zhi and K. Mu, *Nano Lett.*, 2008, **8**, 323–327.

100 P. Martin, *Chem. Rec.*, 2009, **9**, 211–223.

101 R. Raccichini, A. Varzi, S. Passerini and B. Scrosati, *Nat. Mater.*, 2015, **14**, 271–279.

102 D. A. C. Brownson, D. K. Kampouris and C. E. Banks, *J. Power Sources*, 2011, **196**, 4873–4885.

103 E. Singh and H. S. Nalwa, *Sci. Adv. Mater.*, 2015, **7**, 1863–1912.

104 N. Zhang, Y. Zhang and Y. J. Xu, *Nanoscale*, 2012, **4**, 5792–5813.

105 R. Yadav, A. Subhash, N. Chemmenchery and B. Kandasubramanian, *Ind. Eng. Chem. Res.*, 2018, **57**, 9333–9350.

106 S. Wu, R. Ge, M. Lu, R. Xu and Z. Zhang, *Nano Energy*, 2015, **15**, 379–405.

107 B. Sun, B. Wang, D. Su, L. Xiao, H. Ahn and G. Wang, *Carbon N. Y.*, 2012, **50**, 727–733.

108 A. Ali Tahir, H. Ullah, P. Sudhagar, M. Asri Mat Teridi, A. Devadoss and S. Sundaram, *Chem. Rec.*, 2016, **16**, 1591–1634.

109 Y. Sun, Q. Wu and G. Shi, *Energy Environ. Sci.*, 2011, **4**, 1113–1132.

110 M. Pumera, *Chem. Soc. Rev.*, 2010, **39**, 4146–4157.

111 K. V Emtsev, A. Bostwick, K. Horn, J. Jobst, G. L. Kellogg, L. Ley, J. L. McChesney, T. Ohta, S. A. Reshanov, J. Röhrl, E. Rotenberg, A. K. Schmid, D. Waldmann, H. B. Weber and T. Seyller, *Nat. Mater.*, 2009, **8**, 203–207.

112 M. R. Habib, T. Liang, X. Yu, X. Pi, Y. Liu and M. Xu, *Reports Prog. Phys.*, 2018, **81**, 036501–036530.

113 S. Park and R. S. Ruoff, *Nat. Nanotechnol.*, 2009, **4**, 217–224.

114 Y. Hernandez, V. Nicolosi, M. Lotya, F. M. Blighe, Z. Sun, S. De, I. T. McGovern, B. Holland, M. Byrne, Y. K. Gun'Ko, J. J. Boland, P. Niraj, G. Duesberg, S. Krishnamurthy, R. Goodhue, J. Hutchison, V. Scardaci, A. C. Ferrari and J. N. Coleman, *Nat. Nanotechnol.*, 2008, **3**, 563–571.

115 C.-Y. Su, Y. Xu, W. Zhang, J. Zhao, A. Liu, X. Tang, C.-H. Tsai, Y. Huang and L.-J. Li, *ACS Nano*, 2010, **4**, 5285–5292.

116 J. N. Coleman, *Adv. Funct. Mater.*, 2009, **19**, 3680–3695.

117 T. Mahmoudi, Y. Wang and Y. B. Hahn, *Nano Energy*, 2018, **47**, 51–65.

118 S. Pei and H. M. Cheng, *Carbon N. Y.*, 2012, **50**, 3210–3228.

119 A. Zuchowska, M. Chudy, A. Dybko and Z. Brzozka, *Sensors Actuators, B Chem.*, 2017, **243**, 152–165.

120 K. Seibert, G. C. Cho, W. Kütt, H. Kurz, D. H. Reitze, J. I. Dadap, H. Ahn, M. C. Downer and A. M. Malvezzi, *Phys. Rev. B*, 1990, **42**, 2842–2851.

121 A. G. Cano-Márquez, F. J. Rodríguez-Macías, J. Campos-Delgado, C. G. Espinosa-González, F. Tristán-López, D. Ramírez-González, D. A. Cullen, D. J. Smith, M. Terrones and Y. I. Vega-Cantú, *Nano Lett.*, 2009, **9**, 1527–1533.

122 D. V Kosynkin, A. L. Higginbotham, A. Sinitskii, J. R. Lomeda, A. Dimiev, B. K. Price and J. M. Tour, *Nature*, 2009, **458**, 872–876.

123 P. Tang, G. Hu, Y. Gao, W. Li, S. Yao, Z. Liu and D. Ma, *Sci. Rep.*, 2014, **4**, 5901–5908.

124 X. Li, W. Cai, J. An, S. Kim, J. Nah, D. Yang, R. Piner, A. Velamakanni, I. Jung, E. Tutuc, S. K. Banerjee, L. Colombo and R. S. Ruoff, *Science (80-.).*, 2012, **324**, 1312–1314.

125 Rashid bin Mohd Yusoff, *Graphene based energy Devices*, Wiley, 2017.

126 V. B. Mohan, K. tak Lau, D. Hui and D. Bhattacharyya, *Compos. Part B Eng.*, 2018, **142**, 200–220.

127 Z. Wu, G. Zhou, L. Yin and W. Ren, *Nano Energy*, 2012, **1**, 107–131.

128 W. Lv, Z. Li, Y. Deng, Q. H. Yang and F. Kang, *Energy Storage Mater.*, 2016, **2**, 107–138.

129 R. R. Salunkhe, Y. H. Lee, K. H. Chang, J. M. Li, P. Simon, J. Tang, N. L. Torad, C. C. Hu and Y. Yamauchi, *Chem. - A Eur. J.*, 2014, **20**, 13838–13852.

130 M. Marcaccio and F. Paolucci, *Making and Exploiting Fullerenes, Graphene, and Carbon Nanotubes*, Springer, 2014.

131 X. Zhang, H. Zhang, C. Li, K. Wang, X. Sun and Y. Ma, *RSC Adv.*, 2014, **4**, 45862–45884.

132 Y. Wang, Y. Wu, Y. Huang, F. Zhang, X. Yang, Y. Ma and Y. Chen, *J. Phys. Chem. C*, 2011, **115**, 23192–23197.

133 J. Li and M. Östling, *Crystals*, 2013, **3**, 163–190.

134 J. Li, J. C. Cui, Z. Z. Yang, H. X. Qiu, Z. H. Tang and J. H. Yang, *New Carbon Mater.*, 2018, **33**, 19–25.

135 M. Beidaghi and C. Wang, *Adv. Funct. Mater.*, 2012, **22**, 4501–4510.

136 C. X. Guo and C. M. Li, *Energy Environ. Sci.*, 2011, **4**, 4504–4507.

137 K. Batrakov, P. Kuzhir, S. Maksimenko, A. Paddubskaya, S. Voronovich, P. Lambin, T. Kaplas and Y. Svirko, *Sci. Rep.*, 2014, **4**, 7191–7196.

138 X. Wang, G. Sun, P. Routh, D.-H. Kim, W. Huang and C. Peng, *Chem Soc Rev*, 2014, **43**, 7067–7098.

139 C. Hu, D. Liu, Y. Xiao and L. Dai, *Prog. Nat. Sci. Mater. Int.*, 2018, **28**, 121–132.

140 M. Mujeeb Khan, Muhammed Nawaz Tahir, Syed Farooq Adil, Hadayat Ullah Khan and W. T. Rafiq H. Siddiqui, Abdulrahman A. Al-warthan, *J. Mater. Chem. A*, 2015, **3**, 18753–18808.

141 A. Jana, E. Scheer and S. Polarz, *Beilstein J. Nanotechnol.*, 2017, **8**, 688–714.

142 Y. Xie, X. W. Lou, C. Yuan, H. Bin Wu, Y. Xie, X. Wen and D. Lou, *Angew. Chemie*, 2014, **53**, 1488–1504.

143 A. W. Anwar, A. Majeed, N. Iqbal, W. Ullah, A. Shuaib, U. Ilyas, F. Bibi and H. M. Rafique, *J. Mater. Sci. Technol.*, 2015, **31**, 699–707.

144 G. H. Jeong, S. Baek, S. Lee and S. Kim, *Chem. Asian J.*, 2016, **11**, 949–964.

145 A. Borenstein, O. Hanna, R. Attias, S. Luski, T. Brousse and D. Aurbach, *J. Mater. Chem. A*, 2017, **5**, 12653–12672.

CHAPTER 2

Thesis Objectives

2. Thesis Objectives

The main objective of the present thesis is to synthesize and develop novel graphene-based hybrids with metal compounds to be employed either as electrode materials or electrocatalysts for energy storage applications. In each section, a facile chemical route is subjected for synthesizing novel samples and following specific objectives were pursued in the course of the thesis:

- Fully chemical and microstructural characterization (e.g. using various techniques such as XRD, TEM, XPS, Raman, etc.) of the prepared samples to correlate the structure with electrochemical response.
- Evaluation of the effects of synthesis conditions (e.g. reagents concentration, reaction time, reaction temperature, or etc.) on composition and structure of the samples (such as morphology, particle sizes, specific surface area, and so on).
- Investigating the effect of metal oxide phase on electrochemical signal and storage properties of the electrodes.
- Shedding light on influence of the metal cation substitution on the electrochemical signal of the metal compounds with the aim to enhance the energy storage performance.
- Evaluating the effect of hybridizing the metallic nanostructures with graphene-based materials on the electrochemical behavior of the samples and looking for synergistic properties.
- Finding out the effects of metal/C ratios on the electrochemical behavior of the hybrid samples and their storage performance.
- Studying the effect of N-doping in carbon matrix on the electrochemical finger-prints and energy storage performance of the hybrid samples.
- Shedding light on electrochemical signal and charge storage mechanism of the metal compounds (e.g. metal sulfides) in alkaline media through ex-situ and operando measurements.
- Evaluating the viability of the developed materials in full cell devices in order to compare their storage or catalytic behavior with the state-of-the-art and attempts to push their performance.

CHAPTER 3

Experimental

3.1 Materials and Chemicals

A list of the reagents employed in the present thesis, along with their formula, purity and supplier, is shown below in ***Table 3.1***.

Table 3.1 Materials and chemicals employed in the present thesis

Materials and Chemicals	Chemical Formula	Purity	Supplier
Natural graphite powder	C	-	Merck/Sigma Aldrich
Acetylene Black	C	99%	Cabot
Carbon Vulcan	C	99%	Fuel Cell Store
Potassium persulfate	$K_2S_2O_8$	99%	Merck/Sigma Aldrich
Phosphorus pentoxide	P_2O_5	98%	Acros Organics
Sulfuric acid	H_2SO_4	95-97%	Scharlau
Potassium permanganate	$KMnO_4$	99%	Scharlau
Sodium nitrate	$NaNO_3$	99.5%	Scharlau
Hydrogen Peroxide Solution	H_2O_2	30%	Merck/Sigma Aldrich
Hydrazine hydrate	$NH_2NH_2{\cdot}xH_2O$	50-60%	Merck/Sigma Aldrich
Iron Oxide	Fe_3O_4	100%	TECNAN
Sodium Hydroxide	NaOH	98%	Merck/Sigma Aldrich
Nitric Acid	HNO_3	65%	Scharlau
Urea	CH_4N_2O	98%	Merck/Sigma Aldrich
Ethanol	EtOH	99.5%	Merck/Sigma Aldrich
Ammonium Hydroxide	NH_4OH	28-30%	Merck/Sigma Aldrich
Nickel (II) nitrate hexahydrate	$Ni(NO_3)_2{\cdot}6H_2O$	99.9%	Merck/Sigma Aldrich
Manganese (II) nitrate tetrahydrate	$Mn(NO_3)_2{\cdot}4H_2O$	98%	Merck/Sigma Aldrich
Cobalt (II) nitrate hexahydrate	$Co(NO_3)_2.6H_2O$	99.9%	Merck/Sigma Aldrich
Sodium bicarbonate	$NaHCO_3$	99.7%	Merck/Sigma Aldrich
Dimethylformamide (DMF)	C_3H_7NO	99.8%	Merck/Sigma Aldrich
Nickel (II) chloride hexahydrate	$NiCl_2.6H_2O$	98%	Merck/Sigma Aldrich
Manganesel (II) chloride tetrahydrate	$MnCl_2{\cdot}4H_2O$	98-100%	Alfa Aesar
Cobalt (II) chloride hexahydrate	$CoCl_2{\cdot}6H_2O$	98%	Merck/Sigma Aldrich
Ni foam	Ni	99.5%	Goodfellow
Hydrochloric Acid	HCl	37%	Scharlau
Thioacetamide (TAA)	C_2H_5NS	99%	Merck/Sigma Aldrich
Manganese (II) acetate tetrahydrate	$Mn(CH_3COO)_2{\cdot}4H_2O$	99%	Merck/Sigma Aldrich
Cobalt (II) acetate tetrahydrate	$Co(CH_3COO)_2{\cdot}4H_2O$	99%	Merck/Sigma Aldrich
Nickel (II) acetate tetrahydrate	$Ni(CH_3COO)_2{\cdot}4H_2O$	99%	Merck/Sigma Aldrich
Thiourea	CH_4N_2S	99%	Merck/Sigma Aldrich
Polytetrafluoroethylene (PTFE)	$(C_2F_4)_n$	60%	Merck/Sigma Aldrich
Nafion Solution	$C_7HF_{13}O_5S{\cdot}C_2F_4$	80%	Merck/Sigma Aldrich
Zn foil	Zn	99.9%	Goodfellow
Gas Difusion Layer (GDL)	C	100%	Fuel Cell Store

3.2 Schematic Diagram of the Thesis

The methodology to achieve these abovementioned objectives involves three important building blocks in the present thesis: the synthesis optimization of the different inorganic materials synthesized with their corresponding physico-chemical characterization, the use of electrochemical techniques to analyze the electrochemical behavior of these graphene-based hybrids materials, as well as their application in lab-scale full devices, high power energy storage devices and Zn-air batteries and the evaluation of their performance. In overall, the research conducted for the present thesis can be condensed in the next schematic diagram of the thesis workflow, as follows:

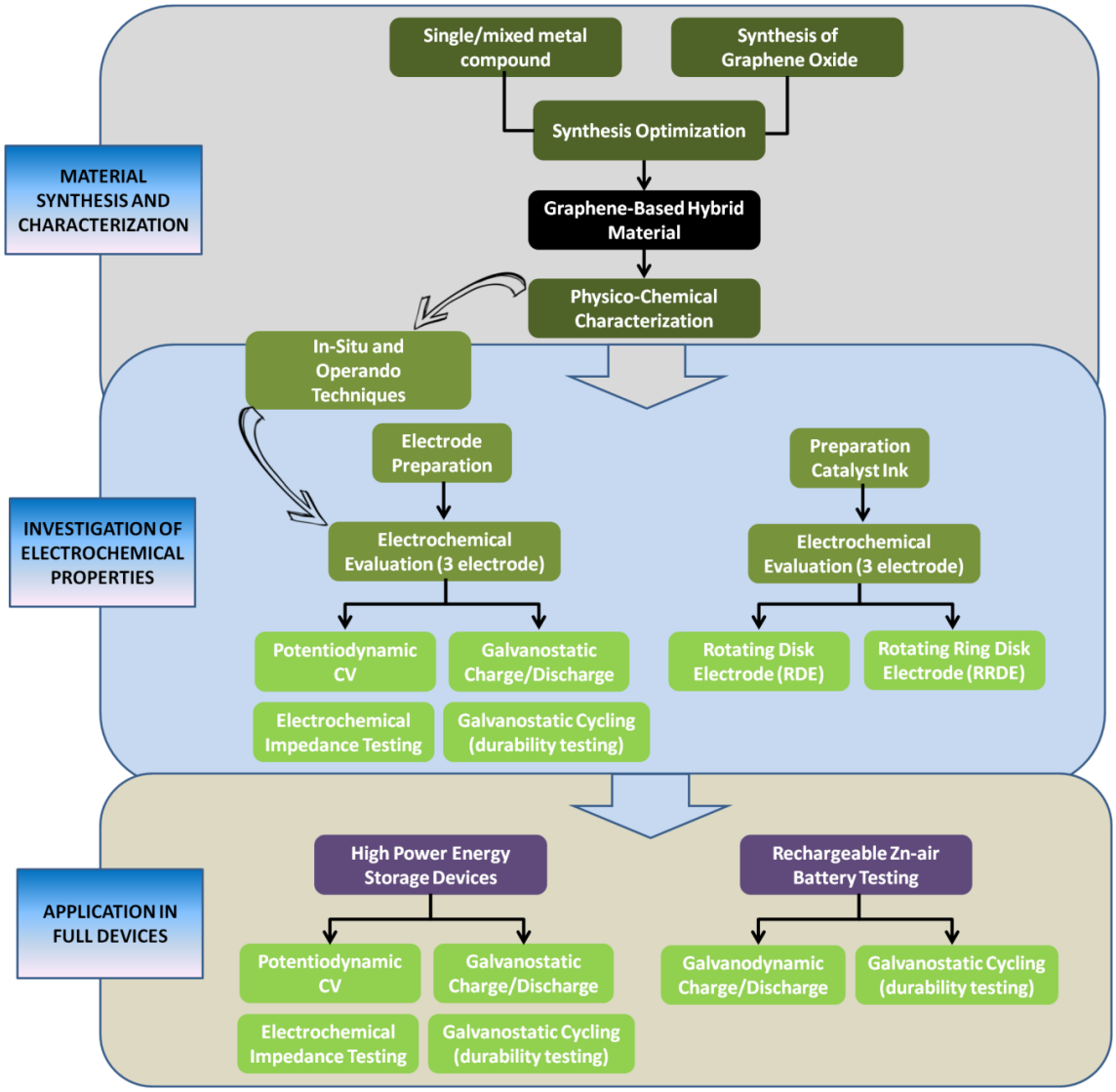

Figure 3.1 Schematic Diagram of the Thesis Workflow

3.3 Synthesis of Materials

The methods employed to prepare the samples in the present thesis have been described in detail as follows:

3.3.1 Graphene Oxide (GO) and reduced Graphene Oxide (rGO)

Graphene oxide (GO) was synthesized using the Hummers method.[1] In a typical synthesis (***Figure 3.2***), 8 g $K_2S_2O_8$ and 8 g P_2O_5 were added to 24 ml of concentrated H_2SO_4 solution. Using a silicon oil bath, the solution was heated to 80°C and 4 g of natural graphite powder was gradually added followed by stirring for 6 h.

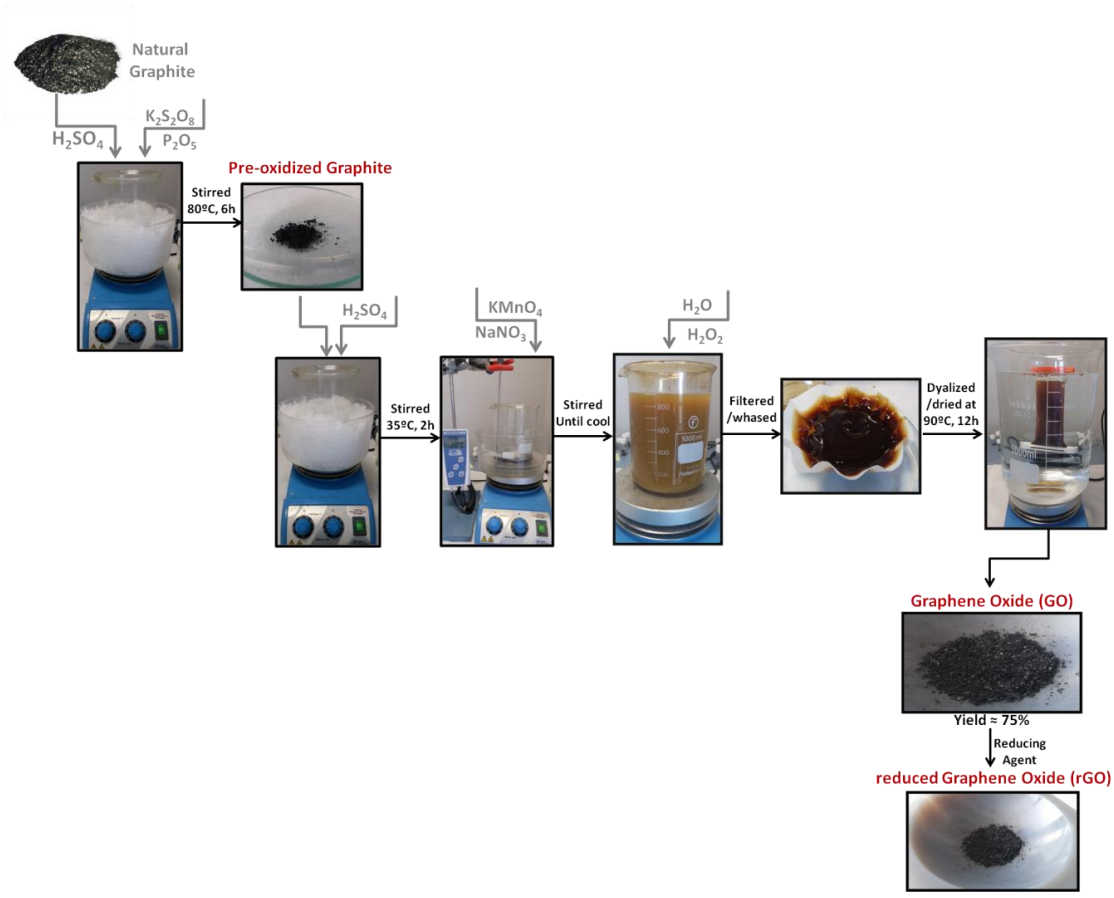

Figure 3.2 Schematic illustration of the modified Hummers method used to synthesize GO and rGO

After cooling to room temperature (RT), the mixture was diluted by 300 ml Milli-Q water and then filtered and dried overnight at 60°C. A 2 g quantity of the as-prepared powder (pre-oxidized graphite) was added to 92 ml concentrated H_2SO_4 solution, cooled in an ice bath, where 12 g

$KMnO_4$ was gradually added under vigorous stirring. After 15 min, 2 g $NaNO_3$ was added and the mixture was stirred at 35°C for 2h. Then 560 ml Milli-Q water and 10 ml H_2O_2 30% solution were introduced resulted in turning the solution to a bright yellow. The sample was filtered, rinsed several times, and dried at 100°C. Next, it was re-dispersed in Milli-Q water and the brown dispersion was dialyzed for at least 1 day to remove residual metal ions and acids. After vacuum filtration, the GO gel was dried at 60°C. Finally GO powder was obtained and employed in all of the cases after dispersion and exfoliation using ultrasound irradiation by means of a high-power ultrasound probe in the synthesis of different graphene-based materials as explained later.

In the present thesis, we have employed a wide variety of reducing agents, such as hydrazine hydrate (Chapter 4), ammonia (Chapters 6,7 and 9) or sodium bicarbonate (Chapter 5) in order to reduce GO to rGO by chemical methods in the synthesis of different graphene-based materials along the different Chapters. To reduce the GO sample following the method proposed by Stankovich et al.,[2] 100 mg of as-prepared sample was re-dispersed in 150 ml Milli-Q water and 70 µl of a hydrazine hydrate solution was added. The solution was then transferred to an oil bath where it was stirred for 6 h at 80°C. The final sample (reduced graphene oxide (rGO)) was rinsed thoroughly with water and dried overnight at 60 °C. Pure rGO synthesized by previous method has been employed as negative electrode material to assemble hybrid energy storage devices in Chapters 5, 6 and 8. In chapters 4, and 7 GO was first hybridized with metal oxide by electrostatic coagulation and the reduction to obtain rGO was then performed in a subsequent step as detailed in next section. On the contrary, in chapters 5, 6 and 9 the corresponding reducing agent is added in a hydrothermal step with the rest of metal precursors.

3.3.2 Electrostatic Coagulation Method

Electrostatic coagulation is one of the most important physico-chemical reactions used in water treatments and it was selected for its simplicity, convenience, reproducibility, and low cost in order to synthesize several graphene-based hybrid materials in the present thesis. In literature some authors refers this method as Electrostatic Co-precipitation, however the action differs from precipitation in that, prior to coagulation, colloids are merely suspended in a liquid and not actually dissolved in a solution. Fe_3O_4-rGO and N-rGO/Co_3O_4 Nanorods (NRs) have been prepared via this route as main step of synthesis and the results and discussion are presented in Chapter 4 and Chapter 9, respectively. Experimental details are shown below.

3.3.2.1 Preparation of Fe_3O_4-rGO

Commercial Fe_3O_4 nanoparticles (NPs) were anchored on graphene oxide layers employing an electrostatic coagulation route, as schematically represented in ***Figure 3.3.*** Before anchoring, the coagulation method was optimized by determining the pH at which the electrostatic attraction forces between Fe_3O_4 nanoparticles and GO nanosheets (NSs) are at a maximum. To this end, a ZetaSizer (Malvern Instrument, Nano series) coupled with an Autotitrator was employed to obtain zeta potential values of samples dispersions (Fe_3O_4 NPs and GO NSs) equilibrated at various pH values. 0.05 M NaOH and 0.05 M HNO_3 solutions were employed to adjust the pH of these suspensions. In a typical synthesis, certain amounts of Fe_3O_4 NPs and GO NSs were separately dispersed in 180 mL of Mili-Q water by using sonication for 30 min (Hielscher, UP400S) to achieve stable Fe_3O_4 and GO dispersions. Subsequently, as-prepared dispersions were mixed, the pH of the mixture was adjusted to 2 (the optimized pH), and the solution was left in steady condition for 2h so that coagulation could be completed.

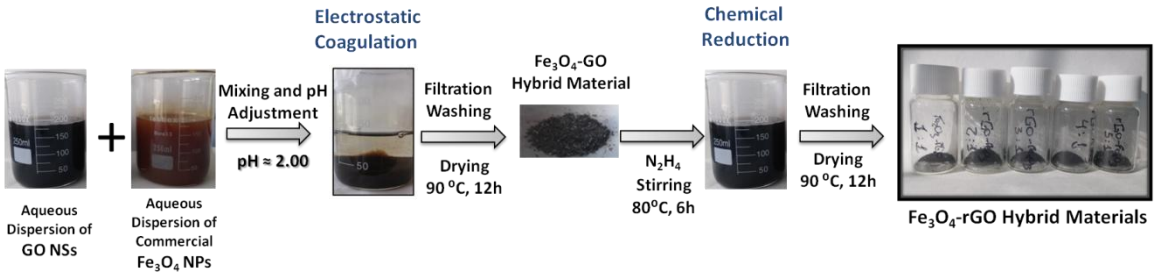

Figure 3.3 Schematic illustration of electrostatic coagulation of Fe_3O_4-rGO hybrids

The resultant sediment was filtered and then dried at 90°C overnight. Afterwards, synthesized samples were chemically reduced to reassure that GO dominantly is converted to its reduced state (rGO). To this end, the product (100 mg) of the previous step was re-dispersed in 150 ml of Mili-Q water and 70 ml of hydrazine monohydrate was added while stirring. The solution was stirred at 80°C for an additional 6h. Eventually, the sample was filtered, rinsed thoroughly with water, and dried at 90°C for 6h. Different hybrid materials were synthesized in a similar way by varying the mass ratio of rGO and Fe_3O_4 NPs, denoting as Fe_3O_4-rGO [x : y], where x and y are percentage content of the components in weight. Physicochemical and electrochemical properties as well as application of the synthesized materials as negative electrodes for high power aqueous batteries are presented in Chapter 4.

3.3.2.2 Synthesis of N-rGO/Co_3O_4 Nanorods

Co_3O_4 nanorods (NRs) were synthesized by the group of Dr. Vinodkumar Etacheri at IMDEA Materials, following a hydrothermal method with a subsequent thermal treatment (***Figure 3.4***).

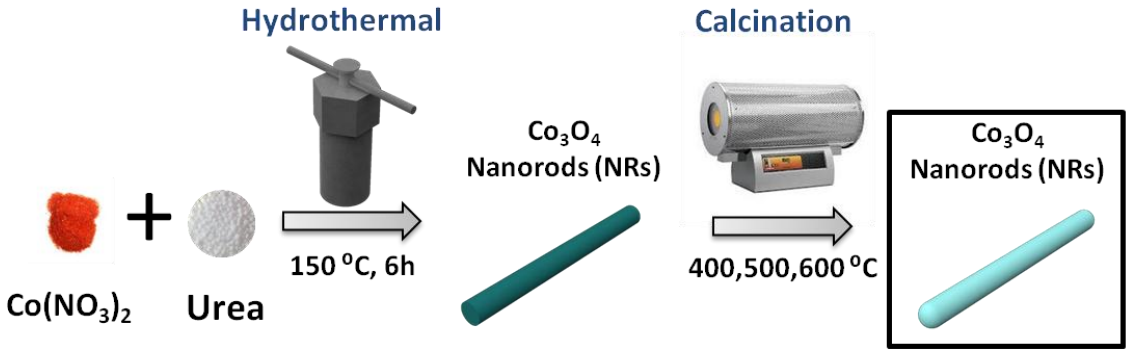

Figure 3.4 Schematic illustration of the Co_3O_4 NRs synthesis process

Subsequently, Co_3O_4 NRs were hybridized with rGO nanosheets (NSs) through an electrostatic coagulation route. Afterwards, the rGO-Co_3O_4 hybrid was further processed via a hydrothermal step to achieve N doped composite, as illustrated in ***Figure 3.5.*** Briefly, 4 mmol of cobalt (II) nitrate hexahydrate $Co(NO_3)_2 \cdot 6H_2O$ and 2 mmol of urea were dissolved in 150 ml of deionized water under stirring. The solution obtained was heated to 150°C for 6 h in Teflon lined stainless steel autoclave at a rate of 10 °C·min^{-1}. The obtained precipitate was thoroughly washed with deionized water and ethanol followed by drying at 80°C and calcination at 400, 500 and 600°C in air for 2 h at a heating rate of 10 °C·min^{-1} obtaining three different samples Co_3O_4 NRs 400°C, Co_3O_4 NRs 500°C and Co_3O_4 NRs 600°C.

Figure 3.5 Schematic illustration of the synthesis procedure for N-rGO/Co_3O_4 NRs

Later, Co_3O_4 NRs 500 °C sample was used to prepared hybrid materials with graphene oxide nanosheets (GO NSs) by using an electrostatic coagulation method. This method was optimized by

determining the pH at which the electrostatic attraction forces between Co_3O_4 NRs and GO NSs are at a maximum with the help of a ZetaSizer coupled with an Autotitrator. Zeta Potential values at different pH were obtained using 0.05M NaOH and 0.05M HNO_3 solutions to adjust the pH (range of 1.5 to 11) of the prepared dispersions (Co_3O_4 NRs and GO NSs). In a typical synthesis, GO NSs and Co_3O_4 NRs were independently dispersed in 180 ml of Mili-Q water by using sonication for 30 min to achieve stable GO NSs and Co_3O_4 NRs dispersions. Afterwards, as-prepared dispersions were mixed and the pH of the mixture was adjusted to 2 (e.g. the optimized pH), letting it in steady condition for a couple of hours so that coagulation could be achieved. The resultant sediment was filtered and then dried at 90 ^oC overnight. As a result, 24 mg of GO-Co_3O_4 was re-dispersed in 35 ml EtOH and stirred overnight. The mixture was then transferred to a Teflon-lined hydrothermal autoclave reactor (50 ml of total capacity), followed by adding 3 ml of Mili-Q water and 2 ml of NH_4OH solution (28-30%), and the reaction was continued at 180 ^oC for 3 h. The resulting precipitate (NrGO-Co_3O_4 NRs) was collected by centrifugation at 6000 rpm for 15 min after washing with pure ethanol and Mili-Q water and dried at 60 ^oC overnight. Successful results of N-rGO/Co_3O_4 Nanorods as bifunctional electrocatalyst for Zn-Air Batteries are reported in Chapter 7 of the present thesis.

3.3.3 Hydrothermal Method

Hydrothermal method is one of the most common and effective inorganic synthetic routes to fabricate nanomaterials with a variety of morphologies.[3] It can be defined as a method of synthesis in water under moderate temperatures (<200 °C) and high pressure conditions. The crystal growth is performed in a sealed steel pressure vessel called autoclave, in which a precursor is supplied along with water. A temperature gradient is maintained between the opposite ends of the growth reactor, so that the hotter end dissolves the precursors and the cooler end facilitates growth of the crystals. Advantages of the hydrothermal method over other methods like electrostatic coagulation include the ability to create large good-quality crystals while maintaining control over their composition. A controlled annealing process usually follows to execute a transformation of the grown crystals to a designated phase or to further increase the crystallinity of the product. A variety of materials (oxides, sulfides and hybrids) have been prepared via hydrothermal route as main step of synthesis in the present thesis. Experimental details are shown below.

3.3.3.1 Synthesis of $NiMnO_3$-rGO

As illustrated in ***Figure 3.6***, $NiMnO_3$-rGO hybrids were synthesized via a facile hydrothermal method followed by thermal treatment according to the following steps: GO NSs were dispersed in 25 ml of Mili-Q water using ultra-sonication for 20 min to achieve stable GO dispersion. Subsequently, equimolar amounts of $Ni(NO_3)_2{\cdot}6H_2O$ and $Mn(NO_3)_2{\cdot}4H_2O$ were dissolved in the above mixture and stirred for 3 h to obtain a transparent solution. Thereafter, 1 ml of 1 M sodium bicarbonate ($NaHCO_3$) solution was added quickly to the mixture. The resultant solution was kept stirring for 2 h. This solution was then transferred into a 50 ml Teflon-lined stainless steel autoclave reactor where the hydrothermal reaction took place at 150°C for 8 h. After naturally cooling down to room temperature, the as-synthesized product was isolated by centrifugation, washed with Mili-Q water and ethanol several times, and finally dried at 70°C overnight. Finally, the precipitate was calcined in a tubular furnace at 450°C (heating rate of 5°C min^{-1}) for 5 h in Ar atmosphere to obtain the $NiMnO_3$-rGO hybrid material. Moreover, pure $NiMnO_3$ and rGO samples were synthesized using the same procedure except GO was excluded in the pure oxide sample and metal precursors were excluded in rGO sample. A complete physicochemical and electrochemical characterization of $NiMnO_3$-rGO hybrid materials as well as their potential application as positive electrodes for hybrid energy storage devices is presented in Chapter 5 of the present thesis.

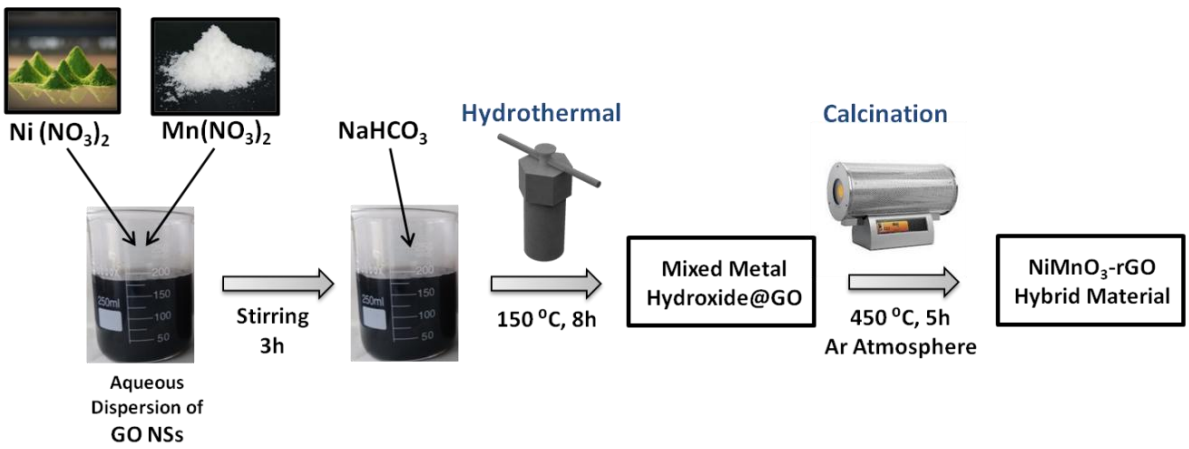

Figure 3.6 Schematic illustration of the synthesis procedure for $NiMnO_3$-rGO hybrid material

3.3.3.2 Synthesis of NCMO_rGO

NCMO_rGO hybrid samples were synthesized via facile hydrothermal method followed by thermal treatment as illustrated in ***Figure 3.7***. First, GO NSs were dispersed in 40 ml of Mili-Q water by using ultra-sonication for 30 min to achieve stable GO dispersions. Dimethylformamide (40 ml) was added to 40 ml of 0.1 $mg \cdot ml^{-1}$ GO gel dispersion, and then stirred for 10 min to form homogenous solution. Next, equimolar amounts of $NiCl_2.6H_2O$, $Mn(NO_3)_2.4H_2O$, and $Co(NO_3)_2.6H_2O$ were dissolved in the solution by magnetic stirring for 1 h to make metal ions adsorbed on the surface of GO sheets. Afterwards, pH value of the mixture was adjusted to ~8 by adding slowly 5% ammonium solution at room temperature. The resultant dark-yellow solution was kept stirring for further 30 min. Then, the solution was transferred into a 200 ml Teflon-lined stainless steel autoclave reactor where the hydrothermal reaction took place at 130°C for different reaction times (2, 8, 14, and 18h) before cooling down naturally to room temperature. The product of this step was rinsed and centrifuged with Mili-Q water several times, and finally dried at 70°C overnight. At last, the precipitate was calcined in an electrical furnace at 300°C (heating rate of 2 $°C \cdot min^{-1}$) for 2h to obtain the NCMO_rGO hybrid samples (***Figure 3.7***).

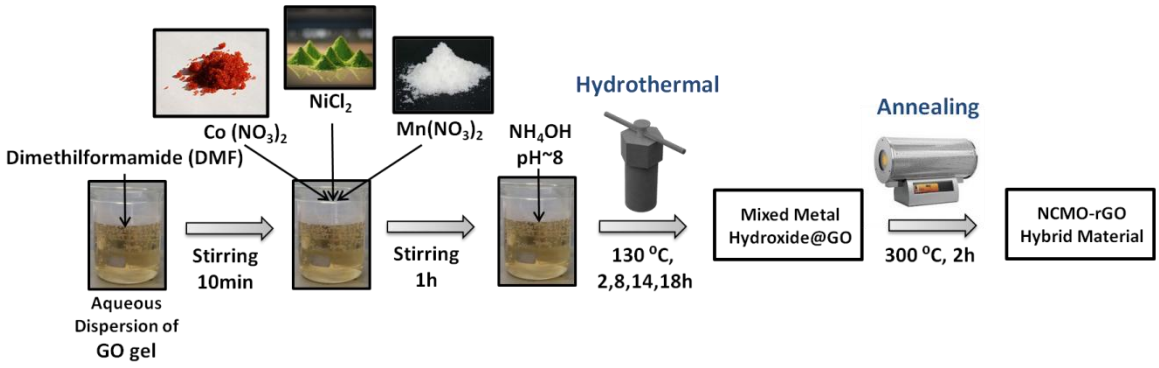

Figure 3.7 Schematic illustration of the synthesis procedure for NCMO_rGO hybrid sample

The reaction conditions (e.g. reaction time) of the samples were systematically optimized to get the highest energy storage performance. Moreover, different hybrid materials were synthesized via similar approach by varying the amount of GO NSs in the reactant mixture. Samples were denoted as NCMO_rGO [*x*:*y*], where *x* and *y* denote the percentage content of the components. A detailed study of NCMO_rGO physicochemical and electrochemical properties together with their application as positive electrodes for hybrid energy storage is presented in Chapter 6.

3.3.3.3 Direct Growth of $NiCoMnS_2$ Nano-Needles on Nickel Foam

Prior to the synthesis, round discs (0.78 cm^2) of Ni foam (NF) were carefully cleaned with 3 M HCl in an ultrasound bath for 20 min to remove oxide surface layer. The $NiCoMnS_2$ nano-needles were then grown on cleaned NF coupons by a facile two-step hydrothermal route as illustrated in ***Figure 3.8***. In the first step, 1 mmol of each metallic salt (e.g. $MnCl_2{\cdot}4H_2O$, $NiCl_2{\cdot}6H_2O$, $CoCl_2{\cdot}6H_2O$) and 0.676 g of urea were added to 30 ml distilled water under vigorous stirring to obtain a homogeneous solution. The resulted pink solution was then transferred into a 50 ml Teflon-lined stainless-steel autoclave where NF coupons were placed inside. Then, the reactor was sealed and maintained at 120°C for 6h. After cooling down to room temperature, the as-synthesized precursor-loaded NF coupons were washed with distilled water and ethanol. In the next step, a 30 ml solution of 0.2 mmol of each metallic salt, 0.3 g of urea and 0.226 g thioacetamide (TAA) along with the precursor-loaded NF coupons were transferred in the reactor and heated at 90°C for 4h and then at 140°C for 6h. After cooling down to the room temperature, the $NiCoMnS_2$ nano-needle arrays on NF coupons were washed with distilled water and ethanol, and then dried in a vacuum oven at 50°C for 4h. For the sake of comparison, NiCoMn hydroxide samples were also synthesized under identical conditions without addition of TAA. The typical mass loading of the deposits of NF after hydrothermal reaction was 5.2-5.5 $mg{\cdot}cm^{-2}$. The formation of the samples is schematically presented in ***Figure 3.8***. A comparative physicochemical and electrochemical study of the as-synthesized materials as well as a detailed structural evolution of $NiCoMnS_2$ upon cycling was investigated in Chapter 8. In addition, their application as positive electrode in hybrid energy storage devices was also probed.

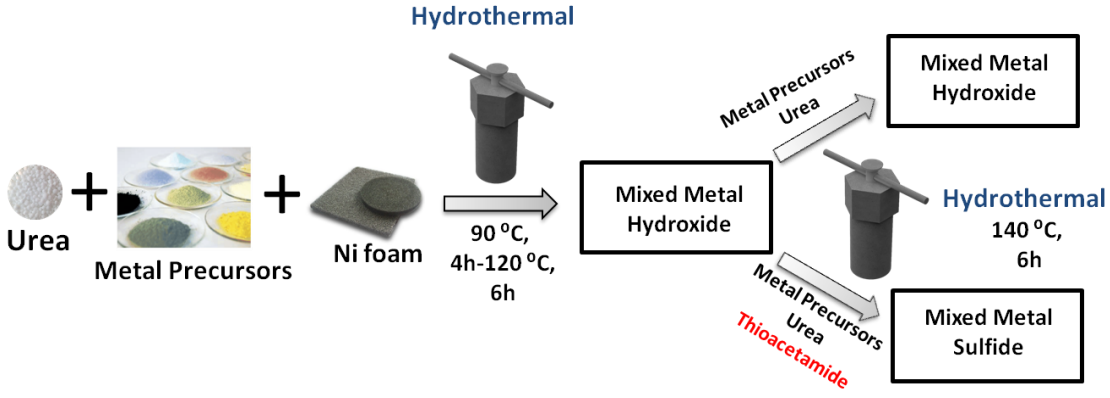

Figure 3.8 Schematic illustration of the synthesis procedure for $(Ni_{1-(x+y)}Mn_xCo_y)OH_2$ urchin-like structure and $NiCoMnS_2$ nano-needles, in the absence and presence of TAA, respectively

3.3.3.4 Synthesis of $NiCoMnS_4$/N-rGO

In a typical synthesis of $NiCoMnS_4$/N-rGO hybrid, 32 mg. of GO powder were dispersed using an ultrasound probe in 30 ml of absolute ethanol, forming a stable dispersion. 1 ml of 0.2 M solution of each metal acetate salt (Ni, Co, and Mn) was added to the GO dispersion while the solution was stirring vigorously. After 1 h, 2 ml of NH_4OH solution (28.0-30.0%) and 3 ml of Mili-Q water was introduced to the mixture as illustrated in ***Figure 3.9***. The mixture was then transferred to a three-neck flask connected to a reflux system and stirred at 80°C for 2h. Afterwards, in the anion-exchange step, 1.2 mmol of thiourea was added to the solution and stirred overnight at 80 °C. The mixture of this step was then transferred to a Teflon-lined hydrothermal autoclave reactor (50 ml of total capacity) and the reaction was continued at 180°C for 5h. The resulting precipitate was collected by centrifugation at 6000 rpm for 15 min after washing with pure ethanol and Mili-Q water. Finally, the sample was dried at 70°C overnight in an electrical furnace. The schematic illustration of the synthesis procedure can be seen in ***Figure 3.9***. Pure $NiCoMnS_4$ and N-rGO samples were prepared using a similar approach by excluding GO and $M(CH_3CO_2)_2$ precursors, respectively. In addition, components ratio in the hybrid sample was also modified by adding various amounts (450, 200, 72, 32, and 16 mg) of GO in initial step of the synthesis. The results of applying $NiCoMnS_4$/N-rGO samples as bifunctional electrocatalyst for rechargeable Zn-Air Batteries are presented in Chapter 9.

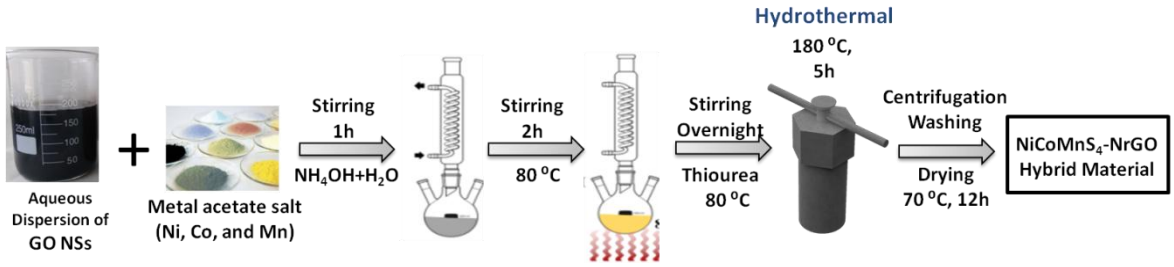

Figure 3.9 Schematic illustration of the synthesis procedure for $NiCoMnS_4$/N-rGO hybrid materials

3.4 Physico-Chemical characterization of materials

Detailed studies of the material characteristics were accomplished by the combination of several physico-chemical characterization techniques as indicated in ***Figure 3.10***.

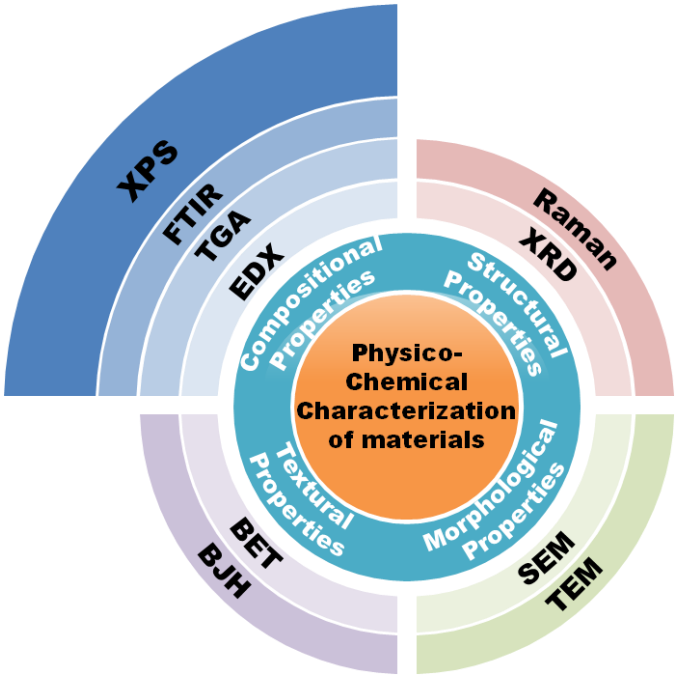

Figure 3.10 Layered Quadrants Diagram of the Physico-Chemical Characterization techniques

3.4.1 Morphological characterization (SEM, TEM, and HR-TEM)

Electron diffraction is an important characterization technique used to study matter by firing a beam of accelerated electrons to a sample to obtain the interference pattern. Experiments are usually performed in a scanning electron microscope (SEM), or a transmission electron microscope (TEM) to study the crystal structure of solids and examine their specific morphology in the micro and nanoscale.[4] SEM utilizes an electron beam focused on the sample's surface to characterize its topology and the sample's morphology. The focused electron beam is scanned over an area in a raster fashion, and the detected electrons are converted into an electric signal and processed by a computer to produce the final image. TEM also utilizes an electron beam as the source to create high resolution images. However, unlike in SEM which detects reflected electrons above the sample, TEM detects electrons which are transmitted through a thin sample which are then converted to an electric signal to produce the final TEM images. This allows TEM to resolve features in the atomic range including the visualization of crystal orientation, lattice

planes, *d*-spacing, etc., so they have better resolution than SEMs. Generally, SEM images are used for preliminary analysis while TEM images are on duty for in-depth investigations of lattice parameters and very fine nanostructures. The high-resolution transmission electron microscopy (HR-TEM) uses both the transmitted and the scattered beams to create an interference image. It has been extensively and successfully used for analyzing crystal structures and lattice imperfections in various kinds of advanced materials on an atomic resolution scale. Another variation of the TEM, the High-angle annular dark-field scanning transmission electron microscopy (HAADF-STEM) provides elemental composition and crystal information at atomic scale. The Scanning TEM works on the same principle as a normal scanning electron microscope by focusing an electron beam into a very small spot which is scanned over the TEM sample.

Hitachi TM-1000 and FIB-FEGSEM Dual-beam microscope (Helios NanoLab 600i, FEI) were employed as scanning electron microscopes (SEM). Philips Tecnai20 with a BaF6 filament and FEG S/TEM (Talos F200X, FEI) were used as transmission electron microscopes (TEM, STEM and HR-TEM) to investigate the morphological structure and particle distribution in the samples of the present thesis.

3.4.2 Compositional Characterization (EDX, TGA, FTIR and XPS)

- Energy dispersive X-ray spectroscopy (EDS or EDX)

Energy dispersive X-ray spectroscopy (EDS or EDX) is an elemental analysis technique which allows identification and quantification of the sample's chemical composition. This technique is commonly coupled to an SEM or TEM system to be conducted simultaneously with microscopic analysis. The EDS signal is obtained by detecting x-rays emitted from the sample during the interaction with the electron beam. The binding energy of the emitted x-ray is specific to each element which provides blue print for elemental identification. A typical EDS results is displayed as a spectrum with x-ray counts versus binding energy to show various elements found in the sample. The EDS can also be used to create elemental "maps", which shows the distribution of localized elements over a selected area of the sample. The maps show varying intensities depending on the amount of the localized elements. This is particularly interesting for hybrid materials consisting of organic and inorganic constituents to clearly identify the elements and their distribution in a

sample. Hitachi TM-1000 and FEG S/TEM (Talos F200X, FEI) were used to collect EDX spectra and Elemental Mapping, respectively.

- Thermogravimetric Analysis (TGA)

Thermogravimetric Analysis (TGA) is a destructive method of thermal analysis to determine the weight changes of samples associated with changes in temperature. This analysis accurately detects the weight of a sample as temperature elevates, drawing a continuous line to identify weight loss processes in relation to the chemical reactions occurring. TGA can be carried out in air or noble gases for different applications. In the case of Graphene-based hybrid materials, TGA is often conducted in air as a quantitative method to determine the composition of Graphene and the embedded metal compound nanostructures in the hybrid. A SDT Q-600, TA Instrument was used to obtain the carbon content by heating the samples in an air atmosphere with a heating rate of 10 °C·min^{-1} from room temperature to 700 °C.

- Fourier Transform Infrared (FT-IR) Spectroscopy

FT-IR spectroscopy is a non-destructive qualitative analysis technique which provides important information about chemical bonding in many newly developed nanomaterials. Here, the spectrometer records the interaction of a single beam IR radiation, measuring the frequencies at which the sample absorbs the radiation and the intensities of the absorptions. Chemical functional groups are known to absorb light at specific frequencies. Thus, the chemical structure can be determined from the frequencies recorded. In this thesis Fourier Transform Infrared (FTIR) spectra were recorded on a Thermo-Scientific model Nicolet 6700 spectrometer and the results are reported in terms of the frequency of absorption (cm^{-1}).

- X-ray photoelectron spectroscopy (XPS)

X-ray photoelectron spectroscopy (XPS), also known as electron spectroscopy for chemical analysis (ESCA), is a surface elemental composition characterization technique which allows the user to identify and quantify elements present at the surface up to a probing depth of 5-10 nm under high vacuum conditions. In addition, XPS allows investigation of the chemical bonding states or electronic (oxidation) states of an element making prediction of the possible empirical chemical formula. This technique works by irradiating X-ray on the material to induce emission of electrons by photoelectric effect. The detected kinetic energy and the number of electrons collected from

the samples are analyzed to produce a pattern with intensity versus binding energy similar to that of XRD. The specific binding energy of the electron acts as the blueprint for identifying the composition of the sample with the intensity corresponding to the quantity of elements. Each element has a unique spectrum. For the purpose of this thesis, XPS was successfully employed to identify and quantify the elements in the developed hybrid materials as well as their electronic oxidation states. X-ray photoelectron spectroscopy (XPS) was conducted on the samples in this thesis by means of a hemispherical analyzer PHOIBOS 150 (SPECS) with an Al Kα (1486.6 eV) or Mg Kα (1253.6 eV) radiation depending of the sample synthesized, a voltage of 12 kV, a current of 6 mA and an energy resolution of 0.1-0.2 eV. The XPS high resolution spectra were analyzed by CasaXPS software. In order to fit each component in the hybrid samples, identify their functional groups and their distribution on the surface, Gaussian (70%)-Lorentzian (30%) profiles were employed after Shirley background corrections.

3.4.3 Structural Characterization (XRD and Raman)

- X-ray diffraction (XRD)

X-ray diffraction (XRD) is a non-destructive and versatile characterization technique which allows the determination of crystal phase and structure. The X-rays from the source interact with the sample to produce diffraction patterns at the angles corresponding to specific crystal planes. The x-ray source is swept over a range of angles (0-2Θ) and the diffracted x-rays at specific angles are collected and processed by the detector showing the diffraction pattern. The angle of diffraction is related to the specific crystal orientation of the sample by Bragg's law as shown by the equation below:

$$2dsin\Theta = n\lambda \ [\text{Eq. } 3.1]$$

where n, λ, d, and θ represent the order of the spectrum, the wavelength of the X-rays, the spacing between diffracting planes, and the incident angle, respectively. The diffraction pattern at specific angles obtained by XRD can be compared to the theoretical diffraction pattern calculated by the crystal planes to help identify the material. Moreover, XRD patterns cannot be produced by amorphous materials as they do not have ordered crystal planes that interact with X-rays to produce diffracted patterns. In this research, the crystalline structure of the samples was determined by PANalytical Empyream diffractometer using Cu Kα radiation (λ=1.54178 Å) at a scanning rate of $0.2 \cdot s^{-1}$, generated at 45 kV and an emission current of 40 mA.

- Raman spectroscopy

Raman spectroscopy is a non-destructive spectroscopic technique used to study vibrational, rotational, and other low-frequency modes in a molecular system. The laser light in the Raman Microscope focuses on the test sample and interacts with its vibrations or excitations at a molecular level, generating shifted laser photons, which are immediately recorded on a Raman spectrum. The resolution of the Raman spectra can be enhanced by accumulated scans with a longer exposed time. In the study of graphene-based materials, carbon atoms are only bonded into a sp2 arrangement forming C-C single bonds, which IR spectroscopy is unable to detect. This makes Raman Spectroscopy really helpful in determining ordered and disordered crystal graphitic structures as supporting evidence for the formation of graphene nanosheets and, also, to distinguish graphene from pristine graphite, graphene oxide or reduced grapheme oxide. Raman spectra in the present thesis were recorded at room temperature using a JASCO NRS-5100 series Raman spectrometer with exciting the sample at 532 nm, by 5 accumulated scans with an average of 20 seconds of exposure time.

3.4.4 Textural Characterization (Physical Ads/Des of N_2)

Analysis of the adsorption/desorption N_2 isotherms is a non-destructive technique employed to provide information about the specific surface area, porosity, average pore volume and the general pore size distribution of the sample. Gas sorption analyses work on the basis that the adsorption occurs on well-defined surfaces, the adsorbed layers do not interact with each other, and the number of layers adsorbed goes to infinity at the saturation pressure. Prior to adsorption, the samples were degassed at certain temperature ~200°C during a period of time ~6h under vacuum, in order to remove any traces of moisture. Nitrogen adsorption/desorption isotherms were measured on a Quantachrome QuadraSorb-S equipment at -196 °C.

The most widely method to estimate the specific surface area of a material was proposed by Brunauer, Emmett and Teller (BET method).[5] The linearization of the N_2 isotherm by the BET equation provided the monolayer capacity (n_m^a) and, subsequently, the specific area of the solids was estimated by [Eq. 3.2] taking into account the area occupied by a molecule of N_2 at -196°C ($\sigma = 0.16\ \mathrm{nm}^2$) and the Avogadro´s number ($\mathrm{N_A}$).

$$S_{BET} = n_m^a \sigma \mathrm{N_A} \quad [\mathrm{Eq.\ 3.2}]$$

For instance, the shape of the curve obtained from the adsorption-desorption isotherm is classified into several types that indicate different surface features and porosity of a material. The majority of physisorption isotherms may be grouped into the six types shown in ***Figure 3.11.***

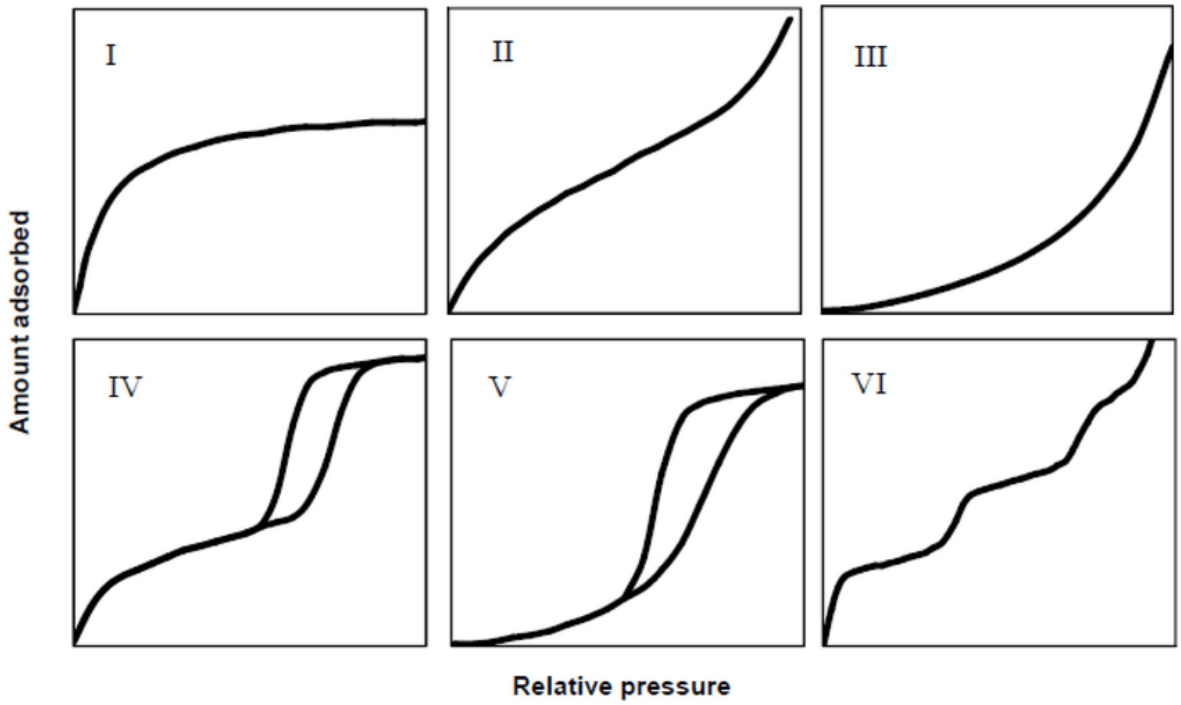

Figure 3.11 Types of physisorption isotherms.[6]

- *Type I* isotherms or pseudo-Langmuir isotherm are given by microporous solids having relatively small external surfaces (e.g. activated carbons, zeolites and certain porous oxides), the limiting uptake being governed by the accessible micropore volume rather than by the internal surface area.
- The reversible *Type II* isotherm is the normal form of isotherm obtained with a non-porous or macroporous adsorbent. The Type II isotherm represents unrestricted monolayer-multilayer adsorption. Low slope region in the middle of isotherm is often taken to indicate the stage at which monolayer coverage is complete and multilayer adsorption about to begin.
- The reversible *Type III* isotherm is convex to the p/p_0 axis over its entire range. Isotherms of this type are not common; the best known examples are found with water vapour adsorption on pure non-porous carbons.

- Characteristic features of the *Type IV* isotherm are its hysteresis loop, which is associated with capillary condensation taking place in mesopores, and the limiting uptake over a range of high p/p_0. The initial part of the Type IV isotherm is attributed to monolayer-multilayer adsorption since it follows the same path as the corresponding part of a Type II isotherm. Type IV isotherms are given by many mesoporous industrial adsorbents.
- The *Type V* isotherm is uncommon; it is related to the Type III isotherm in that the adsorbent-adsorbate interaction is weak, but is obtained with certain porous adsorbents.
- The *Type VI* isotherm represents stepwise multilayer adsorption on a uniform non-porous surface. Amongst the best examples of Type VI isotherms are those obtained with argon or krypton on graphitized carbon blacks at liquid nitrogen temperature.

Moreover, hysteresis appearing in the multilayer range of physisorption isotherms are usually associated with capillary condensation in mesopore structures. Such hysteresis loops may exhibit a wide variety of shapes. All possible types are shown in ***Figure 3.12.***

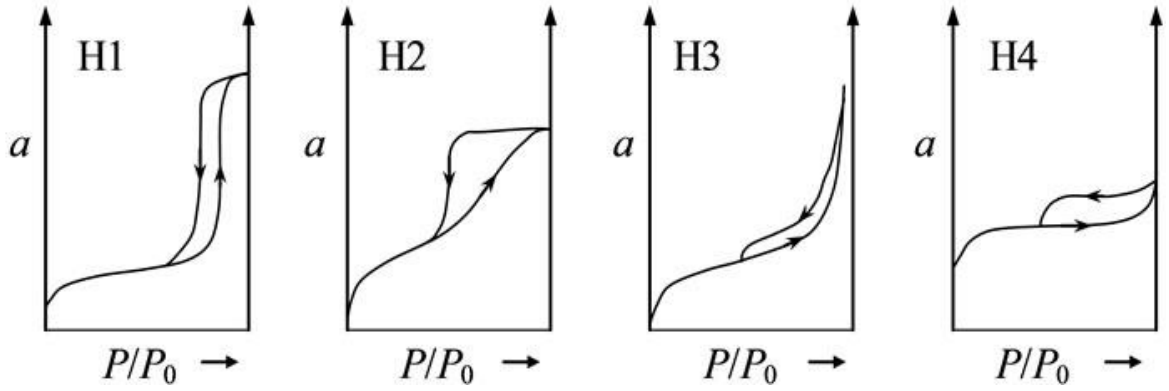

Figure 3.12 Types of hysteresis loops

- *H*1: Typical for materials formed by spheres packing or agglomeration and ordered mesoporous materials.
- *H2*: Typical for mesoporous materials with a highly interconnected pore network.
- *H3*: Typical for mesoporous materials with slit pore geometry and elastic materials that undergo swelling during adsorption.
- *H*4: Typical for microporous materials with slit pore geometry.

In particular, nanostructured hybrid materials and/or porous catalyst studies rely on this surface analysis tool since all electrochemical reactions that are facilitated are mostly surface reactions, including the oxygen reduction and oxygen evolution reactions. Increasing the specific surface area of an electrocatalyst or an electrode material through hybrid nanostructures with grapheme is one of the main goals of the research. On the other hand the pore size distribution curves of the samples were derived from the desorption branches of the associated isotherms using the Barrett-Joyner-Halenda (BJH) method.

3.4.5 In Situ and Operando Characterization

The electrochemical properties of active materials (e.g., specific capacity, reversibility, rate capability, cycling behavior, etc.) are strongly dependent on the structure and compositional changes during electrochemical reaction processes. Therefore, the establishment of clear relationships between electrochemical and structural/compositional data through In-situ or Operando experiments is no doubt one key issue for better understanding and further improving the electrochemical performance of electrode materials for high-performance energy storage devices. In-situ or Operando experiments can be defined as analytical methodologies wherein the spectroscopic characterization of materials is coupled simultaneously with electrochemical measurements in order to obtain valuable information about the reaction mechanism involved in the process.

During our research period, we had always the thirst of going deeper in charge storage or catalysis mechanism that governs the faradaic processes in alkaline environment of transition metals compounds by in-situ or Operando measurements. Thereby, we decided to perform Raman operando measurements on a mixed metal sulphide electrode and the results are shown in Chapter 8 of the present Thesis. A real image of the experimental Operando Raman set-up and the schematic representation of a home-made three electrode operando Raman cell with an acquired optical image can be seen in ***Figure 3.13***. In-situ Raman spectroscopy is a convenient and non-destructive tool for studying electrochemical reaction processes within numerous electrodes in aqueous and non-aqueous energy storage devices. Raman spectroscopy has been found to be very sensitive to the state of metal oxide, with the Raman frequencies being dependent on the metallic oxidization state. Therefore, it is particularly suitable for the investigation of underlying mechanism for redox couples involved in many aqueous electrochemical energy storage systems.

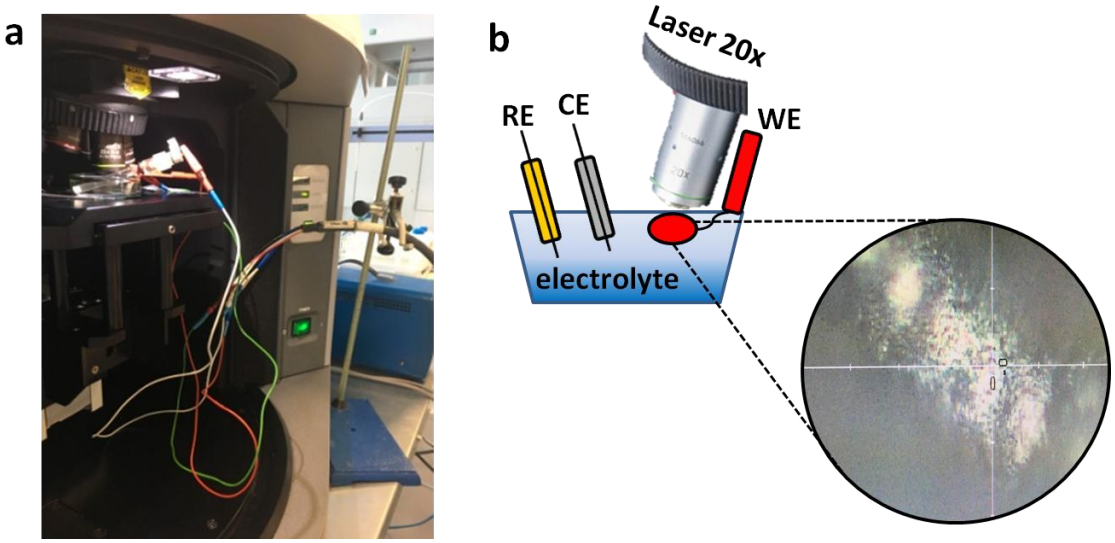

Figure 3.13 (a) Photography of experimental Operando Raman set-up (b) Schematic representation of a home-made three electrode Operando Raman cell with an acquired optical image

3.5 Electrochemical Characterization of materials

A combination of several electrochemical characterization techniques were employed to determine the electrochemical performance of the difference materials reported in this thesis.

3.5.1 Electrode Preparation and Half-Cell Electrochemical Set up

In the case of powder samples synthesized with the aim to applied as electrode materials for energy storage devices, working electrodes were prepared as follow. As a standard procedure, an homogeneous paste was prepared by vigorous mixing the active material (70 wt %), acetylene black (10 wt %) as the conducting agent and polytetrafluoroethylene (PTFE 60 wt % dispersion in water) as a binder in 2 ml of pure ethanol. The paste was manually applied by rolling on coupons of pre-cleaned nickel foam, as shown in ***Figure 3.14***.

Figure 3.14 Working electrode: back (left) and front (right)

Nickel foam is widely used as current collector in the preparation of electrodes for aqueous energy storage systems due to an efficient charge transport between active material and support. As we mentioned earlier, nickel foam was pre-treated in an ultrasonic bath during 30 min first in HCl, later in distillated water. The as-prepared electrodes were pressed at room temperature under a pressure of 200 $kg \cdot cm^{-2}$ on a uniaxial press (CARVER model 3853-0) during 5 min and dried at 90°C overnight ensuring the intimate contact between the active material and current collector. The mass loading of the dried electrodes were in the range of 3-9 $mg \cdot cm^{-2}$. The same procedure was followed for the preparation of Fe_3O_4-rGO (8.4 $mg \cdot cm^{-2}$), $NiMnO_3$-rGO (3-6 $mg \cdot cm^{-2}$) and NCMO_rGO (6-8 $mg \cdot cm^{-2}$) electrode materials, described in chapters 4, 5 and 6, respectively. During the electrode preparation, one should be aware that the material performance greatly depends on the mass loading and significantly declines in highly loaded electrodes. It is misleading to take advantage of the high capacity by a low active material mass loading, far away from practical purposes that typically reach 8–10 $mg \cdot cm^{-2}$ in commercial devices. In order to have a fair comparison, it is of great importance to develop electrode materials capable of providing high energy storage performance with high mass loadings.[7] On the other hand, $NiCoMnS_2$ electrodes (5.2 $mg \cdot cm^{-2}$) described in chapter 8, were fabricated by direct growth method onto Ni foam (Goodfellow, 99.5% purity) as described in details in previous section 3.3.3.3.

The as-prepared electrodes were first electrochemically characterized in a three-electrode configuration in 3 M KOH electrolyte (***Figure 3.15***). A platinum mesh and a Hg/HgO (1 M NaOH, ALS Co., Ltd Japan) electrode were employed as the counter and reference electrodes, respectively. The three-electrode cell is left for 30 min. before any electrochemical testing and the reference electrode is placed as close as possible to the working electrode.

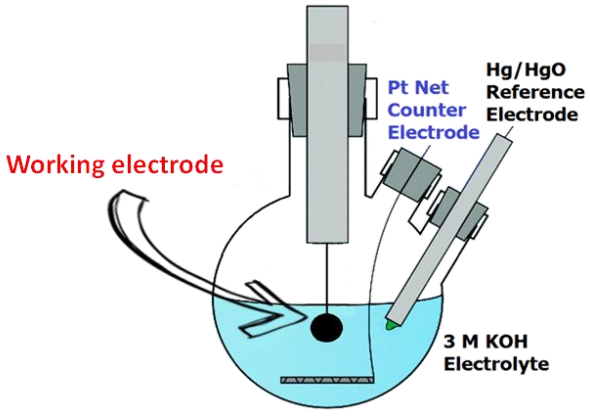

Figure 3.15 Schematic illustration of the Half-Cell Electrochemical Set up (3-electrode cell)

3.5.2 Rotating Disk and Rotating Ring-Disk Electrode Measurements (RDE and RRDE)

In order to prepare active electrocatalyst inks for Zn-air battery applications, typically, 4 mg of catalyst and 4 mg of Vulcan carbon (VC) were mixed carefully and dispersed in 500 µl of N-Methyl-2-pyrrolidone (NMP) by sonicating the mixture for 30 min in an ultrasonic bath to attain a homogeneous ink. 3 µl of the catalyst ink was drop-casted on a glassy carbon electrode (GCE, ALS Co., Japan) yielding a deposit 3 mm in diameter (electrocatalyst mass loading of ~0.34 $mg \cdot cm^{-2}$) and eventually dried at 80°C for ~30 min. Experiments were conducted in an electrochemical cell sealed with Teflon® cap using modified GCE as the working electrode, Pt spring as counter electrode, 0.1 M KOH as electrolyte and Saturated Calomel Electrode (SCE, Saturated KCl, ALS, RE-2BP) as reference electrode (***Figure 3.16***). Electrochemical measurements were conducted on a Bio-Logic (VMP3) multichannel station. Before starting measurements, the electrolyte was saturated with pure oxygen or argon (control experiments) by bubbling the gas into the electrolyte for at least 30 min. In order to ensure electrolyte saturation, purging was continued above the solution during the experiments. The modified GCE was scanned cathodically at a scan rate of 20 $mV \cdot s^{-1}$ at various rotating speed from 400 to 2300 rpm employing a RRDE-3A (ALS Co. Ltd) equipment.

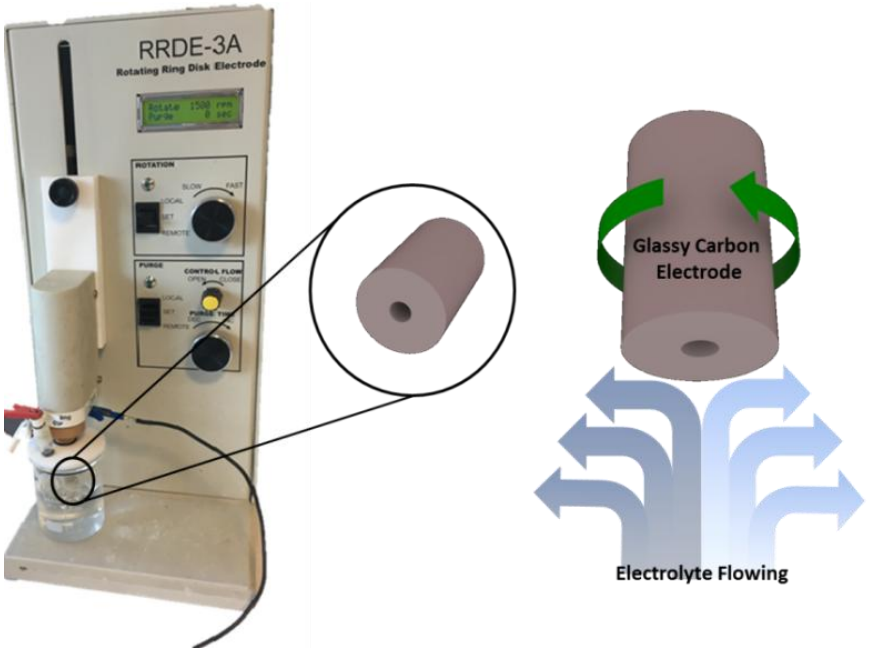

Figure 3.16 Rotating Disk and Rotating Ring-Disk Electrode Set up and schematic illustration of the working electrode

Koutecky-Levich theory was applied to interpret ORR kinetics. Therefore, number of electrons transferred (n) was estimated on the basis of following equation:[8]

$$\frac{1}{J} = \frac{1}{J_L} + \frac{1}{J_K} = \frac{1}{B_{\omega^{1/2}}} + \frac{1}{J_K} \quad [\text{Eq } 3.3]$$

where J is the experimental current density (mA·cm^{-2}), J_K is kinetic-limiting current density ($J_K = nFkC_{O_2}$), J_L is the diffusion-limiting current density, ω is the angular velocity, and B can be defined as follows:

$$B = 0.62nFC_{O_2}(D_{O_2})^{2/3}\nu^{-1/6} \quad [\text{Eq } 3.4]$$

where F is the Faraday constant (96,485 C·mol^{-1}), C_{O_2} is the bulk concentration of O_2 (1.15×10^{-6} mol·cm^{-3} in 0.1 M KOH), D_{O_2} is the diffusion coefficient of O_2 (1.90×10^{-5} cm^2·s^{-1}), and ν is the kinematic viscosity of the electrolyte (0.01 cm^2·s^{-1}). For the tafel plots, the kinetic current has been estimated from the mass-transport correction of RDE using the following equation:[9]

$$J_K = \frac{(J \times J_L)}{(J_L - J)} \quad [\text{Eq. } 3.5]$$

A Tafel plot is a graphical plot (usually logarithmic) showing the relationship between the current generated in an electrochemical cell and the electrode potential of a specific metal. Tafel plots give the information about kinetics for ORR/OER with change in Tafel slop value. Smaller Tafel slopes in the Tafel plot imply that the reaction can attain higher currents at lower over-potentials which further demonstrate the superior catalytic performance of the sample.

Rotating Ring-Disk Electrode (RRDE) Measurements

Rotating Ring-Disk Electrode was prepared according to the above mentioned recipe, the catalyst ink (4 µl) was drop-cast on the surface of a glassy carbon disk (Pt ring/GC disk electrode, ALS Co., Ltd) yielding a deposit of 4 mm in diameter. After drying in an oven at 80°C for ~30 min, the disk electrode was scanned cathodically at a scan rate of 20 mV·s^{-1} while a constant potential of 1.49 V vs. RHE was applied to the ring electrode. The number of electrons transferred and percentage of peroxide formation were calculated according to:

$$n = 4 \times \frac{I_D}{I_D + \frac{I_R}{N}} \text{ [Eq. 3.6]}$$

$$\%HO_2^- = 200 \times \frac{\frac{I_r}{N}}{I_D + \frac{I_r}{N}} \text{ [Eq. 3.7]}$$

where I_D is disk current, I_r is ring current, and N is the current collection efficiency (N= $-I_r/I_D$) of the Pt ring electrode. *N* was measured by scanning GC disk electrode from 1.44 to 0.99 V vs. RHE at 20 $mV \cdot s^{-1}$ and applying a constant potential of 1.44 V to the ring electrode in an aqueous solution of 5 mM $K_3Fe[CN]_6$ and 0.1 M KCl.[10]

3.5.3 Electrochemical techniques

The assembled 3-electrode electrochemical cell, RDE and RRDE were electrochemically tested for a systematic study of the electrochemical properties of the active materials. These electrochemical measurements often included Cyclic Voltammetry (CV), Linear sweep voltammetry (LSV) galvanostatic charge/discharge (GCD) and Electrochemical Impedance Spectroscopy (EIS), which will be discussed below. All experiments were performed at room temperature (RT).

All electrochemical techniques were conducted using an electrochemical workstation device (Bio-Logic (VMP3) multichannel station, ***Figure 3.17***).

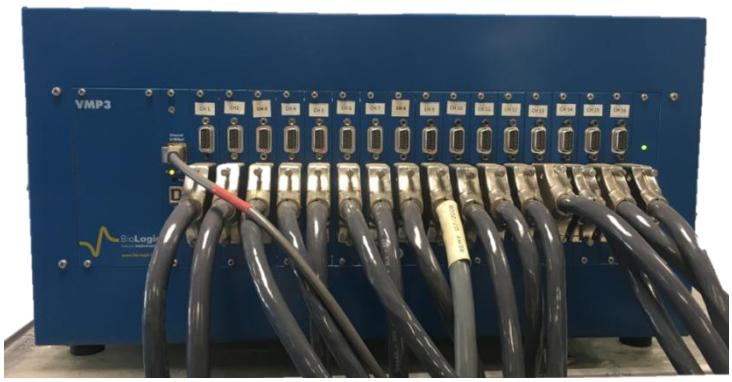

Figure 3.17 Electrochemical workstation device

The cell cables of each channel in the Bio-Logic (VMP3) multichannel station have a total of four connectors: working electrode (WE), counter electrode (CE), reference electrode (RE), and ground. The potential is always measured between the RE (white) and the WE (red) and the current is always measured between the WE (red) and CE (blue).

The working electrode (WE) is the electrode in an electrochemical system on which the reaction of interest is occurring. The counter electrode (CE), is an electrode which is used to close the current circuit in the electrochemical cell. It is usually made of an inert material (e.g. Pt, Au, graphite) and usually it does not participate in the electrochemical reaction. Because the current is flowing between the WE and the CE, the total surface area of the CE (source/sink of electrons) must be higher than the area of the WE so that it will not be a limiting factor in the kinetics of the electrochemical process under investigation. Finally, the reference electrode (RE) is an electrode which has a stable and well-known electrode potential and it is used as a point of reference in the electrochemical cell for the potential control and measurement.

- *Cyclic Voltammetry and Linear Sweep Voltammetry*

Cyclic Voltammetry (CV) is a type of potentiodynamic electrochemical measurement, recording the relationship between current vs. voltage when the potential at the working electrode is raised linearly versus time to a set potential at a certain sweep rate and reversed back to the original fixed potential at the same scan rate. In potentiostatic mode, a potentiostat/galvanostat will accurately control the potential of the Counter Electrode (CE) against the Working Electrode (WE) so that the potential difference between the working electrode (WE) and the Reference Electrode (RE) is well defined, and correspond to the value specified by the user.

CV is generally employed as a preliminary electrochemical technique to evaluate the electrochemical properties of an analyte in solution upon a single or a few scans.

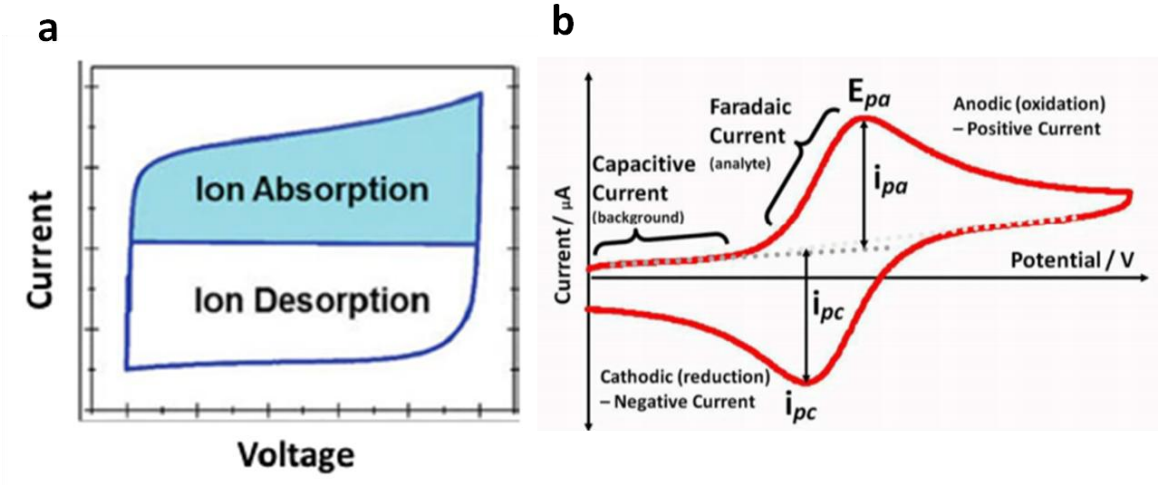

Figure 3.18 Scheme of a CV for (a) capacitive material (b) faradaic material

In the examining voltage range, an analyte can be oxidized or reduced on a forward scan and then re-oxidized or re-reduced on the return scan, as an indication of highly reversible redox couples. A CV test is also able to reveal the specific reactions occurring in the different electrochemical processes, which can be determined from the redox peak potentials, and further confirm the energy storage mechanism involved. The typical voltammograms obtained for a capacitive electrode material and a faradaic type electrode material are represented in ***Figure 3.18.***

Moreover, CV curves can be also employed to compute the specific capacity of the active material using the relationship shown below for faradaic-type electrodes:

$$Q = \frac{\int \mathrm{Idt}}{\mathrm{m}} \text{ [Eq. 3.8]}$$

where Q is the specific capacity ($C \cdot g^{-1}$ or $mAh \cdot g^{-1}$) based on the mass of active material, I is the current, m is the mass of active material (g) and dt is the time differential.

The specific capacitance of the capacitive electrodes (e.g. capacitor-type or pseudocapacitive) ($C_{electrode}$) was also calculated from the integral of the CV curves as expressed by [Eq.3.9] and [Eq.3.10]

$$C = \frac{Q}{\Delta V} = \frac{\int IdV}{s \cdot \Delta V \cdot m_t} \text{ [Eq. 3.9]}$$

$$C_{electrode} = 4C \text{ [Eq. 3.10]}$$

Where C is the specific capacitance calculated for the device ($F \cdot g^{-1}$), $C_{electrode}$ is the specific capacitance of the individual electrodes ($F \cdot g^{-1}$), Q is the charge stored, ΔV is the applied potential window, I is the applied current, s is the scan rate and m_t is the total mass of the electrode material.

In a Linear Sweep Voltammetry (LSV) a fixed potential range is employed much like CV measurements. However, in LSV the voltage is scanned from a lower limit to an upper limit (OER) or from an upper limit to a lower limit (ORR).

Kinetic parameters can be also gained from CV curves to shed light on the different charge storage phenomena. The current and the sweeping rate obey the power-law relationship expressed as $i = aV^b$, with the b-value providing insight into the charge storage mechanism:

$$i(V) = a \cdot V^b;\ \log i(V) = b \cdot logV + loga \quad [Eq. 3.11]$$

For a redox reaction confined by semi-infinite linear diffusion, the b-value would be 0.5; for a surface-confined process, the b-value would be 1. Moreover, the b-value could act as an indicator for differentiating pseudocapacitor-type from battery-type materials.

On the other hand, the ability to decompose the total current into contributions from faradaic capacity and double layer capacitance is critically important in terms of providing an understanding of the charge-storage mechanism; in this regard Dunn´s method was employed:

$$i(V) = K_1 \cdot v + K_2 \cdot v^{1/2}; \frac{i(V)}{v^{1/2}} = K_1 \cdot v^{1/2} + K_2 \quad [\text{Eq. } 3.12]$$

- *Galvanostatic Charge/Discharge*

Galvanostatic charge/discharge (GCD) experiment is an electrochemical test in which a constant current pulse is applied through an electrolytic cell measuring the voltage signal against a reference electrode as a function of time. Specifically, for charging the cell a positive current is applied and for discharging a negative current should be applied. In galvanostatic mode, the current flow between the WE and the CE is controlled. The potential difference between the RE and WE and the current flowing between the CE and WE are continuously monitored. The typical representation of these experiments is represented in ***Figure 3.19.***

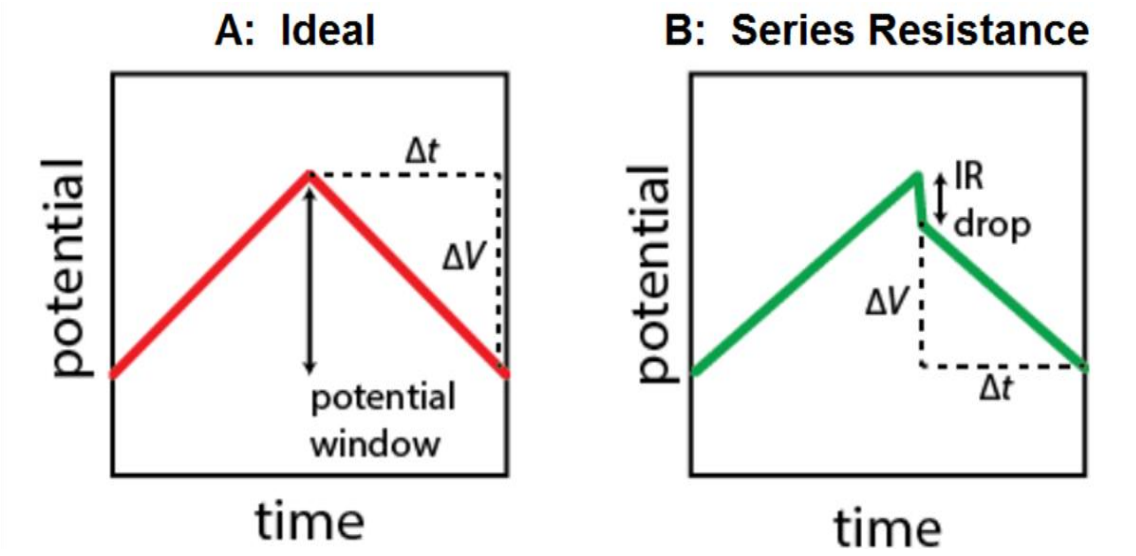

Figure 3.19 Schematic illustration of a GCD curve of a Supercapacitor (a) ideal (b) non-ideal

For three-electrode test cells, the galvanostatic charge/discharge performance is examined by a chronoamperometry technique, where the maximum and minimum voltage are fixed. Galvanostatic charge/discharge tests exhibit electrochemical information on charge/discharge profiles, Columbic efficiency, and long-term cycling properties.

Specific capacity was also obtained based on discharge curves , as follow:

$$Q = \frac{i\Delta t}{m_t} \quad [\text{Eq. } 3.13]$$

where i is discharge current, Δt is discharge time and m_t is the total active mass. This equation has been applied either in a three electrode systems considering the mass of the working electrode or in a two-electrode device considering the total mass of both electrodes.

- *Electrochemical Impedance Spectroscopy*

The electrochemical impedance spectroscopy (EIS), also called Alternating Current (AC) Impedance, consists of varying the excitation frequency *f* of the applied potential *E*, over a range of frequencies, while the impedance (both resistance and reactance) is measured to characterize the dynamics of an electrochemical process. The use of EIS in batteries and SCs often provides an estimation of the internal resistance (electrolyte resistance, charge-transfer resistance and diffusion resistance) at an open circuit potential or under other conditions. In this powerful electrochemical technique, a sinusoidal voltage perturbation with small amplitude is applied meanwhile the frequency is swept from high values to small ones. Thus the response of the device is recorded. The impedance (Z) is defined by the relation between the voltage applied and the current response of the system, as follow:

$$Z(\omega) = \frac{1}{jf\ C(2\pi f)} \quad [\text{Eq. } 3.14]$$

where ω is the angular frequency, *f* is the frequency and *C* is the capacitance. The typical graph to represent impedance results is called Nyquist Plot, where the imaginary part of the impedance ($-Z_{im}$) is plotted versus the real part of the impedance (Z_{re})

The use of EIS tests to accompany other electrochemical results leads to a better understanding of the internal electrochemical processes .This technique has been employed to measure the internal

resistance either in a three electrode configuration, to have an idea about the conductivity of the working electrode material tested or in two electrode Swagelok cells (full devices) to measure the resistance of the overall system.

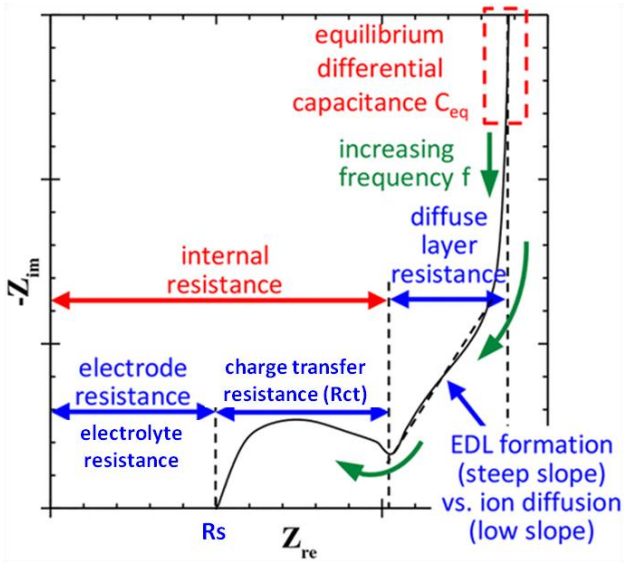

Figure 3.20 Schematic of a typical Nyquist plot for EDLC electrodes or devices (adapted from [11])

EIS experiments were performed over a frequency range going from 200 kHz to 10 mHz using a bias voltage of 0 V and 10 mV of amplitude. To perform a proper impedance experiment, the system must be as much stable as possible, any external disturbances such as electrical noise must be avoided. For impedance data fitting, the ZView Impedance Analysis Software was employed to adjust the electrical equivalent circuits.

3.6 Application of materials in energy storage devices

3.6.1 Assembly and electrochemical characterization of aqueous energy storage devices.

Aqueous hybrid energy storage devices were assembled in Swagelok cells (2-electrode cell) by sandwiching a cellulosic filter paper embedded with the electrolyte (3M KOH solution) between the positive electrode (our active material) and rGO electrode as a negative electrode ***(Figure 3.21)***. In a two-electrode cell setup (***Figure 3.21***); CE and RE are shorted on one of the electrodes while the WE is on the opposite electrode. The potential across the complete cell is measured. This includes contributions from the CE/electrolyte interface and the electrolyte itself.

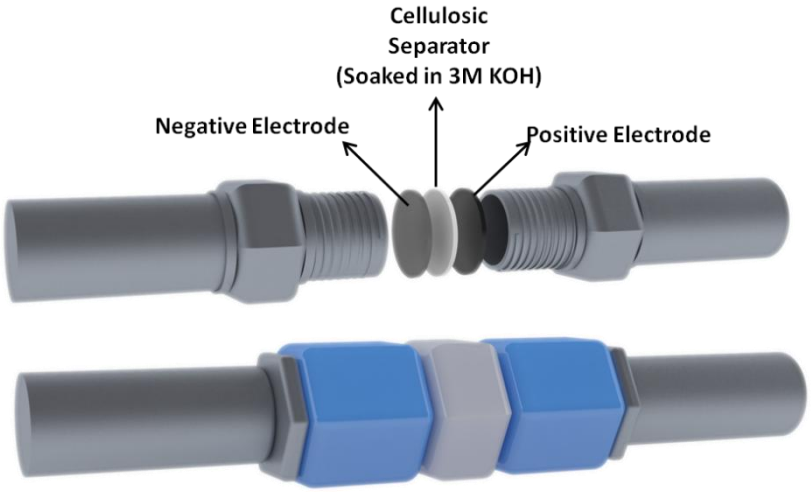

Figure 3.21 Two electrode configuration in a Swagelok$^{(R)}$ cell

The results of the fabrication of different aqueous hybrid cells are discussed in Chapter 5, 6 and 8 of the present thesis. High power aqueous batteries were also assembled in Swagelok cells by integration of Fe_3O_4-rGO hybrid materials as the negative electrode and $NiCoMnO_4$ as the positive electrode in 3 M KOH solution, that cell was extensively discussed in Chapter 4.

Swagelok cells® can also be presented in a three-electrode configuration (T-shape Swagelok® cell or three-neck Swagelok® cell). In Chapter 8, certain results were obtained with this type of configuration were the positive, the separator and the negative electrodes were pressed between two stainless steel rods from two necks of the Swagelok cells and the third neck was used to place the reference electrode into the cell, as illustrated in ***Figure 3.22.***

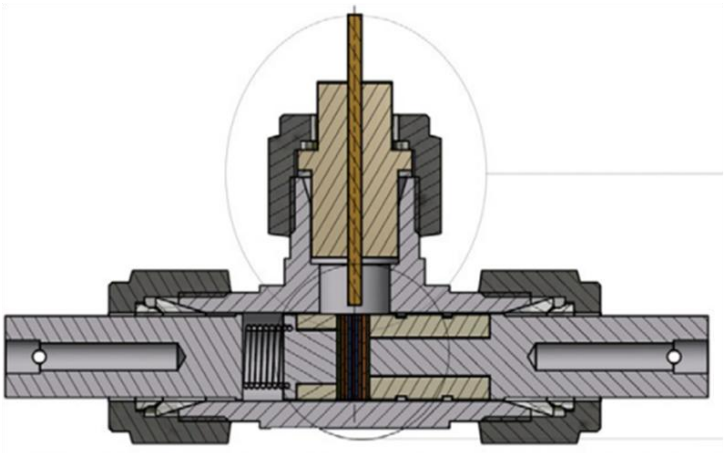

Figure 3.22 Schematic representation of a three-electrode configuration Swagelok cell (adapted from [12])

Inserting a reference electrode in the Swagelok cell allows the potentials of the positive and negative electrodes to be monitored separately in order to be sure that the charge of electrodes are well balanced by adjusting the mass of electrodes. The potential and the current are always measured between the negative and the positive electrode, similar to a standard two electrode configuration.

To correctly evaluate the electrochemical performance of a hybrid energy storage system, it is completely necessary to calculate an electrode mass balancing due to the differences between the charges and mass loading contributions in each electrode. The mass loading of the positive and negative electrodes was adjusted in all of the cases according to the charge balance theory, as follow:

$$m^+ \cdot Q^+ \cdot \Delta V^+ = m^- \cdot Q^- \cdot \Delta V^- \quad [\text{Eq. } 3.15]$$

where m^+ and m^- are the mass of the positive and negative electrode, respectively. Q^+ and Q^- is the specific capacity/capacitance of positive and negative electrode, respectively and ΔV^+ and ΔV^- are the working potential windows of positive and negative electrodes, respectively.

After assembly, energy storage devices were examined by CV, GCD and EIS measurements.CV profiles of the hybrid energy storage system can provide an idea of the charge storage mechanism which governs the process, if redox peaks appear, faradaic charge storage mechanisms are taking place. Moreover, forward and backward scans can provide an idea of how symmetric or reversible is the system, suggesting high or low columbic efficiency of the electrodes in the device. Furthermore, peak separation over the course of increased scan rates, demonstrate as well good performance of the device at high scan rates. [Eq 3.8] and [Eq 3.9] can be also employed to calculated the specific capacity/capacitance of the full device.

GCD profiles in a hybrid system can also give an idea of the charge storage mechanism governing the process, GCD profiles clearly deviated from triangular linear-shape as would be found in EDLC-based SCs suggest a Faradaic mechanism. Moreover, if charge and discharge profiles show nearly identical counterparts these evidence suggest excellent reversibility and coulombic efficiency of the cell. Furthermore, the appearances of plateaus at certain potentials in the GCD profiles usually are well matched with the observed peaks potentials in CV curves. As we mentioned previously Eq. [3.13] can be also employed to calculate the specific capacity of the full device. Real specific

energy and specific power of the device were also calculated according to the following equations, directly determined from the discharge curves.

$$E_{sp} = \frac{1}{m_t}\int I \cdot V \cdot dt \quad [Eq.3.16]$$

$$P_{sp} = \frac{E_{sp}}{t_{discharge}} \; [Eq.3.17]$$

Where E_{sp} ($Wh \cdot kg^{-1}$) is specific energy, I (A) is the discharging current, V (V) is the potential, m_t (kg) is total mass of the active materials in negative and positive electrodes, P_{sp} ($W \cdot kg^{-1}$) is the specific power and $t_{discharge}$ (h) is the time of discharge.

Finally, cycling performance of the device is tested over a range of cycles at a specific current density. Moreover, the typical EIS experiments in a hybrid device are usually performed before and after cycling in order to demonstrate the changes in the overall impedance after cycling which further proves the excellent cycling stability of the hybrid system.

Additionally, in order to probe the viability of the hybrid devices assembled for practical applications, usually 2 cells were connected in series and employed for powering LEDs for a certain period of time.

3.6.2 Assembly and electrochemical characterization of Zn-air batteries

In order to assembly full Zn-Air batteries, air cathodes were fabricated by drop-casting of the nanocatalyst ink on gas diffusion layers (GDL). The catalyst ink was prepared by adding 15 mg of the nanocatalyst and 15 mg of Vulcan carbon to 1.5 ml of absolute ethanol plus 50 µl of Nafion solution (5 wt. % in lower aliphatic alcohols and water, contains 15-20% water). The prepared electrodes were assembled in a 3D-printed designed cell with small holes on cathode side, together with a Zn foil as anode. The cell was filled with 6 M KOH and 0.02 M $ZnSO_4$ (~ 3 ml) as the electrolyte without the necessity of a separator ***(Figure 3.23).*** After assembly, Zn-Air batteries were examined by galvanodynamic discharge curves and GCD measurements in an electrochemical workstation showed in ***Figure 3.17***. Galvanodynamic charge-discharge polarization and power density curves provide the peak of maximum power density achieved for the Zn-Air battery system. Moreover, the experiment total exhaustion of Zn, provide the capacity

value in $mAh \cdot g_{Zn}^{-1}$ of the battery once the Zn in the anode is completely gone. On the other hand, GCD measurements provide how stable is the battery at different current loads by evaluating the stability of the different plateaus for a certain period of time.

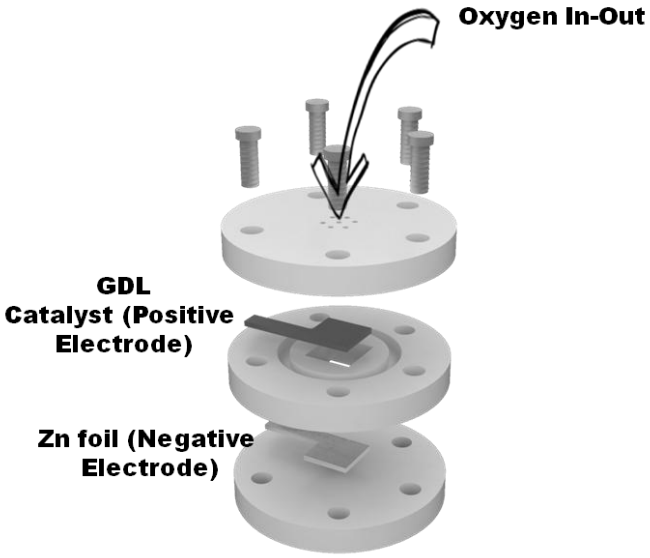

Figure 3.23 3D-printed cell as a Zn-Air Battery

Finally, cycling performance was tested over a range of cycles at a specific current density to evaluate the round-trip voltage for the device (difference between charging and discharging voltage) and the stability of the battery along the cycles. The results of the fabrication of Zn-Air batteries are extensively discussed in Chapter 7 and 9 of the present thesis.

3.7 References

1 W. S. Hummers and R. E. Offeman, *J. Am. Chem. Soc.*, 1958, **80**, 1339.

2 S. Stankovich, D. a. Dikin, R. D. Piner, K. a. Kohlhaas, A. Kleinhammes, Y. Jia, Y. Wu, S. T. Nguyen and R. S. Ruoff, *Carbon N. Y.*, 2007, **45**, 1558–1565.

3 J. Zubieta, *Solid State Methods, Hydrothermal*, Elsevier, 2013.

4 R. Kohli, *Methods for Monitoring and Measuring Cleanliness of Surfaces*, Elsevier, 2012.

5 S. Brunauer, P. H. Emmett and E. Teller, *J. Am. Chem. Soc.*, 1938, **60**, 309–319.

6 K. S. Sing, *Pure Appl. Chem.*, 1982, **54**, 2201–2218.

7 Y. Gogotsi and P. Simon, *Science (80-.).*, 2011, **334**, 917–918.

8 R. Zhou, Y. Zheng, M. Jaroniec and S.-Z. Qiao, *ACS Catal.*, 2016, **6**, 4720–4728.

9 Y. Liang, Y. Li, H. Wang, J. Zhou, J. Wang, T. Regier and H. Dai, *Nat. Mater.*, 2011, **10**, 780–786.

10 C. Pozo-Gonzalo, O. Kartachova, A. A. J. Torriero, P. C. Howlett, A. M. Glushenkov, D. M. Fabijanic, Y. Chen, S. Poissonnet and M. Forsyth, *Electrochim. Acta*, 2013, **103**, 151–160.

11 B. A. Mei, O. Munteshari, J. Lau, B. Dunn and L. Pilon, *J. Phys. Chem. C*, 2018, **122**, 194–206.

12 G. Garcia, W. Schuhmann and E. Ventosa, *ChemElectroChem*, 2016, **3**, 592–597.

CHAPTER 4

Anchored Fe_3O_4 NPs on rGO NSs as High-Power Negative Electrodes for Aqueous Batteries

4.1 Research Background

Specific power and energy of electrochemical storage systems need to be significantly improved to face the ever increasing energy challenges. For instance, the viability of many new technologies like electrical vehicles is tied to the development of energy storage devices capable of fast uptake/deliver of high amount of energy. Considering the shortcomings of current Li-ion battery technology in high-power applications (specific power ~10^3 $W \cdot kg^{-1}$) and safety concerns (flammability of their organic-based electrolytes), developing new storage systems operating with affordable materials and relatively safe aqueous electrolytes is of great interest and demand.[1,2] Although lead acid batteries utilize aqueous electrolytes and they are relatively safe, the presence of lead and sulfuric acid make them potentially hazardous for the environment. In addition they suffer from less energy and power densities (~50 $Wh \cdot kg^{-1}$ and ~200 $W \cdot kg^{-1}$) and shorter cycle life (~ 500 cycles) than Li-ion technology.

In recent years, different metal oxides were introduced and studied as high power electrode materials through nanostructuring and materials engineering. Having high surface areas, porous accessible channels, and small ion diffusion paths in these structures, faradaic reactions can be facilitated and taken place in faster discharge regimes. However, several of these oxides suffer from inherently low electrical conductivity, geological scarcity, and high cost hindered their utilization in commercial devices. On the other hand, most of these oxide materials that have been investigated in literature include fancy nanostructures synthesized through complex, expensive, and/or time-consuming processes. Therefore, a key factor in the commercialization of new technologies is the need of develop cheap, facile and easily scale-up syntheses for active materials with high electrochemical performance.

Among all transition metal oxides, the iron oxide family is especially attractive due to high abundance of iron in the earth crust, their low cost, and low environmental impact. ***Table 4.1*** estimates the merit of dollars per mAh^{-1} for common metal oxides based on their theoretical capacity. High cost of Co and Mo limits their potential application, and thus metal oxides with much lower dollars per mAh^{-1}, such as iron oxide are considered excellent candidates as electrode materials.

Table 4.1 Dollars per mAh^{-1} for the common transition-metal oxides [3]

Metal	Oxide	($·kg^{-1})&	Theoretical capacity ($mAh·g^{-1}$)#	$·$mAh^{-1}$
Fe	FeO	0.08	746	0.11
Co	CoO	30.05	715	41.96
Ni	NiO	12.50	718	17.41
Cu	CuO	6.15	674	9.12
Mo	MoO_2	24.00	838	28.64

& Prices obtained from daily*metalprice.com*, February 2019.
# Theoretical capacity obtained based on 1 electron transfer and 0.6V window. $C = nF/(VM)$, where n is the charge transfer number, F is the Faraday constant, and M is the molecular weight.

In all different iron oxide phases, magnetite (Fe_3O_4) is of special interest in several fields due to its favorable electric, magnetic and optical characteristics.[4] Particularly, Fe_3O_4 has been widely investigated as anode material in Li-ion batteries, showing high performance capability when morphologically or compositionally engineered.[5] Lately, it has attracted attention as negative electrode for aqueous-based energy storage devices[6] due to its large working potential window (~ 1.25V), as shown in ***Figure 4.1***.

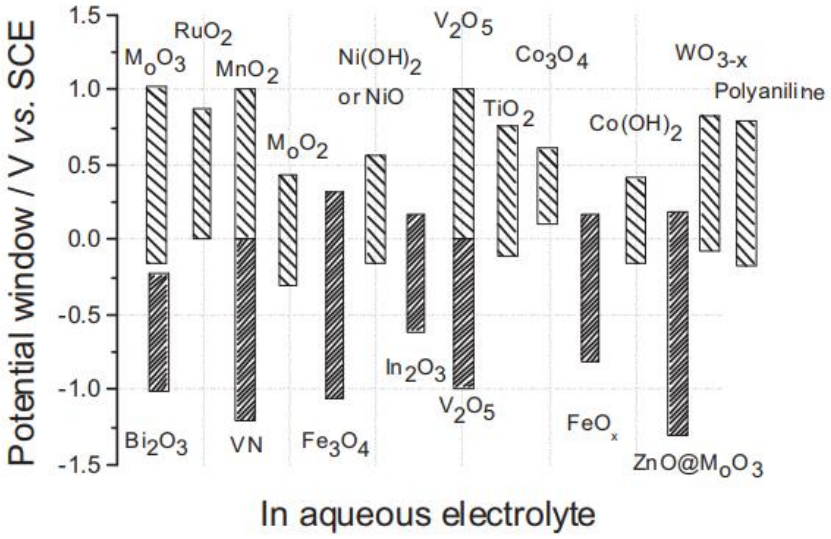

Figure 4.1 Working potential windows of various metal oxides in aqueous electrolyte (adapted from [7])

However, as many other metal oxides, Fe_3O_4 suffers from poor electronic conductivity and hence, the strategy of its combination with electrically conductive carbonaceous materials can circumvent this shortcoming. It has been already demonstrated that by combining Fe_3O_4 with carbonaceous

materials one can obtain high values of conductivity and improved overall electrochemical behavior due to synergistic effects between the oxide and the carbon material. [8,9]

Here, it has been attempted to provide a glance at the literature on this matter. It should be noticed that in most of the articles we reviewed, metal oxide-based electrodes were considered capacitive instead of faradaic and the electrochemical performance was reported based on $F \cdot g^{-1}$ (referred as capacitance). However, the faradaic nature of these materials was evidenced by the non-rectangular shape of the CV signals and changing of the slope in charge-discharge profiles. Therefore, as mentioned in the introduction chapter, the formalisms and equations commonly adopted for capacitive materials are not accurate and the appropriate magnitude is "capacity".[10] In order to make a fair comparison with our obtained results, capacity values were calculated using the provided information in the articles and here reported based on either $C \cdot g^{-1}$ or $mAh \cdot g^{-1}$.

In one of the pioneering examples, Qu et al. electrochemically fabricated 2D sandwich-like graphene-supported Fe_3O_4 nanocomposites, showing a high capacity of 456 $C \cdot g^{-1}$ (126$mAh \cdot g^{-1}$) at 0.5 $A \cdot g^{-1}$ in 1 M LiOH solution as electrolyte.[7] Wang et al. hydrothermally grew Fe_3O_4 nanoparticles (NPs) on reduced graphene oxide (rGO) and carbon nanotubes (CNTs), improving the capacity from 18 to 61 and 30 $mAh \cdot g^{-1}$, respectively.[11] Later, Liu et al. synthesized quasi-cubic Fe_3O_4@rGO composite via a colloid electrostatic self-assembly method. Although this obtained a facile method to prepare the composite material, it exhibited a moderate capacity of 45 $mAh \cdot g^{-1}$ in 6 M KOH.[12] More recently, Li et al. reported hydrothermal synthesis of anchored Fe_3O_4 on rGO, showing a capacity as high as 67 $mAh \cdot g^{-1}$ at 1 $A \cdot g^{-1}$.[8] In spite of these attempts to hybridize Fe_3O_4 with different carbon materials, there has generally been a failure to develop a strategy by which to obtain an electrode material having high capacity via a facile, scalable and commercially viable synthesis method. Moreover, it should be mentioned that in most of the reported works, low mass loadings of the active materials (< 1 to 2 $mg \cdot cm^{-2}$) have been employed, resulting in unrealistic storage capabilities for a practical device.[13,14] Therefore, it is still a huge challenge to develop active materials capable of retaining high capacity at high mass loadings at a competitive cost.

In this chapter, we employed an already commercialized and scaled-up material and turned it into a high performance active material via a simple route. This consists of anchoring Fe_3O_4 nanoparticles on rGO nanosheets (NSs) without any surface modification through an electrostatic

coagulation method. By the use of different characterization techniques, it has been proven that the electrostatic coagulation results in tight anchoring of the nanoparticles on the surface of graphene layers. By finding the optimized component ratio, we could significantly enhance the electrochemical performance of the pure Fe_3O_4 NPs in aqueous media even with high mass loading of active material in the hybrid electrodes (8.4 $mg \cdot cm^{-2}$). Furthermore, we integrated the hybrid material as negative electrode with $NiCoMnO_4$ as positive electrode (Fe_3O_4-rGO//$NiCoMnO_4$) demonstrating their potential applicability for high-power aqueous batteries.

4.2 Results and discussion

4.2.1 Synthesis and Physico-Chemical Analysis of Fe_3O_4-rGO

As detailed in Chapter 3, Fe_3O_4-rGO hybrid materials were synthesized through an electrostatic coagulation route followed by a chemical reduction step, illustrated in ***Figure 4.2***.

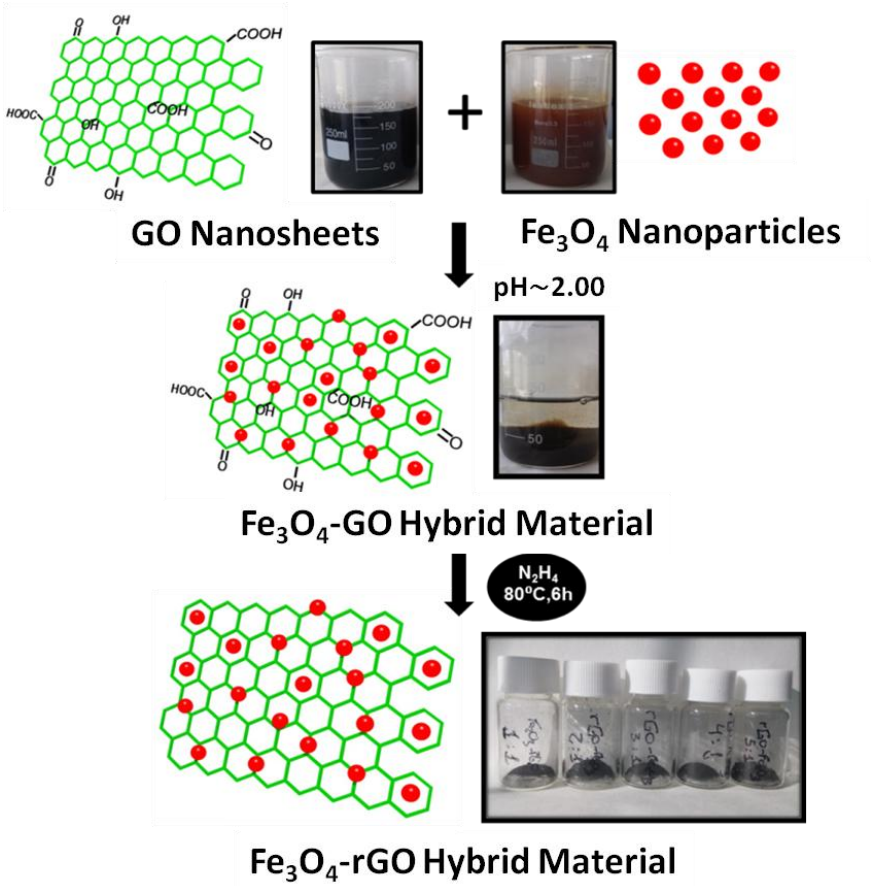

Figure 4.2 Schematic illustration of electrostatic coagulation of Fe_3O_4-rGO hybrids

The electrostatic interaction between particle dispersions was investigated over a pH range of 1.5 to 11 by monitoring zeta-potential (Z_p) of the particles. ***Figure 4.3*** shows the Z_p profiles of Fe_3O_4 NPs and GO NSs as a function of pH. As it is seen, GO NSs were negatively charged in the measured pH range with slight Z_p change, due to ionization of the functional groups on surface of graphene layers. In contrast, Fe_3O_4 NPs are heavily positive at low pH but the Z_p value sharply decreases at higher pH values. This can be ascribed to the protonation/deprotonation of hydroxyl ions on the surface of metal oxides in aqueous solution. Obviously, the opposite surface charges governed the anchoring of Fe_3O_4 NPs on GO NSs and the maximal Z_p potential difference between two samples and therefore the strongest attraction force can be achieved at pH = 2 (***Figure 4.3***), which has been used for synthesis of the hybrid materials.

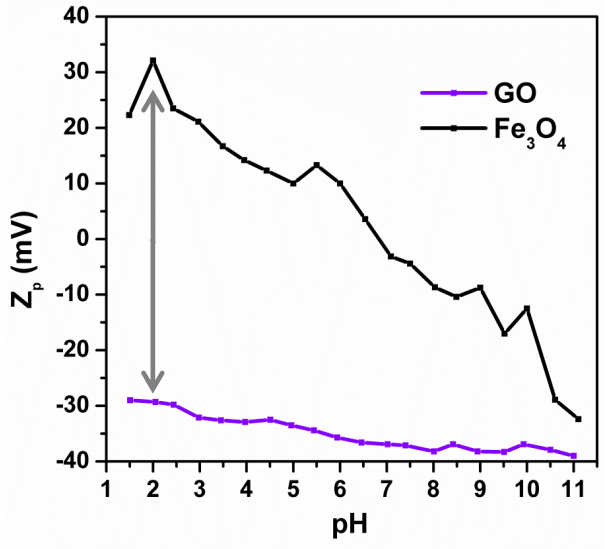

Figure 4.3 Zeta potential evolution of GO and Fe_3O_4 dispersions at various pHs

Different samples of Fe_3O_4-rGO were prepared by altering the oxide/carbon ratio. The structural and compositional properties of these hybrids and pure Fe_3O_4 NPs were identified by powder XRD analyses, as shown in ***Figure 4.4a***. In the case of pure Fe_3O_4 NPs (black pattern) all diffraction peaks could be easily indexed to the face-centered cubic (fcc) magnetic phase (marked with corresponded hkl crystallographic planes) with space group of Fd-3m, matching well with the JCPDS card no. 98-011-1282. The Fe_3O_4 peaks can be still tracked in all hybrid materials with different ratios after chemical reduction, revealing that no change occurred in the crystalline structure of the Fe_3O_4 nanoparticles during the hybridization and reduction steps.[12] Furthermore,

other crystalline phases like Fe_2O_3 and Fe were not detected, confirming the phase purity of the magnetite iron NPs.[15] A broad and low-intense (002) graphitic peak can be seen at 2θ =23.8° in the majority of Fe_3O_4-rGO samples, suggesting effective reduction of the graphene oxide layers. The bigger the iron oxide ratio during synthesis, the smaller and broader the (002) peak; e.g. due to the presence of Fe_3O_4 NPs anchored on graphene layers that can suppress the restacking of graphene layers.[16]

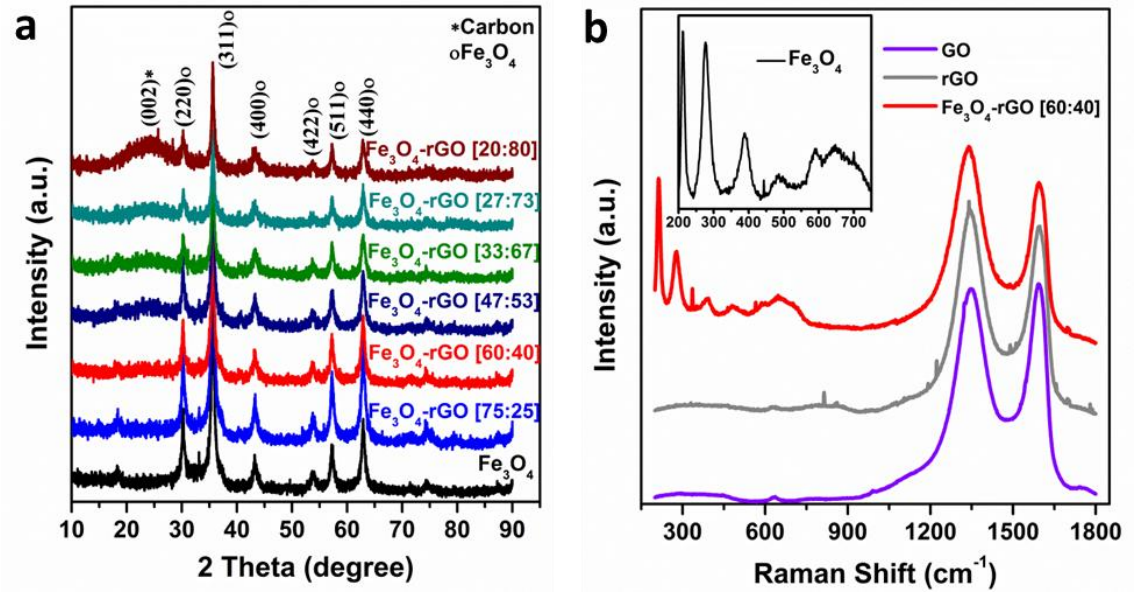

Figure 4.4 Physico-Chemical Analysis: (a) XRD of Fe_3O_4 NPs and Fe_3O_4-rGO hybrid materials; (b) Raman spectroscopy of GO, rGO and Fe_3O_4-rGO hybrid. Inset shows Raman spectrum of pure Fe_3O_4 sample

Raman spectroscopy is known as a representative technique in characterizing carbonaceous materials and has been employed in this work to obtain structural information of the samples and monitor possible defects in the graphene oxide layers in the hybrids. The Raman spectra of GO, rGO, and Fe_3O_4-rGO [60:40] are displayed in ***Figure 4.4b***. Two main Raman bands around 1348 (D-band) and 1592 cm^{-1} (G-band) can be ascribed to defects of the sp^2 domain, and the first order scattering of the E_2g vibrational mode in graphitic carbon, respectively.[17] Density of structural defects on the surface of graphene layers can be understood from the intensity ratio (I_D/I_G). In this regard, it can be observed that the I_D/I_G ratio increased in the case of rGO (1.06) in comparison with that of GO (0.98), attributed to the increased number of smaller poly-aromatic domains and a highly defective carbon lattice.[18] In Fe_3O_4-rGO hybrid material, the I_D/I_G ratio further increased (1.15), suggesting that anchoring Fe_3O_4 NPs on graphene layers resulted in an increase of

structural defects. This can be due to reduced sp^2 domains in the course of dehydration reactions and anchoring metal oxide nanoparticles on the basal plane of reduced graphene oxide. The inset of ***Figure 4.4b*** shows Raman spectrum of Fe_3O_4 NPs where Raman lines appeared at 212, 277, 388, 486, 589, 647, and 699 cm^{-1}, indicating the presence of α-Fe_2O_3 phase. As previously reported in literature, this could be attributed to decomposition of Fe_3O_4 NPs to the hematite phase (α-Fe_2O_3) by the strong laser light used during Raman measurements [19,20] or may be ascribed by the strong oxidization at pH=2 of transition metal ions using GO.[8] Similar peaks can be also seen in the hybrid material, revealing the presence of iron oxide particles hybridized with the graphene matrix which is in agreement with previously discussed XRD results.

To further characterize the composition of the samples and estimate the amount of Fe_3O_4 NPs anchored on graphene layers, thermogravimetric analysis (TGA) was performed. ***Figure 4.5*** shows TGA profiles of the samples in air from room temperature to 700 °C. In the case of Fe_3O_4 NPs, only a small mass loss (2.8 %) is observed, ascribed to adsorbed hydroxyl groups on the surface sample and/or trapped water in the lattice.[21] On the contrary, all hybrids showed a significant mass decrease between 400 to 500 °C due to combustion and decomposition of rGO. In this regard, the Fe_3O_4 content was estimated to be 75, 60, 47, 33, 27, and 20 % in the samples.

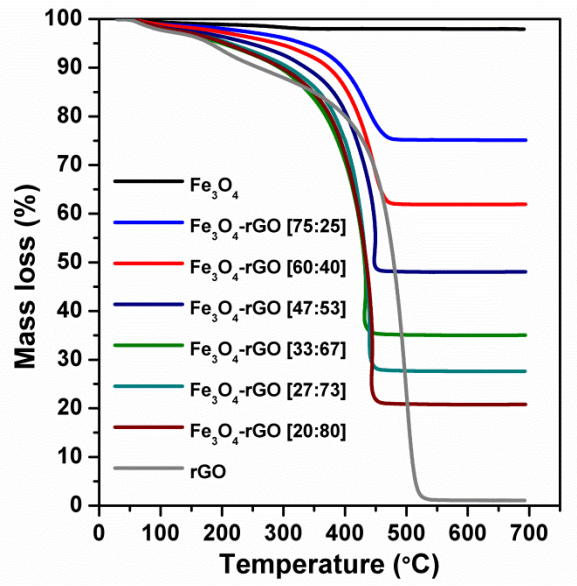

Figure 4.5 TGA curves of the Fe_3O_4-rGO hybrid materials, rGO and Fe_3O_4 in Air at a heating rate of 10°C·min^{-1}

In order to explore textural properties of different synthesized samples, N_2 adsorption/desorption experiments were conducted and represented in ***Figure 4.6a***. Specific surface area of the samples

were estimated following BET equation (S_{BET}), and the results were 127, 143, 158, 151, 165, and 160 $m^2.g^{-1}$, for [75:25], [60:40], [47:53], [33:67], [27:73], and [20:80] hybrids, respectively, as shown in ***Table 4.2***.

Table 4.2 BET Surface Area of the different samples synthesized

Sample	Fe_3O_4 NPs	rGO NSs	[75:25]	[60:40]	[47:53]	[33:67]	[27:73]	[20:80]
BET ($m^2 \cdot g^{-1}$)	93	148	127	143	158	151	165	160

Although the S_{BET} are not very different among various hybrid materials, it is significantly higher than pure Fe_3O_4 NPs (S_{BET} = 93 $m^2 \cdot g^{-1}$), showing that the hybridization with pure rGO NSs (S_{BET} = 148 $m^2 \cdot g^{-1}$) decisively enhanced surface area. As shown in ***Figure 4.6a***, all samples displayed a type-IV isotherm (IUPAC classification) revealing the mesoporous character of these materials. However, the different shape of hysteresis loops demonstrates a different pore structure. In the case of pure Fe_3O_4 NPs (black isotherm), a H3-type hysteresis loop appears characterized by an adsorption branch ascending rapidly over the total range of relative pressure. This reveals inter-particle adsorption arising from the voids between the NPs. On contrary, a H2-type hysteresis loop, typical for complex pore networks with wide pore size distribution, was observed in pure rGO and hybrid materials.

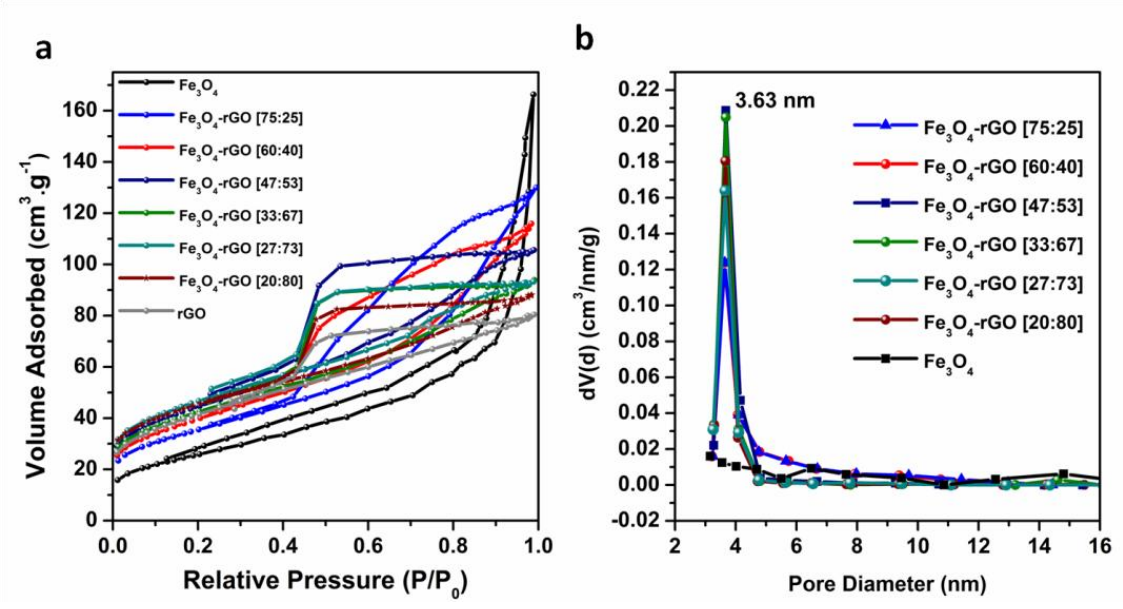

Figure 4.6 (a) N_2 adsorption-desorption isotherms of Fe_3O_4 and Fe_3O_4-rGO hybrid materials (b) Pore size distributions of the Fe_3O_4-rGO hybrid material and Fe_3O_4 sample

The hybrids with higher content of graphene ([47:53], [33:67], [27:73] and [20:80]) show type-H2(a) hysteresis loops explained as a consequence of the interconnectivity of pores having different size. In those hybrids, the very steep desorption branch can be attributed to pore-blocking/percolation in smaller pores that acts as necks. On the other hand, hybrids with a lower content of graphene ([75:25] and [60:40]) show intermediate behavior similar to a type-H2(b) hysteresis loop, also associated with pore blocking, but the size distribution of the width of the necks are now much larger. All this results are in well agreement with Barret-Joyner-Halenda (BJH) pore size distribution plot (***Figure 4.6b***), where the average diameter of pores in all hybrids is centered at around 3.6 nm, while in the case of pure oxide no specific pore size could be observed, suggesting that the porosity in pure oxide is only originated from inter-particle voids. This aspect is really important for energy storage applications since it is well accepted that mesopores facilitate the diffusion of electrolyte ions into the pores of the material and therefore access to active sites thereby improving the electrochemical behavior of these materials.[22]

The prepared samples were morphologically investigated by TEM measurements. ***Figure 4.7*** shows TEM micrographs of the different synthesized samples, clearly revealing that the Fe_3O_4 NPs were tightly anchored on the surface of thin graphene layers. As can be seen in ***Figure 4.7a***, in the Fe_3O_4-rGO [60:40] sample, Fe_3O_4 NPs are uniformly and densely distributed on the surface of graphene layers. The NPs are mostly spherical in shape with different sizes ranging from 10 to 20 nm in diameter. Isolated NPs were not found, suggesting that most Fe_3O_4 NPs are likely attached strongly to the graphene basal plane. In addition, one can appreciate that the population density of NPs has been gradually reduced in different samples from ***Figure 4.7a to 4.7e***, which is in agreement with the lower Fe_3O_4 content in the corresponding samples. Moreover, it can be seen that in the samples with lower Fe_3O_4 content, very few NPs are observed at the edges of the graphene layers. This may be attributed to epoxide-rich basal planes in graphene layers which provide more active sites for NPs attachment in comparison with carboxyl and carbonyl decorated peripheral sites.[23] A representative HRTEM image is shown in ***Figure 4.7f*** to further confirm the crystalline phase of Fe_3O_4. As can be observed, the lattice fringes have a d-spacing of 0.25 nm which corresponds to the (311) plane of the face-centered cubic magnetite Fe_3O_4.

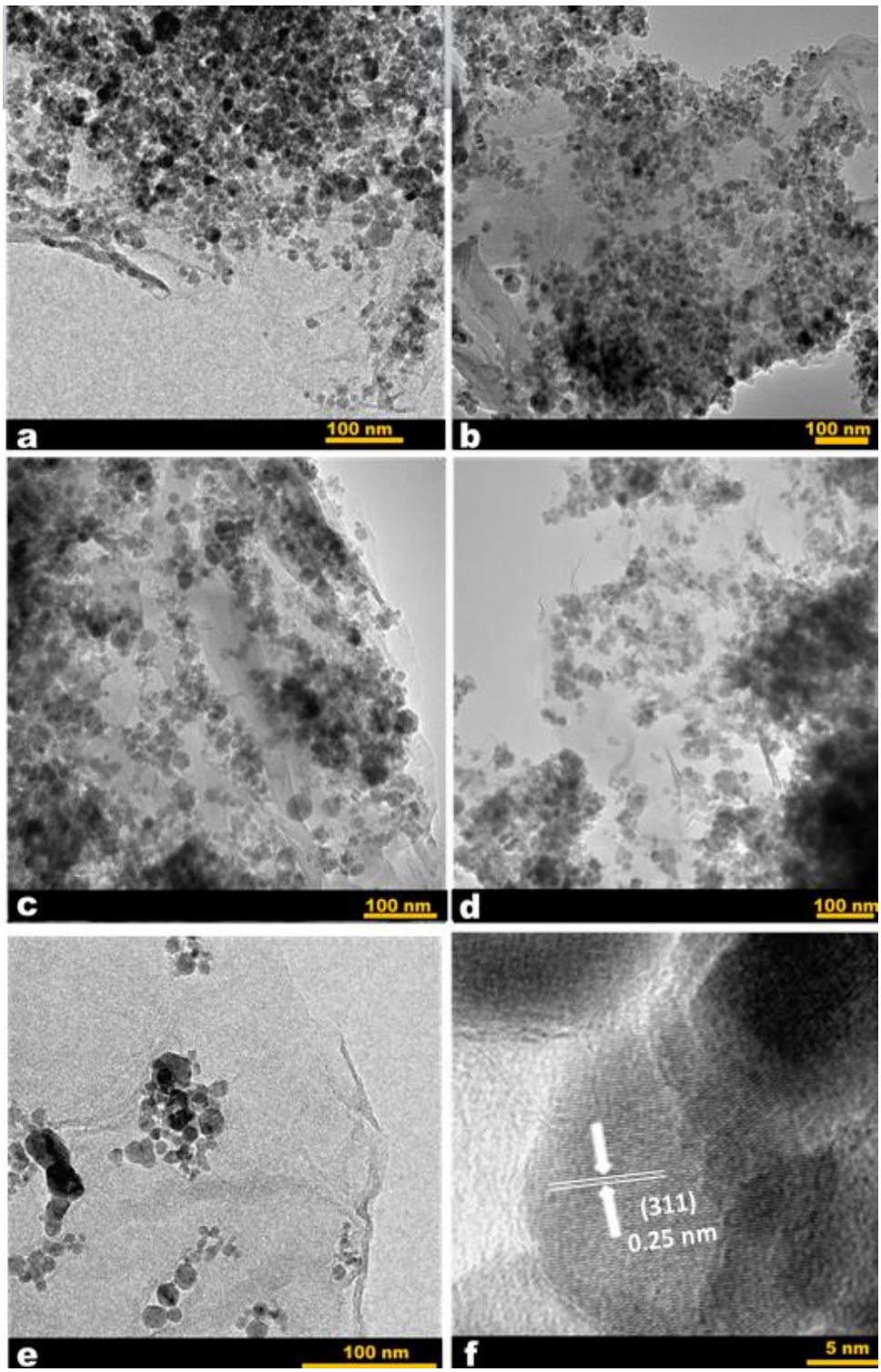

Figure 4.7 TEM images of Fe_3O_4-rGO Hybrid Material: (a) [60:40], (b) [47:53], (c) [33:67], (d) [27:73], and (e) [20:80] samples. (f) HRTEM image of a Fe_3O_4 Nanoparticle

4.2.2 Electrochemical Evaluation of Fe_3O_4-rGO

To analyze the electrochemical response of the as-prepared samples, various electrochemical techniques including CV, GCD and EIS measurements were accomplished in a three-electrode cell in 3M KOH as the electrolyte. ***Figure 4.8a*** shows CV curves of rGO NSs, pure Fe_3O_4 NPs, and Fe_3O_4-rGO [60:40] hybrid material over a voltage window from -0.3V to -1.2V (vs. Hg/HgO) at a scan rate of 5 $mV{\cdot}s^{-1}$. As can be observed, the rGO electrode exhibited quasi-rectangular curve without redox peaks, typical from capacitor-type materials. On the contrary, redox peaks can be clearly tracked in the pure Fe_3O_4 signal and hybrid material, demonstrating the faradaic nature of the charge storage mechanism in these battery-type electrodes. The already mentioned faradaic reactions are associated with the reversible surface reactions corresponding to $Fe^{(III)}/Fe^{(II)}$ redox pairs and a possible energy storage mechanism can be proposed:[24]

$$\mathbf{Fe_3O_4 + 4H_2O + 2e^- \leftrightarrow 3Fe(OH)_2 + 2OH^-} \quad [\mathbf{Eq.\ 4.1}]$$

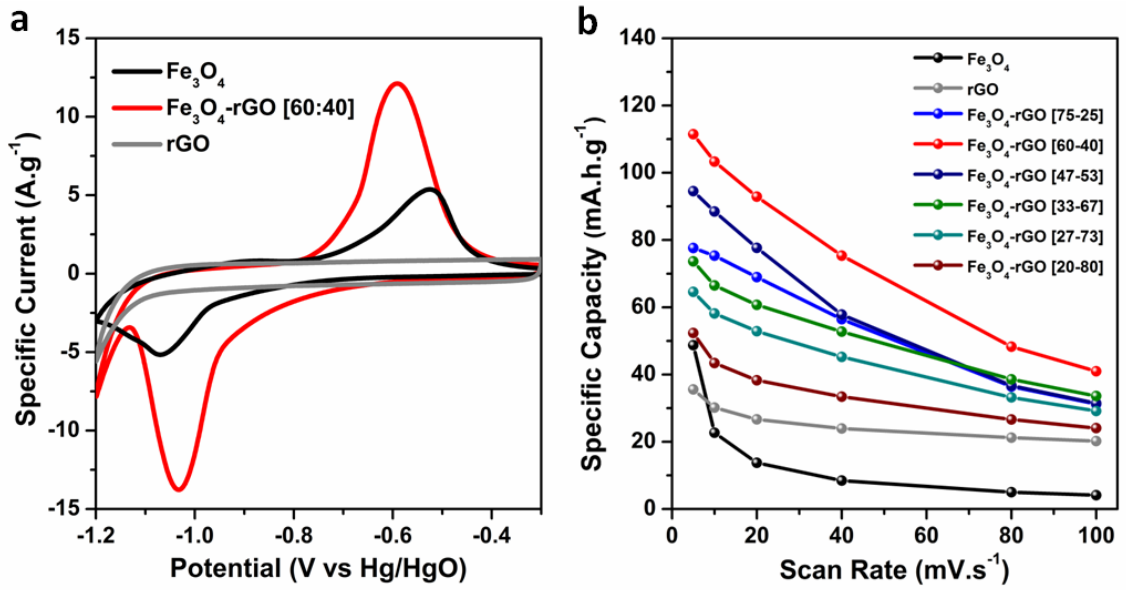

Figure 4.8 Electrochemical evaluation of the Fe_3O_4-rGO hybrids and Fe_3O_4 sample as energy storage electrode materials in 3 M KOH solution: (a) CV curves of the rGO, Fe_3O_4 and Fe_3O_4-rGO [60:40] samples at a scan rate of 5 $mV.s^{-1}$; (b) Rate capability of the samples at various scan rates

Interestingly, it can be observed that the peak separation (ΔEp) has been remarkably decreased in the hybrid sample (from 0.55V in Fe_3O_4 NPs to 0.44 V in the Fe_3O_4-rGO [60:40] sample), suggesting

enhanced reversibility of the faradaic reaction in the hybrid in comparison with the pure iron oxide. This observation may be attributed to the fact that anchoring Fe_3O_4 NPs on conducting graphene NSs can provide new pathways for electron transfer thus facilitating the above mentioned redox reaction.[25] Moreover, the peak current intensities have notably increased in the Fe_3O_4-rGO [60:40] as compared to the pure Fe_3O_4 sample which can be associated to improved electrical conductivity and higher surface area with more accessible active sites in the hybrid. As we described in Chapter 3 of the present thesis, the charge stored is directly correlated with the area under the CV curve and the highest initial capacity between all the samples synthesized was obtained for the Fe_3O_4-rGO [60:40] sample as shown in ***Figure 4.8a***. Accordingly, the Fe_3O_4-rGO [60:40] hybrid showed a high specific capacity of 112 $mAh \cdot g^{-1}$ (0.94 $mAh \cdot cm^{-2}$) at 5 $mV \cdot s^{-1}$, considerably higher than the one obtained for the pure Fe_3O_4 NPs (49 $mAh \cdot g^{-1}$, or 0.37 $mAh \cdot cm^{-2}$) at the same scan rate. This can be associated by enhanced S_{BET} in hybrid sample which reassures participation of almost all active sites in the redox reaction, as well as increased conductivity and synergistic effects resulting from the combination of capacitive and faradaic mechanisms.

As can be observed in ***Figure 4.8b***, all hybrid samples demonstrated higher capacities than pure rGO NSs and Fe_3O_4 NPs which further corroborate enhanced electrochemical properties as a result of hybridization. More importantly, it can be seen that the Fe_3O_4-rGO [60:40] hybrid has superior performance in comparison with the rest of the samples synthesized and even improved capacity values than summation of the ones for pure Fe_3O_4 NPs and rGO NSs. This clearly verify the existence of the already mentioned synergistic effects in the hybrid, resulting from tight contact and a desirable distribution of Fe_3O_4 NPs on graphene layers which is in agreement with the observed results from TEM measurements in ***Figure 4.7***. It can be also appreciated that capacity retains around 40% in the Fe_3O_4-rGO [60:40] hybrid after increasing the scan rate by a 20 factor. This is equivalent to 0.345 $mAh \cdot cm^{-2}$ at a high scan rate of 100 $mV \cdot s^{-1}$, demonstrating low internal resistance of the electrodes despite their high mass loadings (ca. 8.5 $mg \cdot cm^{-2}$) which further demonstrates promising characteristics of the optimized hybrid sample as negative energy storage electrode material for high power applications.

Figure 4.9a shows GCD profiles of the Fe_3O_4-rGO [60:40] hybrid sample and pure Fe_3O_4. As can be seen, the GCD profiles clearly reveal the intrinsic faradaic nature of the charge storage mechanism. Moreover, the superiority of the hybrid sample in terms of higher discharge compared to the pure

oxide sample is observed. Additionally, the existence of voltage plateaus at around -0.7V during charge and -1.0V during discharge for the Fe_3O_4-rGO [60:40] hybrid sample is in good agreement with the observed redox peaks in CV (***Figure 4.8a***). In order to shed more light on the reasons behind enhanced performance of the hybrid samples, EIS measurements were conducted and Nyquist plots were shown in ***Figure 4.9b***. As can be seen, the Nyquist curves consist of three main regions: (a) intercept with the real axis in high frequencies, known as uncompensated resistance (R_s), attributed to the electrical resistance of the electrode material, electrolyte and interface between electrode/electrolyte[26] (b) semicircle at high frequencies associated to the faradaic redox reaction called charge-transfer resistance (R_{ct}) and (c) linear part in medium/low frequencies which can be interpreted in terms of diffusion controlled phenomena. Experimental results were fit by using an equivalent circuit, as shown in ***Figure 4.9b*** inset. In this circuit, R_s, R_{ct}, W, and CPE refer to uncompensated resistance, faradaic charge transfer resistance, Warburg impedance, and constant phase element, respectively.

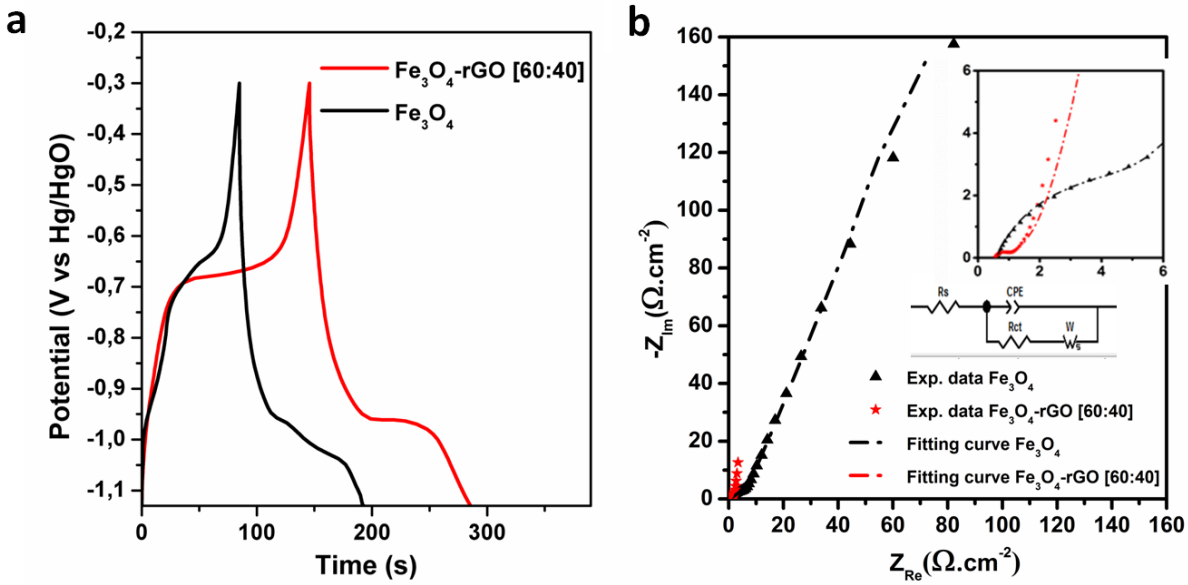

Figure 4.9 Electrochemical evaluation of the Fe_3O_4-rGO hybrid and Fe_3O_4 sample as energy storage electrode materials in 3 M KOH solution: (a) charge–discharge profiles of the Fe_3O_4 and Fe_3O_4-rGO [60:40] samples at a current density of 2 $A.g^{-1}$; (b) Nyquist plots of the Fe_3O_4 and Fe_3O_4-rGO [60:40] samples. Inset show proposed equivalent circuit by which the experimental results were fitted and the magnified Nyquist plot

Table 4.3 summarizes the obtained fit results. The smaller R_s for the Fe_3O_4-rGO [60:40] sample demonstrates its improved electrical conductivity due to hybridization with rGO NSs.[27,28] With respect to the R_{ct}, a significant smaller diameter for the semicircle in the Fe_3O_4-rGO [60:40] hybrid (0.31 Ω) in comparison with Fe_3O_4 nanoparticles (6.21 Ω) reveals that the redox reaction of $Fe^{(III)}/Fe^{(II)}$ pairs could occur much faster in the hybrid sample. Moreover, as expected the low-frequency line is more vertical in the case of the Fe_3O_4-rGO [60:40] hybrid than Fe_3O_4, showing lower ionic diffusion resistance and better capacitive behavior due to the existence of graphene.

Table 4.3 The calculated values of Rs, Rct, W and CPE through fittings of the experimental impedance spectra based on the proposed equivalent circuit in Fig.4.9b

Sample	R_s (Ω cm^{-2})	R_{ct} (Ω)	W	CPE (mF)
Fe_3O_4-rGO [60-40]	0.55	0.31	8.73	0.98
Fe_3O_4	0.64	6.21	14.21	0.77

Furthermore, the estimated Warburg impedance (W) for Fe_3O_4-rGO [60:40] hybrid (8.73) is much lower than that of pure Fe_3O_4 (14.21), revealing higher accessibility of active sites in Fe_3O_4-rGO [60:40] hybrid material for electrolyte ions. All of these observations confirm enhanced electrochemical performance of the Fe_3O_4-rGO [60:40] hybrid as a result of tight and constructive anchoring of commercial Fe_3O_4 NPs on graphene layers.

Figure 4.10a shows the capacity retention of Fe_3O_4-rGO [60:40] and pure Fe_3O_4 as a function of the cycle number in three electrode configuration. It can be found that Fe_3O_4-rGO [60:40] hybrid is able to retain around 79% of the initial value after 2000 cycles at a high current density of 20 $A{\cdot}g^{-1}$, with an initial fading of 3% after the first 100 cycles, demonstrating superior long-term electrochemical stability compared with pure Fe_3O_4 (60% of retention and a significant 27% of initial fading after the first 100 cycles). XRD measurements were conducted on Fe_3O_4-rGO electrode before and after cycling to characterize the structural stability of the Fe_3O_4-rGO [60:40] samples after cycling. As can be seen in ***Figure 4.10b***, position and shape of the main peaks remained almost intact after cycling, revealing stable composition and crystalline structure of the Fe_3O_4-rGO sample upon cycling.

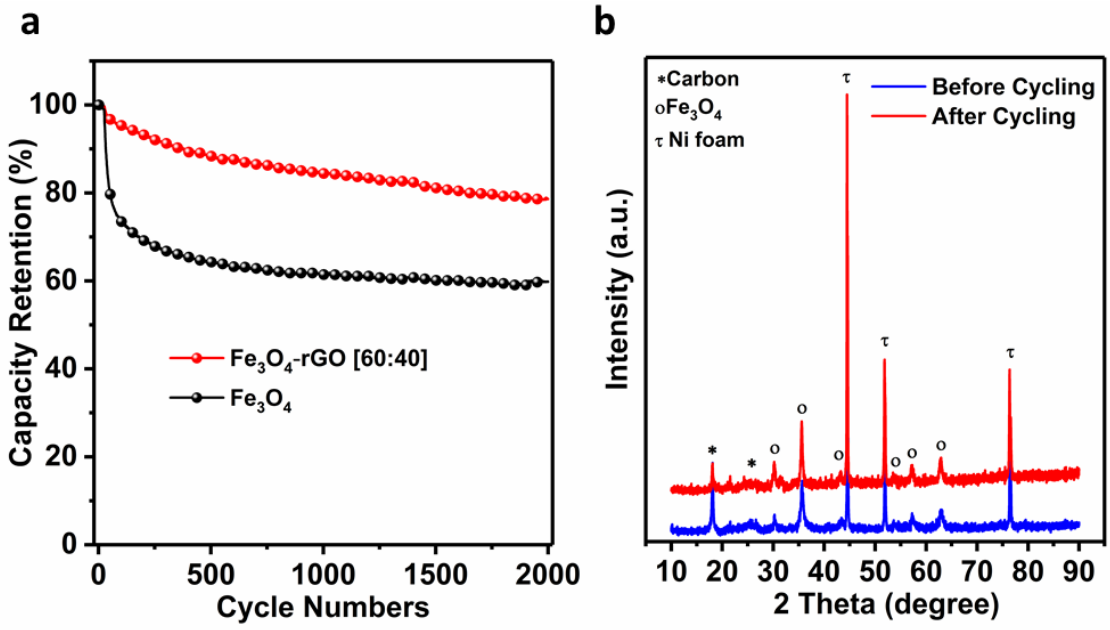

Figure 4.10 (a) Cycling performance of Fe_3O_4-rGO [60:40] and pure Fe_3O_4 at 20 $A.g^{-1}$ in three electrode configuration. (b) XRD patterns of Fe_3O_4-rGO electrode before and after cycling

Table 4.4 provides an overall comparison of performance between corresponding previous studies published on Fe_3O_4 magnetite phase with the Fe_3O_4-rGO [60:40] sample. As can be observed, our Fe_3O_4-rGO hybrid shows superior or at least comparable performance in terms of specific capacity to that of previously reported hybrid materials. However, it can be clearly seen that in terms of areal capacity, the Fe_3O_4-rGO [60:40] hybrid material outperformed all previous results due to the much higher mass loadings of our electrodes. This is an important criteria for energy storage applications, considering the fact that the mass loading of commercialized electrodes is ~10 $mg{\cdot}cm^{-2}$, as we addressed previously in Chapter 1. All these results demonstrate the promise of Fe_3O_4-rGO hybrid material as a low-cost high performance negative electrode material as well as suggesting the hybridization approach as a facile, efficient strategy for enhancing electrochemical characteristics, specially cycling performance of different oxides.

Table 4.4 Comparison of the electrochemical properties of the Fe_3O_4-rGO hybrids with some previous corresponding reports of magnetite phase and its hybrids with graphene

Sample	Electrolyte	Synthesis method	Specific Capacity ($mAh \cdot g^{-1}$)	Discharge Regime	Mass loading ($mg \cdot cm^{-2}$)	Areal Capacity ($mAh \cdot cm^{-2}$)	Cycling stability	Ref.
Fe_3O_4-rGO	6M KOH	Hydrolysis	43	1 $A \cdot g^{-1}$	8	0.855	100% (100mV·s^{-1} 10000 cycles)	29
Fe_3O_4-rGO	1M LiOH	Direct Growth of FeOOH NRs on Graphene Sheets	126	0.5 $A.g^{-1}$	-	-	95% (2 $A.g^{-1}$ 1000 cycles)	7
Fe_3O_4-rGO	1M KOH	Solvothermal	133	5 $A \cdot g^{-1}$	-	-	100% (5 $A.g^{-1}$ 1000 cycles)	21
Fe_3O_4-rGO	1M Na_2SO_4	Solvothermal	64	1 $mA \cdot cm^{-2}$	2	0.128	89.1%(8 $mA.cm^{-2}$ 1000 cycles)	30
Fe_3O_4-rGO	0.5M Na_2SO_4	Electrophoretic Deposition	34	1 $A \cdot g^{-1}$	0.18	0.006	97% (1 $A.g^{-1}$ 500 cycles)	31
Fe_3O_4-rGO	6M KOH	Colloid electrostatic and Hydrothermal	84	0.5 $A.g^{-1}$	3	0.253	73.2% (0.5 $A.g^{-1}$ 3000 cycles)	12
Fe_3O_4-rGO	1M KOH	Hydrothermal	61	0.5 $A.g^{-1}$	-	-	100% (0.5 $A.g^{-1}$ 3000 cycles)	11
Fe_3O_4-rGO	1M KOH	Hydrothermal	183	1 $A \cdot g^{-1}$	1	0.183	-	
CNF- Fe_3O_4	1M Na_2SO_3	Solvothermal	37	420 $mA \cdot g^{-1}$	-	-	91%(420 $mA.g^{-1}$ 1000 cycles)	32
Fe_3O_4-rGO	1M Na_2SO_3	Solution precipitation and Hydrogen reducing	49	1 $A \cdot g^{-1}$	5	0.327	100% (1 $A.g^{-1}$ 1000 cycles)	15
Fe_3O_4-rGO	6M KOH	One step solution approach	45	1 $A \cdot g^{-1}$	5	0.223	67.8% (2 $A.g^{-1}$ 1000 cycles)	33
Fe_3O_4-rGO [60-40]	**3M KOH**	**Electrostatic Coagulation**	**112**	**1 $A \cdot g^{-1}$**	**8.4**	**0.937**	**79% (20 $A.g^{-1}$ 2000 cycles)**	**Our work**

4.2.3 Fe_3O_4-rGO//$NiCoMnS_4$ High Power Aqueous Battery

With the purpose to examine the viability of the optimized Fe_3O_4-rGO [60:40] as an energy storage material in practice, we assembled high power aqueous batteries by integrating Fe_3O_4-rGO [60:40] hybrid material as negative and $NiCoMnO_4$ NPs (NMCO) as positive electrodes. The employed $NiCoMnO_4$ was previously reported by our research group as high performance positive electrode material with a specific capacity of 85 mAh·g^{-1}, as shown in ***Figure 4.11***.[34]

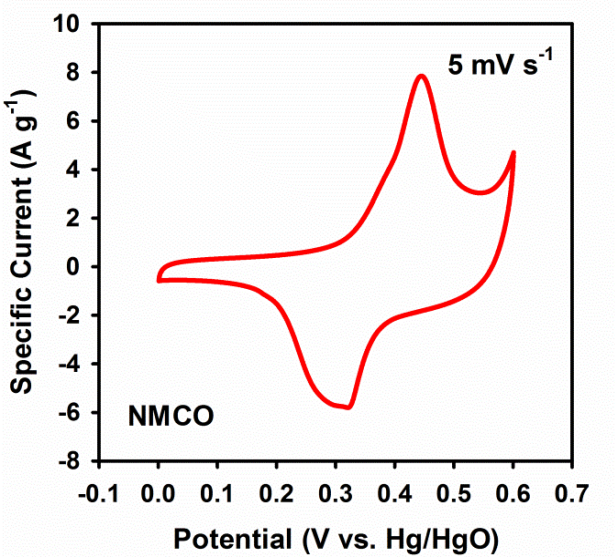

Figure 4.11 CV curve of the $NiCoMnO_4$ NPs (NCMO) sample

The mass loading of the positive and negative electrodes was adjusted with the charge balance theory (m^+/m^-) = 1.32 **,** according to [Eq. 3.15]. ***Figure 4.12*** shows a schematic representation of the high power aqueous battery assembled.

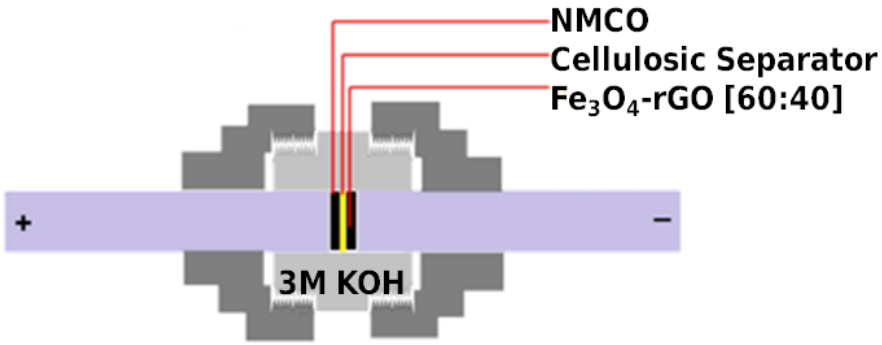

Figure 4.12 Schematic representation of the Fe_3O_4-rGO [60:40]//NMCO aqueous battery

Figure 4.13a shows CV curves of the Fe_3O_4-rGO [60:40]//NMCO battery at different scan rates. As it was expected, well defined redox peaks clearly appeared due to the presence of two battery-type materials, showing the dominance of faradaic charge storage mechanism.

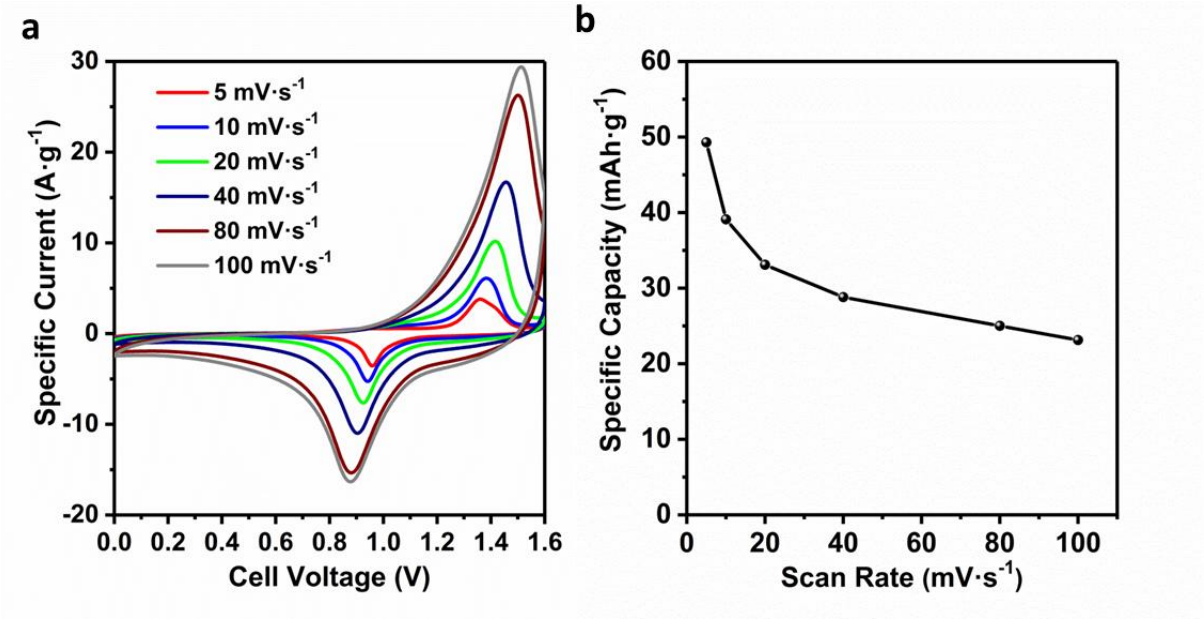

Figure 4.13 Electrochemical performance of porous nanostructured Fe_3O_4-rGO [60:40]//NMCO aqueous battery: (a) CV curves of the nanostructured Fe_3O_4-rGO [60:40]//NMCO aqueous battery at various scan rates in a working voltage window of 1.6 V; (b) rate capability of the aqueous battery at various scan rates

Moreover, forward and backward scans are nearly symmetric, suggesting low polarization, good reversibility and high coulombic efficiency of the electrodes in the battery.[35] More importantly, peak separation showed only a slight increase within the increase of the scan rate, revealing desirable performance of the battery at high scan rates. ***Figure 4.13b*** displays rate capability of Fe_3O_4-rGO [60:40]//NMCO battery at different scan rates. As seen, a high initial specific capacity of 49 $mAh \cdot g^{-1}$ was achieved at 5 $mV \cdot s^{-1}$, upon increasing the scan rate by 20-fold, battery could still retain a capacity of 24 $mAh \cdot g^{-1}$ (47 % of capacity retention) operating at a fast scan rate of 100 $mV \cdot s^{-1}$. These Fe_3O_4-rGO [60:40]//NMCO devices were further examined by GCD testing and the results are shown in ***Figure 4.14a***. As can be seen, GCD profiles are clearly deviated from triangular linear-shape as would be found in capacitor-type materials, suggesting a redox mechanism with well-defined plateaus typical from battery-type materials. Moreover, the already mentioned battery plateaus are well matched with the observed peaks in CV curves, appearing at the same

cell voltage (***Figure 4.13a).*** GCD profiles displayed nearly identical counterparts during charge and discharge, suggesting excellent coulombic efficiency and redox reversibility of the cell, in good agreement with CV in ***Figure 4.13a***.

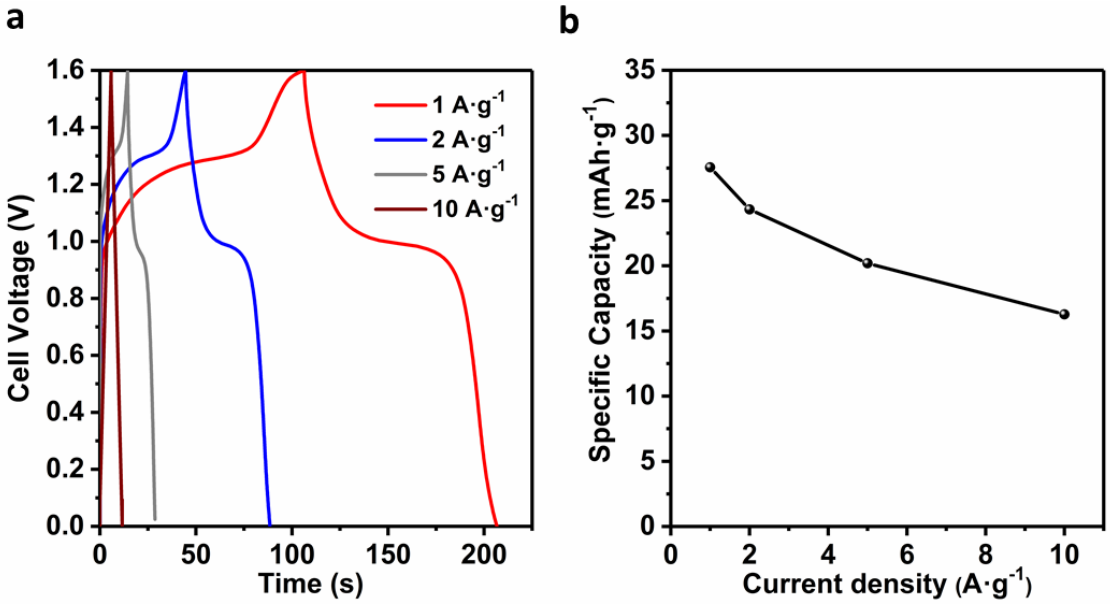

Figure 4.14 Electrochemical performance of porous nanostructured Fe_3O_4-rGO [60:40]//NCMO aqueous battery: (a) GCD profiles of Fe_3O_4-rGO [60:40]//NMCO battery at various current densities (b) Rate capability of the battery at various specific currents

Figure 4.14b shows rate capability of the Fe_3O_4-rGO [60:40]//NMCO device at various specific currents, revealing around 60% capacity retention at current density as high as 10 $A{\cdot}g^{-1}$. Ragone plot that represents energy density vs. power density is considered a common and powerful tool for evaluating the performance of different energy storage devices. Herein, Ragone plot for the Fe_3O_4-rGO [60:40]//NMCO device is compared with previous literature reports in ***Figure 4.15a.*** As can be observed, a maximum energy density of 26 $Wh{\cdot}kg^{-1}$ was achieved at a power density of 0.95 $kW{\cdot}kg^{-1}$. By increasing the current load up to 10 $A{\cdot}g^{-1}$, a maximum power density of 6.9 $kW{\cdot}kg^{-1}$ was obtained, still delivering 13 $Wh{\cdot}kg^{-1}$ energy density. As noticed, the Fe_3O_4-rGO [60:40]//NMCO device showed either superior (e.g. Fe_3O_4-rGO//Activated Carbon[16] and symmetric rGO-based devices [34]) or comparable performance (e.g. Fe_3O_4-Fe_2O_3//Fe_3O_4-MnO_2[36] and Fe_3O_4-rGO//MnHCF [30]) in comparison with previous works.

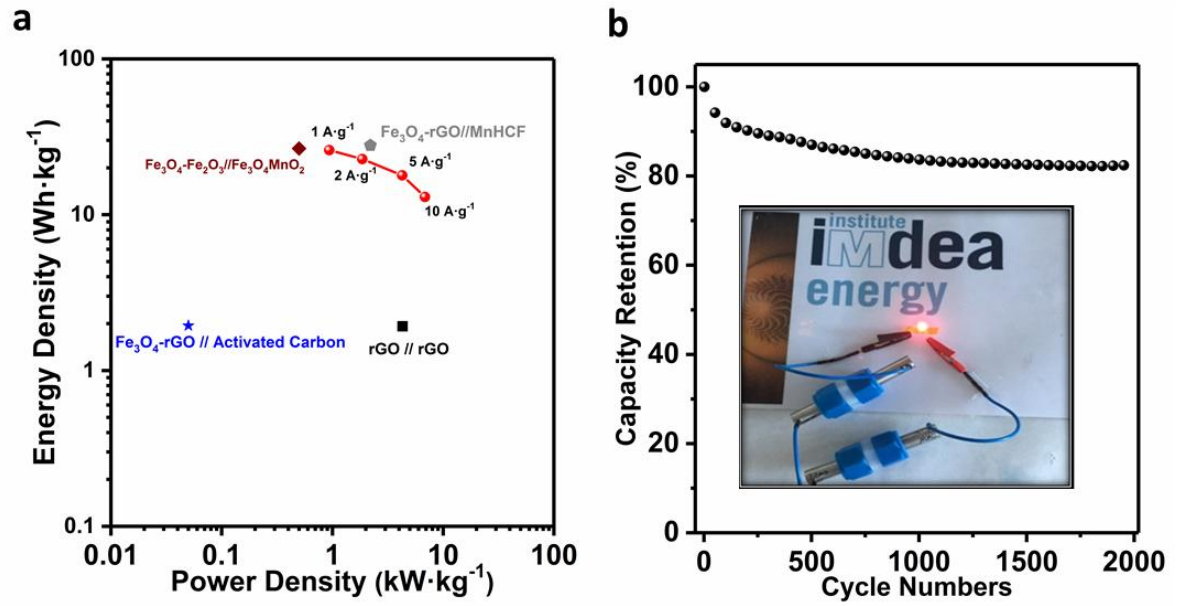

Figure 4.15 (a) Ragone plot of the Fe_3O_4-rGO [60:40]//NMCO aqueous battery at various current densities (in red) and comparison with previous literature reports (b) Cycling performance of the porous nanostructured Fe_3O_4-rGO [60:40]//NMCO aqueous battery at 2 $A \cdot g^{-1}$. Inset shows a photograph of red LED powered on by 2 cells in series

Finally, we further evaluated the stability of Fe_3O_4-rGO [60:40]//NMCO device over 2000 cycles at 2 $A \cdot g^{-1}$ (***Figure 4.15b***), demonstrating acceptable capacity retention of 83%. Moreover, ***Figure 4.15b Inset*** provides an indication regarding the potential applicability of Fe_3O_4-rGO [60:40]//NMCO devices. In this regard, a red LED (20mA) was powered by connecting 2 cells in series.

4.3 Conclusions

In summary, Fe_3O_4 NPs were feasibly anchored on rGO NSs via electrostatic coagulation method followed by a chemical reduction. According to the obtained results, hybridization of Fe_3O_4 nanoparticles with rGO nanosheets could remarkably boost the modest performance of a Fe_3O_4 electrode to a high-performance Fe_3O_4-rGO hybrid electrode. By properly balancing the ratio of these oxide/carbon components a maximum capacity of 111.6 $mAh \cdot g^{-1}$ was achieved for a [60:40] component ratio at 5 $mV \cdot s^{-1}$ (~3 times greater than the pure oxide). Moreover, highly mass loaded (~8.5 $mg \cdot cm^{-2}$) Fe_3O_4-rGO electrodes showed a good rate capability (~40% capacity retention after increasing the scan rate from 5 to 100 $mV \cdot s^{-1}$). All of these results suggest that by anchoring of Fe_3O_4 NPs on rGO NSs, we can significantly improve the electrochemical properties of magnetite phase thanks to synergistic effects between the graphene and the oxide NPs, coming from combination of enhanced conductivity, electrochemical activity, and surface area.

Additionally, as-prepared samples were furtherly studied as electrode materials with high mass loadings (8.5 $mg \cdot cm^{-2}$) in aqueous batteries to assess their viability in practical application. In this fashion, Fe_3O_4-rGO electrodes were integrated with NMCO in aqueous batteries, resulting a maximum energy density of 26 $Wh \cdot kg^{-1}$ and a maximum specific power density of 6.8 $kW \cdot kg^{-1}$. This work reveals the promise of the Fe_3O_4-rGO [60:40] graphene-based hybrid material as a high performance negative electrode in high power aqueous batteries. Accordingly, Fe_3O_4-rGO [60:40] hybrid opens future opportunities and can be integrated with any high capacity positive electrode to achieve high-performance sustainable energy storage devices.

FUNDAMENTALS & APPLICATIONS
CHEMELECTROCHEM
ANALYSIS & CATALYSIS, BIO & NANO, ENERGY & MORE

ChemPubSoc Europe

Volume 4, Issue 6
June 2017
Pages 1295-1305

Article

Anchored Fe_3O_4 Nanoparticles on rGO Nanosheets as High-Power Negative Electrodes for Aqueous Batteries

Jaime S. Sanchez, Dr. Afshin Pendashteh, Dr. Jesus Palma, Prof. Marc Anderson, Dr. Rebeca Marcilla

First published: 27 February 2017 | https://doi.org/10.1002/celc.201700048 | Cited by: 1

Read the full text >

PDF TOOLS SHARE

Abstract

Fe_3O_4 nanoparticles were anchored on GO nanosheets and evaluated as negative electrode materials for high-performance aqueous batteries. The prepared samples were characterized by using XRD, Raman spectroscopy, TGA, and TEM. The energy-storage behavior of the samples was investigated by testing high-mass-loaded (ca. 8.5 $mg \cdot cm^{-2}$) Fe_3O_4–rGO electrodes with different electrochemical techniques, including cyclic voltammetry, galvanostatic charge/discharge, and electrochemical impedance spectroscopy. The nanocomposites showed better electrochemical storage properties than pure Fe_3O_4 nanoparticles and rGO nanosheets, suggesting superior performance through synergistic effects. Accordingly, the Fe_3O_4–rGO nanocomposite with an optimized composition of [60 : 40] showed a maximum capacity of 402 $C \cdot g^{-1}$ (111.6 $mA \cdot h \cdot g^{-1}$) and superior rate capability (ca. 40 % capacity retention with a 20-fold increase in scan rate) compared to the pure oxide. To further evaluate the applicability of the Fe_3O_4–rGO nanocomposite, aqueous batteries based on the Fe_3O_4–rGO [60 : 40] nanocomposite as negative electrodes and $NiCoMnO_4$ as positive electrodes were assembled and examined by using various electrochemical techniques. Fe_3O_4–rGO//$NiCoMnO_4$ cells demonstrated a maximum specific energy of 26 $Wh \cdot kg^{-1}$ and a maximum specific power of 6.8 $kW \cdot kg^{-1}$, with a desirable rate capability. All of the obtained results suggest the Fe_3O_4–rGO nanocomposite as a promising negative electrode material for high-power aqueous batteries.

Related Information

Metrics

Citations: 1

Am score 1

Details

© 2017 Wiley-VCH Verlag GmbH & Co. KGaA, Weinheim

Keywords

Citations: 1

Am score 1

Details

© 2017 Wiley-VCH Verlag GmbH & Co. KGaA, Weinheim

Keywords

aqueous | Fe_3O_4 | nanocomposites | graphene | high-power batteries

Funding Information

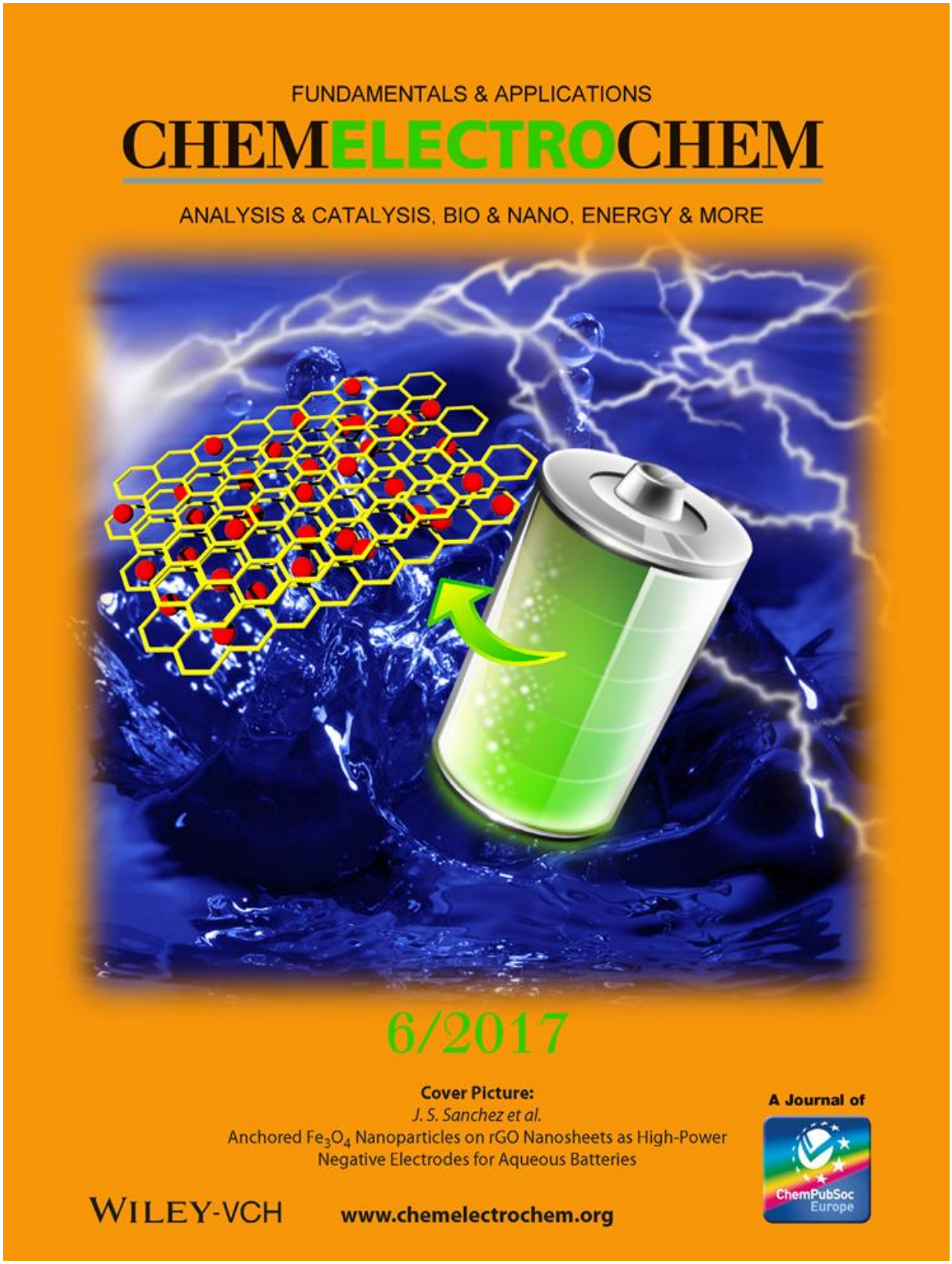
FUNDAMENTALS & APPLICATIONS
CHEMELECTROCHEM
ANALYSIS & CATALYSIS, BIO & NANO, ENERGY & MORE
6/2017
Cover Picture:
J. S. Sanchez et al.
Anchored Fe3O4 Nanoparticles on rGO Nanosheets as High-Power Negative Electrodes for Aqueous Batteries
A Journal of
ChemPubSoc Europe
WILEY-VCH
www.chemelectrochem.org

4.4 References

1 P. Simon, Y. Gogotsi and B. Dunn, *Science (80-.).*, 2014, **343**, 1210–1211.

2 M. R. Lukatskaya, B. Dunn and Y. Gogotsi, *Nat. Commun.*, 2016, **7**, 12647–12660.

3 Daily Metal Prices-https://www.dailymetalprice.com/.

4 T. Ozkaya, M. S. Toprak, A. Baykal, H. Kavas, Y. Köseoğlu and B. Aktaş, *J. Alloys Compd.*, 2009, **472**, 18–23.

5 J. Luo, J. Liu, Z. Zeng, C. F. Ng, L. Ma, H. Zhang, J. Lin, Z. Shen and H. J. Fan, *Nano Lett.*, 2013, **13**, 6136–6143.

6 L. Wei, M. C. Wu, T. S. Zhao, Y. K. Zeng and Y. X. Ren, *Appl. Energy*, 2018, **215**, 98–105.

7 Q. Qu, S. Yang and X. Feng, *Adv. Mater.*, 2011, **23**, 5574–5580.

8 L. Li, P. Gao, S. Gai, F. He, Y. Chen, M. Zhang and P. Yang, *Electrochim. Acta*, 2016, **190**, 566–573.

9 S. Zhu, L. Fan and Y. Lu, *RSC Adv.*, 2017, **7**, 59939–59946.

10 Y. Gogotsi and R. M. Penner, *ACS Nano*, 2018, **12**, 2081–2083.

11 Q. Wang, L. Jiao, H. Du, Y. Wang and H. Yuan, *J. Power Sources*, 2014, **245**, 101–106.

12 T. Liu, X. Zhang, B. Li, J. Ding, Y. Liu, G. Li, X. Meng, Q. Cai and J. Zhang, *RSC Adv.*, 2014, **4**, 50765–50770.

13 X. Li, J. Shen, W. Sun, R. Wang, X. Hong, X. Zhao and X. Yan, *J. Mater. Chem. A*, 2015, **3**, 13244–13253.

14 H. Chen, J. Jiang, L. Zhang, D. Xia, Y. Zhao, D. Guo, T. Qi and H. Wan, *J. Power Sources*, 2014, **254**, 249–257.

15 J. P. Cheng, Q. L. Shou, J. S. Wu, F. Liu, V. P. Dravid and X. B. Zhang, *J. Electroanal. Chem.*, 2013, **698**, 1–8.

16 K. Wasiński, M. Walkowiak, P. Półrolniczak and G. Lota, *J. Power Sources*, 2015, **293**, 42–50.

17 K. N. Kudin, B. Ozbas, H. C. Schniepp, R. K. Prud, I. A. Aksay and R. Car, *Nano Lett.*, 2008, **8**, 36–41.

18 N. Wu, X. She, D. Yang, X. Wu, F. Su and Y. Chen, *J. Mater. Chem.*, 2012, **22**, 17254–17261.

19 M. Sathish, T. Tomai and I. Honma, *J. Power Sources*, 2012, **217**, 85–91.

20 O. N. Shebanova and P. Lazor, *J. Raman Spectrosc.*, 2003, **34**, 845–852.

21 W. Shi, J. Zhu, D. H. Sim, Y. Y. Tay, Z. Lu, X. Zhang, Y. Sharma, M. Srinivasan, H. Zhang, H. H. Hng and Q. Yan, *J. Mater. Chem.*, 2011, **21**, 3422–3427.

22 D.-W. Wang, F. Li, M. Liu, G. Q. Lu and H.-M. Cheng, *Angew. Chemie*, 2008, **47**, 373–376.

23 L. Dai, *Acc. Chem. Res.*, 2013, **46**, 31–42.

24 K. Vijayamohanan, T. S. Balasubramanian and a. K. Shukla, *J. Power Sources*, 1991, **34**, 269–285.

25 N. A. Zubir, C. Yacou, J. Motuzas, X. Zhang and J. C. Diniz da Costa, *Sci. Rep.*, 2014, **4**, 4594–4602.

26 R. Kötz, R. Kötz, M. Carlen and M. Carlen, *Electrochim. Acta*, 2000, **45**, 2483–2498.

27 G. J. Brug, A. L. G. van den Eeden, M. Sluyters-Rehbach and J. H. Sluyters, *J. Electroanal. Chem. Interfacial Electrochem.*, 1984, **176**, 275–295.

28 E. Umeshbabu, G. Rajeshkhanna, P. Justin and G. Ranga Rao, *RSC Adv.*, 2015, **5**, 66657–66666.

29 T. Qi, J. Jiang, H. Chen, H. Wan, L. Miao and L. Zhang, *Electrochim. Acta*, 2013, **114**, 674–680.

30 K. Lu, D. Li, X. Gao, H. Dai, N. Wang and H. Ma, *J. Mater. Chem. A*, 2015, **3**, 16013–16019.

31 S. Ghasemi and F. Ahmadi, *J. Power Sources*, 2015, **289**, 129–137.

32 J. Mu, B. Chen, Z. Guo, M. Zhang, Z. Zhang, P. Zhang, C. Shao and Y. Liu, *Nanoscale*, 2011, **3**, 5034–5040.

33 W. Zhang, F. Liu, Q. Li, Q. Shou, J. Cheng, L. Zhang, B. J. Nelson and X. Zhang, *Phys. Chem. Chem. Phys.*, 2012, **14**, 16331–16337.

34 A. Pendashteh, J. Palma, M. Anderson and R. Marcilla, *RSC Adv.*, 2016, **6**, 28970–28980.

35 T.-W. Lin, C.-S. Dai and K.-C. Hung, *Sci. Rep.*, 2014, **4**, 7274.

36 X. Tang, R. Jia, T. Zhai and H. Xia, *ACS Appl. Mater. Interfaces*, 2015, **7**, 27518–27525.

CHAPTER 5

$NiMnO_3$-rGO as Positive Electrode Materials for Hybrid Energy Storage Devices

5.1 Research Background

As previously mentioned in general introduction, hybrid energy storage has recently sparked research interest due to the possibility of merging high-energy batteries and high-power SCs. This interesting approach can be achieved by hybridization at either the device or the material level, which is also known as external and internal hybrids, respectively. At the device level, a battery-type material (usually as a positive electrode) can be integrated with a capacitor/pseudocapacitor-type material (usually as a negative electrode) in a full device. In material level hybridization, a hybrid system involves a battery-type material (e.g. transition metal oxides, sulfides, nitrides) with a capacitor/pseudocapacitor-type material (e.g. graphene, CNT, conducting polymer) in the same electrode, where the former serves as the energy source, while the latter serves as the power source; as an example of these hybridization, Fe_3O_4-rGO hybrid reported in previous Chapter 4.[1–3]

Among different transition metal oxides for energy storage applications, the iron oxide family; as we demonstrated in Chapter 4 has attracted interest as potential high performance negative electrodes for aqueous-based energy storage devices. However, as positive electrode materials, different families like nickel oxides (e.g. NiO) and several manganese oxides (e.g. MnO_2, Mn_2O_3, etc.) have received extensive attention due to their rich electrochemistry, environmentally friendliness, as well as their relative low cost and earth abundance.[4,5] Furthermore, mixed transition metal oxides have been demonstrated to possess better electrochemical responses in comparison with ordinary or single metal oxides as a consequence of their richer redox chemistry and improved electrical conductivity.[6–10] Therefore, several scientific groups have investigated nickel manganese binary oxides as electrode materials. In general, two different types of Ni-Mn binary oxide phases are known; spinel ($NiMn_2O_4$) and ilmenite ($NiMnO_3$). The spinel phase has been widely investigated as an electrode for energy storage devices.[11–15] For instance, Kim and coworkers hydrothermally decorated $NiMn_2O_4$ NSs on a porous carbon and after optimizing the components ratio they could achieve a maximum capacity of 58.8 $mAh \cdot g^{-1}$ at 1 $A \cdot g^{-1}$.[11] On the other hand, although ilmenite phase $NiMnO_3$ has been studied in catalysis,[16–18] there are only a few reports evaluating this material as an electrode material for energy storage application.[19–21] One of these few works was published by Giri and coworkers who could achieve a capacity of ~112 $mAh \cdot g^{-1}$ by hybridizing $NiMnO_3$ with N-doped rGO in a one-pot hydrothermal synthesis.[20] Despite their unquestionable success in synthesizing and testing a high capacity graphene-based ilmenite

electrode they used extremely low mass loaded electrode (0.1 $mg \cdot cm^{-2}$). As we addressed in previous chapters, such small mass loading is far away from practical applications (typically 8-10 $mg \cdot cm^{-2}$) in commercial devices, considering that the material performance greatly depends on the mass loading and significantly declines in highly loaded electrodes.[22] Consequently, it is of great importance and interest to develop electrode materials capable of providing high energy storage performance with highly mass loaded electrodes.

In this chapter, we report a facile hydrothermal synthesis of $NiMnO_3$ (ilmenite phase)-rGO hybrid material followed by a thermal treatment. Electrochemical characteristics of $NiMnO_3$-rGO hybrid material were thoroughly studied in 3M KOH solution using various electrochemical techniques and they were compared with pure $NiMnO_3$ (ilmenite phase), demonstrating the enhanced performance with the hybridization. Moreover, highly mass loaded $NiMnO_3$-rGO hybrid material was evaluated as positive electrode in a hybrid energy storage device in combination with purely capacitive rGO negative electrode.

5.2 Results and discussion

5.2.1 Synthesis and Physico-Chemical Analysis of $NiMnO_3$-rGO

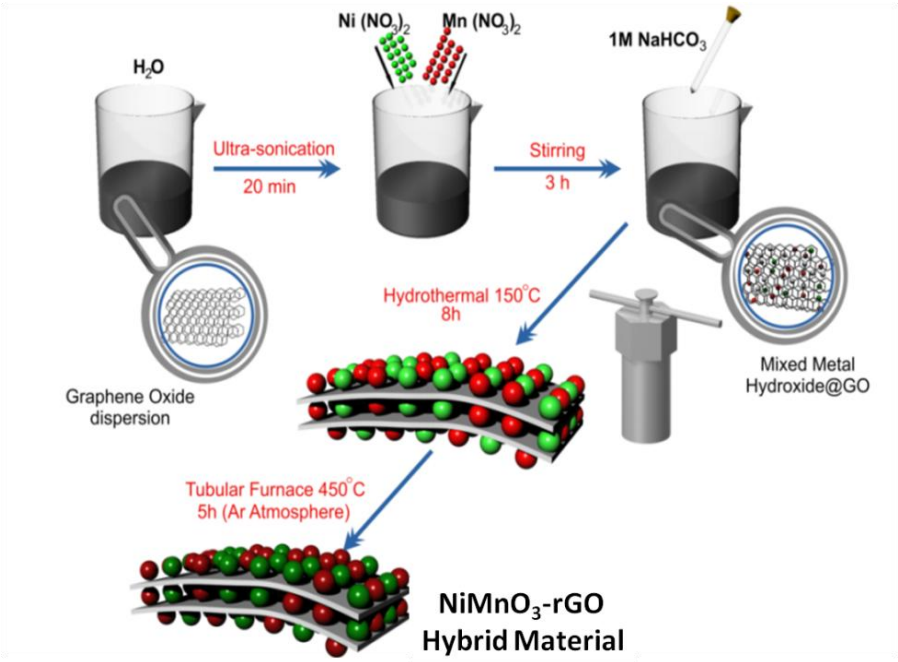

Figure 5.1 Schematic illustration of the synthesis procedure for $NiMnO_3$-rGO hybrid material

As detailed in Chapter 3, $NiMnO_3$-rGO hybrids were synthesized via a facile hydrothermal method by mixing metallic salt precursors with a graphene oxide dispersion into an autoclave reactor (150°C, 8h) followed by thermal treatment as illustrated in ***Figure 5.1***. For the sake of fair comparison, pure $NiMnO_3$ and rGO samples were synthesized using the same procedure except GO was excluded in the pure oxide sample and metal precursors were excluded in rGO sample.

The structural properties and crystalline phase(s) of the different samples after thermal treatment (5h at 450°C under Ar atmosphere) were identified by powder XRD experiments, as shown in ***Figure 5.2a***. All diffraction peaks in pure $NiMnO_3$ sample can be easily indexed to rhombohedral ilmenite phase (JCPDS card no. 98-001-3753, space group: R-3).[21,23] As observed, all peaks can be also readily identified in the $NiMnO_3$-rGO hybrid sample, demonstrating that no major change occurred in the crystalline structure during hybridization.

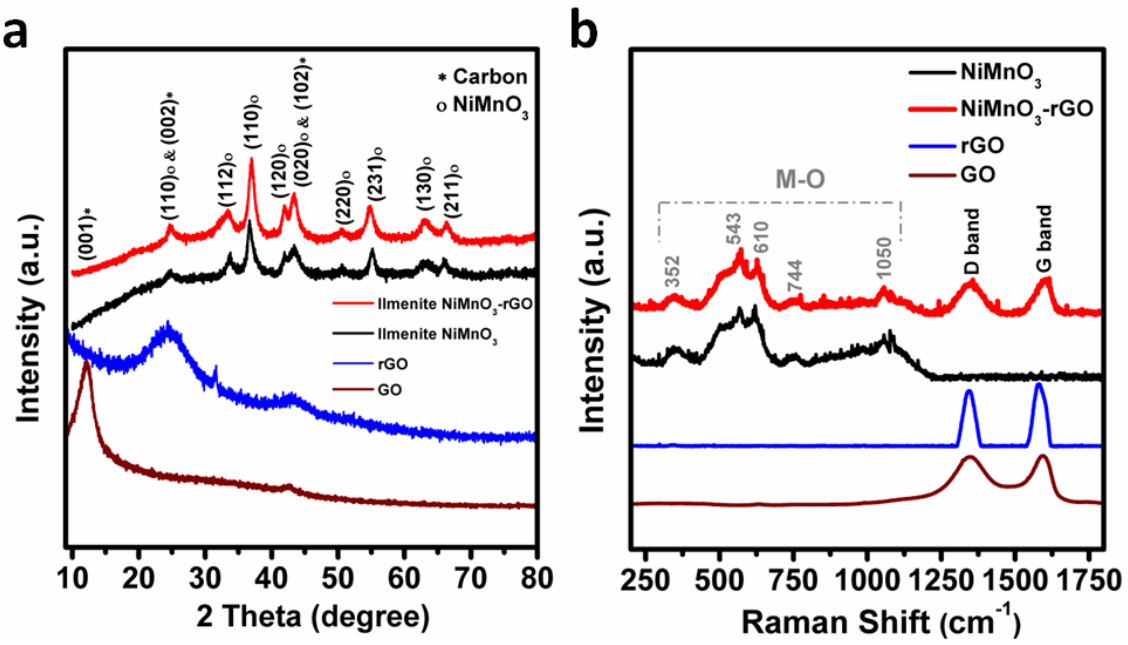

Figure 5.2 Microstructural analysis of the samples: (a) XRD and (b) Raman spectroscopy of $NiMnO_3$-rGO, $NiMnO_3$, GO and rGO samples

It should be also mentioned that, the absence of any appreciable peak at 2θ = 11.4° (characteristic of GO) confirms the successful reduction of GO in the hybrid material and during the synthesis of pure rGO sample. Moreover, no other peaks are observed, implying the high purity of the obtained samples. As can be seen in ***Figure 5.2b***, the Raman spectra of $NiMnO_3$ and $NiMnO_3$-rGO

hybrid material show similar vibration modes in the range of 200-700 cm^{-1}, which can be associated to metal-oxygen (M-O) bands. The peaks centered at 543, 610 and 744 cm^{-1} can be associated to strong vibrations of the Mn–O bond, while the ones around 352 and 1050 cm^{-1} belong to Ni–O bond.[21,24] $NiMnO_3$-rGO hybrid material, GO and rGO show two additional bands typical from carbonaceous materials appeared at 1329 cm^{-1} (D band) and 1583 cm^{-1} (G band). In this regard, a significant decreased I_D/I_G ratio in the hybrid (0.92) and rGO (0.93) samples in comparison with that of GO (0.98) further demonstrates the successful reduction of GO to rGO (***Figure 5.2b***). Raman results are in good agreement with the ones observed by XRD ***(Figure 5.2a)*** revealing successful hybridization of the binary oxide with the graphene structure.

In order to determine the amount of $NiMnO_3$ in the hybrid material, TGA measurements were conducted in air. ***Figure 5.3*** shows that only a gradual reduction of ~5.5% in mass loss was observed for pure $NiMnO_3$ which can be attributed to adsorbed hydroxyl groups on the surface and/or trapped water in the lattice.[25] On the contrary, as it was expected almost all the mass of pure rGO was lost by increasing the temperature to 500°C, confirming its complete decomposition. On the other hand, $NiMnO_3$-rGO hybrid showed an abrupt mass loss from 300°C to 400°C due to combustion and decomposition of carbon framework. Accordingly, binary oxide content was estimated to be 42% in the hybrid sample, which is well in accordance with the amount of initial precursors employed during the synthesis process.

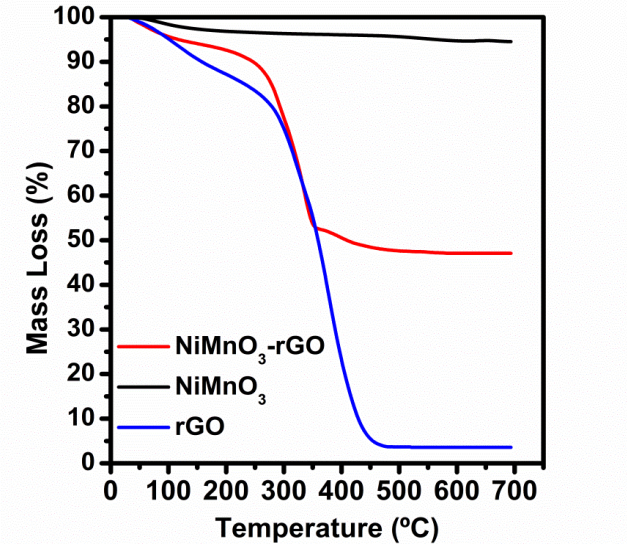

Figure 5.3 TGA curves of the $NiMnO_3$-rGO hybrid materials, rGO and $NiMnO_3$ in Air at a heating rate of 10°C·min^{-1}

In order to shed some light on the textural properties of the samples, N_2 adsorption-desorption isotherms (***Figure 5.4a***) were carried out for all the samples. In all cases, isotherms displayed a type-IV isotherm but with different shape hysteresis loops, suggesting they possess different porosity types.

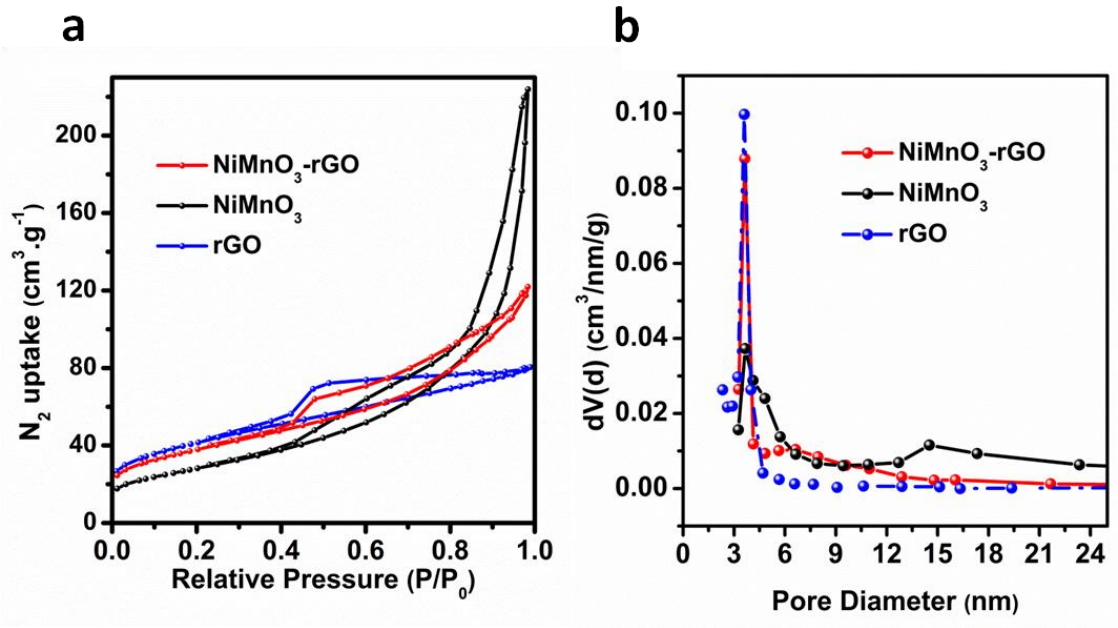

Figure 5.4 (a) N_2 adsorption-desorption isotherms of $NiMnO_3$-rGO hybrid, rGO and $NiMnO_3$ samples (b) Pore size distribution of the rGO, $NiMnO_3$-rGO hybrid and $NiMnO_3$ sample

As can be seen, the adsorption branch in the case of pure $NiMnO_3$ ascends continuously over the whole range of relative pressure, indicating a H3-type hysteresis loop and revealing typical condensation of large inter-particle voids. On contrary, a H2-type hysteresis loop was observed in pure rGO sample, fairly representative for mesoporous networks. Interestingly, common features of both pure $NiMnO_3$ and rGO samples were observed in the hysteresis loop of $NiMnO_3$-rGO hybrid. Moreover, specific surface area (S_{BET}) of $NiMnO_3$-rGO hybrid was found to be as high as 136 $m^2 \cdot g^{-1}$, significantly higher than that of pure $NiMnO_3$ (102 $m^2 \cdot g^{-1}$), demonstrating that hybridization with rGO NSs (148 $m^2 \cdot g^{-1}$) resulted in enhanced specific surface area of the hybrid sample. This aspect is of great significance as it increases the number of electroactive sites and consequently improves the electrochemical performance of the sample.[26] Furthermore, Barret-Joyner-Halenda (BJH) pore size distribution plots (***Figure 5.4b***) confirm the mesoporous character of the samples. As seen, the average diameter of pores in $NiMnO_3$-rGO hybrid material is centered at 3.7 nm, with

mesopores mostly smaller than 15 nm. In the case of pure oxide, there is no specific average diameter in the distribution and the pore sizes are extended to values larger than 15 nm. This is in good agreement with the continuously ascending adsorption branch observed in the isotherm for the binary oxide, suggesting that its porosity is predominantly coming from inter-particle voids. On contrary, the (BJH) pore size distribution of pure rGO shows an average diameter of pores smaller than 5 nm, confirming that the tinier mesopores in $NiMnO_3$-rGO hybrid come from the rGO while the larger come from the binary oxide. These results undoubtedly conform with the obtained higher surface area in the hybrid sample, suggesting possible short ion transport pathways and low-resistance diffusion routes through the mesoporous structure.[27]

To investigate the surface chemical composition and oxidation states of the $NiMnO_3$-rGO hybrid, XPS measurements were carried out.

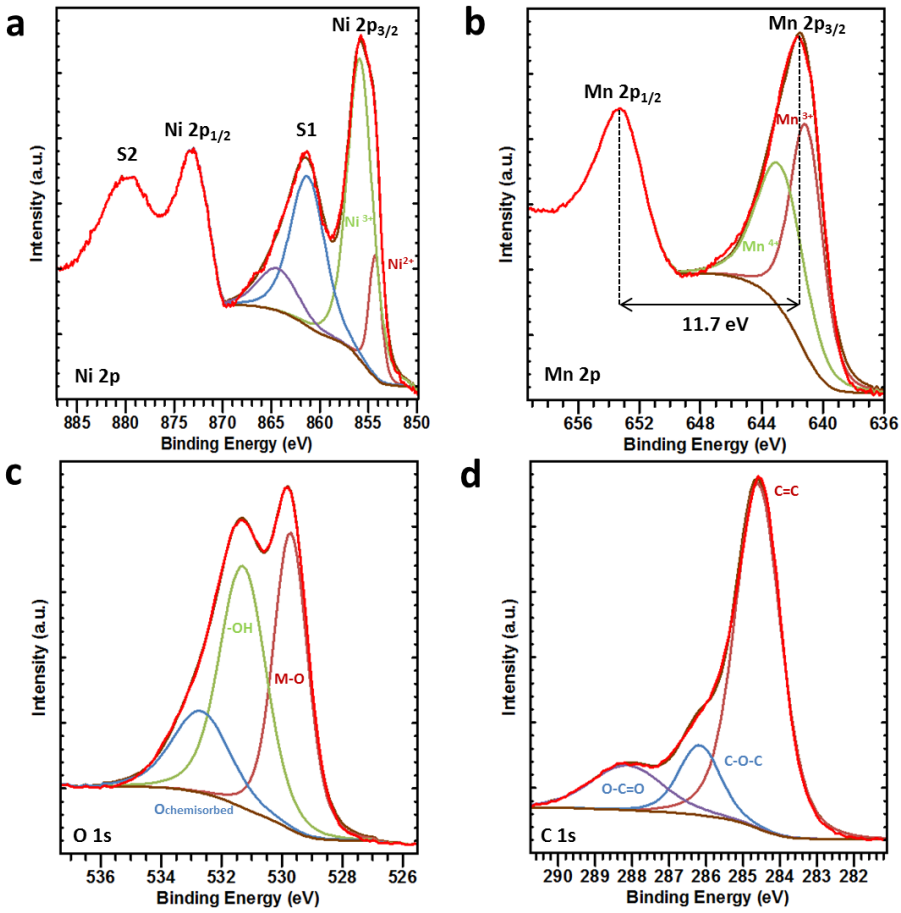

Figure 5.5 High-resolution XPS analysis of $NiMnO_3$-rGO hybrid material, (a) Ni 2p, (b) Mn 2p, (c) O 1s and (d) C 1s core levels

High-resolution spectra for different core levels are shown in ***Figure 5.5***. As observed in ***Figure 5.5*****a**, the Ni 2p core level consists of two main characteristic peaks centered at 855.7 and 873.2 eV, suggesting the presence of Ni^{2+} and Ni^{3+} species on the hybrid.[28] ***Figure 5.5*****b** displays the core level of Mn 2p, showing two spin orbits at 641.4 eV ($2p_{3/2}$) and 653.3 eV ($2p_{1/2}$). Particularly, for the manganese oxides, the Mn $2p_{3/2}$ signal is useful in distinguishing between the potential valences. Based on Gaussian-fitting and evidenced by the strong energy splitting of 11.7 eV, Mn^{3+} and Mn^{4+} species likely coexist in the $NiMnO_3$-rGO hybrid.[29,30] In ***Figure 5.5*****c**, it is appreciated that the O 1s signal can be de-convoluted to three main peaks at 529.7 eV, 531.3 eV and 532.8 eV representing the M-O-M bonding (M= Ni or Mn), -OH groups and O chemisorbed, respectively.[31] Additionally, three different components can be distinguished in the C 1s region (***Figure 5.5*****d**) at B.E. of 284.5, 286.1 and 288.2 eV, corresponding to graphitic carbon, C-O-C and O-C=O, respectively; in good agreement with previous reports.[32]

The morphologies of the pure ilmenite $NiMnO_3$ and $NiMnO_3$-rGO hybrid material were observed and investigated first by SEM. ***Figure 5.6a*** shows that pure $NiMnO_3$ is formed by uniform sphere-shaped particles with an average diameter size of 1 µm.

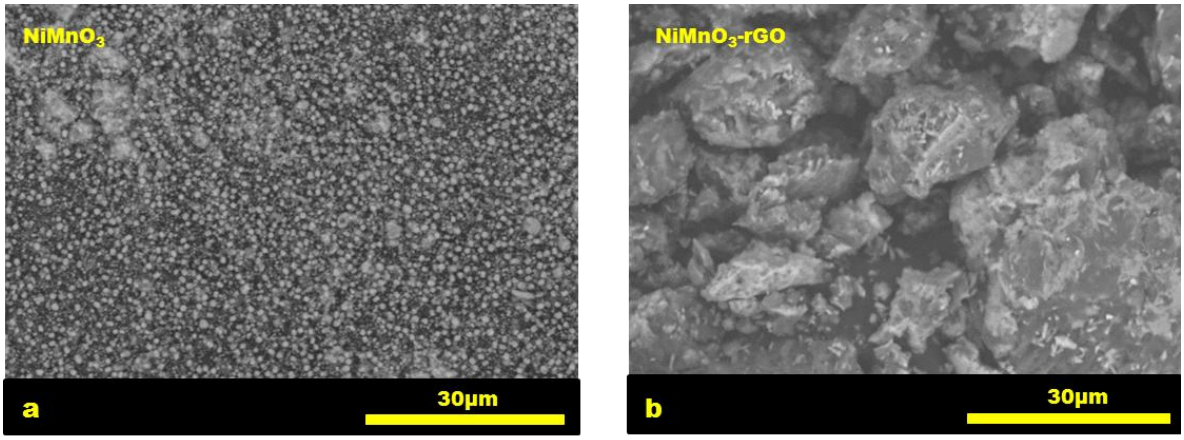

Figure 5.6 SEM (a, b) of ilmenite $NiMnO_3$ and $NiMnO_3$-rGO hybrid material, respectively

SEM image of the $NiMnO_3$-rGO sample ***(Figure 5.6b)*** is quite different revealing that the hybrid material consists of a few micrometer-scale particles with irregular shapes. This might be due to anchoring of the small metal oxide NPs on micrometer-sized graphene flakes (~20 µm) which underwent certain degree of agglomeration in specific regions, possibly during the drying process.

In order to gain a better perspective of the distribution of binary oxide particles on graphene NSs, TEM measurements were conducted on the hybrid sample. As observed in ***Figure 5.7a***, the rGO NSs are composed of thin layers on which wrinkles can be easily noticed. Upon higher magnification, it can be clearly observed in ***Figure 5.7b*** that the surface of the conductive graphene layers is densely and homogeneously decorated with very fine $NiMnO_3$ NPs with an average diameter of 5 nm. Moreover, the NPs do not possess clear boundaries and certain agglomeration of such particles formed the nanoporous structure of the $NiMnO_3$-rGO hybrid sample. It can be also appreciated in ***Figure 5.7b*** that some edges of the graphene layers are not covered with $NiMnO_3$ NPs. This aspect can be associated to the fact that epoxide and hydroxyl groups located on the basal-plane of the graphene layer are surface functional groups more attractive for metal oxide attachment than carboxyl and carbonyl groups on the edges of the layers.[33,34] It is well-known that a proper distribution and optimum interaction of metal oxide NPs with graphene matrix play an important role on the final electrochemical performance of the material as they result in increased electrical conductivity and shorten ion transport pathways leading to facilitate redox reactions.[35]

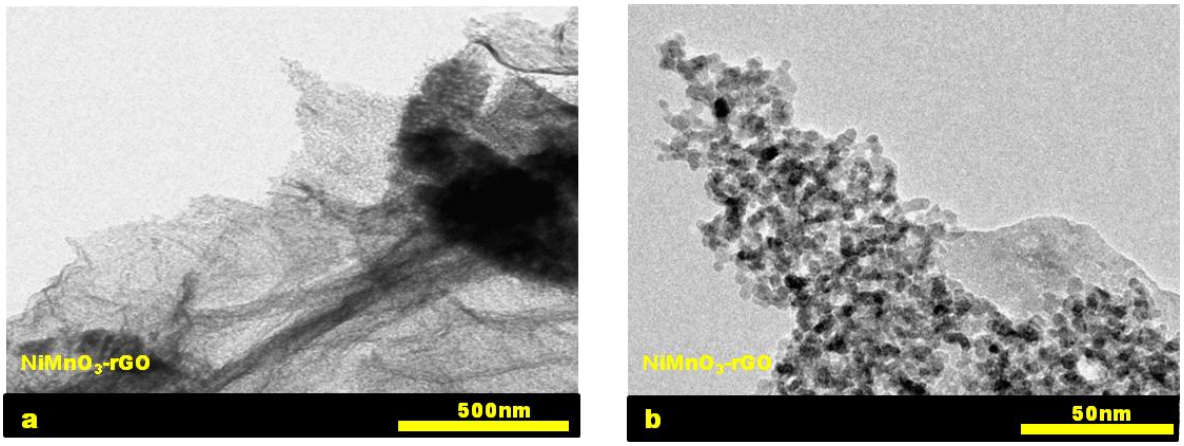

Figure 5.7 TEM (a, b) images of $NiMnO_3$-rGO hybrid material at different magnifications

5.2.2 Electrochemical Evaluation of $NiMnO_3$-rGO

Electrochemical performance of the as-prepared samples was evaluated by CV measurements in a typical three-electrode configuration employing 3M KOH as electrolyte. As shown in ***Figure 5.8***, the CV responses of the pure oxide and the hybrid sample are quite similar in shape with strong and broad redox peaks centered at 0.36 V, indicating the obvious faradaic nature of the charge

storage mechanism. Moreover, it can be appreciated that specific current of the redox peaks has remarkably increased in the hybrid sample in comparison with the binary oxide. Accordingly, the specific capacity was calculated with Eq. [3.8] as 90.57 $mAh \cdot g^{-1}$ for $NiMnO_3$-rGO hybrid, which was around two times greater than the capacity of pure $NiMnO_3$ (47.7 $mAh \cdot g^{-1}$).

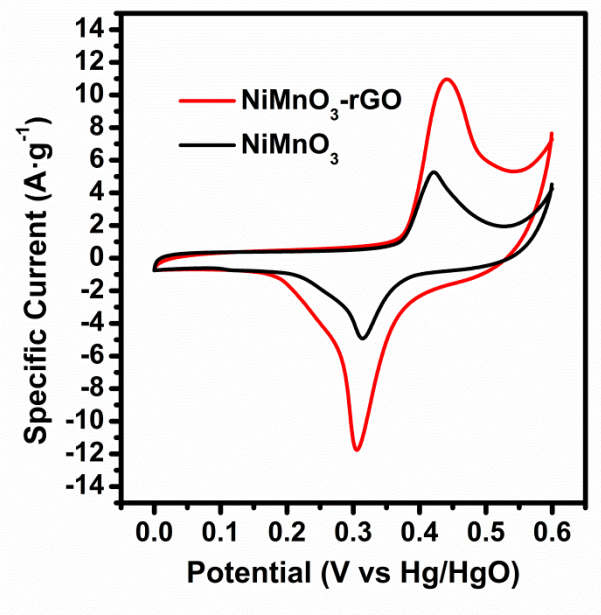

Figure 5.8 CV curves of the $NiMnO_3$ and $NiMnO_3$-rGO samples at a scan rate of 5 $mV \cdot s^{-1}$

On the other hand, the overall shape of the CV profiles in both cases did not change significantly by increasing the scan rate up to 80 $mV \cdot s^{-1}$ ***(Figure 5.9 a,b)***, although the peak separation has been slightly enlarged as a consequence of quasi-reversible origin of the involved reactions. In addition, it can be appreciated that current intensities of the $NiMnO_3$-rGO hybrid are much higher than that of the pure $NiMnO_3$ in all scan rates. ***Figure 5.9c*** displays the rate capability of $NiMnO_3$ and $NiMnO_3$-rGO samples calculated from CV curves at various scan rates. As seen, the specific capacity decreases gradually by increasing the scan rate in both cases. This can be explained by the fact that not all the pores of the sample are accessible at higher scan rates, resulting in decreased charge storage performance.[37] However, the specific capacity of $NiMnO_3$-rGO at 40 $mV \cdot s^{-1}$ (45 $mAh \cdot g^{-1}$) is similar to the specific capacity of $NiMnO_3$ sample at a much smaller scan rate of 5 $mV \cdot s^{-1}$ (47 $mAh \cdot g^{-1}$). This clearly reveals superior rate capability of the hybrid as compared to the binary metal oxide, which can be associated to the improved electrical conductivity, increased specific

surface area and smaller mesopores in the pore size distribution plot of the hybrid material arising from possible synergism in hybridization of single components.

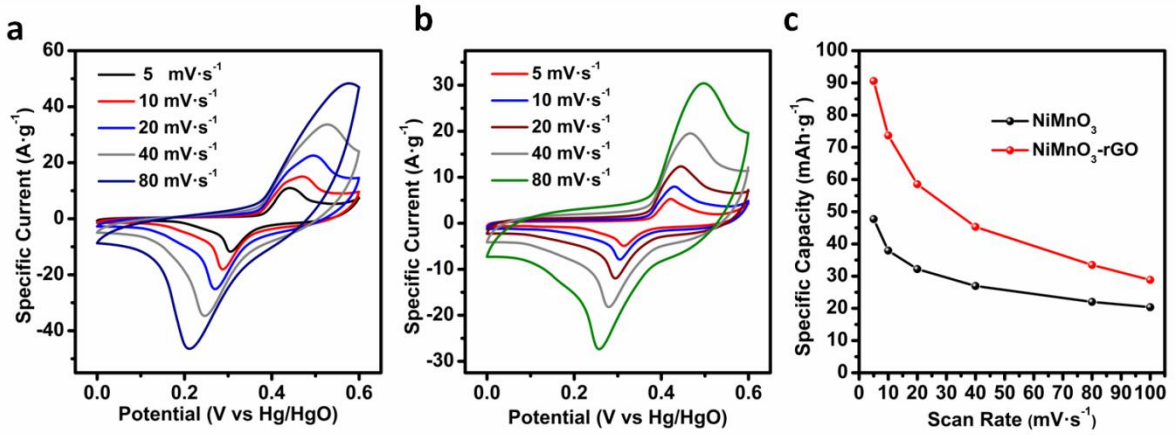

Figure 5.9 CV curves at different scan rates in three-electrode configuration: (a) $NiMnO_3$-rGO. (b) $NiMnO_3$. (c) Rate capability of the samples at various scan rates

Although the observed redox peaks in CVs can be attributed to fast and quasi-reversible redox reactions, clarifying the exact redox mechanism is very challenging due to the complex structure and various possible phases of mixed transition metal oxides in alkaline electrolytes. However, based on the obtained results from XPS and previous proposed mechanisms,[16,36] the charge storage mechanism in Ilmenite samples is likely governed by a two-step process where firstly conversion of Ni^{2+}/Ni^{3+} occurs, involving oxide-hydroxide species (e.g. NiOOH), whereas in a second step the transformation of Mn^{3+}/Mn^{4+} couple would take place.

In order to further justify the superior performance of the hybrid sample, GCD measurements were conducted at 1 $A{\cdot}g^{-1}$ (***Figure 5.10a***) for both pure oxide and hybrid sample. Accordingly, a high capacity of 61.4 $mAh{\cdot}g^{-1}$ was obtained for the hybrid sample which is much higher than that of pure oxide (35.2 $mAh{\cdot}g^{-1}$). The existence of clear voltage plateaus at around 0.45 V during charge and about 0.3 V during discharge are in good agreement with the CVs (***Figure 5.8***) and are another proof of the redox nature of the storage mechanism in these samples. As seen, the charge-discharge counterparts are almost symmetric which implies once again, excellent reversibility and coulombic efficiency of the as-prepared samples. GCD profiles at different currents and rate capability performance of $NiMnO_3$-rGO hybrid and $NiMnO_3$ are shown in ***Figure***

5.10 (b-d), respectively. Note that the specific capacity of the $NiMnO_3$-rGO hybrid is much higher than that of the pure $NiMnO_3$ in all-current range, showing superiority of the hybrid sample.

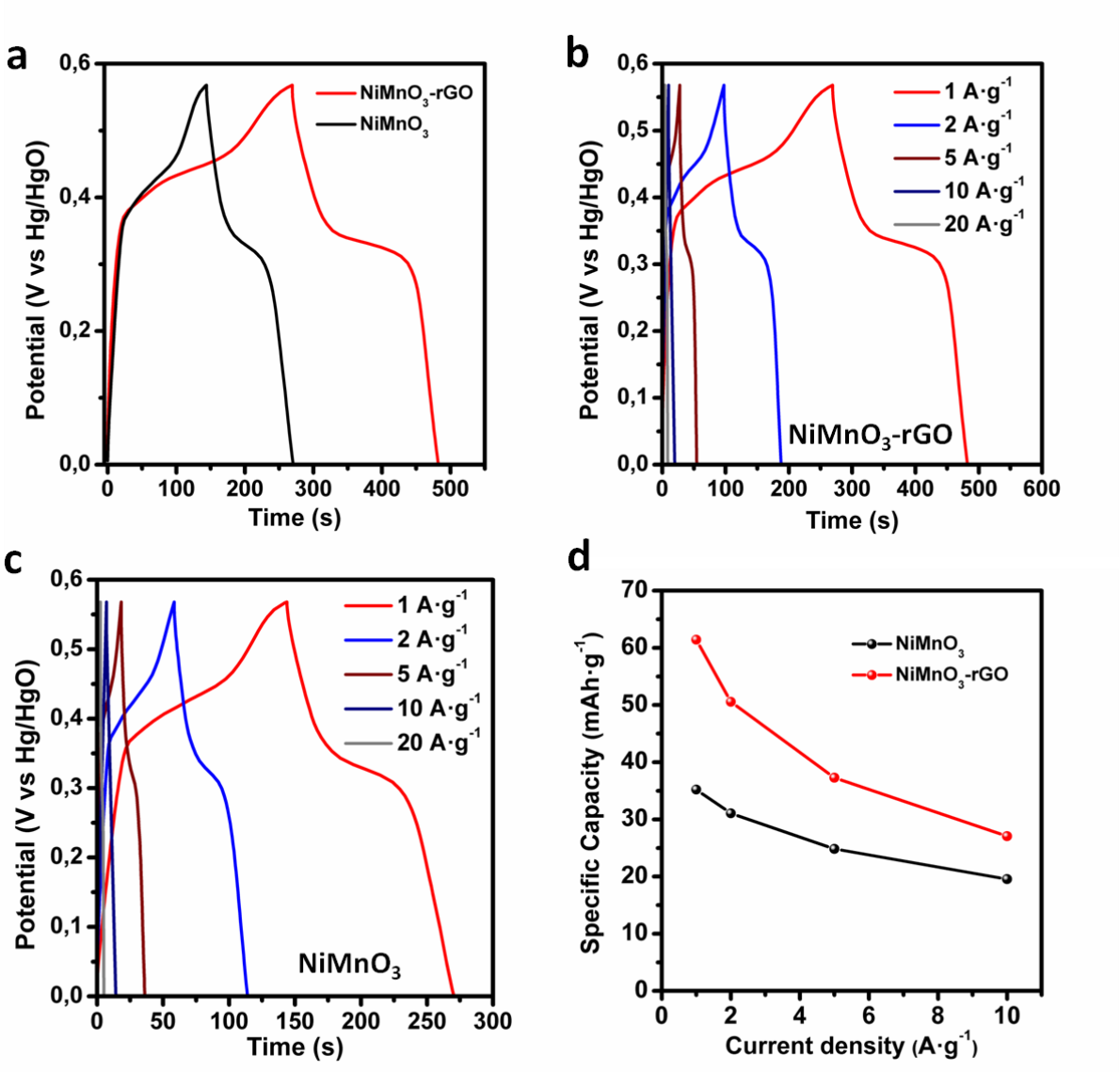

Figure 5.10 (a) GCD profiles of $NiMnO_3$ and $NiMnO_3$-rGO at a current density of 1 $A.g^{-1}$. GCD at different current densities: (b) $NiMnO_3$-rGO (c) $NiMnO_3$ (d) rate capability of the samples at different specific currents

To further illuminate the effect of hybridization on electrochemical performance of electrodes, EIS measurements were conducted and Nyquist plot is shown in ***Figure 5.11.*** Experimental results were fitted by using an equivalent circuit. In this equivalent circuit model R_s, R_{ct}, W, CPE and C_{dl} refer to the uncompensated resistance, charge transfer resistance, Warburg impedance, Constant

Phase Element and double-layer capacitance, respectively.[38] The observed semicircle at high frequencies represents the charge transfer resistance (R_{ct}) in parallel with the constant phase element. According to the fitting results, R_{ct} is significantly smaller in the $NiMnO_3$-rGO hybrid (0.53 Ω) in comparison with pure $NiMnO_3$ (3.21 Ω), suggesting that hybridization facilitates the kinetics of the reaction. Moreover, the C_{dl} value obtained for $NiMnO_3$-rGO (0.40 F) is higher than that of the pure oxide (0.32 F) due to the presence of carbon matrix. These results, match well with the performance obtained in CV and GCD experiments and further demonstrate superior electrochemical performance of the $NiMnO_3$-rGO hybrid, as a result of the optimum distribution and strong interaction of the binary metal oxide NPs on conductive graphene network.

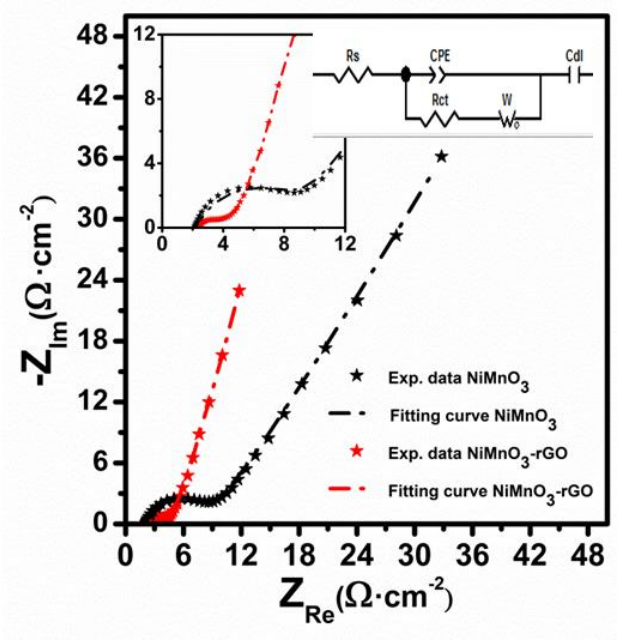

Figure 5.11 Nyquist plots of the $NiMnO_3$ and $NiMnO_3$-rGO samples. Inset shows proposed equivalent circuit by which the experimental results were fitted and the magnified Nyquist plot

Table 5.1 summarizes some recently reported studies concerning mixed nickel manganese oxides and their hybrids with graphene in energy storage application thereby providing a comparison of their performances with our $NiMnO_3$-rGO hybrid reported here in this chapter. As can be observed in the table, our $NiMnO_3$-rGO hybrid exhibited superior or comparable specific capacity in comparison with the listed reports. Only references [20] and [13] exhibited a higher specific capacity than our $NiMnO_3$-rGO hybrid, however in these works extremely small mass loadings were employed which are far from practice.

Table 5.1 Comparison of the electrochemical properties of the $NiMnO_3$-rGO hybrid with some previous corresponding reports on ilmenite phase, spinel $NiMn_2O_4$ and its hybrid materials

Sample	Electrolyte	Synthesis method	Specific Capacity ($mAh \cdot g^{-1}$)	Discharge Regime	Mass loading ($mg \cdot cm^{-2}$)	Areal Capacity ($mAh \cdot cm^{-2}$)	Potential window	Ref.
$NiMnO_3$-rGO $NiMnO_3$-NrGO $NiMnO_3$	1 M Na_2SO_4	Hydrothermal	79.4 111.2 33.3	5 $mV \cdot s^{-1}$	0.1	0.008 0.011 0.003	0.8	[20]
Carbon@ $NiMn_2O_4$	2M KOH	Hydrothermal	58.8	1 $A \cdot g^{-1}$	-	-	0.45	[11]
$NiMn_2O_4$ nanofibers	1M KCl	Electrospinning	113	1 $A \cdot g^{-1}$	1	0.113	1	[13]
$NiMn_2O_4$ nanosheet	6M KOH	Hydrothermal	73	1 $A \cdot g^{-1}$	1	0.073	0.4	[15]
$NiMnO_3$/rGO	6M KOH	Electrostatic Co-precipitation	55	1 $A \cdot g^{-1}$	-	-	0.7	[21]
$NiMnO_3$-rGO Nanosheets	**3M KOH**	**Hydrothermal**	**91 62**	**5 $mV \cdot s^{-1}$ 1 $A \cdot g^{-1}$**	**3-6**	**0.45 0.31**	**0.6**	**Our work**

Moreover, in terms of areal capacity, our $NiMnO_3$-rGO hybrid material outperformed all previous listed reports. All of these observations reveal that the synthesized $NiMnO_3$-rGO hybrid can serve as a promising positive electrode material with a reasonable mass loading for practical energy storage applications.

5.2.3 rGO//$NiMnO_3$-rGO Hybrid Energy Storage Device

In order to evaluate practical application of $NiMnO_3$-rGO, an aqueous hybrid energy storage device was assembled by integrating the $NiMnO_3$-rGO material as positive electrode and rGO NSs capacitor-type material as negative electrode. In this regard, the $NiMnO_3$-rGO positive electrode serves as a high capacity material that combines both electrical double layer capacitance (EDLC) and faradaic mechanism. On the other hand, rGO in the negative pole provides only capacitive character as observed in the CVs and GCD of the rGO material performed in 3-electrode configuration and in negative voltage range (***Figure 5.12***). In the case of rGO electrode, a semi-rectangular response without any observed redox peak was observed in CV whereas a triangular shape was observed in GCD profile. This is typical of capacitor-type materials without any heteroatom doping effect and it is governed by the electrochemical double layer capacitance (EDLC).

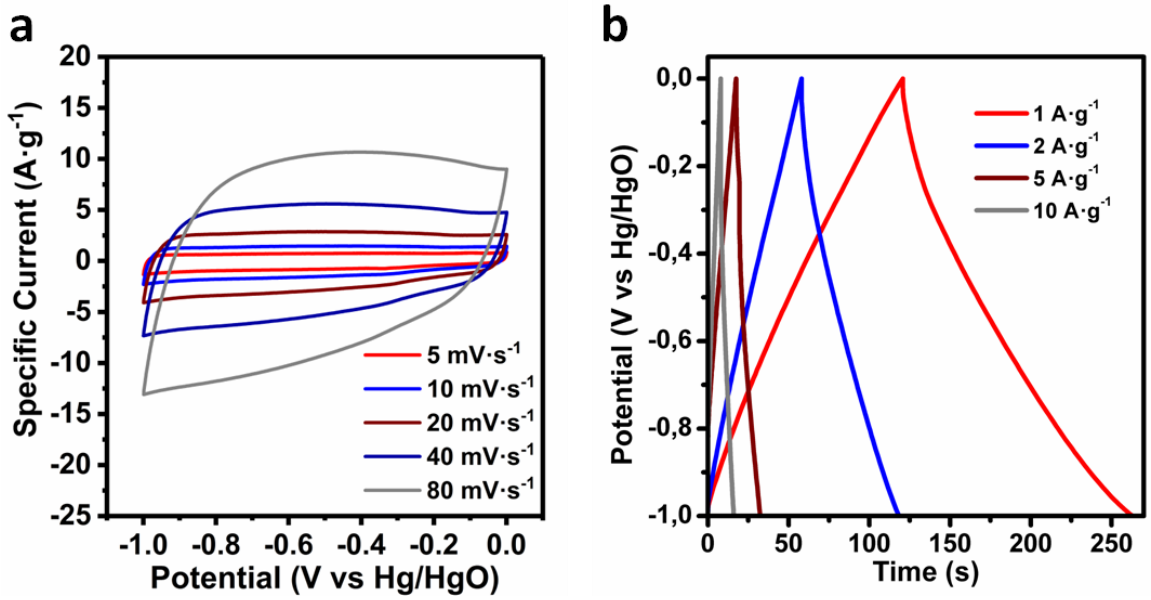

Figure 5.12 (a) CVs and (b) GCD profiles of the rGO material performed in 3-electrode configuration at different scan rates and current densities, respectively

The mass loading of the positive and negative electrodes was adjusted employing the charge balance theory (m^+/m^-) = 0.44***,*** according to [Eq. 3.15]. ***Figure 5.13*** shows a schematic representation of the hybrid system.

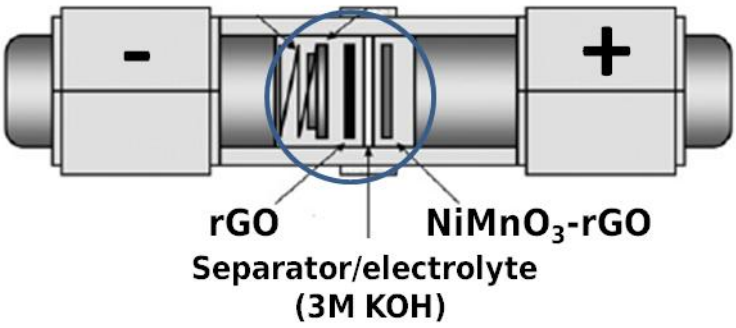

Figure 5.13 Schematic representation of the rGO NSs//$NiMnO_3$-rGO hybrid device

Figure 5.14a shows the CV profiles of rGO NSs//$NiMnO_3$-rGO hybrid device. It is clearly observed that at low scan rate the capacitive mechanism is dominating the process, however by increasing the scan rate the redox peaks emerged, demonstrating the effect of combined faradaic and capacitive mechanisms. ***Figure 5.14b*** displays the rate capability of the hybrid device, demonstrating a maximum specific capacity for the device of 28 $mAh \cdot g^{-1}$ at 5 $mV \cdot s^{-1}$, calculated by [Eq 3.8] in experimental.

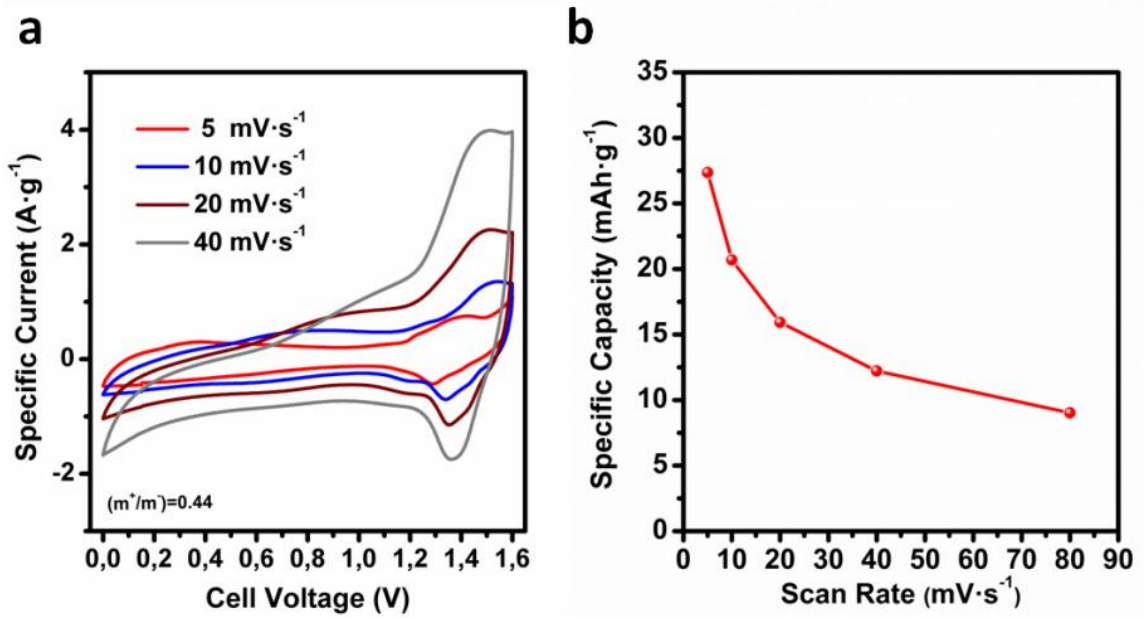

Figure 5.14 Electrochemical performance of rGO NSs//$NiMnO_3$-rGO hybrid device: (a) CV curves of rGO NSs//$NiMnO_3$-rGO hybrid device at various scan rates; (b) rate capability of the hybrid device at various scan rates

Increasing the scan rate by a factor of 16, the device could still retain 37% of its initial capacity. The rGO NSs//$NiMnO_3$-rGO device was further examined by GCD measurements and the results are shown in ***Figure 5.15a.***

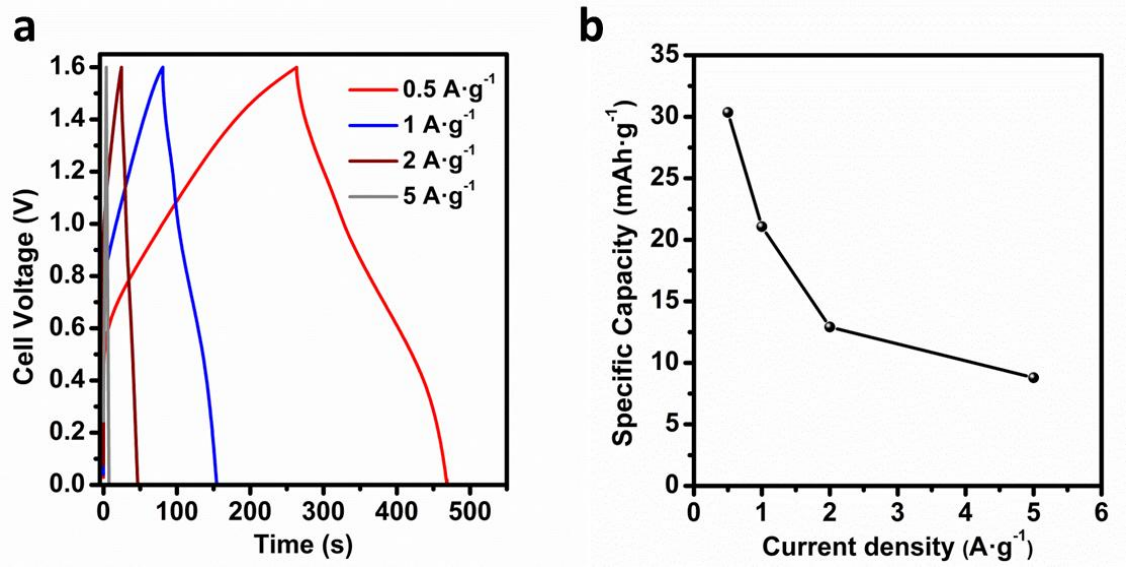

Figure 5.15 Electrochemical performance of rGO NSs//$NiMnO_3$-rGO hybrid device: (a) GCD profiles at different specific currents and (b) rate capability of the hybrid device

As expected, the GCD profiles are slightly deviated from linear triangular shape suggesting the effective combination of two different charge storage mechanisms in the hybrid cell (capacitive + faradaic). In addition, GCD curves displayed almost symmetric charge-discharge profiles, indicating excellent reversibility and coulombic efficiency of the full cell. On the right panel, ***Figure 5.15b*** shows the rate capability of the aqueous hybrid device at various specific currents, revealing an initial specific capacity of 31 $mAh \cdot g^{-1}$ at 0.5 $A \cdot g^{-1}$, according to [Eq 3.13] with a 30% capacity retention at 5 $A \cdot g^{-1}$, which is in good agreement with the obtained results from previous CV analysis.

As we mentioned in Chapter 4, Ragone plot is considered a very useful tool to evaluate the overall performance of any electrochemical energy storage device. ***Figure 5.16*** displays the Ragone Plot of the rGO NSs//$NiMnO_3$-rGO hybrid device in comparison with some recent similar hybrid devices.

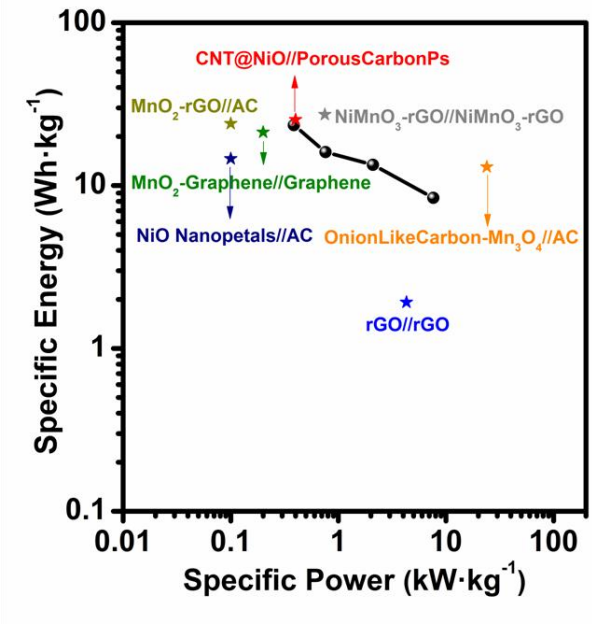

Figure 5.16 Ragone plot of the hybrid energy storage device at various specific currents and comparison with previous reports

Accordingly, our hybrid rGO NSs//$NiMnO_3$-rGO device achieved a maximum specific energy of 23.5 $Wh \cdot kg^{-1}$ at 0.5 $A \cdot g^{-1}$ with a specific power of 0.4 $kW \cdot kg^{-1}$, according to [Eq 3.16] and [Eq 3.17], respectively. By increasing the current load up to 5 $A \cdot g^{-1}$, a maximum power of 7.64 $kW \cdot kg^{-1}$ was reached while the specific energy could be retained as high as 8.4 $Wh \cdot kg^{-1}$. As observed, the rGO NSs//$NiMnO_3$-rGO hybrid device showed either superior (e.g. NiO Nanopetals//AC,[39] Onion-Like

Carbon-Mn_3O_4//AC[40] and symmetric rGO-based devices[36]) or comparable performance (e.g. MnO_2-Graphene//Graphene,[41] CNT@NiO//PorousCarbonPolyhedrons,[42] MnO_2-rGO//AC,[43] and symmetric $NiMnO_3$-rGO// $NiMnO_3$-rGO [21]) in comparison to previous studies.

Finally, cycling performance of the rGO NSs// $NiMnO_3$-rGO device was also evaluated using GCD measurements over 2000 cycles.

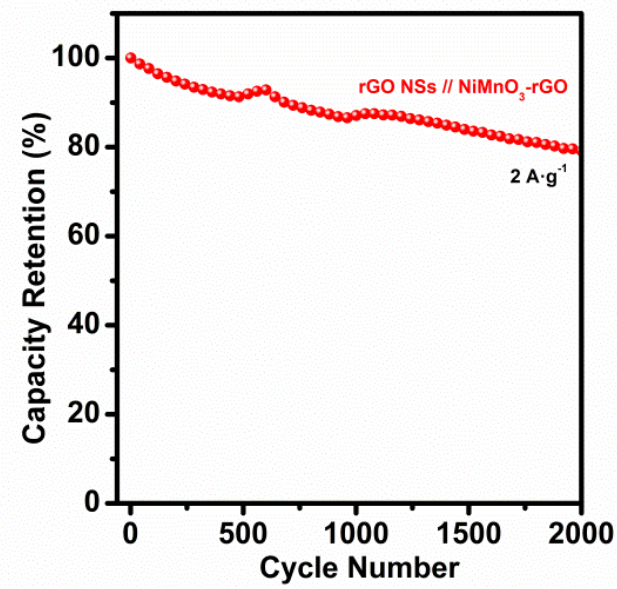

Figure 5.17 Cycling performance of the rGO NSs//$NiMnO_3$-rGO hybrid device at specific current of 2 $A \cdot g^{-1}$

From ***Figure 5.17***, one can observe that around 80% of the initial capacity of the full device was retained thereby demonstrating good structural stability and capacity retention of the full device. All of these results manifest the promise of $NiMnO_3$-rGO hybrid material as a high-performance positive electrode material for hybrid energy storage devices.

5.3 Conclusions

As a summary, in the present chapter $NiMnO_3$ NPs were feasibly anchored on rGO NSs via facile hydrothermal method followed by a thermal treatment. As-prepared $NiMnO_3$-rGO hybrid materials were electrochemically evaluated as potential electrode materials for energy storage applications. According to the obtained results, hybridizing $NiMnO_3$ NPs with rGO NSs could remarkably enhance the modest performance of ilmenite $NiMnO_3$ electrodes to a high-performance $NiMnO_3$-rGO hybrid electrode material. A maximum capacity of 91 $mAh{\cdot}g^{-1}$ was achieved at 5 $mV{\cdot}s^{-1}$ (c.a. 2 times greater than pure binary oxide). Furthermore, $NiMnO_3$-rGO positive electrodes were integrated with rGO negative electrodes in aqueous hybrid devices resulting a maximum specific energy of 23.5 $Wh{\cdot}kg^{-1}$ and a maximum specific power of 7.64 $kW{\cdot}kg^{-1}$, revealing their promise for green hybrid energy storage applications.

Applied Surface Science 460 (2018) 74–83

Contents lists available at ScienceDirect

Applied Surface Science

journal homepage: www.elsevier.com/locate/apsusc

Full length Article

Synthesis and application of $NiMnO_3$-rGO nanocomposites as electrode materials for hybrid energy storage devices

Jaime S. Sanchez[a], Afshin Pendashteh[a,*], Jesus Palma[a], Marc Anderson[a,b], Rebeca Marcilla[a,*]

[a] Electrochemical Processes Unit, IMDEA Energy Institute, Avda. Ramon de la Sagra 3, Parque Tecnológico de Móstoles, 28935 Móstoles, Spain
[b] Department of Civil and Environmental Engineering, University of Wisconsin, Madison, USA

ARTICLE INFO

Article history:
Received 30 September 2017
Received in revised form 24 January 2018
Accepted 16 February 2018
Available online 26 February 2018

Keywords:
$NiMnO_3$
Nanocomposite
Graphene
Hybrid device

ABSTRACT

Demand for more efficient and ecofriendly energy storage systems arouse research efforts in seeking to develop new energy materials with promising properties. In this regard, mixed transition metal oxides have recently attracted great attention due to their improved electrochemical and electrical properties in comparison with simple oxides. Herein, $NiMnO_3$ and their composites with reduced graphene oxide ($NiMnO_3$-rGO) were synthesized via a facile hydrothermal route, followed by a thermal treatment and their electrochemical properties have been evaluated as electrode materials for hybrid energy storage devices. The prepared samples were characterized by using X-ray diffraction (XRD), Raman spectroscopy, Thermogravimetric analysis (TGA), Scanning electron microscopy (SEM), Transmission electron microscopy (TEM) and N_2 adsorption measurements. The energy storage behavior of the samples was investigated using different electrochemical techniques including cyclic voltammetry, galvanostatic charge/discharge, and electrochemical impedance spectroscopy. Accordingly, a $NiMnO_3$-rGO nanocomposite showed a high capacity of 91 mAh g^{-1} at a scan rate of 5 mV s^{-1}, 48% higher than that of the pure $NiMnO_3$ sample (47.7 mAh g^{-1}). Furthermore, this nanocomposite was integrated as a positive electrode with reduced graphene oxide nanosheets as the negative electrode in an aqueous hybrid energy storage device. This system displayed a high specific energy of 23.5 Wh kg^{-1} and a maximum specific power of 7.64 kW kg^{-1}.

© 2018 Elsevier B.V. All rights reserved.

5.4 References

1 W. Zuo, R. Li, C. Zhou, Y. Li, J. Xia and J. Liu, *Adv. Sci.*, 2017, **4**, 1600539.

2 M. R. Lukatskaya, B. Dunn and Y. Gogotsi, *Nat. Commun.*, 2016, **7**, 12647–12660.

3 P. Simon, Y. Gogotsi and B. Dunn, *Science (80-.).*, 2014, **343**, 1210–1211.

4 D. Belanger, T. Brousse and J. W. Long, *Electrochem. Soc. Interface*, 2008, **17**, 49–52.

5 T. Nguyen, S. Eugénio, M. Boudard, L. Rapenne, M. J. Carmezim, T. M. Silva and M. F. Montemor, *Nanoscale*, 2015, **7**, 12452–12459.

6 Y. Xie, X. W. Lou, C. Yuan, H. Bin Wu, Y. Xie, X. Wen and D. Lou, *Angew. Chem. Int.*, 2014, **53**, 1488–1504.

7 D. Chen, Q. Wang, R. Wang and G. Shen, *J. Mater. Chem. A*, 2015, **3**, 10158–10173.

8 J. Zhao, M. Li, J. Li, C. Wei, Y. He and Y. Huang, *Appl. Surf. Sci.*, 2017, **425**, 1158–1167.

9 C. Wei, H. Pang, C. Cheng, J. Zhao, P. Li and Y. Zhang, *CrystEngComm*, 2014, **16**, 4169–4175.

10 C. Cheng, D. Kong, C. Wei, W. Du, J. Zhao, Y. Feng and Q. Duan, *Dalt. Trans.*, 2017, **46**, 5406–5413.

11 M. R. Kim, R. Mohan, N. Kalla, S. Kim, M. Kim and I. Kim, *ChemElectroChem*, 2017, **4**, 1214–1221.

12 Z. Wang, Z. Zhu, C. Zhang, C. Xu and C. Chen, *Electrochim. Acta*, 2017, **230**, 438–444.

13 J. Bhagwan, S. Rani, V. Sivasankaran, K. L. Yadav and Y. Sharma, *Appl. Surf. Sci.*, 2017, **426**, 913–923.

14 W. Kang, Y. Tang, W. Li, X. Yang, H. Xue, Q. Yang and C.-S. Lee, *Nanoscale*, 2015, **7**, 225–231.

15 H. Wei, J. Wang, L. Yu, D. Hou and T. Li, *Ceram. Int.*, 2016, **42**, 14963–14969.

16 X. He, F. Yin, Y. Li, H. Wang, J. Chen, Y. Wang and B. Chen, *Appl. Mater. Interfaces*, 2016, **8**, 26740–26757.

17 D. Mehandjiev, E. Zhecheva, G. Ivanov and R. Ioncheva, *Appl. Catal. A*, 1998, **167**, 277–282.

18 D. Hong, Y. Yamada, A. Nomura and S. Fukuzumi, *Phys Chem Chem Phys.*, 2013, **15**, 19125–19128.

19 Y. Xiao, J. Zai and X. Qian, *J. Alloys Compd.*, 2017, **716**, 270–277.

20 S. Giri, D. Ghosh and C. Kumar Das, *Dalt. Trans.*, 2013, **42**, 14361–14364.

21 P. Kakvand, M. S. Rahmanifar, M. F. El-kady, A. Pendashteh, M. A. Kiani, H. Masumeh, M. Najafi, A. Abbasi, M. F. Mousavi and R. B. Kaner, *Nanotechnology*, 2016, **27**, 315401.

22 Y. Gogotsi and P. Simon, *Science (80-.).*, 2011, **334**, 917–918.

23 W. H. CLOUD, *Phys. Rev.*, 1958, **111**, 1046–1049.

24 D. S. Hall, D. J. Lockwood, C. Bock, B. R. Macdougall and D. J. Lockwood, *Proc. R. Soc. A*, 2015, **471**, 20140792.

25 W. Shi, J. Zhu, D. H. Sim, Y. Y. Tay, Z. Lu, X. Zhang, Y. Sharma, M. Srinivasan, H. Zhang, H. H. Hng and Q. Yan, *J. Mater. Chem.*, 2011, **21**, 3422–3427.

26 J. Zhang, L. B. Kong, J. J. Cai, H. Li, Y. C. Luo and L. Kang, *Microporous Mesoporous Mater.*, 2010, **132**, 154–162.

27 G. Lee and S. Pyun, *Langmuir*, 2006, **22**, 10659–10665.

28 A. P. Grosvenor, M. C. Biesinger, R. S. C. Smart and N. S. Mcintyre, *Surf. Sci.*, 2006, **600**, 1771–1779.

29 A. Pendashteh, J. Palma, M. Anderson and R. Marcilla, *Appl. Catal. B Environ.*, 2017, **201**, 241–252.

30 N. Watanabe, H. Nakayama, K. Fukao and F. Munakata, *J. Appl. Phys.*, 2011, **110**, 023519.

31 L. An, L. Huang, P. Zhou, J. Yin, H. Liu and P. Xi, *Adv. Funct. Mater.*, 2015, **25**, 6814–6822.

32 S. Jerng, D. S. Yu, J. H. Lee, C. Kim, S. Yoon and S. Chun, *Nanoscale Res. Lett.*, 2011, **6**, 565–571.

33 J. S. Sanchez, A. Pendashteh, J. Palma, M. Anderson and R. Marcilla, *ChemElectroChem*, 2017, **4**, 1295–1305.

34 L. Dai, *Acc. Chem. Res.*, 2013, **46**, 31–42.

35 B. Wang, C. Hu and L. Dai, *Chem. Commun.*, 2016, **52**, 14350–14360.

36 A. Pendashteh, J. Palma, M. Anderson and R. Marcilla, *RSC Adv.*, 2016, **6**, 28970–28980.

37 H. B. Li, M. H. Yu, F. X. Wang, P. Liu, Y. Liang, J. Xiao, C. X. Wang, Y. X. Tong and G. W. Yang, *Nat. Commun.*, 2013, **4**, 1894–1991.

38 G. J. Brug, A. L. G. van den Eeden, M. Sluyters-Rehbach and J. H. Sluyters, *J. Electroanal. Chem. Interfacial Electrochem.*, 1984, **176**, 275–295.

39 G. Cheng, Q. Bai, C. Si, W. Yang, C. Dong, H. Wang, Y. Gao and Z. Zhang, *RSC Adv.*, 2015, **5**, 15042–15051.

40 K. Makgopa, K. Raju, P. M. Ejikeme and K. I. Ozoemena, *Carbon N. Y.*, 2017, **117**, 20–32.

41 L. Deng, G. Zhu, J. Wang, L. Kang, Z. Liu, Z. Yang and Z. Wang, *J. Power Sources*, 2011, **196**, 10782–10787.

42 H. Yi, H. Wang, Y. Jing, T. Peng and X. Wang, *J. Power Sources*, 2015, **285**, 281–290.

43 E. Miniach, A. Sliwak, A. Moyseowicz, L. Fernández-garcia, Z. González, M. Granda and R. Menendez, *Electrochim. Acta*, 2017, **240**, 53–62.

CHAPTER 6

Porous NiCoMn Ternary Metal Oxide/Graphene as Positive Electrode Materials for Hybrid Energy Storage Devices

6.1 Research Background

Considered as the building block of the carbon allotropes with excellent electric double layer capacity, graphene has been widely employed in energy storage due to its excellent conductivity and high specific surface area.[1,2] However, pristine graphene as we mentioned in the introduction chapter, achieves only a moderate capacitance/capacity (typically 100 $F \cdot g^{-1}$/27 $mAh \cdot g^{-1}$ respectively) due to inevitable restacking of graphene nanosheets.[3] Therefore, graphene and its derivatives (i.e. graphene oxide or reduced graphene oxide) could be best exploited in hybridization with battery-type materials such as single or mixed metal oxides, which can intercalate between graphene layers mitigating their restacking and at the same time offering high specific capacities. In such hybrid materials, high electrical conductivity emerges from the carbon component while the high capacity arises from the battery-like material (e.g. metal oxide). A variety of graphene-based materials with single or mixed metal oxides have been successfully investigated as hybrid electrode materials for high performing hybrid energy storage devices.[3–10] In fact, in previous chapters we used this hybridizing strategy with Fe_3O_4 (chapter 4) and $NiMnO_3$, (chapter 5).

Among the various transition metal oxides, cobalt oxides have drawn great attention, as very promising electrode materials in Li-ion batteries[11,12] and as excellent active materials for SCs and hybrid energy storage systems.[13,14] Hence, tremendous efforts have been focused on partially substitution of Co with less expensive and more benign elements to form mixed transition metal oxides. Additionally, mixed transition metal oxides have drawn growing attention in electrochemistry also due to their multiple oxidation states, better electrochemical performance and improved electrical conductivity compared to their single counterparts, as we highlighted in Chapter 5. Nanostructured binary/ternary transition metal oxides exhibit exceptionally high specific capacitances/capacities.[15–24] In one of the pioneering examples, the group of David Lou reported a facile co-electrodeposition method followed by thermal treatment of a $NiCo_2O_4$ supported on Ni foam, showing an ultrahigh specific capacitance of 201 $mAh \cdot g^{-1}$ (1450 $F \cdot g^{-1}$), even at a very high current density of 20 $A \cdot g^{-1}$, however it should be mentioned that electrode mass loading was not reported.[15] Later, Sahoo and coworkers reported a facile electrodeposition method for the synthesis of $MnCo_2O_4$ nanosheet showing a capacity of 40 $mAh \cdot g^{-1}$ (290 F g^{-1}) at 1 $mV \cdot s^{-1}$ in 2 M KOH solution as electrolyte for energy storage application.[19]

One step forward towards the substitution of Co is the use of two metals. For instance, in a previous work of our research group, $NiCoMnO_4$ spinel nanostructures were successfully employed as promising positive electrode material for aqueous hybrid devices with a high capacity of 79 $mAh \cdot g^{-1}$ and improved electrochemical performance with respect to the single oxides[25] (NiO, Mn_3O_4 and Co_3O_4) as shown in ***Figure 6.1***. That work showed the promise of bare $NiCoMnO_4$ spinel oxide as electrode material but our hypothesis is that its hybridization with graphene could further improve their electrode performance. Moreover, the effect of the different phases of the NiCoMn ternary metal oxide other than the spinel (e.g. rocksalt) on its electrochemical behavior has not yet been evaluated yet to be evaluated.

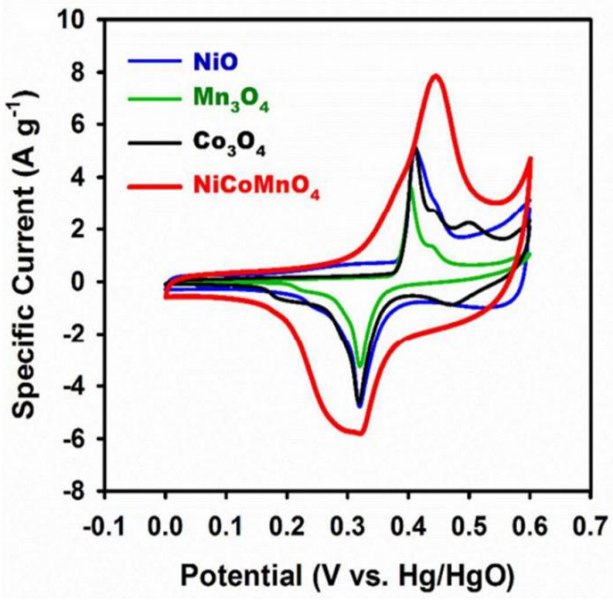

Figure 6.1 CV of different oxides at a scan rate of 5 $mV \cdot s^{-1}$ in 3M KOH (reported with permission [25])

Herein, in this chapter we report the synthesis of NiCoMn ternary metal oxide (NCMO) nanosheets on reduced graphene oxide layers (rGO) by employing a simple hydrothermal reaction and the study of their electrochemical behavior as electrode materials for aqueous hybrid energy storage devices. We are also interested on the effect of the synthetic conditions on the crystallographic nature of the obtained samples (i.e. spinel and rocksalt) and it effect on the electrochemical performance. To further demonstrate the promising potential of this material in hybrid energy storage devices, highly mass-loaded electrodes will be employed as positive electrodes integrated with an rGO negative electrode.

6.2 Results and Discussion

6.2.1 Synthesis and Physico-Chemical Analysis of NCMO_rGO

NCMO_rGO hybrid samples were synthesized via facile hydrothermal method followed by thermal treatment according to the steps schematically illustrated in ***Figure 6.2*** (synthesis details described in Chapter 3).

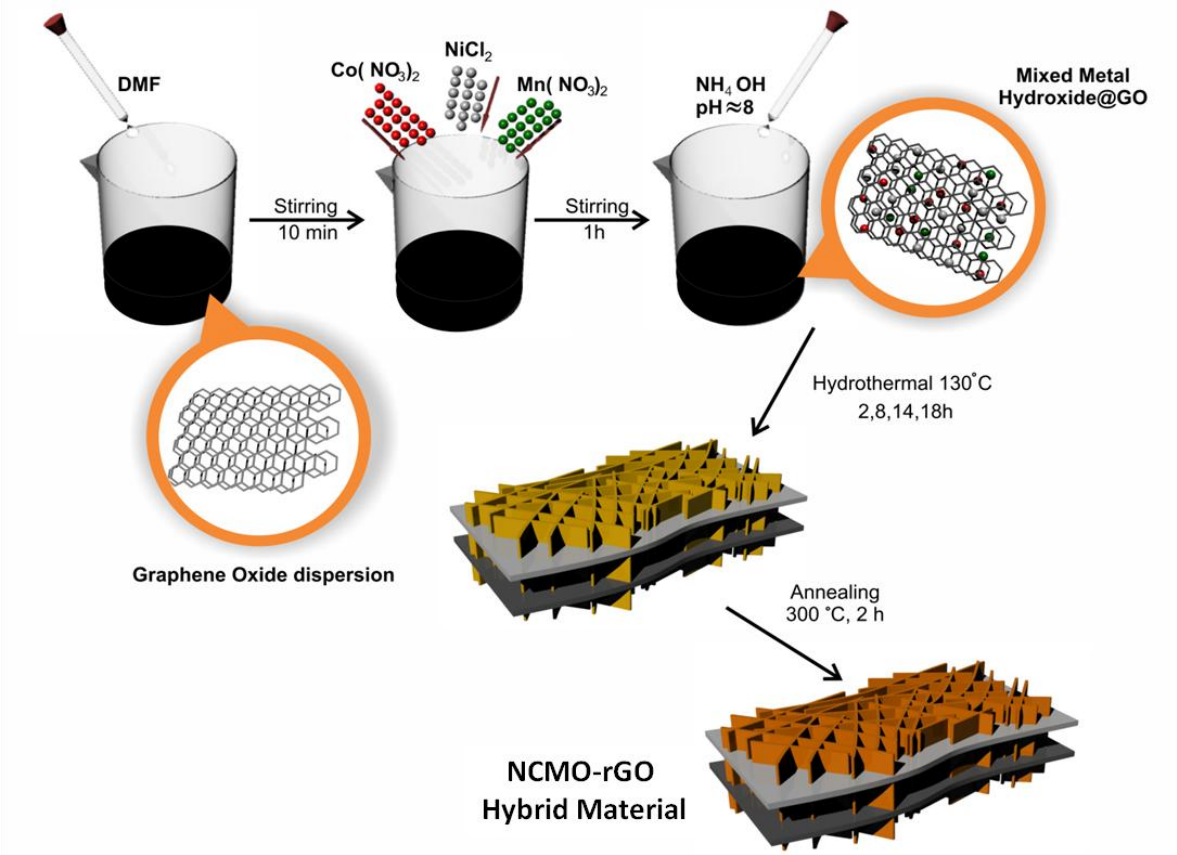

Figure 6.2 Schematic illustration of synthesis of the NCMO_rGO hybrids samples

First, GO nanosheets were dispersed in water forming a homogenous solution. Then, metallic salts were added into the solution and stirred for 1 h before adjusting the pH at ~8. After that, the hydrothermal reaction took place at 130 °C for different reaction times (2, 8, 14, and 18 h) before cooling down naturally to room temperature. At last, the precipitate was calcined in an electrical furnace at 300 °C for 2 h to obtain the NCMO_rGO hybrid materials. Different hybrid materials were synthesized via similar approach by varying the duration of the hydrothermal method

(ranging from 2 to 18h) and the amount of GO nanosheets in the reactant mixture. Samples were denoted as NCMO_rGO [x:y], where x and y denote the percentage content of the components. For the sake of comparison, bare NCMO samples were synthesized using the same protocol but without adding GO.

In order to illuminate the relationship between crystalline phase and electrochemical properties, different phases of NCMO_rGO were prepared by altering the hydrothermal reaction time (the amount of rGO in the hybrid material was kept constant, 25%). XRD measurements were carried out on different samples and the obtained patterns are shown in ***Figure 6.3a***.

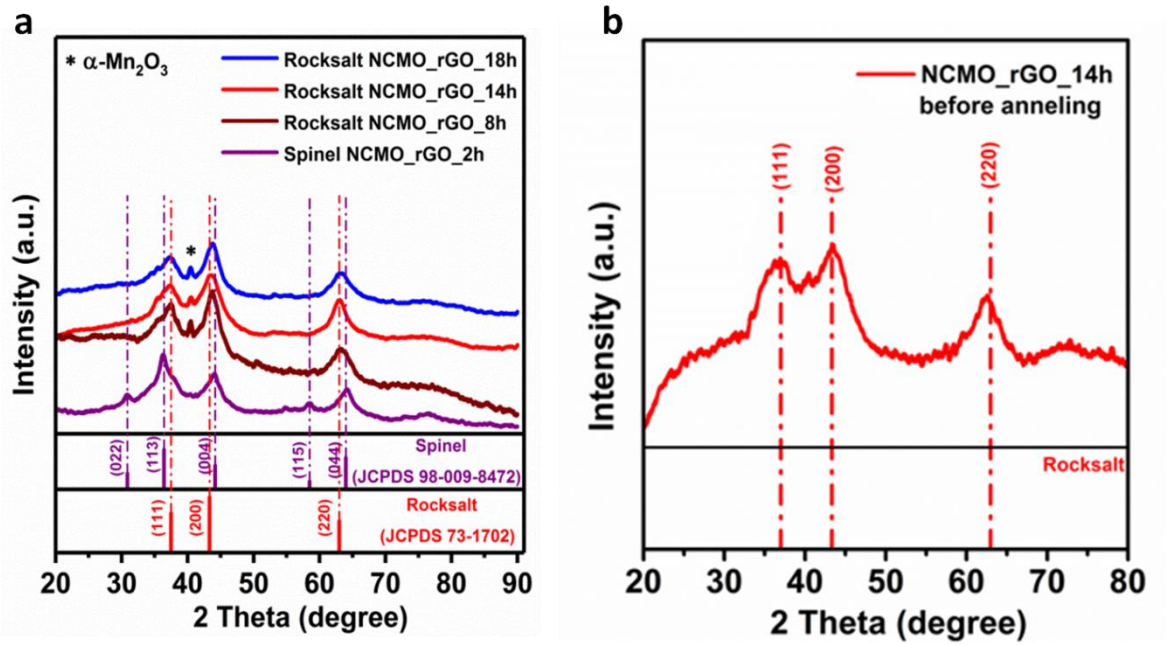

Figure 6.3 (a) XRD of the different samples (b) XRD study of NCMO_rGO_14h before thermal treatment at 300°C

As seen, relatively wide and low intense diffraction peaks indicate small crystalline domains of metal oxide particles in all the samples, which is favorable in charge storage applications as demonstrated in previous reports due to the possible mixture of polycrystalline and amorphous phases.[26] As seen in NCMO_rGO_2h sample (e.g. prepared in 2h reaction time), the diffracted peaks can be easily ascribed to cubic spinel phase with the space group of *Fd-3m* and lattice parameters of a = b = c = 8.1233 Å (JCPDS 98-009-8472), in agreement with previous reports.[25,27] Interestingly, by prolonging the reaction time (e.g. in 8h,14h and 18h), the spinel phase changed to

rock-salt cubic crystal structure (JCPDS card no. 73-1702) with the space group of *F43m.*[10,28] As a matter of fact, it has been previously reported by in situ XRD that crystalline oxide phase changes from a layered structure to spinel, and then to rock-salt by increasing the temperature to 500 °C.[29,30] Here, in order to confirm that the phase conversion spinel-rocksalt is taking place during the hydrothermal step at low temperature (e.g. 130 °C) just by prolonging the hydrothermal reaction time beyond 2h, XRD was conducted before thermal treatment on NCMO_rGO_14h sample (***Figure 6.3b***). As seen, it was discarded that the phase conversion is occurring during the annealing step of the synthesis, showing the rocksalt diffraction pattern even before the thermal treatment at 300 °C. The additional peak seen around 40° in ***Figure 6.3a*** can be ascribed to α-Mn_2O_3 phase, possibly related to incomplete conversion of the spinel phase.[29] From the structural point of view, while all of the octahedral sites are occupied in rocksalt structure, only half of these sites are filled in spinel phase (***Figure 6.4***). On the other hand, the unoccupied tetrahedral sites in the rocksalt are partially occupied (one-eighth) in the spinel phase. This results in more open octahedrally coordinated sites in rocksalt than tetrahedrally coordinated ones in a spinel structure, allowing easier oxidation of the cation 2+ to 3+ causing a higher electrochemical activity in rocksalt structure.[31,32] Furthermore, the O^{2-}-O^{2-} closest packing distance in rocksalt which is ~5% larger than in the spinel provides better ion mobility, which may result in higher energy storage capacity in the rocksalt structure.[31,33]

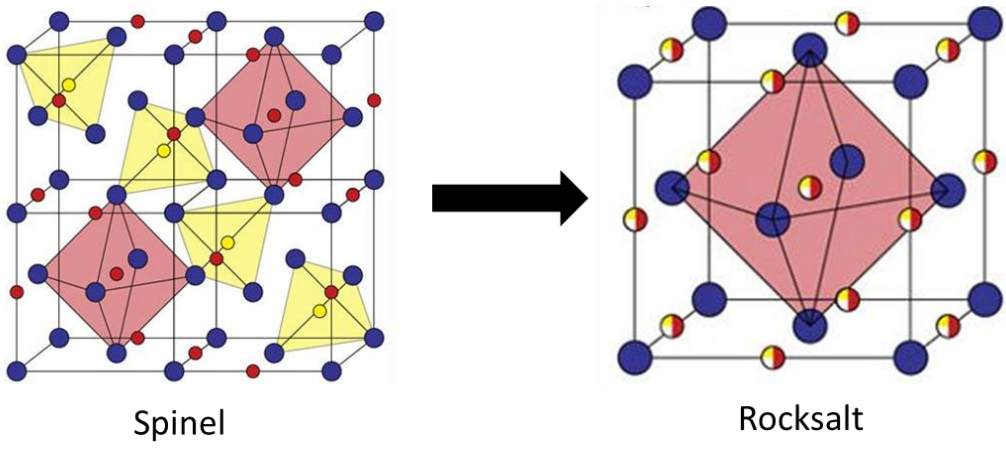

Figure 6.4 Schematic illustrations of spinel and rock-salt structures. Blue spheres represent oxygen while yellow spheres and red spheres are X cations. The mixed spheres indicate sites with mixed (random) populations (adapted from [34])

In order to quantify the atomic ratio of Ni, Co and Mn, the as-prepared NCMO-rGO samples were further analyzed by EDX analysis. As seen in ***Figure 6.5***, the Ni, Co and Mn elements can be clearly recognized with an average atomic ratio of Ni: Co: Mn of ~0.42:0.42:0.16, suggesting a nearly consistent elemental composition upon different hydrothermal reaction times.

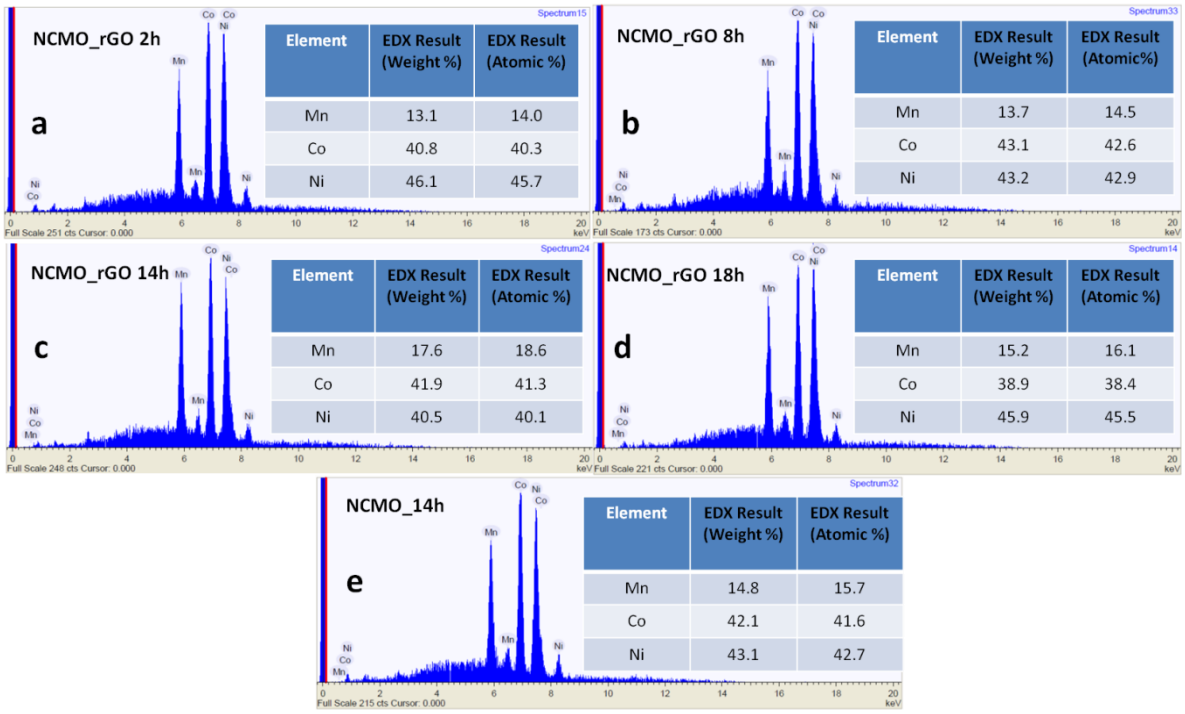

Figure 6.5 EDX spectra of nanostructured samples: NCMO-rGO 2h (a) NCMO-rGO 8h (b) NCMO-rGO 14h (c) NCMO-rGO 18h (d) NCMO 14h (e)

The Raman spectroscopy was further employed to characterize the structure of the samples and to confirm the successful hybridization of the metal oxide and carbon network ***Figure 6.6***. In all hybrid samples (***Figure 6.6a***), several peaks can be identified in the range of 300-1050 cm^{-1} which may be attributed to the vibrational modes of M-O (M = Ni, Co, or Mn) bonds as also seen in the case of pure oxides NCMO (samples 2h and 14h) (***Figure 6.6b***).[35,36] Moreover, two characteristic peaks typical for carbonaceous materials can be readily distinguished at 1357 cm^{-1} (D band) and 1582 cm^{-1} (G band), as in the pure rGO sample (***Figure 6.6b***). Overall, in all hybrid materials a combination of pure components' peaks without significant changes in peak positions can be distinguished, confirming that the main structure remained intact without any major structural alteration in the course of hybridization.

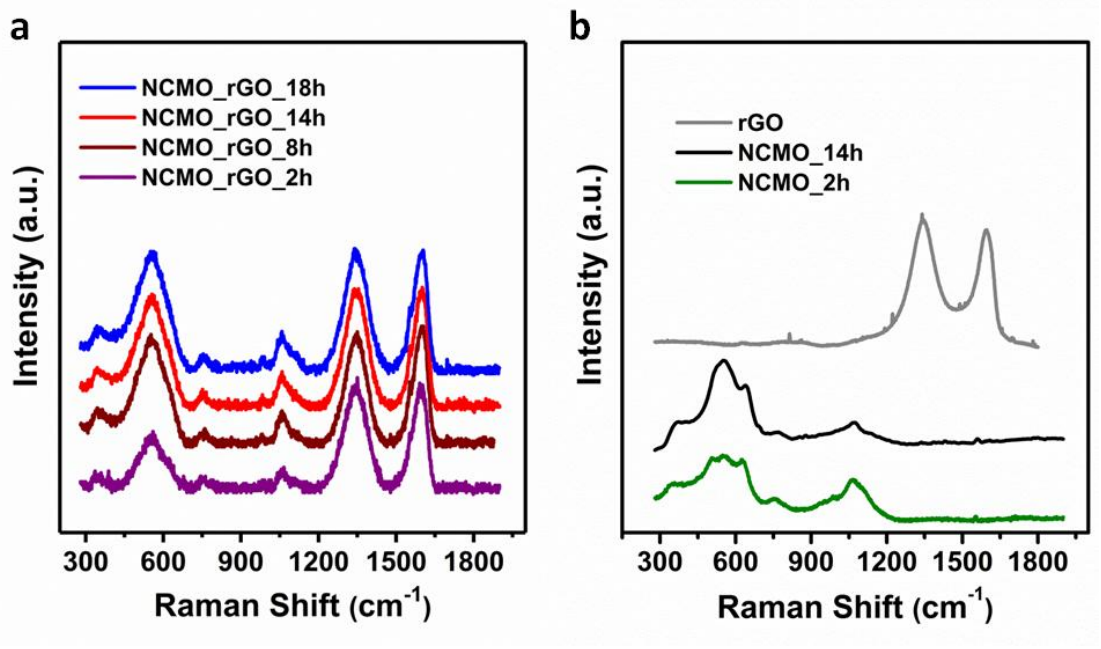

Figure 6.6 Raman spectra of (a) hybrid materials synthesized at different reaction times and (b) rGO, pure oxides (NCMO_2h, NCMO_14h)

In order to explore textural properties of the as-synthesized samples, nitrogen ad/de-sorption measurements were conducted both on NCMO_rGO hybrids and in bare oxides and rGO. ***Figure 6.7*** depicts the isotherms and their corresponding BJH pore size distributions of all samples. Specific surface area of the samples was also estimated based on BET theory (S_{BET}), and the results were summarized in ***Table 6.1***, as follow:

Table 6.1 BET Surface Area of the different samples synthesized

Sample	NCMO_rGO 2h	NCMO_rGO 8h	NCMO_rGO 14h	NCMO_rGO 18h	rGO NSs	NCMO 2h	NCMO 14h
BET ($m^2 \cdot g^{-1}$)	196	187	200	98	148	153	166

Accordingly, specific surface area of the hybrid materials NCMO_rGO_2h (196 $m^2 \cdot g^{-1}$) and NCMO_rGO_14h (200 $m^2 \cdot g^{-1}$) are remarkably higher than their pure components, rGO (149 $m^2 \cdot g^{-1}$), NCMO_2h (153 $m^2 \cdot g^{-1}$) and NCMO_14h (166 $m^2 \cdot g^{-1}$), demonstrating that the hybridization decisively enhanced the surface area of pure components. Higher values of surface area in the hybrid materials may be largely attributed to finer pores in comparison with pure oxides and the additional porous nature arising from hybridization with rGO layers.[7] Moreover, NCMO_rGO 18h

present the smaller value of S_{BET} between all hybrids synthesized. Furthermore, all samples display a type IV isotherm with distinct hysteresis shapes, revealing presence of different porous structures.

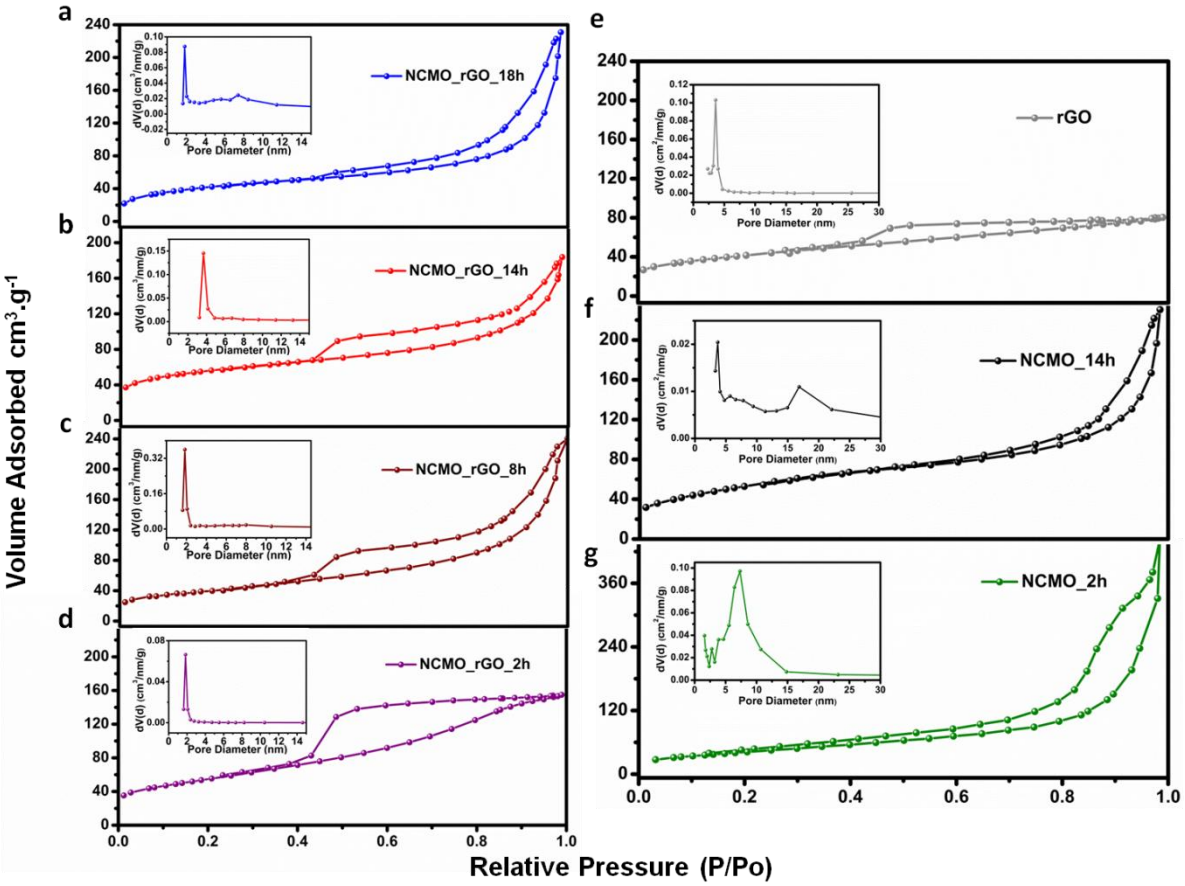

Figure 6.7 N_2 adsorption-desorption isotherms and BJH Pore size distribution of: (a) NCMO_rGO 18h, (b) NCMO_rGO 14h, (c) NCMO_rGO 8h, (d) NCMO_rGO 2h (e) rGO, (f)NCMO_14h, and (g) NCMO_2h

NCMO_rGO_2h hybrid material (***Figure 6.7d***) and rGO (***Figure 6.7e***) present a H2-type hysteresis loop as a consequence of an interconnected porous network. In contrast, the isotherms of pure oxides (***Figure 6.7f-g***) and the rest of the hybrid materials (***Figure 6.7a-c***) show a H3-type hysteresis while the adsorption branch increased rapidly at a relative pressure close to unity, indicating condensation of large inter-particle voids.[7] Theoretically, such large inter-particle channels are easily accessible for KOH electrolyte ions and further facilitate the ion diffusion, resulting in enhanced electrochemical properties.

The detailed chemical composition and oxidation state of the cations in the as-prepared NCMO_rGO 14h sample were further analyzed by X-ray photoelectron spectroscopy (XPS), and the results are depicted in ***Figure 6.8.***

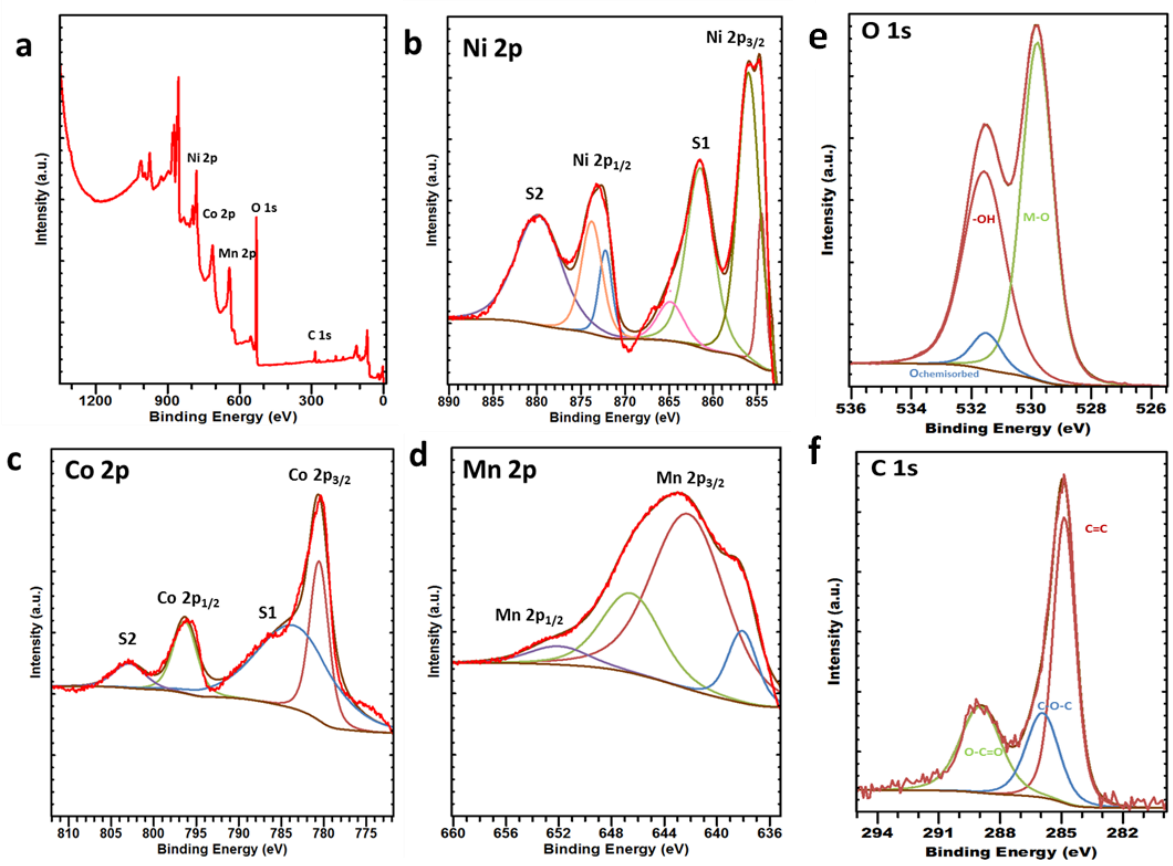

Figure 6.8 XPS surface analysis of NCMO_rGO 14h hybrid material, (a) Survey, (b) Ni 2p; (c) Co 2p (d) Mn 2p (e) O 1s, (f) C 1s

As seen in the XPS survey spectrum (***Figure 6.8a***), the NCMO_rGO 14h hybrid is comprised of nickel, cobalt, manganese, oxygen and carbon elements, without any other impurity elements. The atomic ratio of Ni:Co:Mn was obtained as 0.44:0.36:0.20, in good agreement with the atomic ratio values obtained with EDX. In the high-resolution XPS spectrum of Ni 2p (***Figure 6.8b***), one can distinguish two major envelopes of Ni $2p_{3/2}$ and Ni $2p_{1/2}$ centered at 855.5 and 873.2 eV, respectively. In addition, two low intensity and broad satellite peaks can be also recognized at 861.5 eV and 879.9 eV suggesting the presence of Ni^{2+} and Ni^{3+} species in the mixed structure.[37] Similarly, the high resolution Co 2p spectrum (***Figure 6.8c***) is composed of two spin-orbit doublets at 796.1 eV for Co $2p_{1/2}$ and 780.5 eV for Co $2p_{3/2}$ together with two shakeup satellites at 786.5 eV

and 803.3 eV indicating the presence of Co^{2+} and Co^{3+}.[38] From Mn 2p core-level, the co-existence of Mn^{3+} and Mn^{4+} in a low-spin state can be realized through two distinguishable signals at 642.5 eV and 653.2 eV attributed to Mn $2p_{3/2}$ and Mn $2p_{1/2}$, respectively.[39,40] The high-resolution XPS data of the cations was used to calculate the overall charge of each element in the NCMO_rGO_14 h sample, summarized in ***Table 6.2***.

Table 6.2 Valence states of Ni, Co and Mn in NCMO_rGO_14h hybrid

Sample	Ni^{2+}/Ni^{3+}	Co^{2+}/Co^{3+}	Mn^{3+}/Mn^{4+}	Ni^{x+}	Co^{y+}	Mn^{z+}	Molecular formula determined from XPS data
NCMO_rGO_14h	0.47	0.72	1.44	x=2.68	y=2.58	z=3.41	$Ni_{0.44}Co_{0.36}Mn_{0.20}O_{0.53}$

In the case of O 1s core level (***Figure 6.8e***), the signal can be attributed to oxygen molecules attached to different atoms. The peak about 529.6 eV is ascribed to metal-oxygen bonds, while the ones at 531.5 and 532.1 eV can be attributed to hydroxyl groups and chemisorbed O, respectively.[41] The C 1s peak (***Figure 6.8f***), originated from the rGO, can be deconvoluted into three different components at binding energies of 284.8, 286.1 and 289 eV, corresponding to graphitic carbon, C-O-C and O-C=O, respectively; in good agreement with previous reports.[42] Therefore, these XPS results demonstrate the mixed-valence nature of the NCMO-rGO sample which may be beneficial for the improvement of the electrochemical performance.

Morphological properties of the as-prepared samples were examined by SEM, TEM and HR-TEM. As can be seen in SEM images depicted in ***Figure 6.9***, the particle size and morphology of the samples have been significantly changed by altering the hydrothermal reaction time. Large agglomerations are observed in NCMO_rGO_2h while the size of the particles is reduced by increasing the reaction time. It can be seen that the particles in NCMO_rGO_14h sample are smaller with a uniform distribution in size and morphology in comparison with the other samples. Comparing the NCMO_rGO_14h hybrid (***Figure 6.9c***) with the pure oxide sample synthesized in the same conditions (***Figure 6.9e***), it can be noticed that the presence of graphene nanosheets results in formation of more uniform sample in shape and size. This can be attributed to the fact that graphene oxide functional groups provide suitable sites for nucleation of metal oxide particles.

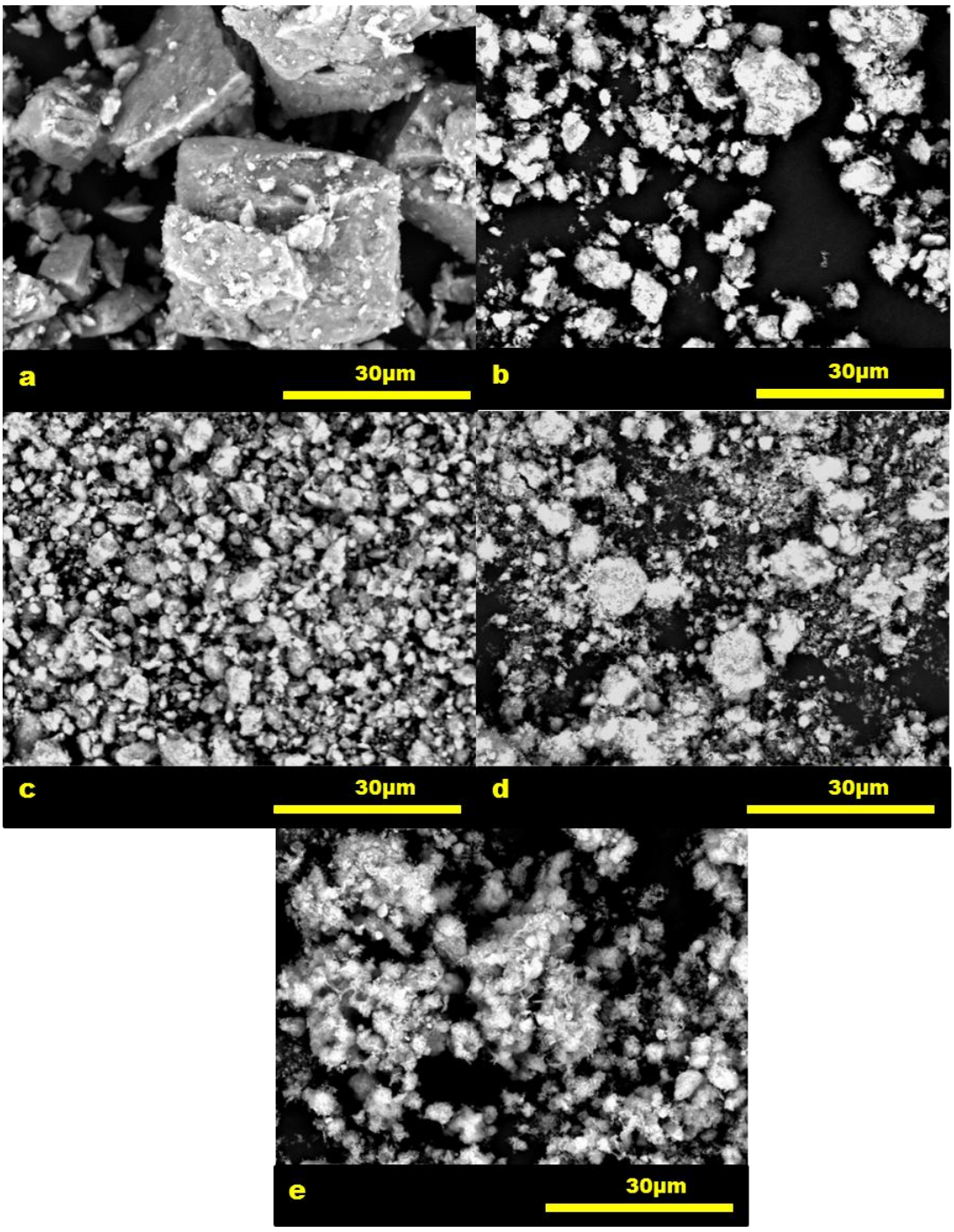

Figure 6.9 SEM images of (a) NCMO_rGO_2h (b) NCMO_rGO_8h (c) NCMO_rGO_14h and (d) NCMO_rGO_18h hybrids along with (e) NCMO_14h pure oxide sample

The detailed morphology of the NCMO_rGO hybrid was further investigated by TEM in ***Figure 6.10*** and ***Figure 6.11.*** As a first glance in low magnification images (***Figure 6.10a, c, e, and g***), one can

appreciate that the hydrothermal reaction time drastically influence the microstructure of NCMO grown on rGO layers. Spinel NCMO_rGO_2h (***Figure 6.10 a,b***) is comprised of irregular shaped particles in which NCMO crystalline domains cannot be readily distinguished.

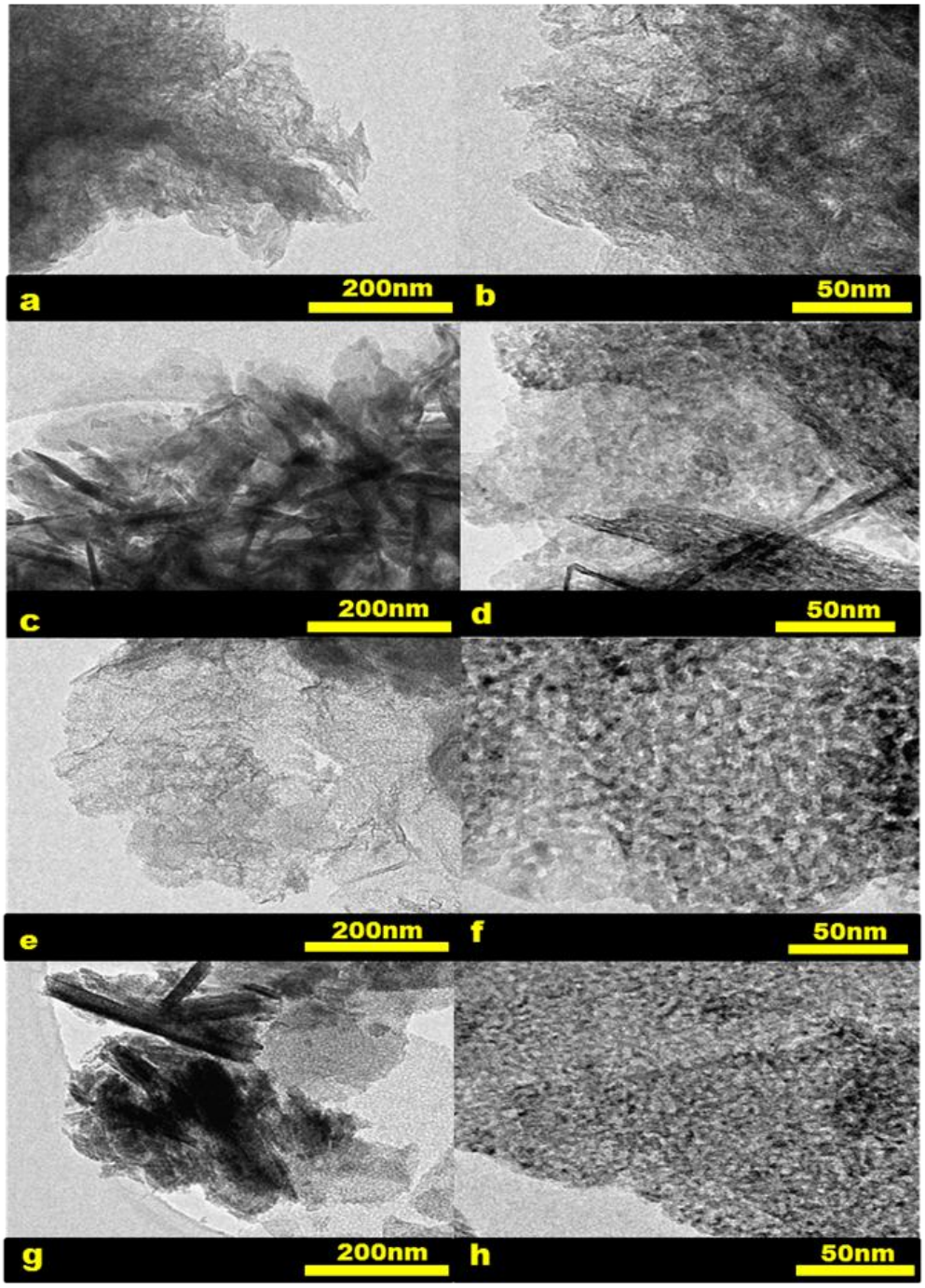

Figure 6.10 TEM images of NCMO_rGO hybrid materials synthesized during (a,b) 2h, (c,d) 8h, (e,f) 14h and (g,h) 18h

Increasing the reaction time, the particles of NCMO_rGO_8h sample (***Figure 6.10 c,d***) have grown in a more oriented manner, forming perpendicular oxide flakes on the carbon network. Prolonging the reaction time to 14h resulted in formation of a uniform, thin film of the mixed metal oxide on rGO nanosheets, as we can notice in ***Figure 6.10 e,f*** and detailed in ***Figure 6.11***. Finally, NCMO_rGO_18h hybrid sample (***Figure 6.10 g,h***), shows a large agglomeration of oxide flakes on graphene layers.[43] As seen in ***Figure 6.11b***, the metal oxide flakes are comprised of aggregating small nanoparticles, resulting in a highly porous structure with a pore size in the range of ~4 nm. This is in agreement with the BJH studies (***Figure 6.7***) and might anticipate a more facile movement of electrolyte ions in NCMO_rGO_14h hybrid sample.

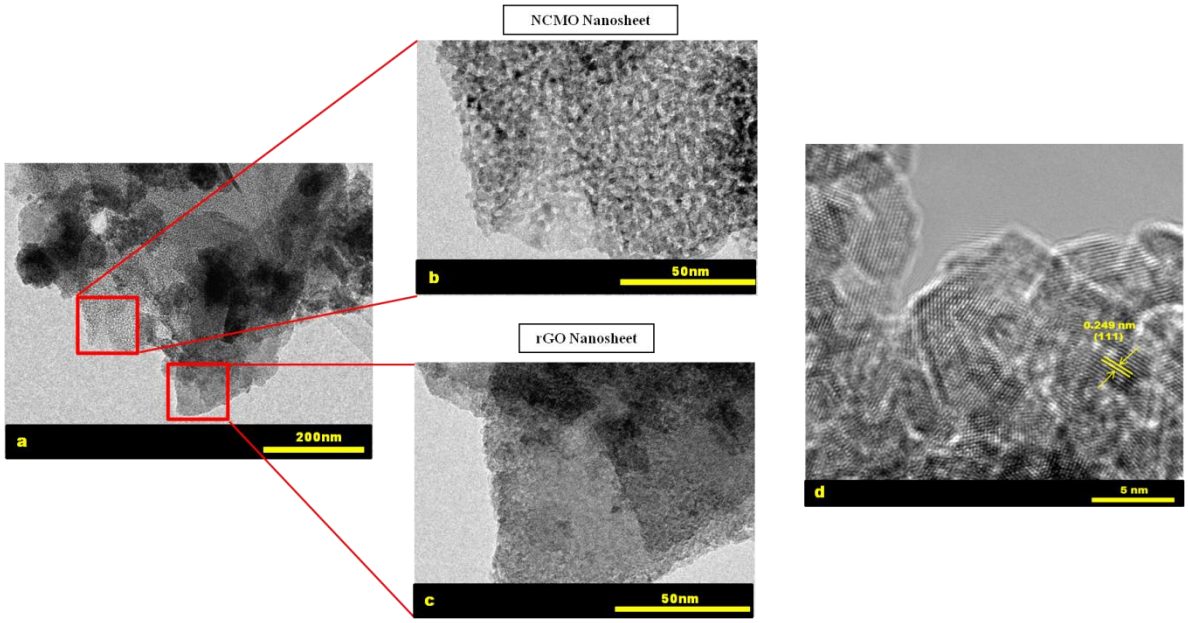

Figure 6.11 (a-c) TEM images of NCMO_rGO_14h [75-25] sample (d) HR-TEM image of NCMO_rGO_14h [75-25] sample

Additionally, the corresponding HR-TEM lattice image is shown in ***Figure 6.11d***, where the d-spacing (inter planar distance) of the plane is 0.249 nm and this corresponds to the Miller indices (111) of rocksalt NCMO-rGO (***Figure 6.3***).

In order to examine how is the distribution of the different metal cations in NCMO_rGO hybrid, STEM elemental mapping and high angle annular dark field scanning transmission electron micrographs (HAADF-STEM) were also carried out. ***Figure 6.12*** evidently confirms the

homogeneous distribution and real coexistence of Ni, Co, Mn, O and C in the NCMO_rGO sample. Such investigation assuredly manifest that the NCMO thin nanosheets are successfully and uniformly distributed on reduced graphene oxide layers.

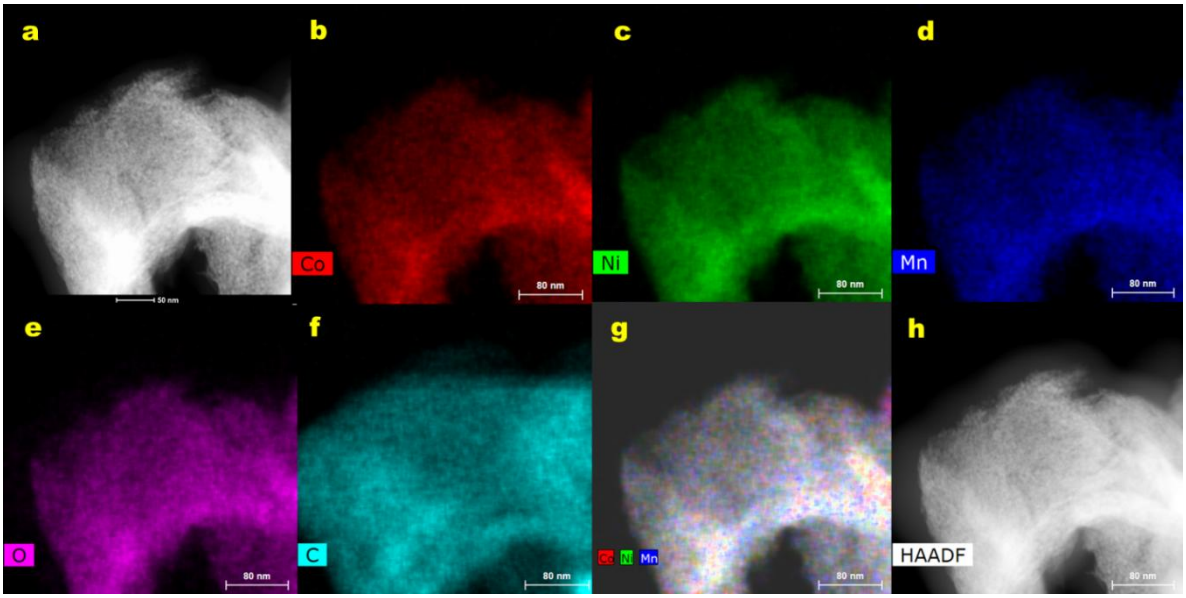

Figure 6.12 Morphological and elemental probing of the NCMO_rGO 14h: (a) TEM micrograph of NCMO_rGO 14h sample (b–g) corresponding EDX-STEM maps of various elements, depicting their distribution in the NCMO_rGO 14h sample (h) high angle annular dark field scanning transmission electron microscopy (HAADF-STEM) image of the sample

6.2.2 Electrochemical Evaluation of NCMO_rGO

The influence of prolonging hydrothermal reaction time and the observed changes in mixed metal oxide phase were evaluated and examined on the electrochemical signal of the samples. ***Figure 6.13a*** displays the CVs for different NCMO_rGO samples at 5 $mV{\cdot}s^{-1}$. All samples show a clear battery-type signal with intense redox peaks arising from the Faradaic nature of the charge storage mechanism. The shape of the CVs is in good agreement with previous reports on similar mixed metal oxides.[35,44,45] As can be appreciated, ***Figure 6.13b*** shows the specific capacity as a function of scan rate for all samples synthesized at different reaction times. In consistence with ***Figure 6.13a***, NCMO_rGO_14h sample possesses superior specific capacity than other samples over all scan rates. The better performance of the NCMO_rGO_14h sample may be attributed to

the unique morphology and porous nature of the oxide (realized already from SEM, TEM, BET, and BJH pore size distribution) on the anchored on graphene layers.

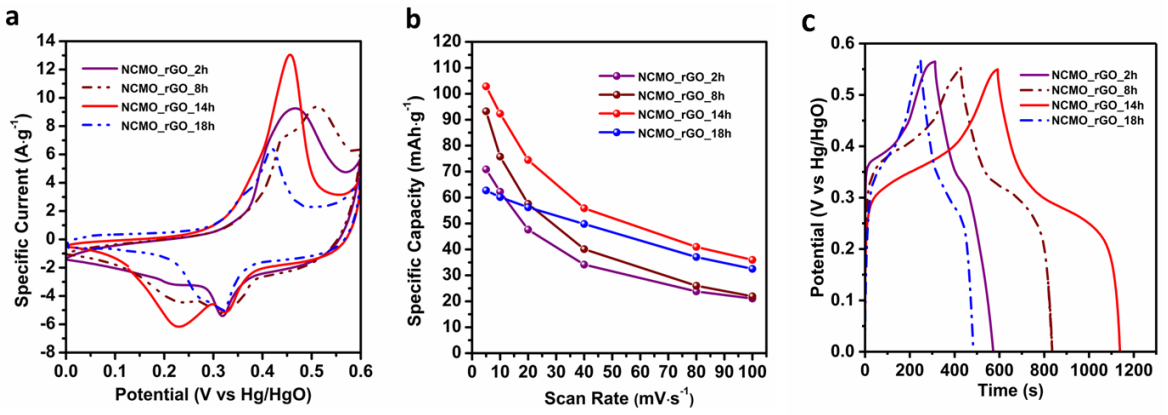

Figure 6.13 Electrochemical evaluation of the NCMO_rGO hybrid materials at different reaction time conditions in 3 M KOH solution: (a) CV curves of the different samples at a scan rate of 5 $mV \cdot s^{-1}$; (b) Rate capability of the samples at various scan rates; (c) Galvanostatic charge-discharge profiles of NCMO_rGO hybrids at 1 $A \cdot g^{-1}$

This particular nanostructure provides better access to the electrolyte ions and enhances the electrical/electrochemical properties of the hybrid sample. On contrary, NCMO_rGO_18h hybrid exhibits the smallest initial capacity, confirming that 14h can be considered as an optimal reaction time. However, the NCMO_rGO_18h sample showed excellent capacity retention in regard to its initial value (***Figure 6.13b***), this can be associated to the larger pore size and interparticle voids in this hybrid already realized from the less-centered pore size distribution of the sample in comparison with the others. The exceptional performance of the optimized sample (NCMO_rGO_14h) was further proved by galvanostatic charge-discharge measurements shown in ***Figure 6.13c***. As seen, the NCMO_rGO_14h exhibited the longest discharge time among all samples, confirming its superior performance as an electrode material for energy storage applications.

Tracking the exact mechanism of the redox reactions in such a complex structure of mixed metal oxides would require further electrochemical experiments coupled with spectroscopy techniques. However, based on previous reports found on similar mixed metal oxides structures,[46,47] together with XPS and EDX results already explained above, the following mechanism can be proposed for NCMO faradaic reactions:

$$NiCoMnO_{4\ (spinel)} + H_2O + OH^- \leftrightarrow NiOOH + CoOOH + MnOOH + e^- \quad [Eq.\ 6.1]$$

$$(Ni_{0.42}Co_{0.42}Mn_{0.16})O_{\ (rocksalt)} + OH^- \leftrightarrow (Ni_{0.42}Co_{0.42}Mn_{0.16})OOH + e^- \quad [Eq.\ 6.2]$$

$$(Ni_{0.42}Co_{0.42}Mn_{0.16})OOH \leftrightarrow 0.42\cdot NiOOH + 0.42\cdot CoOOH + 0.16\cdot MnOOH \quad [Eq.\ 6.3]$$

$$MnOOH + OH^- \leftrightarrow MnO_2 + H_2O + e^- \quad [Eq.\ 6.4]$$

$$CoOOH + OH^- \leftrightarrow CoO_2 + H_2O + e^- \quad [Eq.\ 6.5]$$

Moreover, to examine the effect of oxide/carbon component ratios, different samples were also synthesized under the optimized reaction time (14h) but adding different amount of GO in the reactant mixture. The components ratio in the hybrid materials was analyzed by TGA in air and the results are shown in ***Figure 6.14***. In the case of pure oxide compound (NCMO_14h), a gradual loss of around 12% below 200°C can be realized, possibly attributed to removal of hydroxyl groups on surface of the sample and/or trapped water in the lattice.[48]

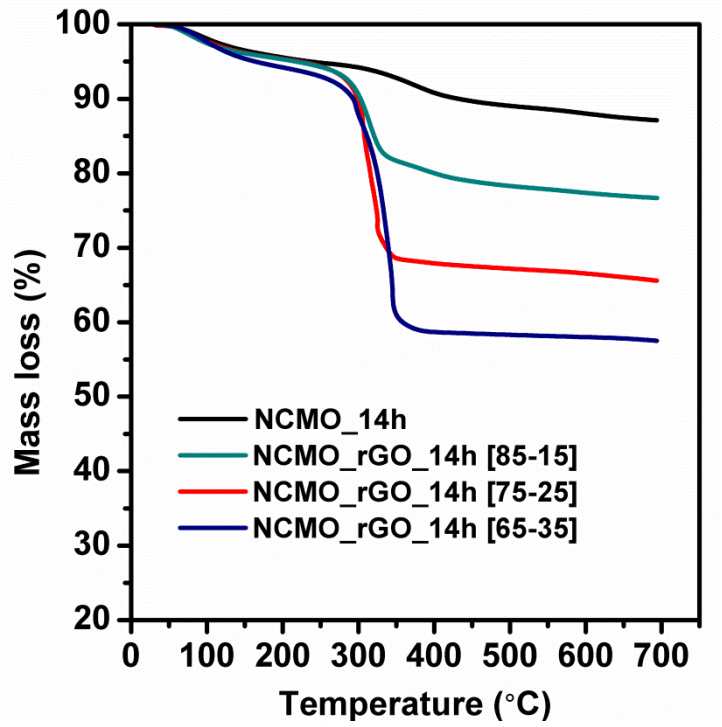

Figure 6.14 TGA curves of the NCMO_14h and NCMO_rGO_14h different reagents ratios in Air with a heating rate of 10°C·min^{-1}

As seen, all hybrids showed an additional abrupt mass loss between 300°C and 400°C, resulting from combustion of graphene. Accordingly, the mixed metal oxide content was estimated to be 85, 75, and 65, taking into account the initial loss related to the mixed oxide. The obtained ratios are in good agreement with the initial mass of metal precursors employed during synthesis.

Figure 6.15a shows CV profiles of pure (rock-salted) NCMO_14h and NCMO_rGO_14h hybrid samples with different reagents ratios at a scan rate of 5 $mV \cdot s^{-1}$. CV shapes clearly reveal the faradaic characteristics of the redox reactions. Compared with pristine oxide (NCMO_14h), the peak of specific current has remarkably increased in all of hybrid samples as a result of hybridization and synergism with rGO, thereby providing a significant improvement in energy storage capabilities of the oxide. This can be attributed to favorable distribution of NCMO sample on conducting graphene layers (as seen in TEM images previously) which facilitates the electron and ion transfer and results in improved electrochemical performance in these hybrid materials.

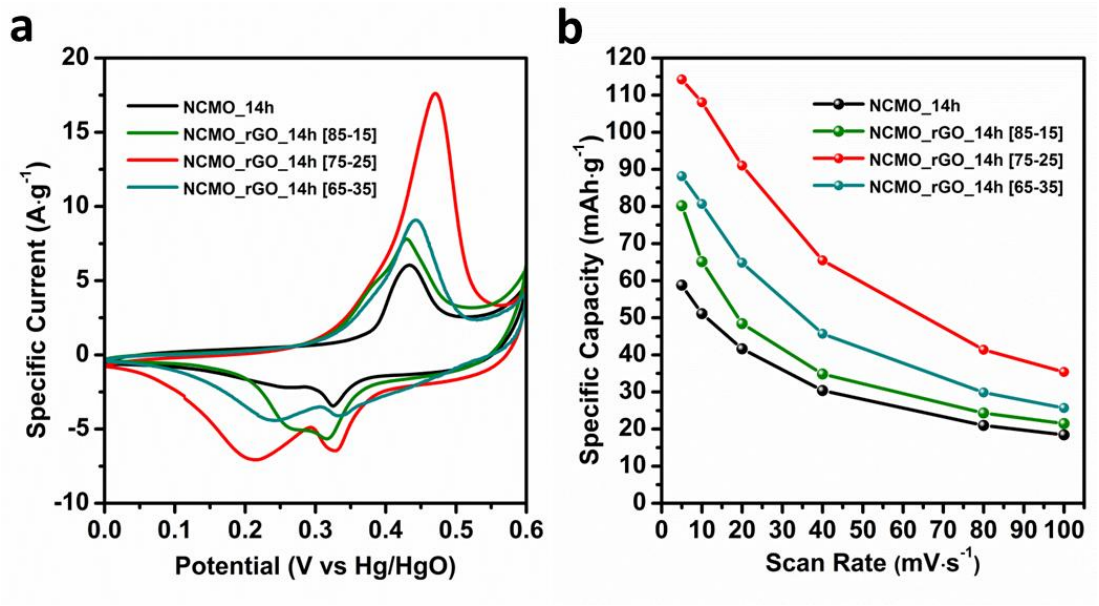

Figure 6.15 Electrochemical evaluation of the NCMO_rGO hybrid materials and NCMO sample as battery-type electrode materials in 3 M KOH solution: (a) CV curves of the NCMO_rGO hybrid materials with different component ratios and pure NCMO sample at a scan rate of 5 $mV \cdot s^{-1}$; (b) Rate capability of the samples at various scan rates

Figure 6.15b illustrates the calculated specific capacity for pure NCMO_14h and NCMO_rGO_14h hybrid samples as a function of scan rate. Among three different ratios of hybrid samples, the

NCMO_rGO_14h [75-25] sample possesses the highest specific capacity (115 mAh·g^{-1} at 5 mV·s^{-1}), significantly higher than the one obtained for pure NCMO_14h (59 mAh·g^{-1}) at the same scan rate.

GCD profiles of the NCMO_rGO_14h [75-25] sample at different specific currents are also depicted in ***Figure 6.16a.*** It can be seen that the discharge time decreases by increasing the specific current from 1 A·g^{-1} to 20 A·g^{-1}. The appearance of plateaus at around 0.4 V during the charge and ~0.25 V during discharge shows a typical battery type performance, and it is in good agreement with the observed redox peaks in CV curves (***Figure 6.15a***). According to the discharges curves, the hybrid achieved much higher capacity (115 mAh·g^{-1}) in comparison with the oxide (65 mA.h.g^{-1}) as seen in ***Figure 6.16b***.

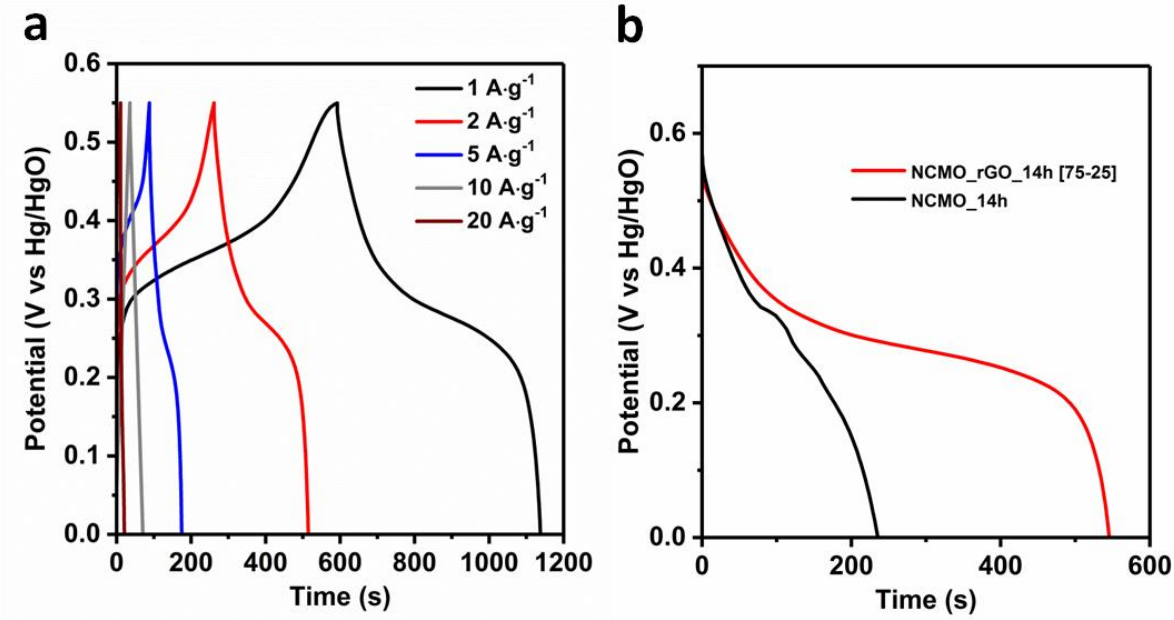

Figure 6.16 Electrochemical evaluation of the NCMO_rGO hybrid materials and NCMO sample as battery-type electrode materials in 3 M KOH solution: (a) charge−discharge profiles of the NCMO_rGO_14h [75-25] sample at different specific currents; (b) Discharge profiles of the NCMO_14h and NCMO_rGO_14h [75-25] samples

For more insight of the reaction mechanism, phase conversion of the sample was probed by XRD measurements of the sample in different applied potentials (at OCP, at 0.3 V and 0.6 V in charge and finally at 0.0 V after complete discharge, ***Figure 6.17***). The potentials were chosen before and after voltage plateau in charge step (***Figure 6.16a***) to track the changes upon electrochemical reaction. As seen, the characteristics diffraction peaks of rock-salt phase, e.g. (111), (200) and

(220) planes remained almost identical after charging the electrode up to 0.3V. However, after applying higher potential (0.6V), the (220) peak has almost disappeared, whereas peaks for (111) and (200) crystal planes became broader and less intense. Interestingly a new peak at 2θ=25.5º appeared which can be ascribed to tetragonal phase of α-MnO_2. This is in agreement with the proposed reaction mechanism in which Mn^{3+} is converted to Mn^{4+}. Decreased intensity and increased broadness of the diffracted peaks suggest significant decrease in crystallinity of the sample upon charging which may justify formation of amorphous layers and absence of other phases proposed in [Eq 6.3] to [Eq 6.5]. After complete discharge to 0.0 V, all peaks can be indexed again to the rock-salt phase, indicating the reversibility of the process.

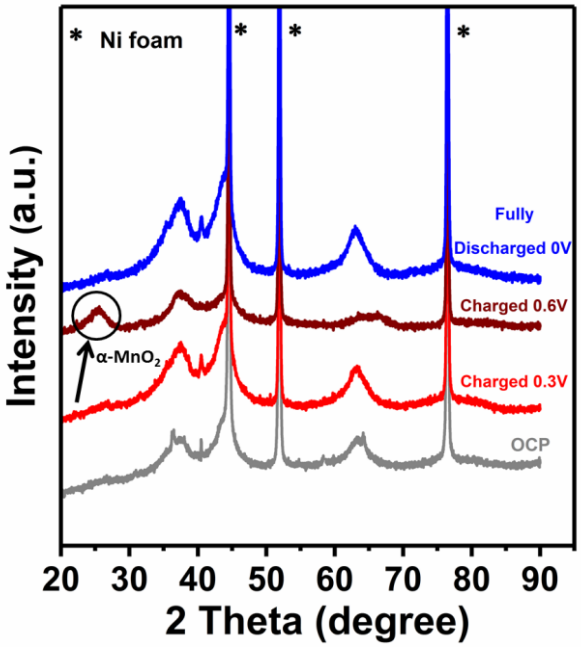

Figure 6.17 Ex-situ X-ray diffraction pattern of NCMO_rGO_14h at different cut off potentials

In order to further probe the superior performance of the NCMO_rGO_14h [75-25] hybrid material in comparison with the NCMO_14h (rock-salt), EIS measurements were conducted. Nyquist plots of the samples are shown in ***Figure 6.18a***. Experimental results were fit by employing an equivalent circuit, shown in the inset. In the fitted model, R_s, R_{ct}, W, and CPE refer to uncompensated resistance, Faradaic charge transfer resistance, Warburg impedance, and constant phase element, respectively.[49] The intercept of the real axis in the high-frequency region corresponds to R_s, mainly attributed to the electrolyte ionic resistance, resulting in ~0.4 Ω·cm^{-2} for both samples. The semicircle at high frequencies indicates the charge transfer resistance (R_{ct}) of

the reaction, and it is significantly smaller in the NCMO_rGO_14h [75-25] sample (2.2 Ω) in comparison with pure NCMO (4.7 Ω), revealing a more facilitated redox reaction in the hybrid sample *(**Figure 6.18b**)*.[50] At low frequencies, Warburg impedance values obtained from fitting of the data for the NCMO_rGO_14h [75-25] hybrid material (21 Ω) are much lower than that of pure NCMO (70 Ω), demonstrating a lower diffusion resistance to electrolyte ions and a higher accessibility of active sites in this hybrid material. These results are in agreement with gas adsorption measurements which showed a large population of mesopores (centered in 4nm) in the hybrid sample (seen in ***Figure 6.7***) in comparison with others. All of these observations further confirm enhanced electrochemical performance of the NCMO_rGO_14h [75-25] sample as a result of hybridization and correct distribution of NCMO nanosheets on conducting graphene layers.

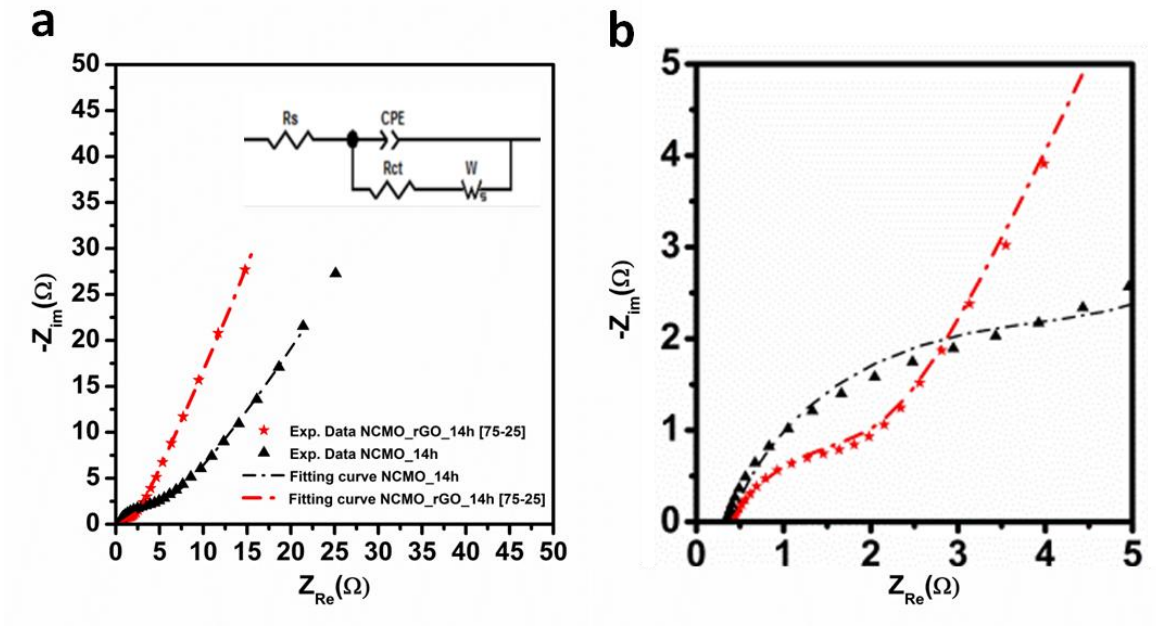

Figure 6.18 (a) Nyquist plots of the NCMO_14h and NCMO_rGO_14h [75-25] samples. Inset shows proposed equivalent circuit by which the experimental results were fitted; (b) the magnified high frequency region

As a summary, ***Table 6.3*** compile corresponding previous reports of mixed transition metal oxides and their hybridizations with graphene, providing an overall overview of their electrochemical performances with respect to our NCMO_rGO_14h [75-25] sample. Interestingly, our NCMO_rGO_14h [75-25] hybrid sample showed superior or comparable areal capacity to that of previously reported mixed metal oxides and hybrid materials. Accordingly, we really believe that

all these results demonstrate the potential application of the synthesized and optimized NCMO_rGO hybrid sample as a positive electrode material for hybrid energy storage devices.

Table 6.3 Comparison of the electrochemical properties of the NCMO_rGO hybrid with some previous reports of mixed transition metal oxides and their possible hybridizations with graphene

Sample	Electrolyte	Synthesis method	Areal Capacity ($mAh \cdot cm^{-2}$)	Discharge Regime	Mass loading ($mg \cdot cm^{-2}$)	Potential window (V)	Ref.
$NiCoMnO_4$ Nanowire	6M KOH	Hydrothermal	0.162	1 $A \cdot g^{-1}$	1.84	0.50	45
$NiCoMnO_4$ Nanoneedles	2M KOH	Hydrothermal	0.112	1 $mA \cdot cm^{-2}$	0.5	0.70	51
$NiCo_2O_4$/Graphene Nanoplatelets	6M KOH	Hydrolysis	0.680	5 $mV \cdot s^{-1}$	10	0.40	7
$NiCo_2O_4$/rGO Nanosheets	6M KOH	Electrostatic Co-precipitation	0.254	1 $A \cdot g^{-1}$	2	0.55	3
MNCO-rGO	6M KOH	Electrostatic Co-precipitation	0.089	1 $A \cdot g^{-1}$	0.5	0.50	52
NCMO_rGO Nanosheets	**3M KOH**	**Hydrothermal**	**0.805 0.784**	**5 $mV \cdot s^{-1}$ 1 $A \cdot g^{-1}$**	**6-8**	**0.6**	**Our work**

6.2.3 rGO//NCMO_rGO Hybrid Energy Storage Device

To really demonstrate the practical application of NCMO_rGO_14h [75-25] in a full cell setup, an aqueous hybrid energy storage device was assembled by integrating two electrodes with different charge storage mechanism: rGO nanosheets as an ideal negative electrode (capacitor-type material) and the NCMO_rGO_14h [75-25] optimized hybrid material as the positive electrode (battery-type material), denoted as rGO NSs//NCMO_rGO following the same strategy already reported in Chapter 5 with $NiMnO_3$-rGO hybrid in the positive. ***Figure 6.19*** shows a schematic representation of the hybrid system.

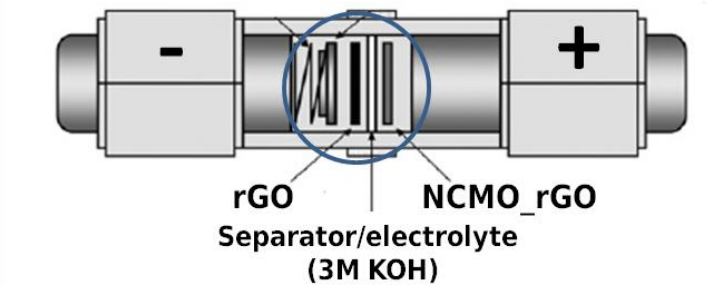

Figure 6.19 Schematic representation of the rGO NSs//NCMO_rGO hybrid device

The mass loading of the positive and negative electrodes was adjusted by the charge balance theory (m^+/m^-) = 0.35**,** according to [Eq. 3.13]. With the purpose of estimating the maximum stable potential window of the hybrid device, the CV curves of rGO and optimized NCMO_rGO sample were recorded at 5mV·s^{-1} in three-electrode configuration (as shown in ***Figure 6.20a***), expanding the operating voltage to 1.6 V (above 1.2 V, the thermodynamic decomposition of water).[53]

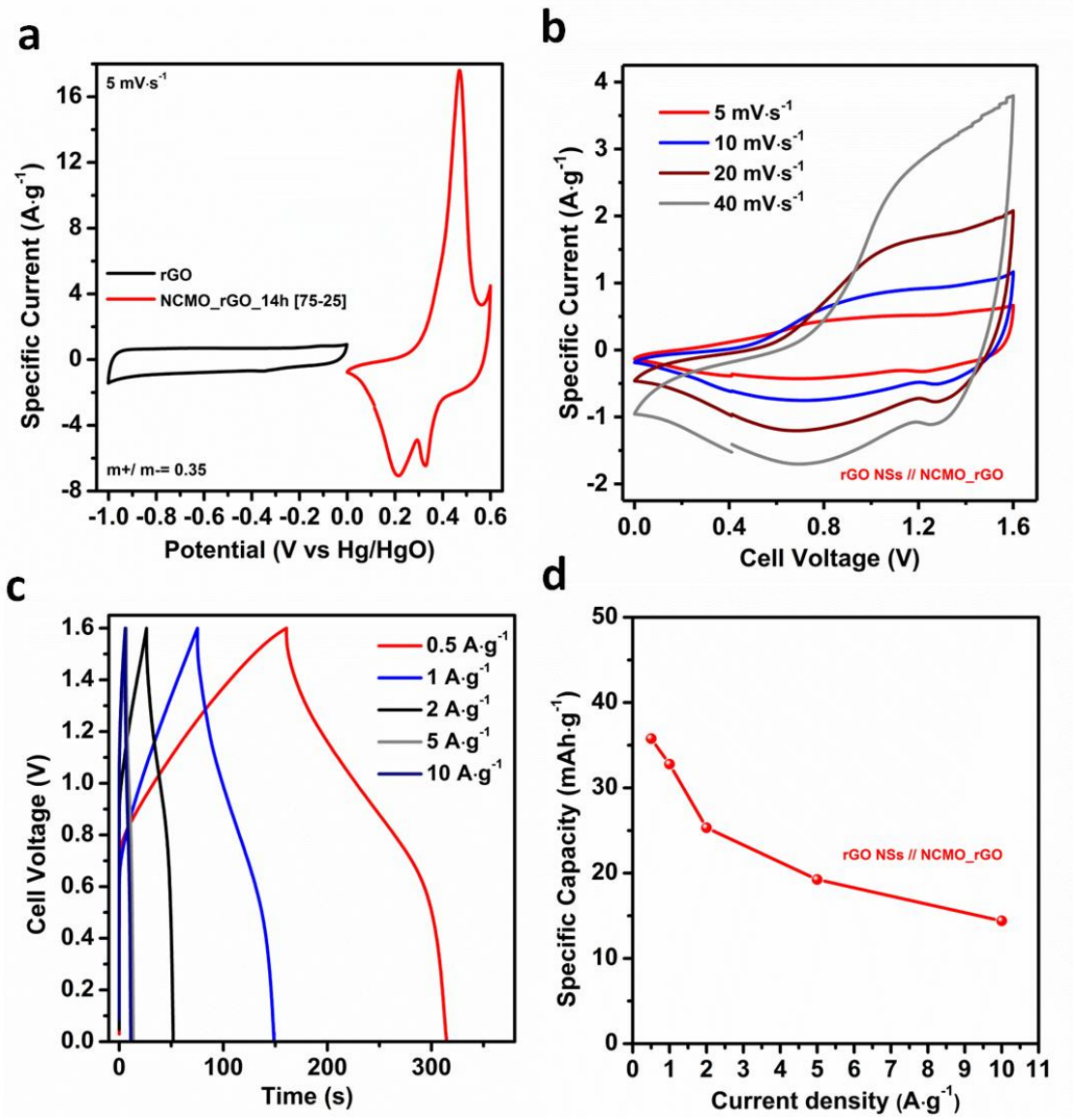

Figure 6.20 (a) CV curves of rGO and NCMO_rGO_14h [75-25] at 5mV·s^{-1} in three-electrode configuration; (b) CV curves of rGO NSs//NCMO_rGO hybrid device at various scan rates (c) GCD curves of the rGO NSs//NCMO_rGO hybrid device at different specific currents; (d) rate capability of the hybrid device at various specific currents

Figure 6.20b show the CV curves of rGO NSs//NCMO_rGO hybrid device at various scan rates ranging from 5 $mV \cdot s^{-1}$ to 40 $mV \cdot s^{-1}$. As can be observed, increasing the scan rate produces no significant changes in shape of the CV profiles, suggesting appropriate rate capability and reversibility. Moreover, these rGO NSs//NCMO_rGO hybrid devices were further examined by conducting GCD measurements at different specific currents ***(Figure 6.20c)***. As can be seen, GCD profiles displayed almost symmetric curves in all specific currents indicating excellent columbic efficiency and reversibility. Furthermore, GCD curves slightly deviate from a linear triangular shape, in agreement with CV signatures and confirming the participation of Faradaic reactions originating from the positive electrode ***(Figure 6.20a).*** Rate capability of the hybrid energy storage device at various specific currents is plotted in ***Figure 6.20d***, achieving a specific capacity of 36 $mAh \cdot g^{-1}$ at 0.5 $A \cdot g^{-1}$ and 43% of capacity retention after a 20-fold increase in current at 10 $A \cdot g^{-1}$.

In order to evaluate the electrochemical performance of any reported energy storage device, specific energy and specific power are two critical parameters. Performance of our hybrid device is compared with previously reported similar devices in a Ragone Plot shown in ***Figure 6.21a***, extracted from GCD profiles in ***Figure 6.20c***. As can be observed, the rGO NSs//NCMO_rGO hybrid device could attain a high specific energy of 27 $Wh \cdot kg^{-1}$ at a specific power of 0.598 $kW \cdot kg^{-1}$ at a specific current of 0.5 $A \cdot g^{-1}$. By increasing the current load to 10 $A \cdot g^{-1}$, a maximum power of 6.714 $kW \cdot kg^{-1}$ at an specific energy of 9.4 $Wh \cdot kg^{-1}$ could be achieved. As can be observed the rGO NSs//NCMO_rGO hybrid device displayed either superior (e.g. AC//$NiCo_2O_4$,[54] rGO//$NiCoMnO_4$ and symmetric rGO-based devices,[25] MEGO//Co_3O_4-MnO_2[55]) or comparable performance (e.g. AC//$NiCo_2O_4$-Au Nanotubes[56] and symmetric $NiMnO_4$-rGO//$NiMnO_4$-rGO[6]) in comparison with previous reports. Also, we should highlighted that we are able to improve the electrochemical performance of our previous rGO NSs//$NiMnO_3$-rGO hybrid device (23.5 $Wh \cdot kg^{-1}$ at 0.5 $A \cdot g^{-1}$ with a specific power of 0.4 $kW \cdot kg^{-1}$) going one step further by playing with the synergistic combination of three dissimilar metal cations and properly balancing the variables ratio oxide/carbon and hydrothermal reaction time in the positive hybrid electrode material. Another critical aspect we have been able to improve with respect to rGO NSs//$NiMnO_3$-rGO is the electrochemical cycling stability of the rGO NSs//NCMO_rGO hybrid device. Therefore, cycling performance of the rGO NSs//NCMO_rGO hybrid device was evaluated using GCD measurements at a specific current of 2 $A \cdot g^{-1}$ over 2000 cycles (***Figure 6.21b***).

Accordingly, outstanding capacity retention of 96% was obtained (80% of the capacity retention with the rGO NSs//$NiMnO_3$-rGO hybrid device) which can be attributed to excellent stability of the hybrid electrode material and the reasons already mentioned above.

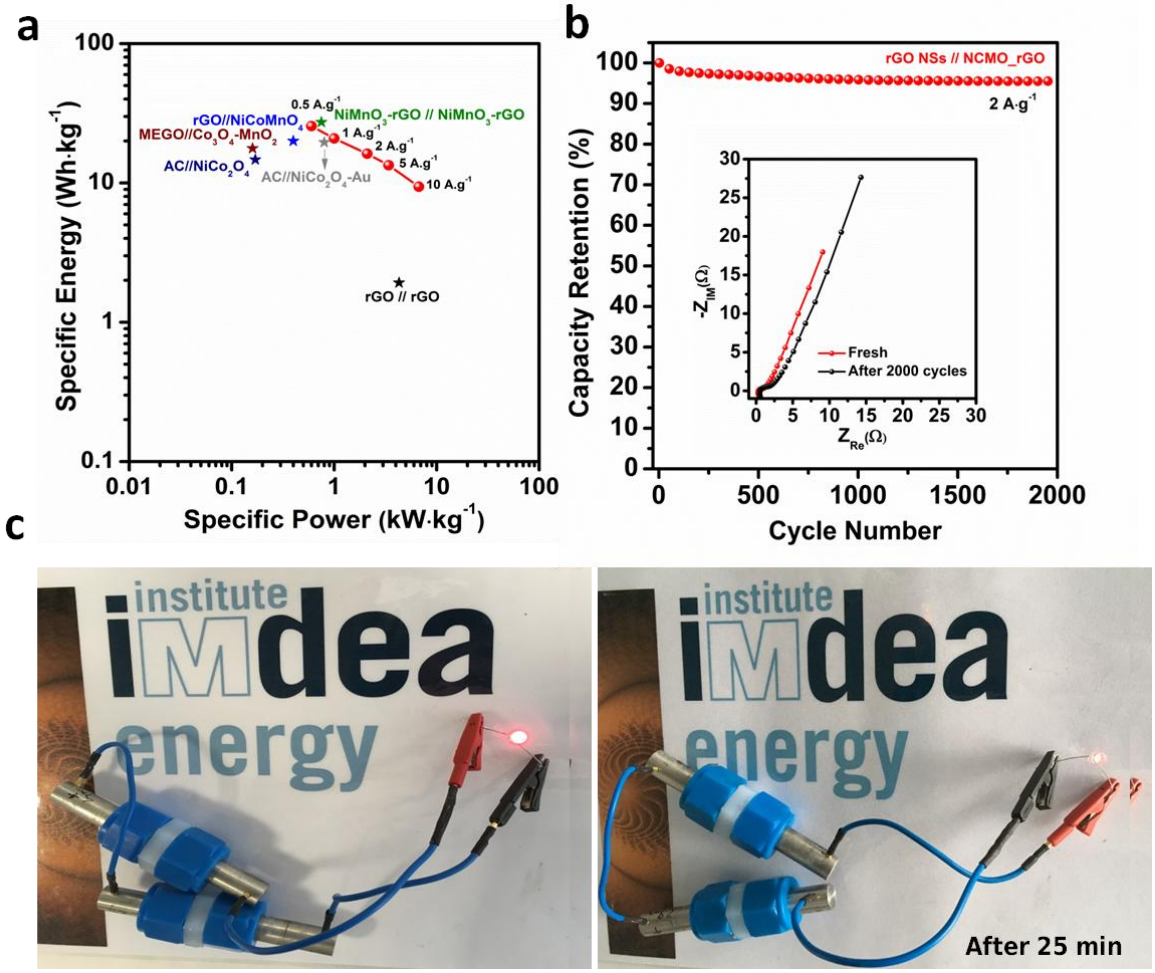

Figure 6.21 (a) Ragone plot of the hybrid energy storage device at various specific currents; (b)Cycling performance of the rGO NSs// NCMO_rGO hybrid device at a specific current of 2 $A \cdot g^{-1}$. Inset shows Nyquist plot of the rGO NSs// NCMO_rGO hybrid device before and after 2000 cycles (c) Photographs of red LED powered on by 2 cells in series before and after 25 min

The inset in ***Figure 6.21b*** provides the Nyquist plots of the hybrid device before and after the cycling revealing insignificant changes in the overall impedance after cycling which further proves the excellent cycling stability of the system. Finally, in order to probe the viability of rGO

NSs//NCMO_rGO system for practical applications, 2 cells were connected in series and employed for powering a red LED, as shown in ***Figure 6.21c***. LED could be kept powered for around 25 min.

To provide further details, ***Table 6.4*** summarizes a comparison of the device performance of rGO NSs//NCMO_rGO with some recent reported hybrid devices. Having into account the mass loading of the electrodes, it can be observed that the performance of our rGO NSs//NCMO_rGO hybrid device is superior or comparable in all the cases, revealing the promise of this NCMO_rGO hybrid material as a positive electrode material for high-performance hybrid energy storage devices.

Table 6.4 Comparison of the device performance of NCMO-rGO//rGO NSs hybrid energy storage cell with some reports on graphene-based hybrid energy storage devices

Hybrid Device	Electrolyte	Mass loading ($mg \cdot cm^{-2}$)	Specific Capacity ($mAh \cdot g^{-1}$)	Capacity Retention	Potential window (V)	Specific Energy ($Wh \cdot Kg^{-1}$)	Specific Power ($kW \cdot Kg^{-1}$)	Ref.
$NiCoMnO_4$ NPs// rGO NSs	3M KOH	4.7-10.6	27.49 (0.5 $A \cdot g^{-1}$) 18.74 (5 $mV \cdot s^{-1}$)	87% (2000 cycles 2 $A \cdot g^{-1}$)	1.5	20 0.5 $A \cdot g^{-1}$	0.377 at 0.5 $A \cdot g^{-1}$	[25] (2016)
$NiCo_2O_4$// Activated Carbon	6M KOH	4	21.29 (0.5 $A \cdot g^{-1}$) 19.72 (5 $mV \cdot s^{-1}$)	85% (2000 cycles 1.5 $A \cdot g^{-1}$)	1.4	14.7 0.5 $A \cdot g^{-1}$	0.175 0.5 $A \cdot g^{-1}$ 0.249 1 $A \cdot g^{-1}$	[54] (2013)
$NiCo_2O_4$-Au// Activated Carbon	2M KOH	1.7	22.15 (1 $A \cdot g^{-1}$)	81% (2000 cycles 2 $A \cdot g^{-1}$)	1.45	19.6 1 $A \cdot g^{-1}$	0.782 at 1 $A \cdot g^{-1}$	[56] (2014)
$NiCo_2O_4$–rGO// Activated carbon	2M KOH	2.5	35.88 (0.5 $A \cdot g^{-1}$)	85% (2000 cycles 2 $A \cdot g^{-1}$)	1.3	23.3 0.5 $A \cdot g^{-1}$	0.325 at 0.5 $A \cdot g^{-1}$	[57] (2012)
$NiCo_2O_4$@MnO_2// Activated Graphene	3M KOH	1.1-2	34.70 (0.5 $A \cdot g^{-1}$)	-	1.6	27.8 0.5 $A \cdot g^{-1}$	0.400 at 0.5 $A \cdot g^{-1}$	[58] (2017)
Ni-P@$NiCo_2O_4$// Activated Carbon	6M KOH	4	27.60 (10 $mV \cdot s^{-1}$)	78% (10000 cycles 4 $A \cdot g^{-1}$)	1.4	21 1 $A \cdot g^{-1}$	0.350 at 1 $A \cdot g^{-1}$	[59] (2016)
$NiCo_2O_4$-Nanoporous Carbon//Nanoporous Carbon	1M KOH	1	32.07 (0.5 $A \cdot g^{-1}$)	85%(2000 cycles 40 $mV \cdot s^{-1}$)	1.5	24 0.5 $A \cdot g^{-1}$	0.700 at 0.5 $A \cdot g^{-1}$	[60] (2017)
NCMO_rGO //rGO NSs	**3M KOH**	**8-10**	**35.55 (0.5 $A \cdot g^{-1}$) 39.10 (5 $mV \cdot s^{-1}$)**	**96% (2000 cycles at 2 $A \cdot g^{-1}$)**	**1.6**	**27 0.5 $A \cdot g^{-1}$ 20.9 1 $A \cdot g^{-1}$**	**0.6 0.5 $A \cdot g^{-1}$ 1.015 1 $A \cdot g^{-1}$**	**Our work**

6.3 Conclusions

Summarizing, in the present Chapter NCMO_rGO hybrid materials with different reaction conditions were prepared via facile hydrothermal method followed by a thermal treatment. The effect of the synthetic conditions (variation of the hydrothermal reaction time) on the crystallographic nature of the obtained samples (i.e. spinel or rocksalt) was probed operating at low temperatures. Subsequently, the influence of prolonging hydrothermal reaction time and the observed changes in mixed metal oxide phase were evaluated and examined on the electrochemical signal of the samples. All NCMO_rGO hybrid materials showed better initial capacity and rate capability than pure NCMO due to synergistic effects between the strongly coupled porous oxide nanosheets and reduced graphene oxide layers, as we could corroborate with the higher S_{BET} of the hybrids with respect to their pure components. Moreover, the hydrothermal reaction time drastically influenced the microstructure of NCMO grown on rGO layers, as we could observe with the TEM images. Therefore, by properly balancing the variables ratio oxide/carbon and hydrothermal reaction time, the best performance (Q=115 $mAh \cdot g^{-1}$) was achieved at a reaction time of 14 h and with 25% of graphene content. According to the obtained results, hybridizing NCMO NSs with rGO NSs could remarkably enhance the performance of ilmenite $NiMnO_3$-rGO hybrid electrodes (91 $mAh \cdot g^{-1}$) in previous Chapter 5, working under similar conditions; same electrolyte and voltage window. Moreover, highly mass loaded electrodes were employed as positive electrode to assemble an aqueous hybrid energy storage device, integrated with rGO negative electrodes revealing a maximum specific energy of 27 $Wh \cdot kg^{-1}$ and a maximum specific power of 6.7 $kW \cdot kg^{-1}$ with an excellent long-term cycling stability of 96% over 2000 cycles. In this aspect, rGO NSs//NCMO_rGO hybrid energy storage device also outperformed rGO NSs//$NiMnO_3$-rGO hybrid device in Chapter 5 which presented a maximum specific energy of 23.5 $Wh \cdot kg^{-1}$ and a maximum specific power of 7.64 $kW \cdot kg^{-1}$ showing an 80% of the capacity retention in the same number of cycles.

6. Porous NiCoMn Ternary Metal Oxide/Graphene as Positive Electrode Materials for Hybrid Energy Storage Devices

Contents lists available at ScienceDirect

Electrochimica Acta

journal homepage: www.elsevier.com/locate/electacta

Porous NiCoMn ternary metal oxide/graphene nanocomposites for high performance hybrid energy storage devices

Jaime S. Sanchez [a], Afshin Pendashteh [a, *], Jesus Palma [a], Marc Anderson [a, b], Rebeca Marcilla [a, **]

[a] Electrochemical Processes Unit, IMDEA Energy Institute, Avda. Ramon de la Sagra 3, Parque Tecnológico de Móstoles, 28935, Móstoles, Spain
[b] Department of Civil and Environmental Engineering, University of Wisconsin, Madison, USA

ARTICLE INFO

Article history:
Received 16 October 2017
Received in revised form
7 May 2018
Accepted 10 May 2018
Available online 12 May 2018

Keywords:
NiCoMn ternary metal oxide
Hybrid material
Graphene
Hybrid device

ABSTRACT

Mixed transition metal oxides have attracted great attention due to their improved properties over simple oxides in energy storage applications. Herein, we report facile hydrothermal synthesis of novel porous NiCoMn ternary metal oxide flakes with reduced graphene oxide (NCMO_rGO) and their application in high performance aqueous-based energy storage devices. The effect of reaction time on composition and morphology was studied by X-ray diffraction, Raman spectroscopy, thermal gravimetric analysis, transmission electron microscopy, and N_2 ad/de-sorption measurements. Accordingly, a high specific surface area of 200 $m^2 g^{-1}$ was achieved for the optimized sample. The sample was electrochemically investigated by cyclic voltammetry, galvanostatic charge/discharge and electrochemical impedance spectroscopy. Porous NCMO_rGO hybrid exhibited a high capacity of 115 $mAh \cdot g^{-1}$ at 1 $A g^{-1}$. Subsequent integration of the hybrid material as a positive electrode with rGO negative electrodes resulted in asymmetric aqueous devices having a specific energy as high as 27 $Wh \cdot kg^{-1}$. Moreover, this NCMO_rGO//rGO hybrid device showed an excellent cycling stability of 96% over 2000 cycles. This work not only reports for the first time the rational design and fabrication of porous NCMO_rGO nanoflakes as high performance electrodes for energy storage but also paves the path towards facile synthesis of mixed metal oxide nanocomposites for other applications.

© 2018 Elsevier Ltd. All rights reserved.

6.4 References

1 R. Raccichini, A. Varzi, S. Passerini and B. Scrosati, *Nat. Mater.*, 2014, **14**, 271–279.

2 M. F. El-kady, Y. Shao and R. B. Kaner, *Nat. Rev.*, 2016, **1**, 1–14.

3 H.-W. Wang, Z.-A. Hu, Y.-Q. Chang, Y.-L. Chen, H.-Y. Wu, Z.-Y. Zhang and Y.-Y. Yang, *J. Mater. Chem*, 2011, **21**, 10504–10511.

4 Z. Song, Y. Zhang, W. Liu, S. Zhang, G. Liu, H. Chen and J. Qiu, *Electrochim. Acta*, 2013, **112**, 120–126.

5 J. Chen, Y. Cui, X. Wang, M. Zhi, M. Lavorgna, A. P. Baker and J. Wu, *Electrochim. Acta*, 2016, **188**, 704–709.

6 P. Kakvand, M. S. Rahmanifar, M. F. El-kady, A. Pendashteh, M. A. Kiani, H. Masumeh, M. Najafi, A. Abbasi, M. F. Mousavi and R. B. Kaner, *Nanotechnology*, 2016, **27**, 315401–315413.

7 H. Wang, C. M. B. Holt, Z. Li, X. Tan, B. S. Amirkhiz, Z. Xu, B. C. Olsen, T. Stephenson and D. Mitlin, *Nano Res.*, 2012, **5**, 605–617.

8 G. He, L. Wang, H. Chen, X. Sun and X. Wang, *Mater. Lett.*, 2013, **98**, 164–167.

9 L. Ma, X. Shen, Z. Ji, X. Cai, G. Zhu and K. Chen, *J. Colloid Interface Sci.*, 2015, **440**, 211–218.

10 Y. Xu, L. Wang, P. Cao, C. Cai, Y. Fu and X. Ma, *J. Power Sources*, 2016, **306**, 742–752.

11 L. Wang, B. Chen, J. Ma, G. Cui and L. Chen, *Chem. Soc. Rev.*, 2018, **47**, 6505–6602.

12 Z. Tian, H. Yu, Z. Zhang and X. Xu, *ChemBioEng Rev.*, 2018, **5**, 111–118.

13 V. A. Online, M. Peyvandipoor and A. Asghari, *RSC Adv.*, 2015, **5**, 76458–76463.

14 H. J. Qiu, L. Liu, Y. P. Mu, H. J. Zhang and Y. Wang, *Nano Res.*, 2015, **8**, 321–339.

15 C. Yuan, J. Li, L. Hou, X. Zhang, L. Shen and X. W. Lou, *Adv. Funct. Mater.*, 2012, **22**, 4592–4597.

16 A. Pendashteh, S. E. Moosavifard, M. S. Rahmanifar, Y. Wang, M. F. El-kady, R. B. Kaner and M. F. Mousavi, *Chem. Mater*, 2015, **27**, 3919−3926.

17 A. Pendashteh, J. Palma, M. Anderson and R. Marcilla, *J. Mater. Chem. A*, 2015, **3**, 16849–16859.

18 S. Ratha and C. S. Rout, *RSC Adv.*, 2015, **5**, 86551–86557.

19 S. Sahoo, K. K. Naik and C. S. Rout, *Nanotechnology*, 2015, **26**, 455401–455409.

20 K. K. Naik, S. Sahoo and C. S. Rout, *Microporous Mesoporous Mater.*, 2017, **244**, 226–234.

21 R. Mondal, S. Sahoo and C. S. Rout, *Am. J. Eng. Appl. Sci.*, 2016, **9**, 540–546.

22 Y. Zhu, Z. Wu, M. Jing, H. Hou, Y. Yang, Y. Zhang, X. Yang, W. Song, X. Jia and X. Ji, *J. Mater. Chem. A*, 2015, **3**, 866–877.

23 K. Zhang, W. Zeng, G. Zhang, S. Hou, F. Wang, T. Wang and H. Duan, *RSC Adv.*, 2015, **5**, 69636–69641.

24 X. Liu, S. Shi, Q. Xiong, L. Li, Y. Zhang, H. Tang, C. Gu, X. Wang and J. Tu, *ACS Appl. Mater. Interfaces*, 2013, **5**, 8790–8795.

25 A. Pendashteh, J. Palma, M. Anderson and R. Marcilla, *RSC Adv.*, 2016, **6**, 28970–28980.

26 Z. Gao, W. Yang, J. Wang, N. Song and X. Li, *Nano Energy*, 2015, **13**, 306–317.

27 X. Qi, L. Chen, C. Zhang, X. Xu, Y. Zhang, Y. Bai and H. Liu, *ACS Appl. Mater. Interfaces*, 2016, **8**, 18675–18683.

28 B. Das, M. V Reddy and B. V. R. Chowdari, *Nanoscale*, 2013, **5**, 1961–1966.

29 X. Yu, E. Hu, S. Bak, Y.-N. Zhou and X.-Q. Yang, *Chinese Phys. B*, 2016, **25**, 018205–018215.

30 M. Guilmard, L. Croguennec and C. Delmas, *Chem. Mater.*, 2003, **15**, 4484–4493.

31 D. Gu, C.-J. Jia, C. Weidenthaler, H.-J. Bongard, B. Spliethoff, W. Schmidt and F. Schüth, *J. Am. Chem. Soc.*, 2015, **137**, 11407–11418.

32 M. A. Langell, J. G. Kim, D. L. Pugmire and W. McCarroll, *J. Vac. Sci. Technol. A*, 2001, **19**, 1977–1982.

33 S. C. Petitto, E. M. Marsh, G. A. Carson and M. A. Langell, *J. Mol. Catal. A Chem.*, 2008, **281**, 49–58.

34 B. P. Uberuaga, M. Tang, C. Jiang, J. A. Valdez, R. Smith, Y. Wang and K. E. Sickafus, *Nat. Commun.*, 2015, **6**, 8750–8758.

35 A. Pendashteh, J. Palma, M. Anderson and R. Marcilla, *Appl. Catal. B Environ.*, 2017, **201**, 241–252.

36 D. Li, Y. Gong, Y. Zhang, C. Luo, W. Li, Q. Fu and C. Pan, *Sci. Rep.*, 2015, **5**, 12903–12911.

37 M. C. Biesinger, B. P. Payne, L. W. M. Lau, A. Gerson and R. S. C. Smart, *Surf. Interface Anal.*, 2009, **41**, 324–332.

38 J.-G. Kim, D. L. Pugmire, D. Battaglia and M. A. Langell, *Appl. Surf. Sci.*, 2000, **165**, 70–84.

39 K. Li, X. Luo, X. Lin, F. Qi and P. Wu, *J. Mol. Catal. A Chem.*, 2014, **383**–**384**, 1–9.

40 N. V. Kosova, E. T. Devyatkina and V. V. Kaichev, *J. Power Sources*, 2007, **174**, 735–740.

41 Z. Wu, W. Ren, L. Wen, L. Gao, J. Zhao, Z. Chen, G. Zhou, F. Li and H. Cheng, *ACS Nano*, 2010, **4**, 3187–3194.

42 S. Jerng, D. S. Yu, J. H. Lee, C. Kim, S. Yoon and S. Chun, *Nanoscale Res. Lett.*, 2011, **6**, 565–571.

43 G. Zhang and X. W. David Lou, *Sci. Rep.*, 2013, **3**, 1470–1476.

44 C. Yuan, L. Zhang, L. Hou, G. Pang and X. Zhang, *Part. Part. Syst. Charact.*, 2014, **31**, 778–787.

45 L. Li, Y. Zhang, F. Shi, Y. Zhang, J. Zhang, C. Gu, X. Wang and J. Tu, *ACS Appl. Mater. Interfaces*, 2014, **6**, 18040–18047.

46 M. Yu, J. Chen, J. Liu, S. Li, Y. Ma, J. Zhang and J. An, *Electrochim. Acta*, 2015, **151**, 99–108.

47 A. N. N. S. Selladurai, *RSC Adv.*, 2015, **5**, 65139–65152.

48 W. Shi, J. Zhu, D. H. Sim, Y. Y. Tay, Z. Lu, X. Zhang, Y. Sharma, M. Srinivasan, H. Zhang, H. H. Hng and Q. Yan, *J. Mater. Chem.*, 2011, **21**, 3422–3427.

49 G. J. Brug, A. L. G. van den Eeden, M. Sluyters-Rehbach and J. H. Sluyters, *J. Electroanal. Chem. Interfacial Electrochem.*, 1984, **176**, 275–295.

50 R. B. Rakhi, W. Chen, D. Cha and H. N. Alshareef, *Nano Lett.*, 2012, **12**, 2559–2567.

51 G. Xiong, P. He, L. Liu, T. Chen and T. S. Fisher, *Front. Energy Res.*, 2015, **3**, 1–9.

52 C. Wu, J. Cai, Y. Zhu and K. Zhang, *Appl. Mater. Interfaces*, 2017, **9**, 19114–19123.

53 S. E. Moosavifard, M. F. El-Kady, M. S. Rahmanifar, R. B. Kaner and M. F. Mousavi, *ACS Appl. Mater. Interfaces*, 2015, **7**, 4851–4860.

54 R. Ding, L. Qi, M. Jia and H. Wang, *Electrochim. Acta*, 2013, **107**, 494–502.

55 M. Huang, Y. Zhang, F. Li, L. Zhang, Z. Wen and Q. Liu, *J. Power Sources*, 2014, **252**, 98–106.

56 J. Zhu, Z. Xu and B. Lu, *Nano Energy*, 2014, **7**, 114–123.

57 X. Wang, W. S. Liu, X. Lu and P. S. Lee, *J. Mater. Chem*, 2012, **22**, 23114–23119.

58 H. Chen, C. Hsieh, Y. Yang and X. Y. Liu, *ChemElectroChem*, 2017, **4**, 2414–2422.

59 X. Li, R. Ding, L. Yi, W. Shi, Q. Xu and E. Liu, *Electrochim. Acta*, 2016, **222**, 1169–1175.

60 C. Young, R. Salunkhe, S. M. Alshehri, T. Ahamad, Z. Huang, J. Henzie and Y. Yamauchi, *J. Mater. Chem. A*, 2017, **5**, 11834–11839.

CHAPTER 7

Co_3O_4 Nanorods Anchored on N-rGO:An Efficient Bifunctional Electrocatalyst for Rechargeable Zn-Air Batteries

7.1 Research Background

Rechargeable Zn-air batteries are considered as one of the promising energy storage alternatives due to their high theoretical energy density (1084 $Wh \cdot kg^{-1}$), low cost and safety.[1,2] However, the sluggish kinetics of oxygen reduction (ORR) and evolution (OER) reactions, as well as their limited stability in harsh alkaline electrolytes are often the main bottleneck of their widespread application.[3,4] For the success in commercialization of such systems, it is also crucial to replace noble metal catalysts such as RuO_2, IrO_2, and Pt with high-performance but inexpensive bifunctional catalysts.[5–9] To address these drawbacks, extensive effort has been made to develop novel active and stable bifunctional electrocatalysts. Accordingly, a wide range of nonprecious metallic alternatives, including transition-metal carbides/nitrides,[10] oxides/hydroxides[11] and sulfides/hydroxisulfides[12,13] have been investigated as bifunctional electrocatalysts for both ORR and OER. Among them, transition metal oxides, specially spinel Co_3O_4, have attracted great attention due to their promising catalytic activity.[14–18] However, the poor electrical conductivity and typical agglomerations in such oxides over cycling restrict their activity for practical applications.

As demonstrated in previous chapters, an effective strategy to mitigate particle agglomeration and improve electronic conductivity of metal oxides is their hybridization with highly conductive reduced graphene oxide. In this regard, impressive effort has been made to improve the catalytic properties of Co_3O_4 catalysts by its coupling with carbonaceous samples. For instance, Dai´s group reported synthesis of Co_3O_4 nanocrystals grown on rGO layers as an excellent synergistic catalyst but only for ORR.[19] Additionally, it was proved that doping porous carbon materials (e.g. graphene or CNT) with heteroatoms like nitrogen can generate effective active sites and further enhance the catalytic activity of the material.[20–25] In this regard, Wang´s group hydrothermally synthesized Co_3O_4 Nanoparticles on Biomass-Derived Nitrogen-Doped Hierarchically Porous Carbon Networks as an efficient bifunctional electrocatalyst for ORR and OER showing the application of Co_3O_4/NHPC as a cathode material in primary Zn−air battery demonstrating a specific capacity of 795 $mAh \cdot g_{Zn}^{-1}$ (at 2 $mA \cdot cm^{-2}$), and a peak power density of 80 $mW \cdot cm^{-2}$. Moreover, the strong coupling between transition metal oxides and N-doped graphene at the interface can normally induce a so-called synergistic effect in the final hybrid material, resulting in substantially enhanced oxygen electrochemistry compared to their counterparts without doped nitrogen.[26,27] It is well-

known that morphology of the oxide, its particle size and its electronic contact with the support material play a crucial role in the performance of the hybrid electrocatalyst. Accordingly, several Co_3O_4 nanostructures (e.g. nanoparticles, nanowires, core shell, etc.) have been investigated in literature as electrocatalysts either for ORR or OER.[28,29] However, the development of Co_3O_4 hybrids with bifunctional catalytic activity towards both ORR and OER with a $\Delta E < 0.80$ V (ΔE = ORR half-wave overpotential - OER overpotential) and at a competitive cost, has not be yet accomplished.

In this Chapter, a facile, scalable and low-cost electrostatic coagulation method (similarly used in Chapter 4) is reported to hybridize hierarchical spinel Co_3O_4 nanorods (NRs) with N-rGO. A rational design of the nanohybrid material was carried out by tuning Co^{2+}/Co^{3+} ratio of the Co_3O_4 NRs and its loading in the hybrid composition. The optimized hybrid (N-rGO/Co_3O_4 NRs) will be evaluated as bifunctional electrocatalyst (ORR/OER). Finally, the N-rGO/Co_3O_4 NRs hybrid will be used as air-cathode for rechargeable Zn-air batteries and stood out among the most efficient bifunctional Co_3O_4-based catalysts reported to date.

7.2 Results and Discussion

7.2.1 Synthesis and Physico-Chemical Characterization of Co_3O_4 NRs

Co_3O_4 nanorods (NRs) were synthesized by the group of Dr. Vinodkumar Etacheri at IMDEA Materials via a facile hydrothermal method (150°C for 6h) followed by a calcination step (10 °C·min^{-1} for 2h), as illustrated in ***Figure 7.1***. Three different samples were prepared by modifying the temperature of the calcination step (400, 500 or 600 °C).

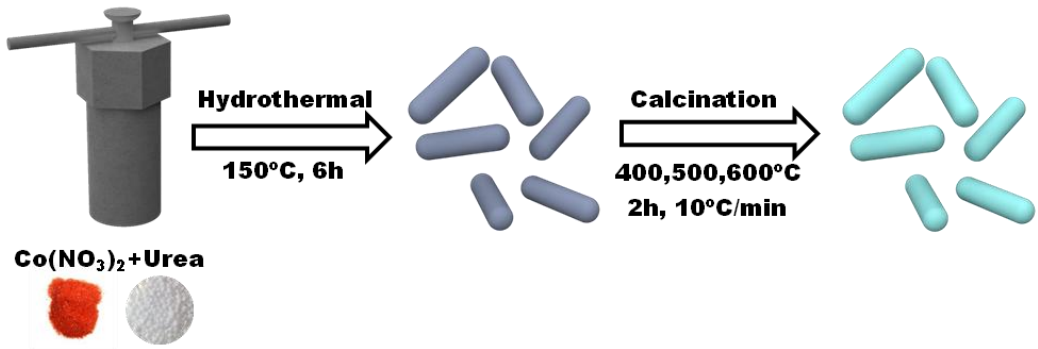

Figure 7.1 Schematic illustration of the synthesis procedure for Co_3O_4 NRs

In the following sections, the hybridization with N-rGO will be complete, although before going to that step, we will evaluate the physico-chemical and electrocatalytic performance of the three different oxides synthesized to determine which one is the most promising Co_3O_4 NRs to be hybridized with N-doped graphene. The crystalline structure and phase purity of Co_3O_4 NRs synthesized at different calcination temperatures was examined by powder X-ray diffraction (XRD) (***Figure 7.2a***).

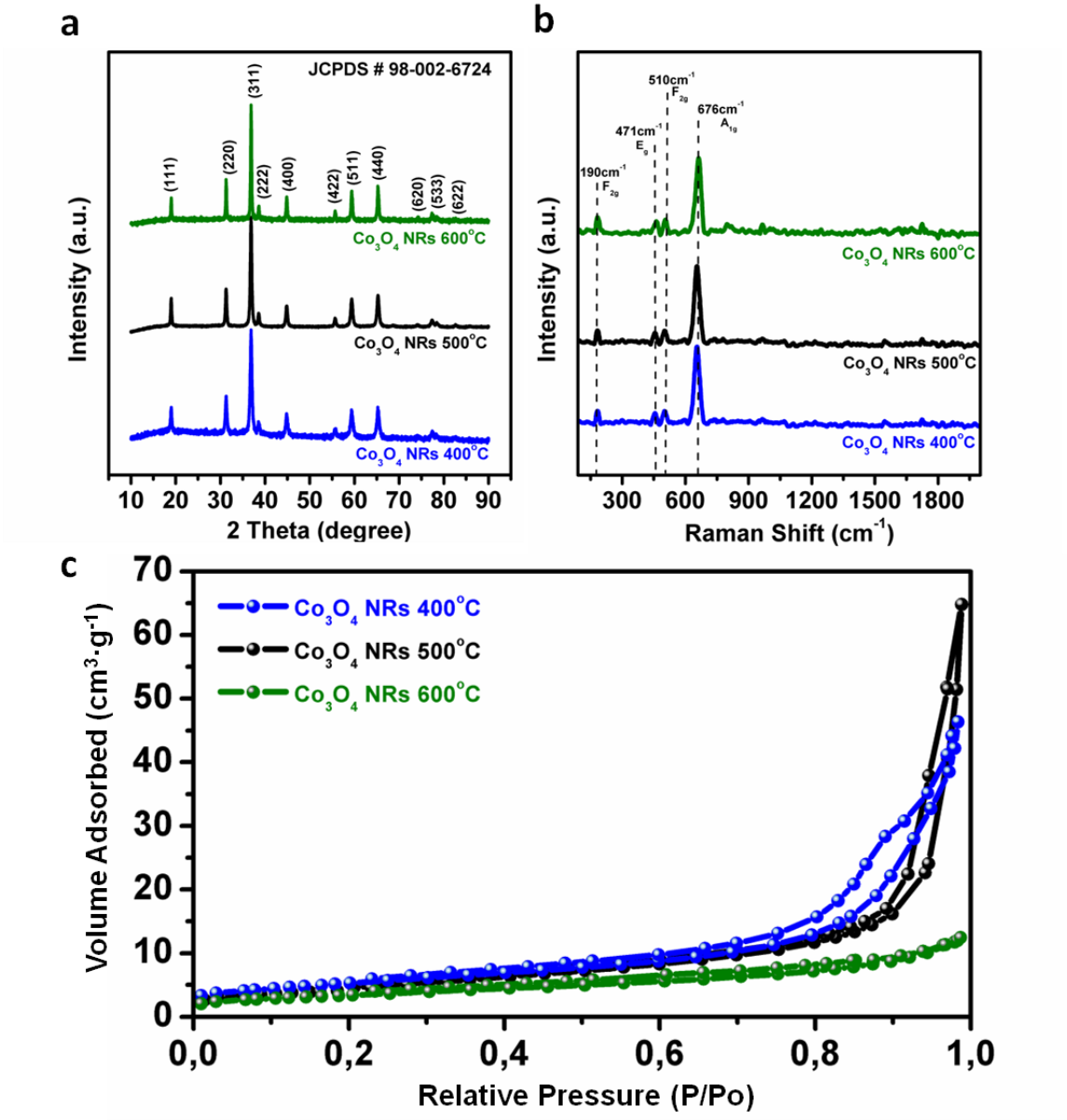

Figure 7.2 (a) X-ray diffraction patterns (b) Raman spectra and (c) N_2 adsorption-desorption isotherms of Co_3O_4 NRs heat treated at different temperatures

All diffraction peaks can be ascribed to spinel Co_3O_4 with a space group of Fd-3m (JCPDS card no. 98-002-6724), in good agreement with previous reports.[30,31] Lack of additional peaks implied the high purity of the oxides crystallized at different calcination temperatures. Phase purity of the cobalt oxide samples was further probed through Raman spectroscopy (***Figure 7.2b***). The appearance of only characteristic F_{2g}, E_g and A_{1g} vibrational modes of spinel Co_3O_4 in all of the samples suggests the absences of any other crystalline or non-crystalline phase.[3,22,24] N_2 adsorption-desorption measurements (***Figure 7.2c***) were also conducted to obtain textural properties of the samples. As it is seen, Co_3O_4 NRs displayed different hysteresis loops with combined features of isotherms type II and type IV, suggesting the presence of macro-pores or interparticle voids, resulted in ascending adsorption branches. Accordingly, a specific BET surface area of 19.1, 16.2, and 12.2 $m^2 \cdot g^{-1}$ was obtained for Co_3O_4 NRs calcined at 400, 500 and 600°C, respectively.

The morphological aspects of the samples calcined at various temperatures were featured by transmission electron microscopy (TEM). TEM images confirmed the hierarchical structure of the NRs, where each NR is composed of numerous nanoparticles. Co_3O_4 NRs calcined at different temperatures showed no significant difference in the morphology (***Figure 7.3***). However, average grain size of the NRs slightly increased with the elevation of calcination temperature.[32] Obtained hierarchical morphology resulted in the formation of reactive interfaces between the individual Co_3O_4 nanoparticles, which might be beneficial for achieving superior catalytic performances.

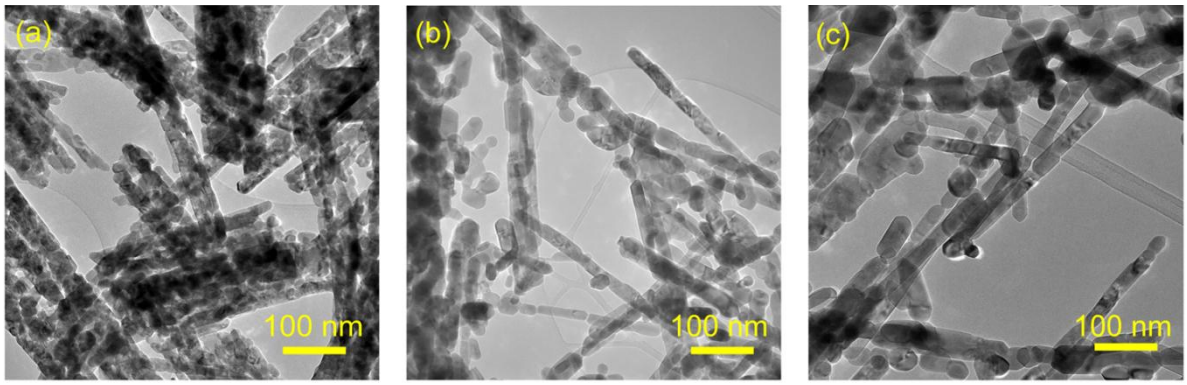

Figure 7.3 TEM images of Co_3O_4 NRs heat-treated at (a) 400°C, (b) 500°C and (c) 600°C

X-ray photoelectron spectroscopy (XPS) was further performed to characterize the surface chemical composition of Co_3O_4 NRs synthesized at various temperatures. The high-resolution Co

2p spectrum of all samples displayed two major peaks at 780.8 and 795.8 eV, ascribed to Co $2p_{3/2}$ and Co $2p_{1/2}$ spin-orbits, respectively (***Figure 7.4***). An approximate energy gap of 15 eV suggests the coexistence of Co^{2+} to Co^{3+} species in all the samples.[33,34] Deconvolution of Co $2p_{3/2}$ envelop reveals that the Co^{3+} is predominant specimen in all of the samples, while the sample calcined at 500°C exhibited the highest Co^{3+}/Co^{2+} ratio (3.81, in comparison with 1.83 and 3.02 for the samples calcined at 400 and 600°C, respectively). This is of great importance as the Co^{3+} are considered to be highly active for H_2O adsorption, and consequently for oxygen electrocatalytic activity.[34,35]

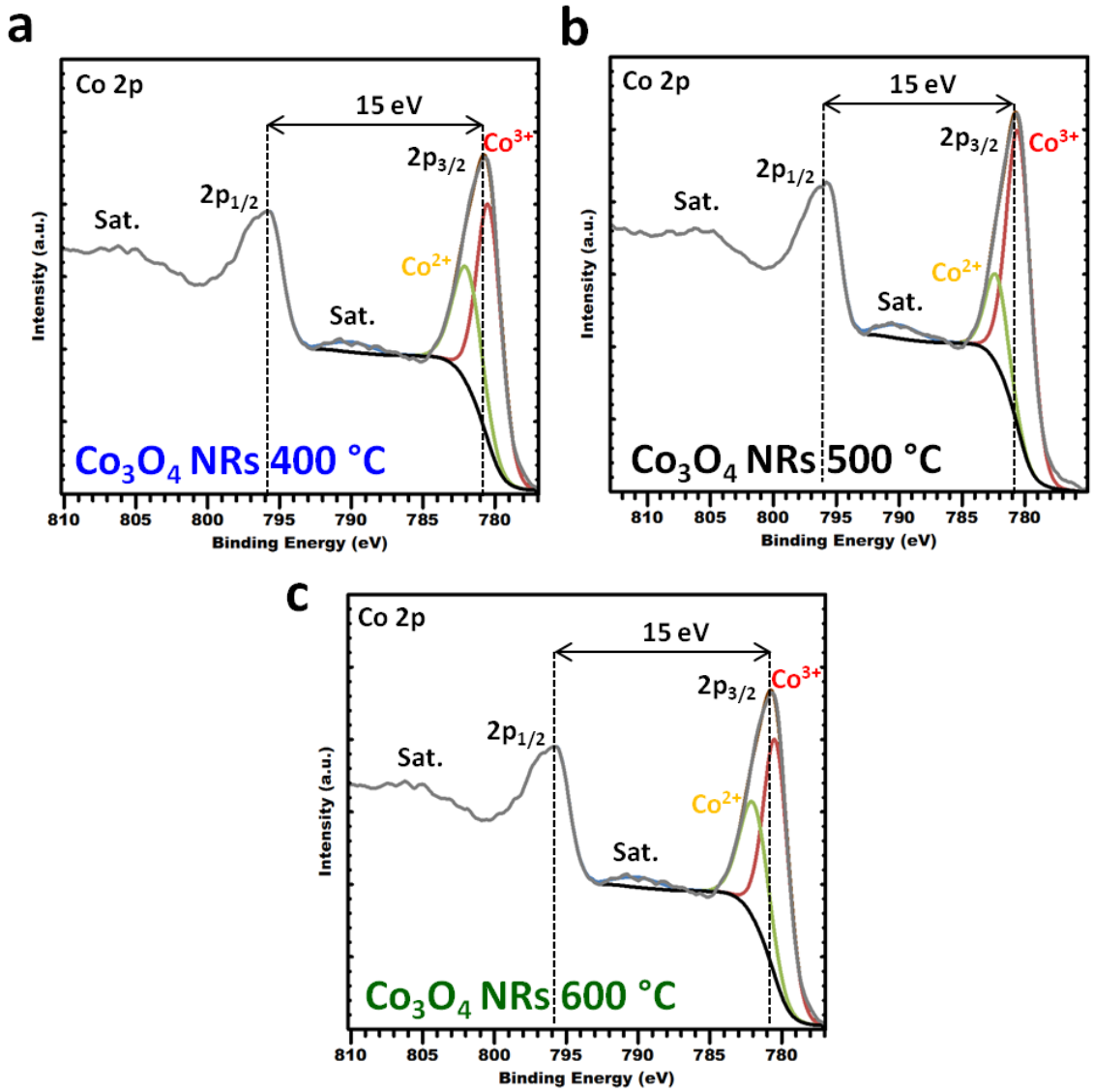

Figure 7.4 XPS profiles of Co_3O_4 NRs samples heat-treated at (a) 400°C, (b) 500°C and (c) 600°C

7.2.2 Evaluation of electrocatalytic activity of Co_3O_4 NRs

Electrocatalytic performance of the cobalt oxides calcined at various temperatures was examined to identify the most promising material for hybridization with N-rGO. ***Figure 7.5*** displays the ORR linear sweep voltammetry (LSV) curves of the samples collected at 1500 rpm in O_2-saturated 0.1 M KOH solution.

Co_3O_4 NRs synthesized at 600°C exhibited a mediocre ORR catalytic activity with an oxygen reduction onset potential of 0.75 V and a poor limiting current density (J_{Levich}=2.93 mA·cm^{-2}). On the other hand, it is observed in ***Figure 7.5*** that the oxide calcined at 500°C clearly unveils a better catalytic performance than 400 and 600°C oxide counterparts with an onset of 0.88 V and a limiting current density of 3.74 mA·cm^{-2}.

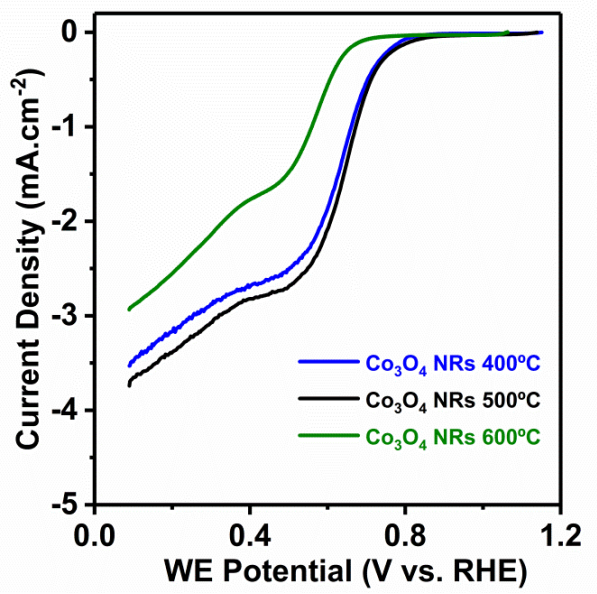

Figure 7.5 Evaluation of ORR catalytic activity of Co_3O_4 NRs 400 °C, Co_3O_4 NRs 500 °C and Co_3O_4 NRs 600 °C mixed with Vulcan Carbon through LSV curves in O_2-saturated 0.1 M KOH solution at a scan rate of 20 mV·s^{-1}

The ORR kinetics and the number of electrons exchange during the oxygen reduction were analyzed by collecting the polarization curves at various rotating rates, as seen in ***Figure 7.6.*** Koutecky-Levich theory (K-L plots) was employed to calculate the number of transferred electrons per oxygen molecule (n) during ORR, and the results were obtained as 3.51, 3.75 and 2.52, for Co_3O_4 NRs calcined at 400, 500 and 600°C, respectively ***(Figure 7.6d-f),*** revealing a superior number of electrons transferred for the oxide calcined at 500°C.

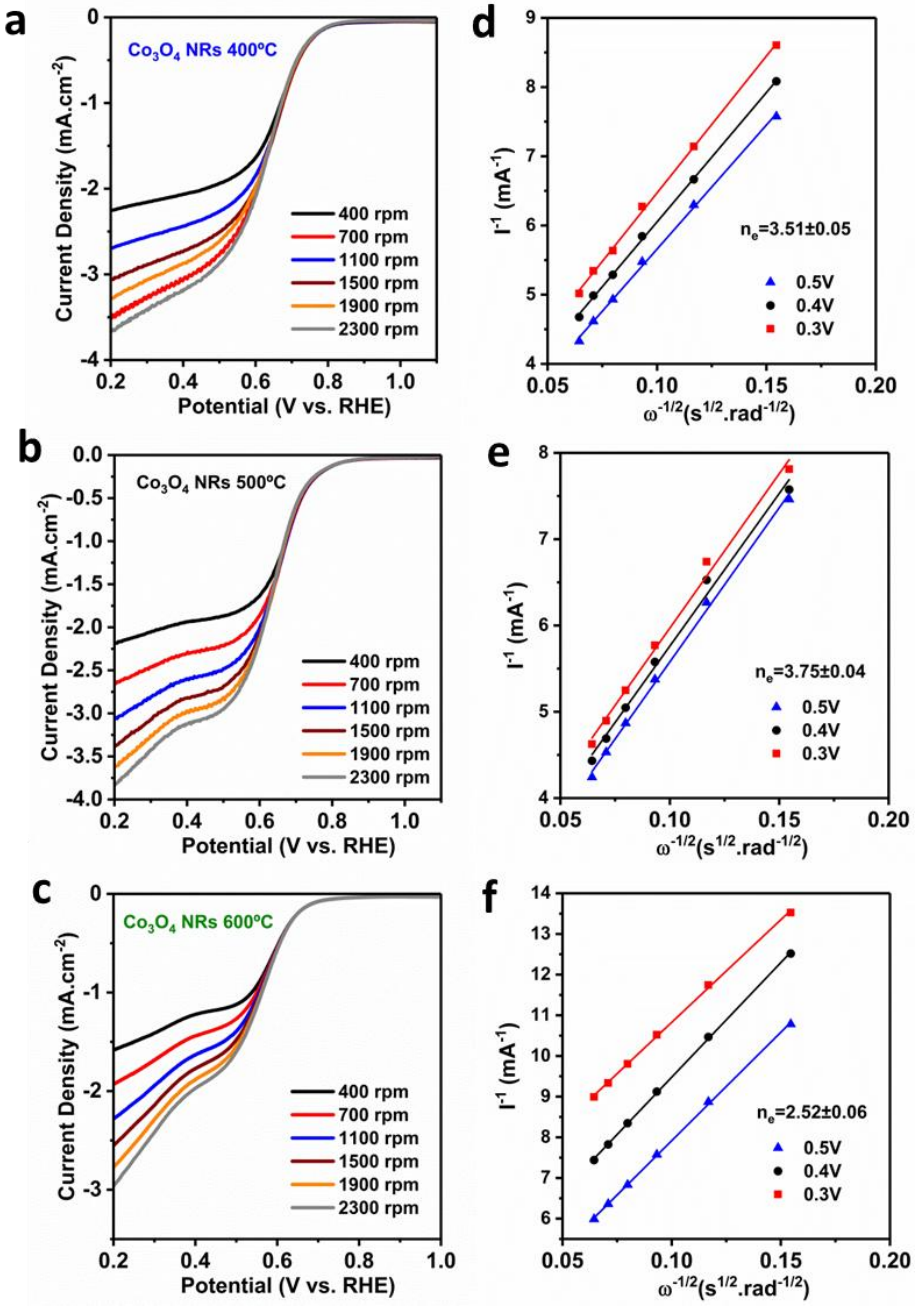

Figure 7.6 (a-c) rotating disk LSV profiles of different catalysts in O_2-saturated 0.1 M KOH solution at various rotation rates ranging from 400 to 2300 rpm with a scan rate of 20 $mV.s^{-1}$, and corresponding *Koutecky-Levich* plot at various potentials: (d) Co_3O_4 NRs 400 °C (e) Co_3O_4 NRs 500 °C and (f) Co_3O_4 NRs 600 °C

In order to evaluate their bifunctional character, the OER properties of the samples were also evaluated by the LSV tests, performed in Ar-saturated 0.1 M KOH with a RDE swept from 1 to 1.8 V (vs. RHE) at 1500 rpm. As can be observed in ***Figure 7.7***, the Co_3O_4 NRs 500°C sample resulted in

smaller overpotential and higher current densities compared to the rest of oxides. Based on these observations, we settled to hybridize Co_3O_4 NRs 500°C with N-rGO to substantially improve their electrocatalytic performance.

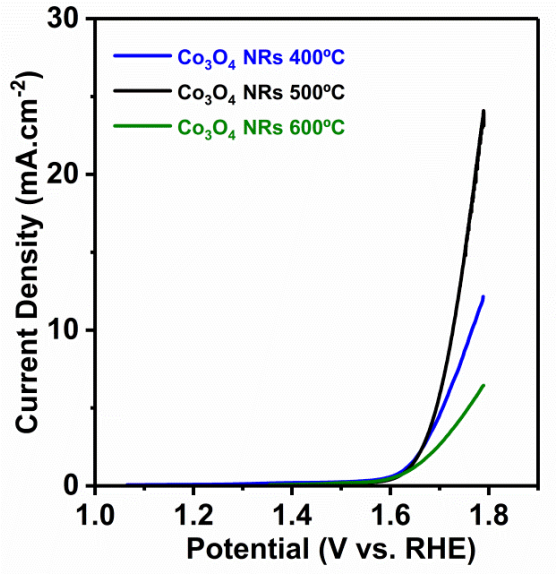

Figure 7.7 Evaluation of OER catalytic activity of Co_3O_4 NRs 400 °C, Co_3O_4 NRs 500 °C and Co_3O_4 NRs 600 °C mixed with Vulcan Carbon through LSV curves in Ar-saturated 0.1 M KOH solution at a scan rate of 20 $mV{\cdot}s^{-1}$

Since the surface area of the oxide samples are not considerably different according to N_2 isotherms, improved electrocatalytic performance of Co_3O_4 NRs 500°C in ORR/OER compared to the other samples can be ascribed to the presence of more surface Co^{3+} as evidenced by XPS measurements.

7.2.3 Preparation and Physico-Chemical characterization of N-rGO/Co_3O_4 NRs

As detailed in Chapter 3, N-rGO/Co_3O_4 NRs hybrid materials were synthesized through an electrostatic coagulation route followed by a simple hydrothermal step, illustrated in ***Figure 7.8***. The electrostatic interaction between the two opposite surface charges of Co_3O_4 NRs and GO NSs, that will ensure the proper anchoring, was investigated over the pH range of 1.5 to 11 by monitoring zeta-potential (Zp) of the materials in aqueous solutions (see ***Figure 7.8***). GO surface was negatively charged in all the measured pH ranges due to ionization of the superficial functional groups. In contrast, Co_3O_4 NRs surface is strongly positive at low pH ranges, but the Zp

value sharply decreases to negative potentials at higher pHs. Hence, the maximal potential difference between two samples and therefore the strongest attraction force can be achieved at pH = 2, which has been used for the synthesis of the hybrid sample.

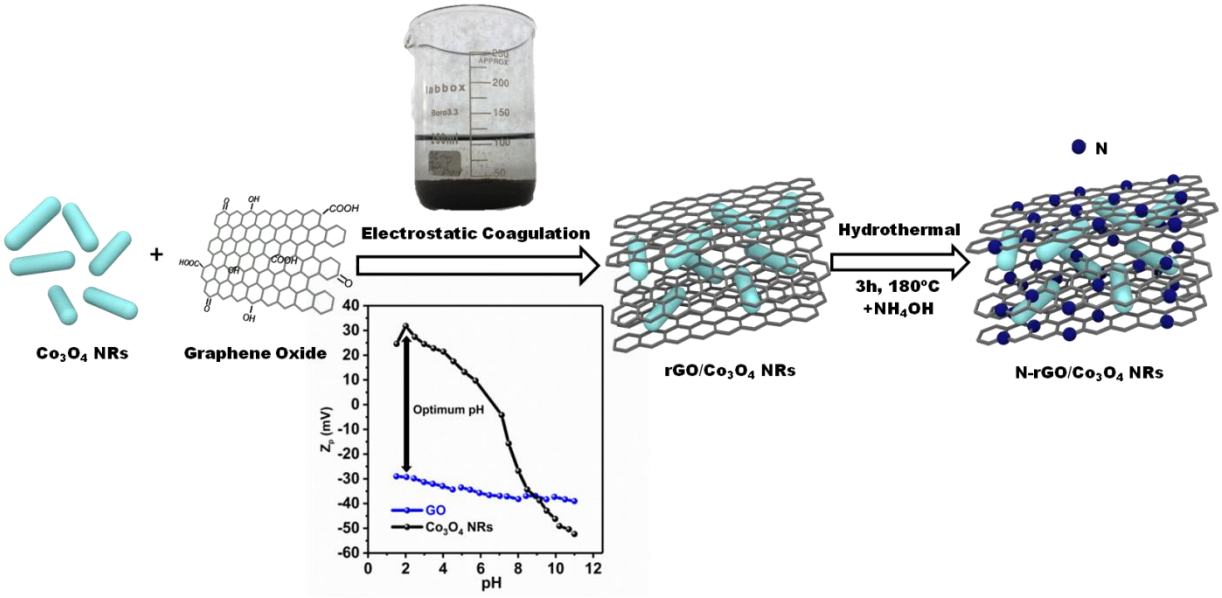

Figure 7.8 Schematic illustration of the synthesis procedure for N-rGO/Co_3O_4 NRs

The Co_3O_4 content on the nitrogen-doped graphene network was estimated to be 70 % by thermal gravimetric analysis (TGA) (see ***Figure 7.9***).

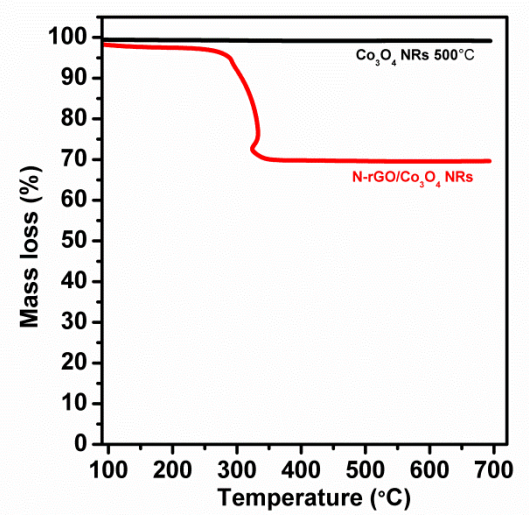

Figure 7.9 TGA profiles of the pure Co_3O_4 NRs 500°C and its hybrid with N-rGO from room temperature to 700°C with a heating rate of 10°C·min^{-1} under air flow

The crystallographic nature of the pure Co_3O_4 NRs 500°C and N-rGO samples as well as the N-rGO/Co_3O_4 NRs hybrid material were tracked by powder XRD analysis, as shown in ***Figure 7.10a.*** As seen, Co_3O_4 spinel phase can be clearly identified in the hybrid N-rGO/Co_3O_4 whereas no other crystalline structures appeared, revealing that no change occurred in spinel phase as a result of the hybridization.[23] N-rGO/Co_3O_4 NRs hybrid showed relatively wider diffracted peaks in comparison with those of the pristine oxide, suggesting the formation of smaller crystallite domains probably due to the presence of the graphene substrate. In addition, a peak at around 24º ascribed to the graphitic plane (002) of carbonaceous materials is not easily recognized in the nanohybrid while it is clearly visible for the pure N-rGO sample. It has been already demonstrated in literature that penetrative growth of metal oxide nanostructures into graphene layers can distort quasi-periodic stacking of graphene nanosheets, resulting in a lower intensity (002) peak in the nanohybrid samples.[36] Furthermore, the absence of any peak at 11.4º confirms the reduction of GO both in the hybrid and in the pure N-rGO sample. These results clearly reveal the successful electrostatic coagulation and anchoring of Co_3O_4 NRs on N-rGO layers.

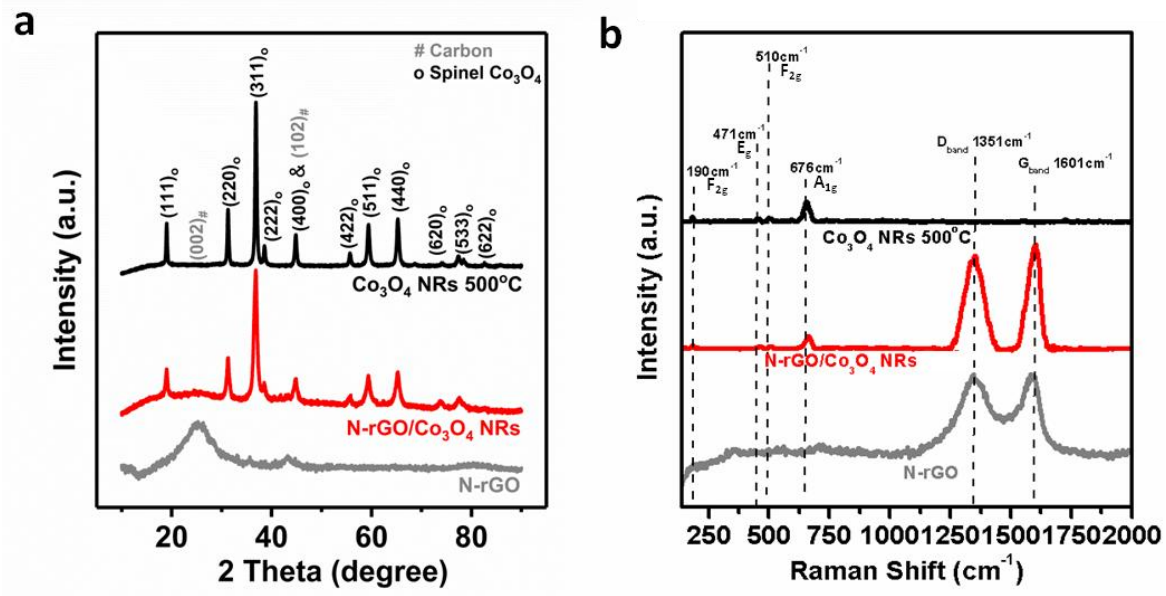

Figure 7.10 Microstructural analysis of the Co_3O_4 NRs 500 °C, N-rGO/Co_3O_4 NRs and N-rGO samples: (a) XRD pattern (b) Raman spectroscopy

On the other hand, Raman spectroscopy was conducted for further confirmation of the nanohybrid formation. As it is seen in ***Figure 7.10b***, the vibrational modes of spinel Co_3O_4 can be observed at 190, 471, 510 and 676 cm^{-1} both in the hybrid sample and in the pure oxide.

Additionally, two strong signals appeared at around 1351 and 1601 cm^{-1} for N-rGO/Co_3O_4 NRs and N-rGO attributed to the edge or defect sites of carbon (D-band) and in-plane vibrations of sp^2 carbon (G-band), respectively.[37]

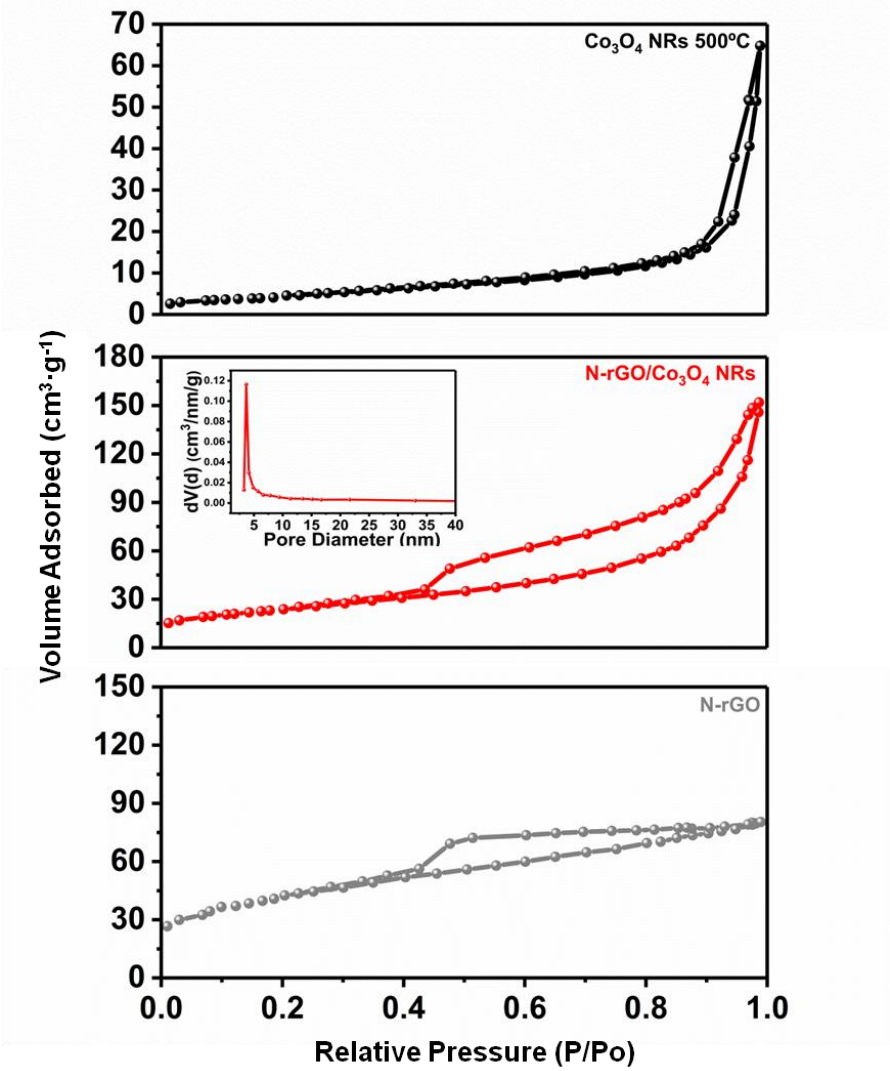

Figure 7.11 N_2 adsorption-desorption isotherms of the samples and BJH Pore size distribution of N-rGO/Co_3O_4 NRs hybrid sample

Figure 7.11 shows and compares the N_2 adsorption-desorption isotherms of the various samples, demonstrating type-IV isotherm and different types of hysteresis loop. Comparing the isotherms, one can observe the formation of large hysteresis in the hybrid in comparison with pure oxide. This hysteresis loop is quite similar to that of the N-rGO, suggesting the formation of mesopores as a result of Co_3O_4 hybridization with N-rGO (average pore diameter of hybrid is 4 nm as illustrated

in the inset of N-rGO/Co_3O_4 NRs ***Figure 7.11***). Additionally, BET specific surface area of the N-rGO/Co_3O_4 NRs hybrid (85.3 $m^2 \cdot g^{-1}$) is remarkably higher than pure oxide (16.2 $m^2 \cdot g^{-1}$), showing that the inclusion of N-rGO (142 $m^2 \cdot g^{-1}$) decisively enhanced the surface area of the oxide and drastically changed the type of porosity of the pristine oxide. These aspects are of great importance since it can remarkably increase the electrolyte access to the electrocatalytic active sites and therefore improve electrochemical performance.[38]

The microstructure and morphology of Co_3O_4 NRs 500°C and N-rGO/Co_3O_4 NRs hybrid samples were investigated by Transmission Electron Microscopy (TEM) and High Resolution Transmission Electron Microscopy (HRTEM)***. Figure 7.12 (a,b)*** show the TEM and HRTEM images of pure Co_3O_4 NRs 500 °C sample, revealing that the diameter of Co_3O_4 NRs ranged from 30 to 50 nm with an average length of 200 nm.

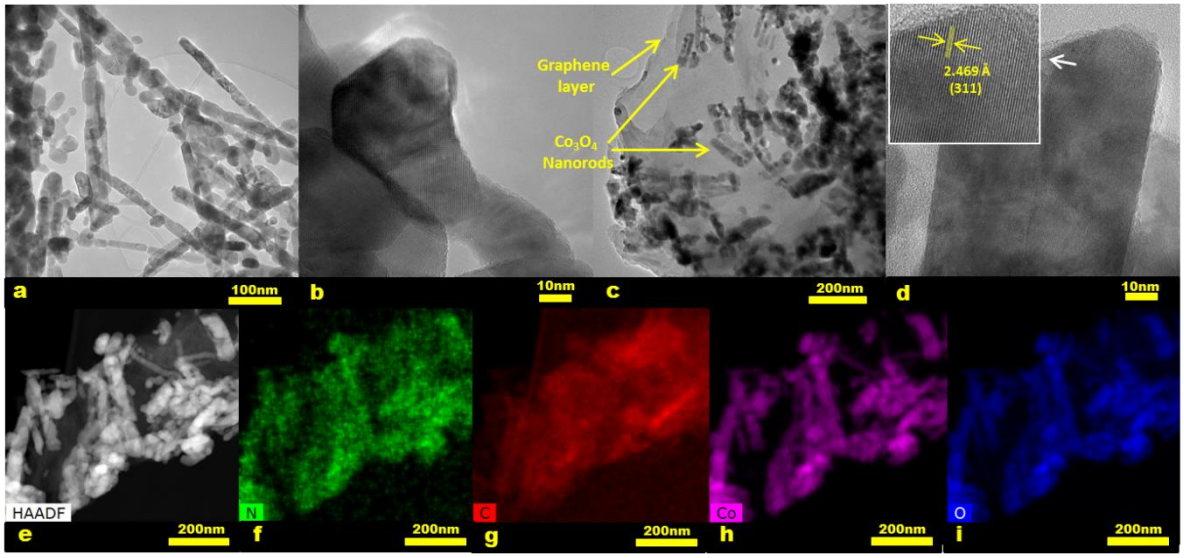

Figure 7.12 TEM and HRTEM micrographs of (a,b) Co_3O_4 NRs 500 °C and (c,d) N-rGO/Co_3O_4 NRs nanohybrid; (e) the corresponding HAADF-STEM micrograph and (f-i) EDX mapping of different elements for the N-rGO/Co_3O_4 NRs nanohybrid

Formation of nanocatalyst hybrid material was further demonstrated in ***Figure 7.12c***, where it can be observed that nitrogen-doped graphene layers are covered by Co_3O_4 NRs. Moreover, the HRTEM image of the hybrid material (***Figure 7.12d***) further confirmed the high crystalline characteristics of the Co_3O_4 NRs where the lattice fringes of 2.469 nm can be clearly distinguished. This corresponds to (311) plane of the face-centered spinel Co_3O_4. To shed more light on the NRs

distribution and chemical composition, HAADF-STEM micrograph (***Figure 7.12e***) and corresponding EDX mapping images (***Figure 7.12f to i***) of the N-rGO/Co_3O_4 NRs nanohybrid were collected, demonstrating homogeneous and uniform distribution of cobalt, oxygen and nitrogen on the carbon matrix.

7.2.4 Evaluation of electrocatalytic activity of N-rGO/Co_3O_4 NRs

Figure 7.13a display the CV profiles of N-rGO/Co_3O_4 NRs hybrid, collected from a cathodic direction in a potential range of 1.2 to 0.2 V vs. RHE with a scan rate of 20 $mV \cdot s^{-1}$. The blue dashed line shows control experiment in Ar-saturated solution, where no clear cathodic peak can be noted, showing an almost rectangular CV curve. On contrary, an intense redox peak at 0.79 V arose in O_2-saturated solution (red solid line), suggesting that N-rGO/Co_3O_4 NRs hybrid catalyzes ORR.

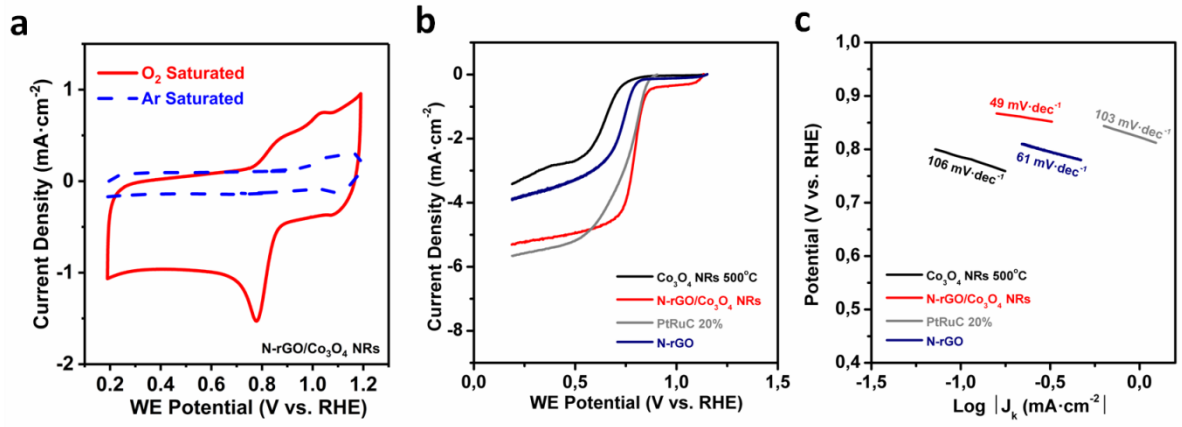

Figure 7.13 (a) CV curves of N-rGO/Co_3O_4 NRs hybrid nanocatalyst; solid line represents the measurement in O_2 and dashed line in Ar. (b) Linear sweep voltammograms of different samples recorded at 1500 rpm in the presence of O_2. (c) Tafel plots of ORR LSV curves in panel b

Figure 7.13b shows the LSV curves of the pure Co_3O_4 NRs 500 °C, its hybrid with nitrogen-doped reduced graphene oxide (N-rGO/Co_3O_4 NRs), pure N-rGO and PtRuC 20% as the state-of-the-art bifunctional catalyst for ORR. It can be seen that pure Co_3O_4 NRs showed a poor electrocatalytic activity with a two-step reduction. On the other hand, N-rGO exhibited a limited ORR electrocatalytic activity with a more positive onset reduction potential. Remarkably, the

microscale coupling of Co_3O_4 NRs with N-rGO in N-rGO/Co_3O_4 NRs nanohybrid exhibited an excellent improvement in ORR activity with an onset potential (E_{onset}=0.91 V), half-wave potential ($E_{1/2}$=0.80 V) and large diffusion-limited current density (J_{Levich}=5.46 mA·cm^{-2}), significantly outperforming pure components. Moreover, the obtained results are comparable to that of the commercial PtRuC 20% (E_{onset}=0.92 V, $E_{1/2}$=0.78 V, and J_{Levich}=5.81 mA·cm^{-2}). The extracted parameters from LSV curves are summarized in ***Table 7.1***, showing superior performance of N-rGO/Co_3O_4 NRs hybrid as an excellent electrocatalyst for ORR. This excellent ORR activity was further confirmed by smaller Tafel slope of 49 mV·dec^{-1} at high potentials in comparison with that of PtRuC 20% (103 mV·dec^{-1}), N-rGO (61 mV·dec^{-1}) and pure Co_3O_4 NRs 500°C (106 mV·dec^{-1}) (***Figure 7.13c***).

Table 7.1 Electrochemical parameters extracted from LSV curves

Sample	E_{onset} (V vs. RHE)	$E_{1/2}$ (V vs. RHE)	J_{Levich} (mA·cm^{-2})
Co_3O_4 NRs 400°C	0.87±0.01	0.66	3.20
Co_3O_4 NRs 500°C	0.88±0.01	0.65	3.41
Co_3O_4 NRs 600°C	0.75±0.02	0.59	2.60
N-rGO	0.86±0.01	0.71	3.88
N-rGO/Co_3O_4 NRs	0.91±0.01	0.80	5.31
PtRuC 20%	0.92±0.01	0.78	5.67

The outstanding ORR catalytic performance of the N-rGO/Co_3O_4 NRs hybrid can be explained due to the uniform and heavy distribution of metal oxide NRs on a two-dimensional highly conductive network (N-doped graphene support), resulting in enhanced surface area and consequently catalytic active spots.[25,39] As it has been demonstrated in previous reports, the enhanced and asymmetric charge density in N-doped carbons (specifically pyridinic and graphitic types) result in facilitated charge transfer between the adsorbing O_2 molecule/carbon framework and consequently smoothed formation of superoxide ions and O-O cleavage.[40–42] The superior electrocatalytic performance of the hybrid material compared to the pure components might be caused by accelerated kinetics with a greater number of electrons per O_2 molecule in ORR. The ORR kinetics was further examined by the polarization experiment in O_2-saturated solution at various rotating speeds, as seen in ***Figure 7.14a***.

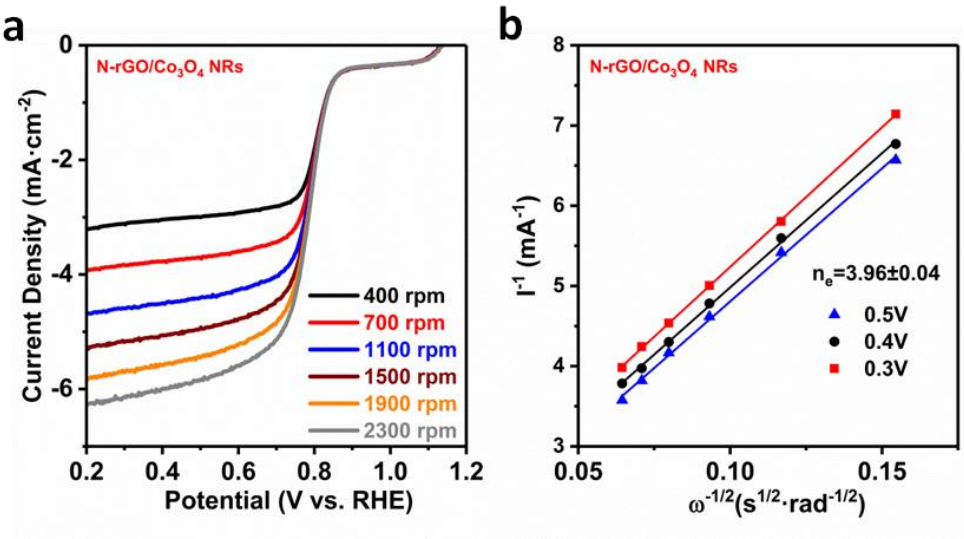

Figure 7.14 (a) LSV curves of N-rGO/Co_3O_4 NRs at various rotation rates in O_2-saturated 0.1M KOH solution with a scan rate of 20 mV·s^{-1} and (b) its corresponding Koutechy Levich plot at different potentials. Note: 0.1 M KOH used as electrolyte

Moreover, the number of transferred electrons per oxygen molecule (n) during ORR is calculated by using Koutecky-Levich theory (K-L plots) in an average at three different potentials (***Figure 7.14b***) according to [Eq 3.6]. Accordingly, the number of transferred electrons was determined as high as 3.96 for N-rGO/Co_3O_4 NRs sample, even higher than that of commercial PtRuC 20% (3.94) (***Figure 7.15***).

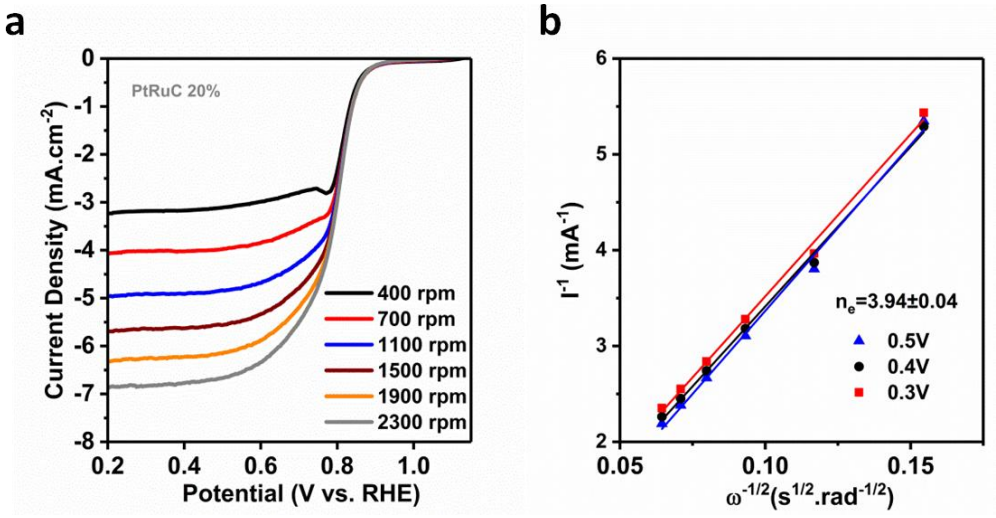

Figure 7.15 (a) LSV curves of PtRuC 20% at various rotation rates in O_2-saturated 0.1M KOH solution with a scan rate of 20 mV·s^{-1} and (b) its corresponding Koutechy Levich plot at different potentials

Moreover, from linearity of the K-L plots, one can conclude the first-order reaction kinetics with respect to the dissolved oxygen concentration. Additionally, identical slopes of the fitting lines imply similar number of transferred electrons at different potentials. These results clearly unveil that N-rGO/Co_3O_4 hybrid outperforms the rest of the electrocatalysts studied in this work, by catalyzing the ORR through a 4e pathway. Additionally, the ORR catalytic durability of the N-rGO/Co_3O_4 NRs hybrid was examined in O_2-saturated 0.1 M KOH through a chronoamperometric measurement applying a potential of 0.65 V vs. RHE.

As observed in ***Figure 7.16***, the hybrid exhibited a desirable stability with around 80% activity retention over 12000 s, significantly superior to that of the commercial PtRuC 20% catalyst (only 64% retention with an abrupt initial fading of more than 20% in the first 50 cycles). This is of particular interest as the electrocatalytic activity of Pt-based catalysts commonly declines over long application.[43]

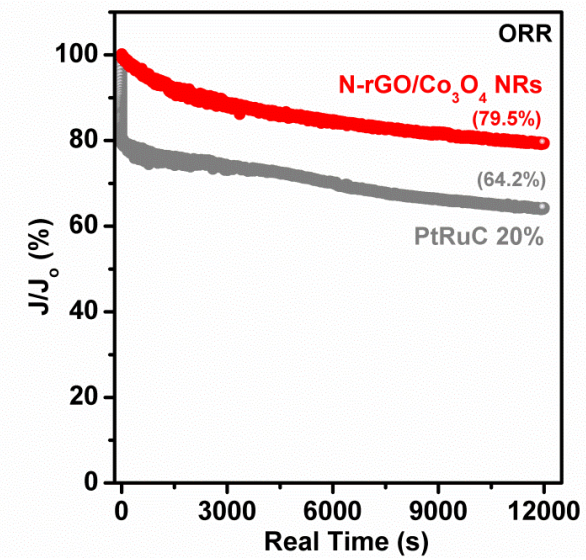

Figure 7.16 ORR catalytic durability of N-rGO/Co_3O_4 NRs in comparison with commercial PtRuC 20%

To further confirm the number of transferred electrons (n) obtained with N-rGO/Co_3O_4 NRs hybrid, RRDE measurements were conducted. ***Figure 7.17a*** displays ring and disk currents for N-rGO/Co_3O_4 NRs hybrid and commercial PtRuC 20%, recorded at 1500 rpm at a scan rate of 20 $mV \cdot s^{-1}$. As can be observed, the I_{disk} arisen from reduction of oxygen molecule is quite similar in both cases. However, the I_{ring} (peroxide oxidation) in N-rGO/Co_3O_4 NRs hybrid is almost negligible in

comparison with commercial PtRuC 20%. These results clearly demonstrate significantly smaller formation of peroxide during ORR on N-rGO/Co_3O_4 NRs, suggesting that the reaction goes mainly from a 4e pathway.

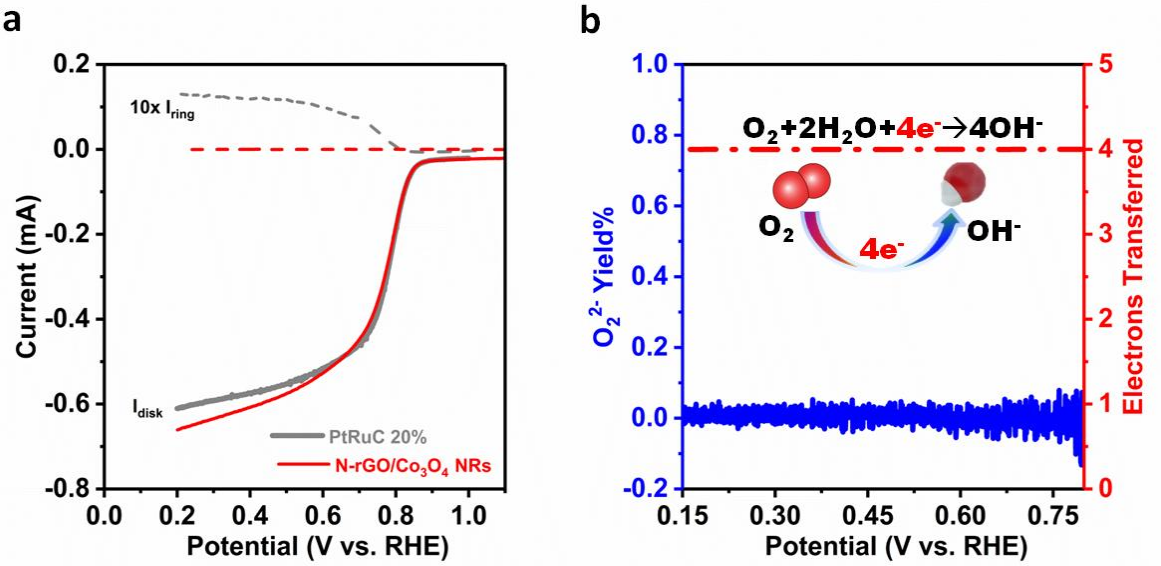

Figure 7.17 (*a*) RRDE LSV profiles of N-rGO/Co_3O_4 NRs and commercial PtRuC 20% (b) corresponding percentage of peroxide and number of transferred electrons with N-rGO/Co_3O_4 NRs hybrid material at various potentials

In addition, number of transferred electrons per O_2 molecule and HO_2^- yield in a wide potential range of 0.8 to 0.15 V for N-rGO/Co_3O_4 NRs hybrid has been depicted in ***Figure 7.17b***. As can be observed, the measured O_2^{2-} yield did not exceed 0.1% in the whole measured potential range and an average number of transferred electrons of 4 was obtained, in good agreement with the results obtained from RDE (3.96). These results further suggested that N-rGO/Co_3O_4 NRs hybrid catalyzes the ORR mainly from a $4e^-$ pathway, producing hydroxyl groups as schematically illustrated in ***Figure 7.17b*** Inset.

As discussed earlier, OER is equally important compared to ORR for energy storage applications.[44] As shown in ***Figure 7.18a***, an excellent OER onset potential of ~1.42 V was obtained for N-rGO/Co_3O_4 NRs hybrid, which is slightly superior to that of the state-of-the-art PtRuC 20% catalyst (~1.44 V).

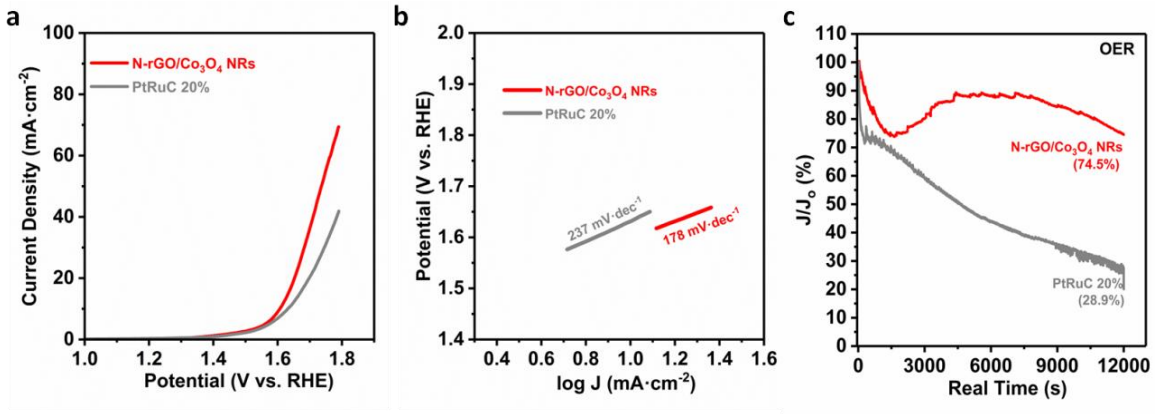

Figure 7.18 Evaluation of OER catalytic activity of N-rGO/Co_3O_4 NRs and commercial PtRuC 20% mixed with Vulcan Carbon through LSV curves and (*d*) corresponding *Tafel* plots. (c) Durability of OER catalytic activity of N-rGO/Co_3O_4 NRs and PtRuC 20%. Note: 0.1 M KOH used as electrolyte

In addition, the potential required to deliver a current density of 10 mA·cm^{-2} ($E_{j=10}$) was determined as 1.58 V for N-rGO/Co_3O_4 NRs hybrid, comparable to that of PtRuC 20% (1.59 V) and considerably lower than most of recently reported cobalt-based bifunctional electrocatalysts (***Table 7.2***). These results clearly demonstrate the outstanding catalytic activity of N-rGO/Co_3O_4 NRs toward OER. In addition, the Tafel slope of N-rGO/Co_3O_4 NRs (***Figure 7.18b***) was calculated to be 178 mV·dec^{-1}, according to [Eq 3.5], considerably smaller than PtRuC 20% (237 mV·dec^{-1}), further confirming the excellent OER performance of the hybrid. Furthermore, the OER electrochemical stability of N-rGO/Co_3O_4 NRs hybrid was evaluated by chronoamperometry in Ar-saturated 0.1 M KOH solution at a rotation rate of 1500 rpm (***Figure 7.18c***). N-rGO/Co_3O_4 NRs revealed a desirable electrochemical stability with approximately 75% relative current retained over 12000 s, remarkably superior than the commercial PtRuC 20% (only retained 29% relative current).

All these results demonstrate the optimal and homogeneous distribution of hierarchical Co_3O_4 NRs on thin N-rGO layers providing plenty of catalytic active sites on a highly conductive support facilitating enhanced charge transfer and synergistic effects between the single components.[17,22]

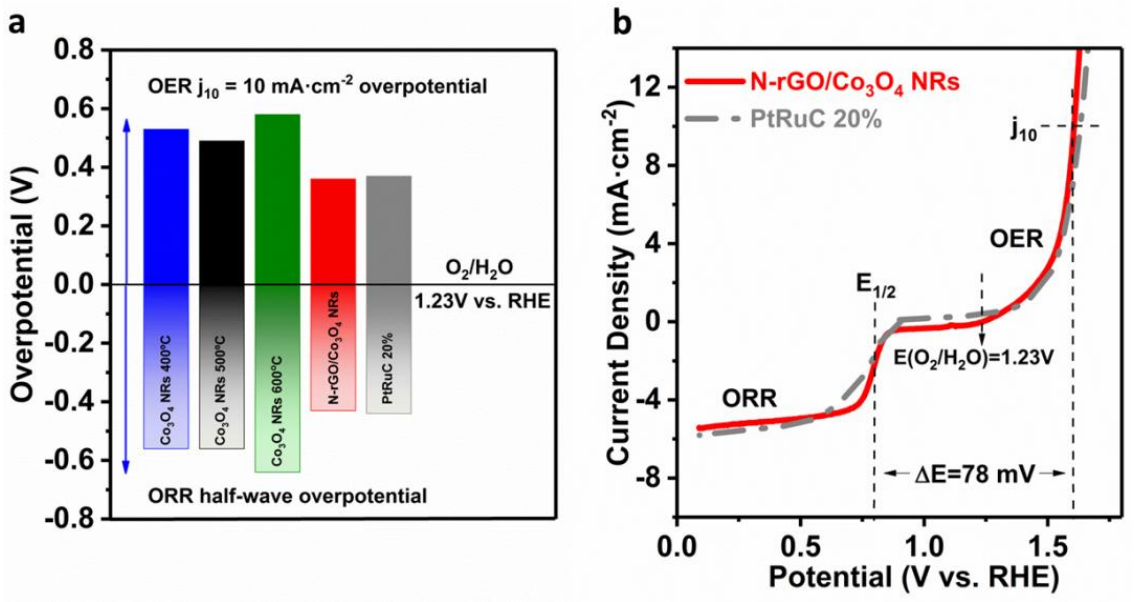

Figure 7.19 Performance as Bifunctional electrocatalyst: (*a*) Potential differences between the $E_{half\text{-}wave}$ of ORR and $E_{j=10}$ of OER for N-rGO/Co_3O_4 NRs and the rest of the samples (*b*) The entire LSV curves for bifunctional activities within the ORR and OER potential window of N-rGO/Co_3O_4 NRs and PtRuC 20% commercial catalyst for comparison at 1500 rpm

Figure 7.19a depicts an overall comparison of the bifunctional electrocatalytic performance of N-rGO/Co_3O_4 NRs hybrid, pure components and state-of-the-art Pt catalyst. It is demonstrated that the N-rGO/Co_3O_4 NRs hybrid achieved the lowest value for both ORR half-wave overpotential and OER overpotential at the current density of 10 mA·cm^{-2} (***Figure 7.19a***), and slightly outperformed commercial PtRuC 20% (***Figure 7.19b***).

Table 7.2 summarizes comparison of bifunctional catalytic activity of our N-rGO/Co_3O_4 NRs hybrid with recently reported cobalt-based catalysts in literature, revealing its superior or comparable performance. Smaller values of ΔE parameter (ΔE = $E_{j=10} - E_{1/2}$) indicates a higher bifunctional catalytic activity for reversible oxygen cathodes. Accordingly, N-rGO/Co_3O_4 NRs hybrid showed a superior catalytic activity with a small ΔE value of 0.78 V which is amongst smallest values reported for similar catalysts, as observed in ***Table 7.2***. In addition, this is slightly smaller than ΔE obtained using commercial PtRuC 20% catalyst (0.80 V), introducing N-rGO/Co_3O_4 NRs as a promising low-cost and efficient bifunctional nanocatalyst for metal-air batteries.

Table 7.2 Comparison of ORR/OER electrocatalytic activity of N-rGO-Co_3O_4 NRs hybrid catalyst with some recently reported hybrid cobalt catalysts

Sample	E_{onset}^{ORR}(V)	$E_{1/2}$ (V)	n_e	E_{onset}^{OER} (V)	$E_{j=10}$ (V)	ΔE (V)	Ref.
N-rGO/Co_3O_4 Nanorods	**0.91**	**0.80**	**3.96**	**1.42**	**1.58**	**0.78**	**This work**
Co_3O_4/N-rmGO	0.88	0.83	3.90	1.51	1.59	0.76	[19]
Co_3O_4/NPGC	0.97	0.84	≈ 4	1.56	1.68	0.84	[16]
Co@Co_3O_4/NC	0.89	0.80	3.78	1.56	1.65	0.85	[45]
Co_3O_4/HPNC	0.96	0.84	3.91	1.48	1.65	0.81	[46]
Co_3O_4/CNTs	0.93	0.83	≈ 4	1.43	1.55	0.72	[25]
Co_3O_4/NPC	0.81	0.74	3.66	1.53	1.63	0.89	[47]
Co_3O_4/N-GAs	0.97	0.87	3.9	1.60	1.66	0.79	[48]

7.2.5 Performance of hybrid electrocatalyst in Rechargeable Zn-Air Battery

The outstanding ORR/OER bifunctional activity and stability of N-rGO/Co_3O_4 NRs prompted us to evaluate its feasibility as air cathode catalyst for rechargeable Zn-air batteries. As it is schematically represented in ***Figure 7.20a***, integrating a Zn foil as the anode with N-rGO/Co_3O_4 NRs nanocatalyst coated on gas diffusion layer (GDL) as the cathode in a home-made 3D printed cell resulted in high open circuit voltage of ~1.49 V. For comparison, Zn-air batteries with commercial PtRuC 20% catalyst as air cathode were also assembled and tested.

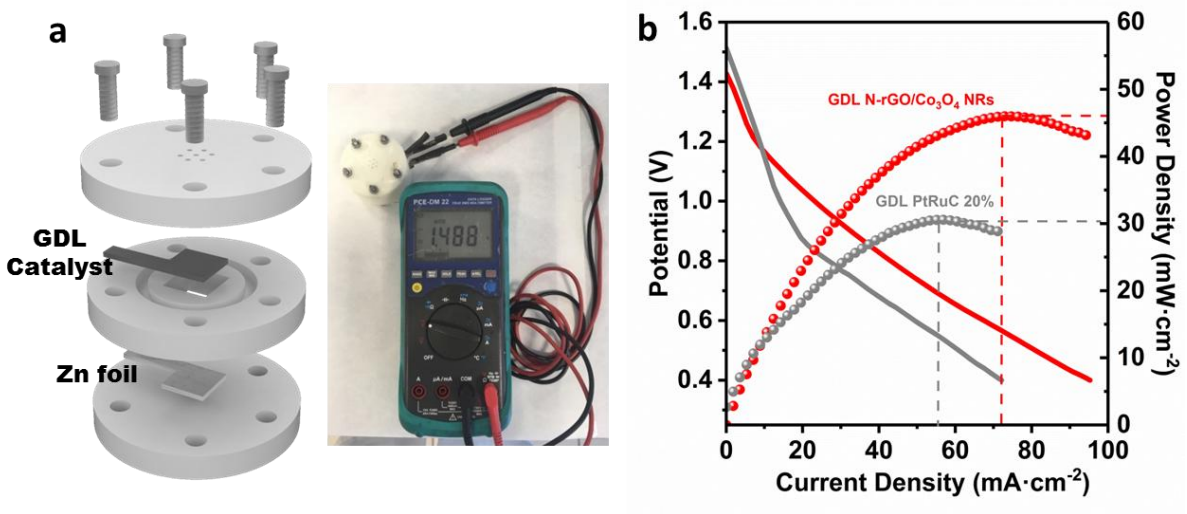

Figure 7.20 (*a*) Schematic illustration of Zn-air cell and images of a cell showing an OCP = 1.488 V. (b) Galvanodynamic discharge profile and power density curve of N-rGO/Co_3O_4 NRs and PtRuC 20% air cathodes

The polarization and power density profiles in ***Figure 7.20b*** showed that the Zn-air battery using N-rGO/Co_3O_4 NRs as air cathode can deliver a peak power density of 47 mW·cm^{-2} at 73 mA·cm^{-2}, outperforming the battery with PtRuC 20% (31 mW·cm^{-2} at 56 mA·cm^{-2}). Moreover, at a discharge current density of 5 mA·cm^{-2} (***Figure 7.21a***), the N-rGO/Co_3O_4 NRs-based Zn-air battery exhibited a large specific capacity of 875 mAh·g^{-1} corresponding to an ultrahigh energy density of 1115 Wh·kg_{Zn}^{-1}. The obtained values are significantly larger than those of the battery assembled using PtRuC 20% (760 mAh·g^{-1} and 912 Wh·kg_{Zn}^{-1}).

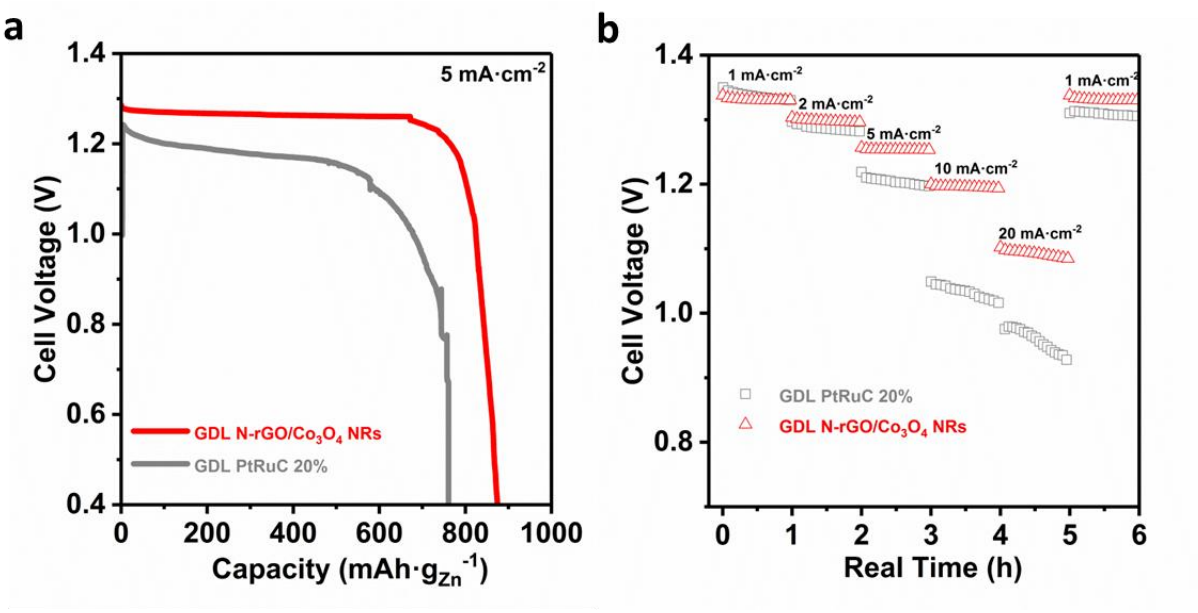

Figure 7.21 (*a*) Discharge curve of Zn-air batteries with N-rGO/Co_3O_4 NRs and PtRuC 20% as oxygen electrode catalysts at 5 mA·cm^{-2}. (*b*) Discharge profiles of the Zn-air battery based on N-rGO/Co_3O_4 NRs and PtRuC 20% catalyst electrodes at various current densities

Figure 7.21b show the discharge profiles of both Zn-air batteries assembled at various current densities. As observed, the battery using N-rGO/Co_3O_4 NRs supply entirely stable plateaus in different current loads (e.g. 1.09 V at 20 mA·cm^{-2}), outperforming the battery assembled with PtRuC 20%.

The long cycling of the Zn-air batteries was tested for more than 160h at 2 mA·cm^{-2} (***Figure 7.22a***). The difference between charging and discharging voltage (round-trip voltage) for the device loaded with the hybrid, increased from 0.75V to 1.03V (equal to a voltage efficiency decrease from 63.2% to 52.3%, ***Figure 7.22b***). In a quick comparison with the battery fabricated with commercial

PtRuC 20% catalyst, although both batteries showed similar charge/discharge profiles at initial stages, the performance of the one using PtRuC 20% catalyst quickly decreased with an increased round trip voltage from 0.77 V to 1.49V only after 9h of cycling.

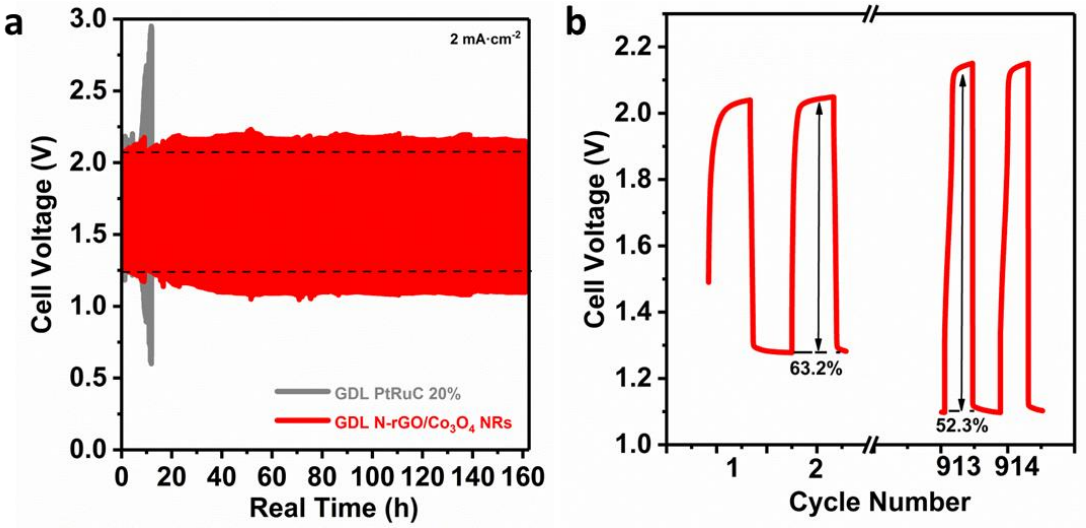

Figure 7.22 (a,b) Charge-discharge profiles of Zn-air batteries with N-rGO/Co_3O_4 NRs 500°C and PtRuC 20% oxygen catalysts at 2 mA·cm^{-2}

These results clearly unveil excellent ORR/OER bifunctional activity and remarkable catalytic durability of N-rGO/Co_3O_4 NRs air cathode. Overall, the rechargeable Zn-air battery assembled with N-rGO/Co_3O_4 NRs as air electrode catalyst demonstrated much better performance compared to the battery assembled using commercial PtRuC 20% catalyst, clearly verifying the superior bifunctional catalytic activity of the hybrid material for rechargeable metal-air batteries.

7.3 Conclusions

In summary, in this Chapter a facile, scalable and low-cost electrostatic coagulation is reported to hybridize hierarchical spinel Co_3O_4 NRs with N-rGO. The electrochemical signature of the prepared materials was probed as oxygen bifunctional electrocatalysts via RDE and RRDE measurements. This hybrid sample even outperformed the examined state-of-the-art bifunctional noble-metal catalyst (PtRuC 20%) with a small ΔE = 0.78 V, excellent durability and stood out among the most efficient bifunctional Co_3O_4-based catalysts reported to date.

The superior electrochemical performance of the hybrid can be attributed to the following reasons: (i) unique morphology of the Co_3O_4 NRs, homogeneously distributed on graphene network enhancing the electronic contact between the oxide and the carbon matrix, and generating a great number of active sites that facilitate oxygen adsorption, (ii) the enhanced porosity and specific surface area of the hybrid material favor the diffusion of the reactants, allowing efficient mass transfer; (iii) a highly conductive network (rGO) with an acceptable surface area along with nitrogen-doping accelerates both surface and bulk charge transfer throughout the nanocatalyst (iv) the existing synergistic effects between Co_3O_4 NRs and N-rGO nanosheets in the hybrid material coming from combination of improved conductivity, surface area and electrochemical activity compared to pure oxide. When integrated within an air cathode electrode in a rechargeable Zn-air battery, the N-rGO/Co_3O_4 NRs nanocatalyst is demonstrated to exhibit exceptionally high capacity of 875 $mAh \cdot g_{Zn}^{-1}$ and outstanding energy density of 1115 $W \cdot h \cdot kg_{Zn}^{-1}$ (around 102.7% of the theoretical energy density of 1086 $Wh \cdot kg^{-1}$) with stable and superior cycling stability compared to the state-of-the-art PtRuC 20% catalyst.

All these observations not only demonstrate the potential applicability of N-rGO/Co_3O_4 NRs as air cathode in metal air batteries but also pave a new path for designing the next generation of highly efficient and earth-abundant bifunctional nanocatalyst for rechargeable Zn-air batteries or other energy conversion applications, such as water electrolyzers or fuel cells.

7.4 References

1 J. Fu, Z. P. Cano, M. G. Park, A. Yu, M. Fowler and Z. Chen, *Adv. Mater.*, 2017, **29**, 1604685–1604719.

2 J. S. Lee, S. T. Kim, R. Cao, N. S. Choi, M. Liu, K. T. Lee and J. Cho, *Adv. Energy Mater.*, 2011, **1**, 34–50.

3 J. Fu, F. M. Hassan, J. Li, D. U. Lee, A. R. Ghannoum, G. Lui, M. A. Hoque and Z. Chen, *Adv. Mater.*, 2016, **28**, 6421–6428.

4 Y. Li and J. Lu, *ACS Energy Lett.*, 2017, **2**, 1370–1377.

5 M. Kuang and G. Zheng, *Small*, 2016, **12**, 5656–5675.

6 D. U. Lee, P. Xu, Z. P. Cano, A. G. Kashkooli, M. G. Park and Z. Chen, *J. Mater. Chem. A*, 2016, **4**, 7107–7134.

7 Y. Li, M. Gong, Y. Liang, J. Feng, J. E. Kim, H. Wang, G. Hong, B. Zhang and H. Dai, *Nat. Commun.*, 2013, **4**, 1805–1807.

8 J. Park, M. Risch, G. Nam, M. Park, T. J. Shin, S. Park, M. G. Kim, Y. Shao-Horn and J. Cho, *Energy Environ. Sci.*, 2017, **10**, 129–136.

9 B. Y. Guan, L. Yu and X. W. Lou, *Energy Environ. Sci.*, 2016, **9**, 3092–3096.

10 Y. N. Regmi, G. R. Waetzig, K. D. Duffee, S. M. Schmuecker, J. M. Thode and B. M. Leonard, *J. Mater. Chem. A*, 2015, **3**, 10085–10091.

11 Q. Wang, L. Shang, R. Shi, X. Zhang, Y. Zhao, G. I. N. Waterhouse, L. Z. Wu, C. H. Tung and T. Zhang, *Adv. Energy Mater.*, 2017, **7**, 1700467–1700474.

12 H. F. Wang, C. Tang, B. Wang, B. Q. Li and Q. Zhang, *Adv. Mater.*, 2017, **29**, 1702327–170336.

13 T. Liu, F. Yang, G. Cheng and W. Luo, *Small*, 2018, **14**, 1703748–1703757.

14 D. Wang and D. Astruc, *Chem. Soc. Rev.*, 2017, **46**, 816–854.

15 F. Cheng, J. Shen, B. Peng, Y. Pan, Z. Tao and J. Chen, *Nat. Chem.*, 2011, **3**, 79–84.

16 G. Li, X. Wang, J. Fu, J. Li, M. G. Park, Y. Zhang, G. Lui and Z. Chen, *Angew. Chemie - Int. Ed.*, 2016, **55**, 4977–4982.

17 Y. Jiang, Y. P. Deng, J. Fu, D. U. Lee, R. Liang, Z. P. Cano, Y. Liu, Z. Bai, S. Hwang, L. Yang, D. Su, W. Chu and Z. Chen, *Adv. Energy Mater.*, 2018, **8**, 1702900–1702911.

18 A. Pendashteh, J. Palma, M. Anderson and R. Marcilla, *Appl. Catal. B Environ.*, 2017, **201**, 241–252.

19 Y. Liang, Y. Li, H. Wang, J. Zhou, J. Wang, T. Regier and H. Dai, *Nat. Mater.*, 2011, **10**, 780–786.

20 S. K. Singh, V. M. Dhavale and S. Kurungot, *ACS Appl. Mater. Interfaces*, 2015, **7**, 21138–21149.

21 H. Jiang, Y. Liu, W. Li and J. Li, *Small*, 2018, **14**, 1703739–1703749.

22 T. Zhang, C. He, F. Sun, Y. Ding, M. Wang, L. Peng, J. Wang and Y. Lin, *Sci. Rep.*, 2017, **7**, 43638–46349.

23 Q. Shen, J. Yang, K. L. Chen, H. Wang, J. B. Liu and H. Yan, *J. Solid State Electrochem.*, 2016, **20**, 3331–3336.

24 K. Kumar, I. Abidat, C. Canaff, A. Habrioux, C. Morais, T. W. Napporn and K. B. Kokoh, *ChemElectroChem*, 2018, **5**, 483–493.

25 M. S. Ahmed, B. Choi and Y.-B. Kim, *Sci. Rep.*, 2018, **8**, 2543–2553.

26 Y. P. Zhu, C. Guo, Y. Zheng and S.-Z. Qiao, *Acc. Chem. Res.*, 2017, **50**, 915–923.

27 X. R. Wang, J. Y. Liu, Z. W. Liu, W. C. Wang, J. Luo, X. P. Han, X. W. Du, S. Z. Qiao and J. Yang, *Adv. Mater.*, 2018, **30**, 1–10.

28 J. Xiao, Q. Kuang, S. Yang, F. Xiao, S. Wang and L. Guo, *Sci. Rep.*, 2013, **3**, 2300–2308.

29 S. K. Singh, V. M. Dhavale and S. Kurungot, *ACS Appl. Mater. Interfaces*, 2015, **7**, 442–451.

30 Y. J. Sa, K. Kwon, J. Y. Cheon, F. Kleitz and S. H. Joo, *J. Mater. Chem. A*, 2013, **1**, 9992–10001.

31 T. H. Yoon and Y. J. Park, *Nanoscale Res. Lett.*, 2012, **7**, 1–11.

32 K. Park and D. Y. Bang, *J. Korean Phys. Soc.*, 2002, **41**, 251–256.

33 X. Han, G. He, Y. He, J. Zhang, X. Zheng and L. Li, *Adv. Energy Mater.*, 2017, **8**, 1702222–1702235.

34 J. Wang, R. Gao, D. Zhou, Z. Chen, Z. Wu, G. Schumacher, Z. Hu and X. Liu, *ACS Catal.*, 2017, **7**, 6533–6541.

35 W. Song, Z. Ren, S. Chen, Y. Meng, P. Nandi, H. A. Elsen, P. Gao and S. L. Suib, *Appl. Mater. Interfaces*, 2016, **8**, 20802–20813.

36 K. H. Wu, Q. Zeng, B. Zhang, X. Leng, D. S. Su, I. R. Gentle and D. W. Wang, *ChemSusChem*, 2015, **8**, 3331–3339.

37 F. Banhart, J. Kotakoski and A. V. Krasheninnikov, *ACS Nano*, 2011, **5**, 26–41.

38 J. Zhang, L. B. Kong, J. J. Cai, H. Li, Y. C. Luo and L. Kang, *Microporous Mesoporous Mater.*, 2010, **132**, 154–162.

39 S. Liu, L. Li, H. S. Ahn and A. Manthiram, *J. Mater. Chem. A*, 2015, **3**, 11615–11623.

40 Z. Chen, D. Higgins, H. Tao, R. S. Hsu and Z. Chen, *J. Phys. Chem. C*, 2009, **113**, 21008–21013.

41 S. Saji, C. Akiba, D. Guo, R. Shibuya, J. Nakamura and T. Kondo, *Science (80-.).*, 2016, **351**, 361–365.

42 Z. S. Wu, S. Yang, Y. Sun, K. Parvez, X. Feng and K. Müllen, *J. Am. Chem. Soc.*, 2012, **134**, 9082–9085.

43 M. Shao, Q. Chang, J.-P. Dodelet and R. Chenitz, *Chem. Rev.*, 2016, **116**, 3594–3657.

44 N.-T. Suen, S.-F. Hung, Q. Quan, N. Zhang, Y.-J. Xu and H. M. Chen, *Chem. Soc. Rev.*, 2017, **46**, 337–365.

45 A. Aijaz, J. Masa, C. Rasler, W. Ia, P. Weide, A. J. R. Botz, R. A. Fischer, W. Schuhmann and M. Muhler, *Angew. Chemie - Int. Ed.*, 2016, **55**, 4087–4091.

46 J. Guan, Z. Zhang, J. Ji, M. Dou and F. Wang, *ACS Appl. Mater. Interfaces*, 2017, **9**, 30662–30669.

47 Y. Huang, M. Zhang, P. Liu, F. Cheng and L. Wang, *Chinese J. Catal.*, 2016, **37**, 1249–1256.

48 D. Yu, C. Xu, Y. Su, D. Liu and X. He, *J. Electroanal. Chem.*, 2017, **787**, 46–54.

CHAPTER 8

Mixed Metal Sulfides Nano-Needles Forming Core-Shell Structures for Hybrid Energy Storage

8.1 Research Background

In previous chapters of this PhD we had contributed to the knowledge of different types of graphene/metal oxides hybrid materials with high electrochemical performance. The application of such materials has been investigated either as high performing electrode materials for hybrid energy storage devices (chapters 4, 5 and 6) or as electrocatalyst for Zn-air batteries (chapter 7). Alternatively, present chapter 8 and next chapter 9 will be focused on the application in energy storage devices of a different type of materials; mixed transition metal sulfides. The investigation on metal sulfides is motivated by their better electrical conductivity and electrochemical performance, in comparison with their metal oxide counterparts, likely due to their lower band-gap energy.[1–8] Moreover, as their mixed transition metal oxides analogues, mixed transition metal sulfides exhibit richer redox reactions and higher electronic conductivity than their single counterparts. A considerable increase in the number of publications in the literature for the last years (***Figure 8.1***) shows the importance of metal sulfides as a family of materials for different energy storage applications.

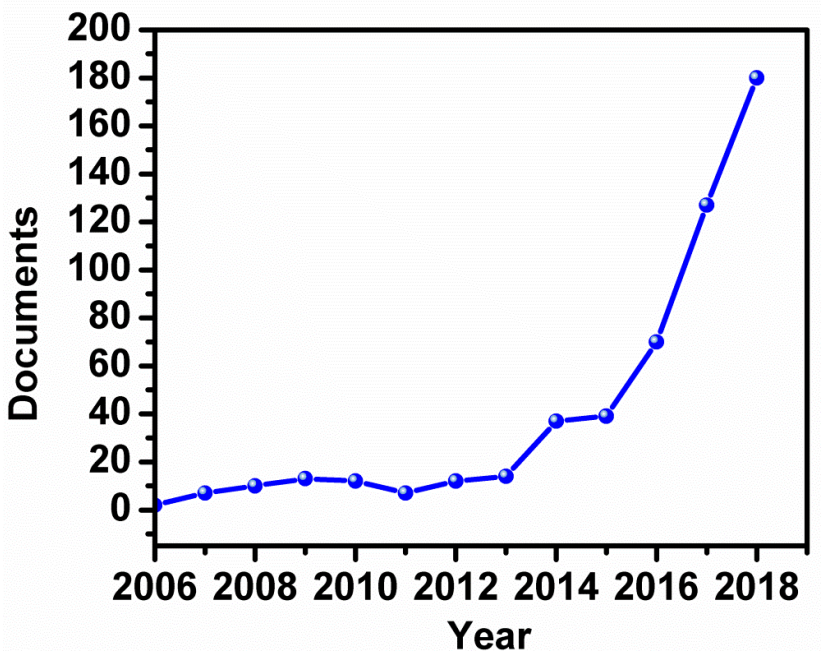

Figure 8.1 Published documents per year according to Scopus with “Metal Sulfide” and “Energy Storage” as searching keywords

With a quick look at recent works in literature, one notes that several metal sulfide phases have been studied as faradaic electrode materials including spinel $NiCo_2S_4$,[5,9,10] $MnCo_2S_4$,[11] heazlewoodite Ni_3S_2[12–15] or $(Co,Ni)_3S_2$.[16] The electrochemical behavior of $NiCo_2S_4$ was first studied by Chen and coworkers.[3] They developed a two-step hydrothermal method to synthesized 3D hierarchical urchin-like $NiCo_2S_4$ nanostructures, showing a high capacity of 159 $mAh \cdot g^{-1}$ (1149 $F \cdot g^{-1}$) at 1 $A \cdot g^{-1}$ in 6 MKOH as electrolyte. In another example, Sahoo and coworkers synthesized $MnCo_2S_4$ via electrodeposition process exhibiting a high specific capacity of 336 $mAh \cdot g^{-1}$ (2421 $F \cdot g^{-1}$) at a current density of 1 $A \cdot g^{-1}$, employing extremely low mass loading of the active materials (1.5 $mg \cdot cm^{-2}$). The favorable storage performance of metal sulfides has been demonstrated in these works and was typically suggested to be arisen from reversible redox reactions involving sulfides and their hydroxides. However, to the best of our knowledge no one supported the proposed mechanisms with experimental evidences on the sulfides at various states of charge.

Therefore, the present chapter not only demonstrate the electrochemical behavior of a mixed metal sulfide ($NiCoMnS_2$ nanoneedles) as novel binder/additive-free high-performance positive electrodes for hybrid devices, in this chapter we also helps to achieve a better understanding of the electro-activation process and charge storage origin of mixed metal sulfides in alkaline media benefited by ex-situ and operando measurements.

8.2 Results and Discussion

8.2.1 Synthesis and Physico-Chemical Analysis of $NiCoMnS_2$ Nano-Needles

Herein, we have employed a systematic combination of structural and electrochemical characterization techniques (e.g. ex-situ XRD and operando Raman spectroscopy at different states of charge and after cycling) to get new insights into the storage mechanism of mixed metal sulfides. To this end, a novel mixed metal sulfide phase of $NiCoMnS_2$ nano-needles was hydrothermally grown on Ni foam (schematically shown in ***Figure 8.2***) by a facile two-step hydrothermal route.

Direct growth synthesis, in comparison with the traditional slurry casting, avoids/reduces “dead mass” (e.g. portions of the sample which do not participate in reaction due to electrochemical

inactivity or electrolyte inaccessibility), in a binder/additive-free fashion. Moreover, direct contact between current collector and the sample results in enhanced electronic conductivity suitable for high-power applications.[17]

As detailed in experimental section, two consecutive hydrothermal steps including metal precursors, urea and thioacetamide (TAA) resulted in formation of $NiCoMnS_2$ nano-needles (~5.2 $mg{\cdot}cm^{-2}$ electrode mass loading). For the sake of comparison, NiCoMn hydroxide samples ($(Ni_{1-(x+y)}Mn_xCo_y)OH_2$ urchin-like) were also synthesized under identical conditions without addition of TAA. The product of the reaction in the presence of TAA differs both in morphology and composition, as illustrated in ***Figure 8.2***.

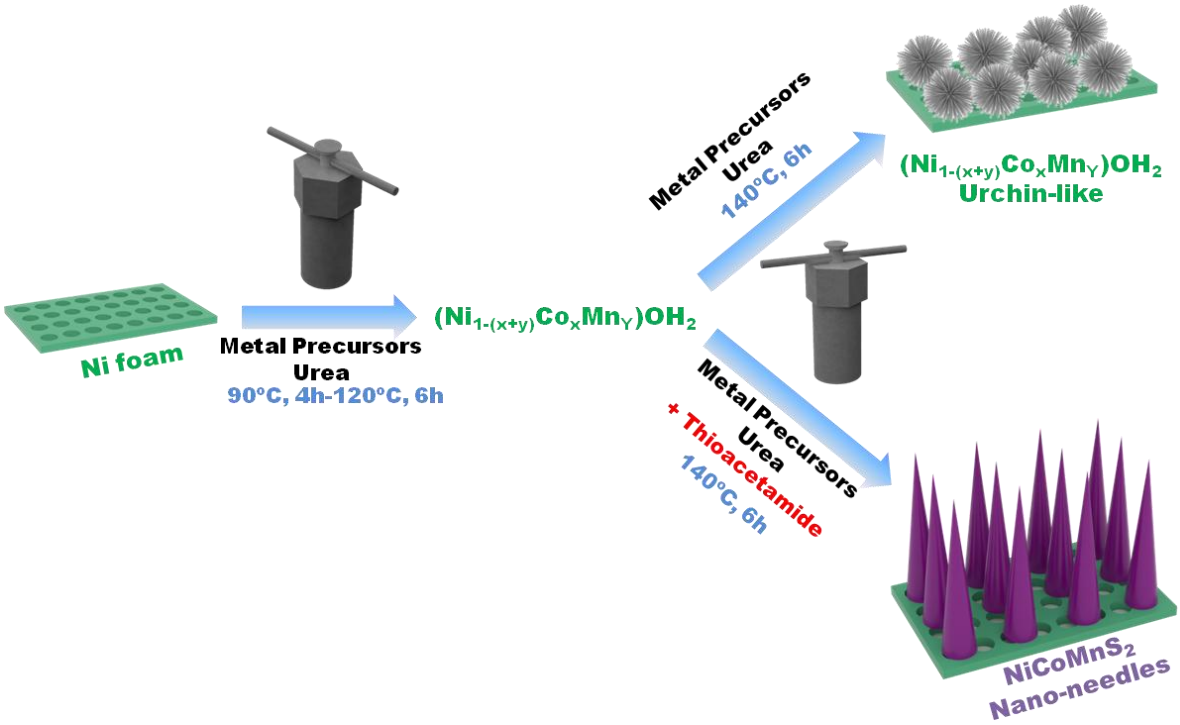

Figure 8.2 Schematic illustration of the synthesis procedure for $(Ni_{1-(x+y)}Mn_xCo_y)OH_2$ urchin-like structure and $NiCoMnS_2$ nano-needles, in the absence and presence of TAA, respectively

As observed from SEM images (***Figure 8.3a***), the surface of Ni foam (Inset) has been thoroughly and uniformly covered with $NiCoMnS_2$ nano-needles. Enlarged SEM image in ***Figure 8.3b*** achieves a clear view of the vertically oriented and homogeneously distributed $NiCoMnS_2$ nano-needles on Ni substrate.

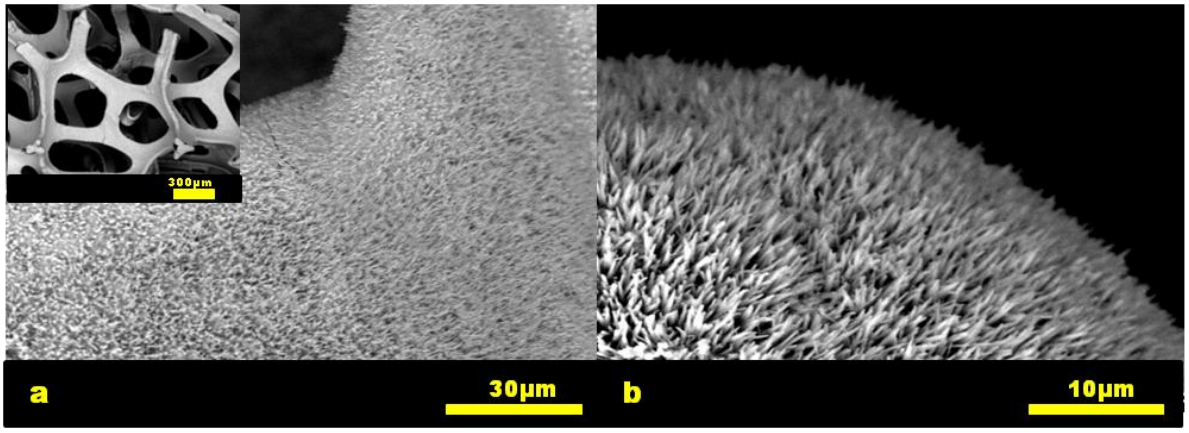

Figure 8.3 SEM micrographs of the $NiCoMnS_2$ nano-needles on Ni foam at different magnifications

In contrary, in the absence of sulfur precursor (TAA), $(Ni_{1-(x+y)}Mn_xCo_y)OH_2$ manifested a significant morphological change forming urchin-like structure (***Figure 8.4***).[18,19]

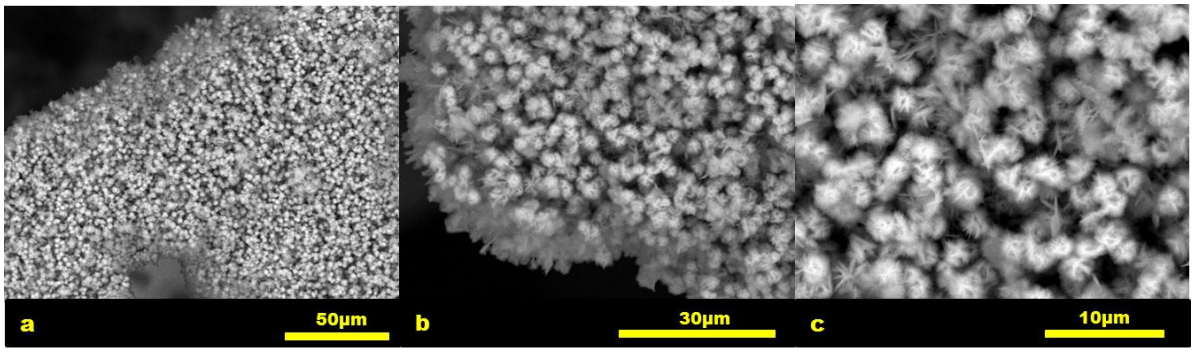

Figure 8.4 SEM micrographs of the $(Ni_{1-(x+y)}Co_xMn_y)OH_2$ urchin-like structure supported on Ni foam at different magnifications

The detailed morphology and composition of the $NiCoMnS_2$ nano-needles were further analyzed by TEM and HR-TEM measurements, as shown in ***Figure 8.5.*** A typical diameter of ~100 nm was obtained for $NiCoMnS_2$ nano-needles (***Figure 8.5b***). As confirmed by HR-TEM image (inset of ***Figure 8.5b***), lattice fringes of 0.30 nm corresponding to [110] crystal plane in Heazlewoodite phase could be readily distinguished. Additionally, Scanning Transmission Electron Microscopy (STEM) (***Figure 8.5c***) and EDX elemental mapping (***Figure 8.5d-g***) demonstrated the uniform distribution and existence of different elements (Ni, Co, Mn and S) along the $NiCoMnS_2$ nano-needles.

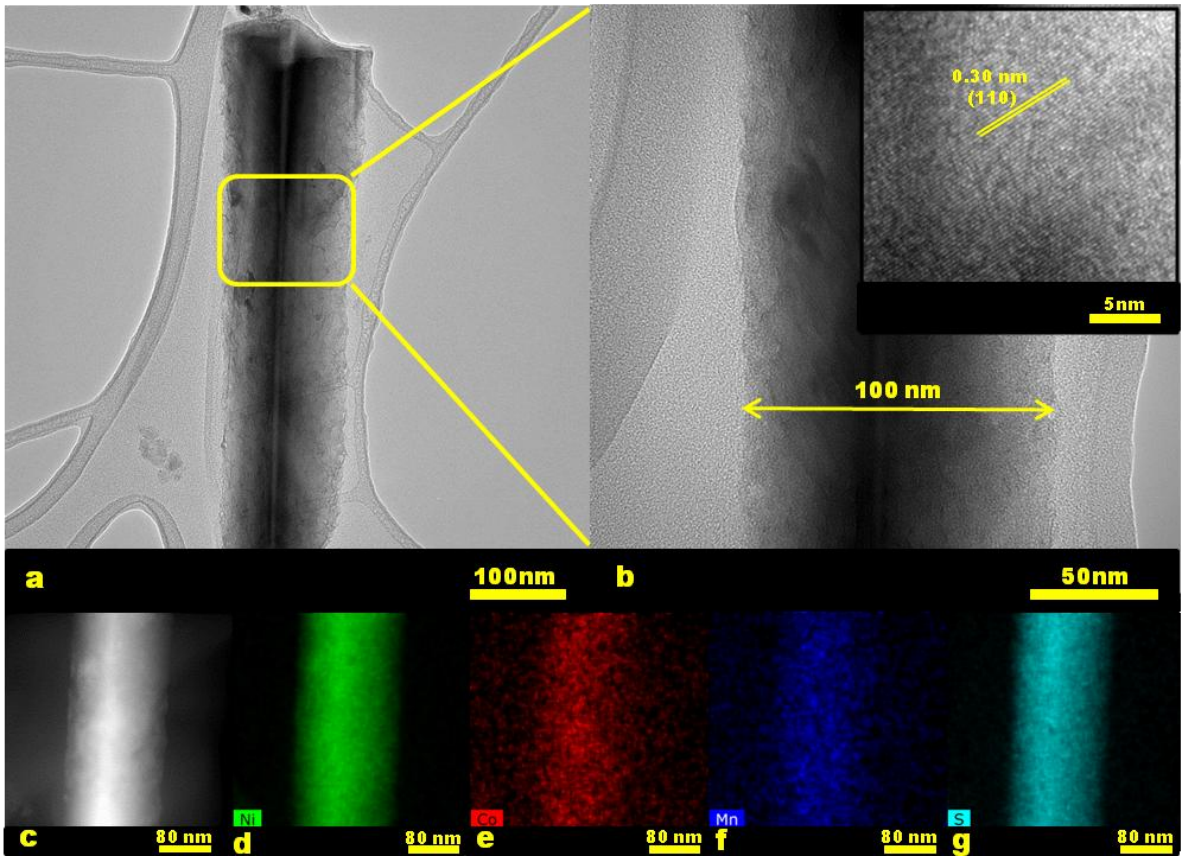

Figure 8.5 (a) TEM of the $NiCoMnS_2$ needle-like structure (b) TEM with its corresponding HR-TEM image (inset) (c) STEM micrograph of the $NiCoMnS_2$ nano-needle and (d-g) its corresponding elemental mappings

On the other hand, XRD measurements were conducted to determine crystallographic structure of the as-synthesized samples (***Figure 8.6***). In the case of $NiCoMnS_2$ nano-needles (red line), all diffracted peaks could be indexed to the pure Heazlewoodite phase (JCPDS 98-000-6248), in well agreement with HR-TEM images and previous reports.[12,14,15,20] The aforementioned Heazlewoodite phase present the diffracted peaks (101),(110),(003),(113) and (122) at 2 theta degrees 21.8, 31.2, 37.8, 51.9 and 58.5, respectively. The absence of any other diffraction peak suggests that the sample is purely crystallized in Heazlewoodite phase. In contrary, all diffraction peaks for the sample prepared in the absence of TAA can be indexed to α-$(Ni_{1-(x+y)}Mn_xCo_y)OH_2$, with a rhombohedral structure (JCPDS no. 38-0715).[21] The diffracted peaks of α-$(Ni_{1-(x+y)}Mn_xCo_y)OH_2$ are (003),(006),(012),(015),(018) and (110) at 2 theta degrees 11.3, 23.0, 31.6,34.5 38.8 and 61, respectively.

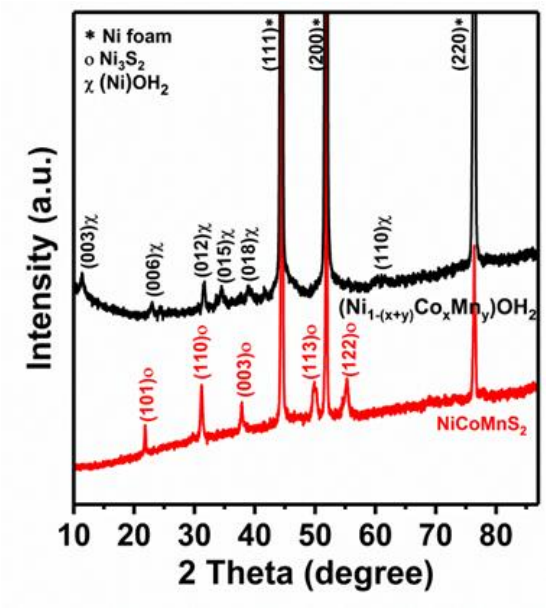

Figure 8.6 (a) XRD of the $NiCoMnS_2$ and $(Ni_{1-(x+y)}Co_xMn_y)OH_2$ samples including the corresponding hkl planes

Further characterization of the different phases was made through Raman Spectroscopy and FTIR (***Figure 8.7***). As can be appreciated in ***Figure 8.7a***, Raman spectra further confirmed the formation of $NiCoMnS_2$ corresponding to the vibration modes of rhombohedral heazlewoodite-phase.[22–25] It has been previously reported based on a factor group analysis using the correlation method given by Fateley et al.[26] that a total of six Raman-active bands exist in rhombohedral heazlewoodite-phase, two A1 and four E vibrations.[22,24]

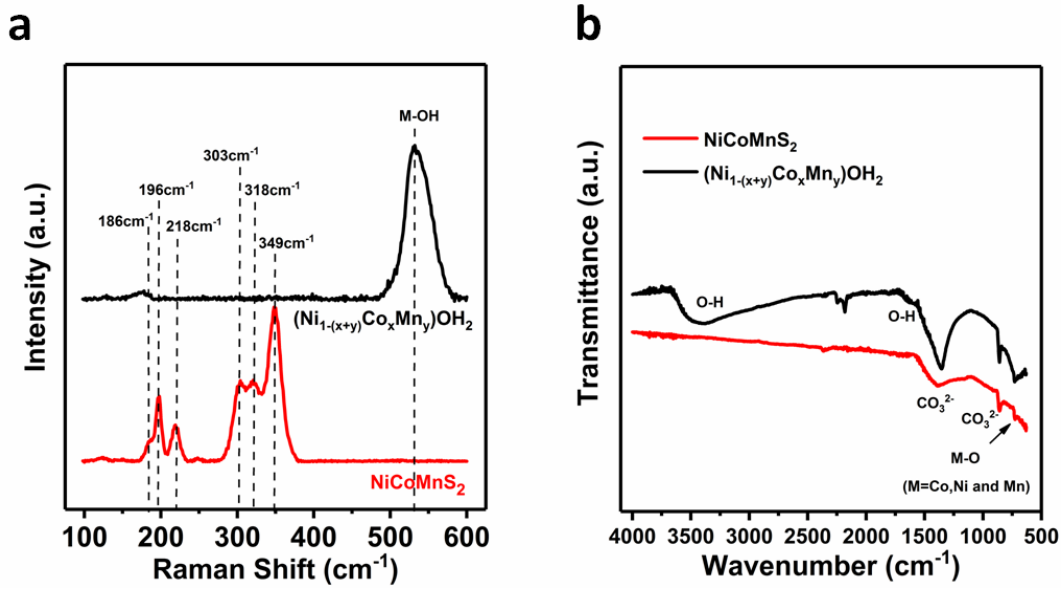

Figure 8.7 (a) Raman and (b) FTIR spectras of the $NiCoMnS_2$ and $(Ni_{1-(x+y)}Co_xMn_y)OH_2$ samples

This is in well agreement with the observed Raman spectrum collected for $NiCoMnS_2$ nano-needles. On the other hand, $(Ni_{1-(x+y)}Mn_xCo_y)OH_2$ showed totally distinct Raman signal with a broad band in the range of 500-600 cm^{-1} attributed to the M–OH.[27] Moreover, clear differences can be distinguished in the FTIR spectra of the samples (***Figure 8.7b***). In the case of hydroxide sample, broad bands at ~3470 and 1600 cm^{-1} can be ascribed to O–H stretching and bending vibrations, respectively. On the other side, in $NiCoMnS_2$, the broad band at 3470 cm^{-1} is disappeared while those appeared in the range of 500-700 cm^{-1} can be assigned to M–O/S, O/S–M–O/S, and M–O/S–M (M= Co, Ni and Mn) lattice vibrations.[28,29] Additionally, EDX analyses of both samples are shown in ***Figure 8.8***, demonstrating the existence of pure mixed metal sulfide without any other impurity in the case of $NiCoMnS_2$. As can be appreciated, both samples shown an excess of nickel originated from the Ni foam substrate.

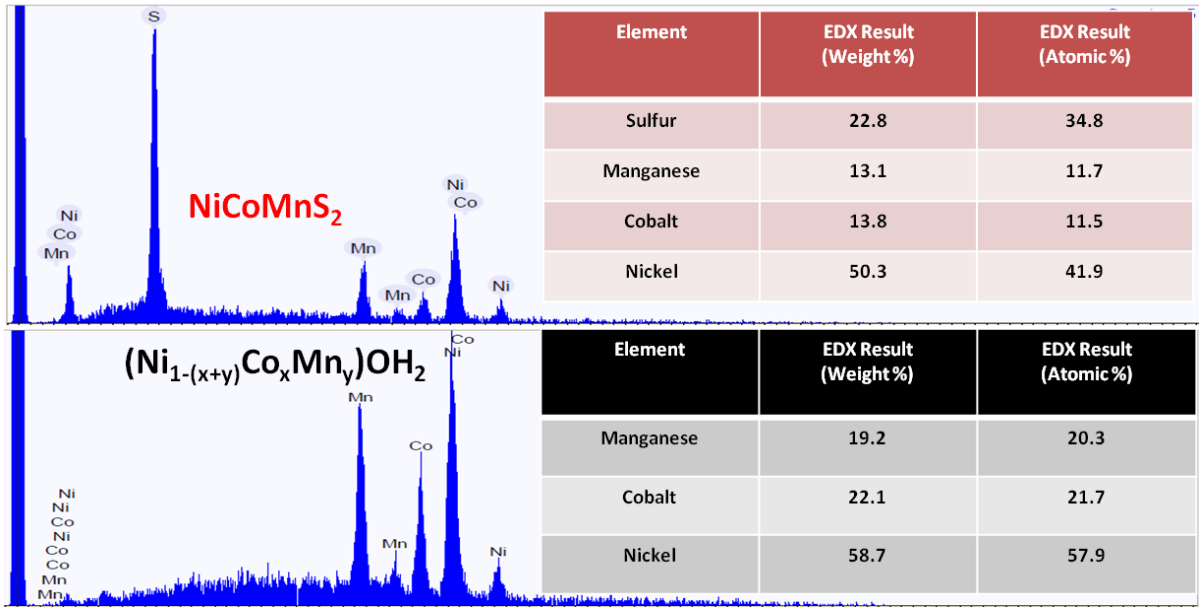

Element	EDX Result (Weight %)	EDX Result (Atomic %)
Sulfur	22.8	34.8
Manganese	13.1	11.7
Cobalt	13.8	11.5
Nickel	50.3	41.9

Element	EDX Result (Weight %)	EDX Result (Atomic %)
Manganese	19.2	20.3
Cobalt	22.1	21.7
Nickel	58.7	57.9

Figure 8.8 EDX spectra of the $NiCoMnS_2$ and $(Ni_{1-(x+y)}Co_xMn_y)OH_2$ samples

The chemical composition and oxidation state of different metal cations in the $NiCoMnS_2$ sample can be further confirmed by XPS analysis. The survey spectrum (***Figure 8.9***) indicated the presence of Ni, Co, Mn and S elements on the sample.

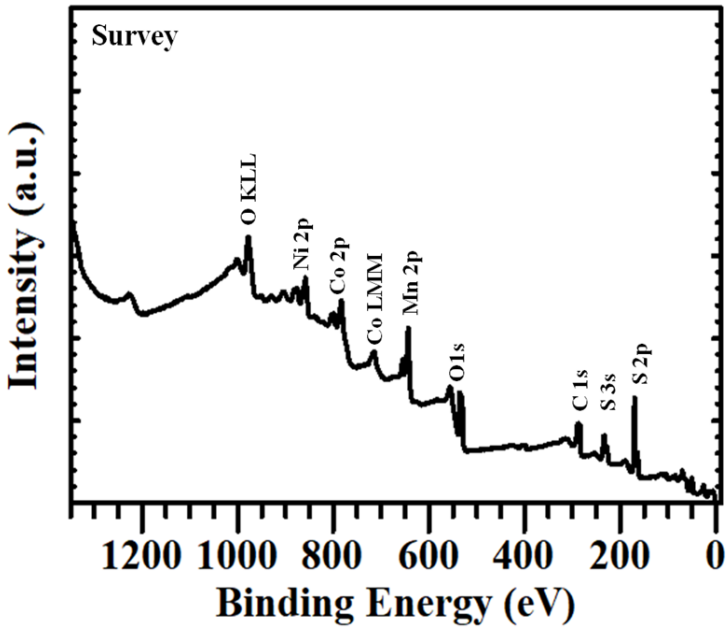

Figure 8.9 XPS Survey Spectra for $NiCoMnS_2$ sample

The high-resolution XPS spectra for various core levels of the sample are shown in **Figure 8.10**. As is seen in ***Figure 8.10a***, the Ni 2p region is comprised of two significantly spin-orbit split components (Ni $2p_{1/2}$ and Ni $2p_{3/2}$) with an energy gap of 17.4 eV, suggesting Ni^{2+} as the dominant component. However, the deconvolution of Ni $2p_{3/2}$ envelope into five components using Gaussian fitting further revealed the presence of some Ni^{3+} species as well.[30] ***Figure 8.10b*** shows the Co 2p core level including a spin-orbit doublet with an energy gap of 15.2 eV. Additionally, two shake-up satellites can be recognized, suggesting the existence of Co^{2+} species (Co-S and Co-O). ***Figure 8.10c*** illustrates the Mn 2p core level, where one can appreciate two main peaks at around 641.9 eV and 653.6 eV corresponding to Mn $2p_{3/2}$ and Mn $2p_{1/2}$, respectively, with a binding energy separation of 11.7 eV, revealing that Mn^{2+} (Mn-S and $MnSO_4$) species are dominant on surface of the sample.[8] The sulfur content in the $NiCoMnS_2$ sample can also be confirmed by the XPS analysis whose results are illustrated in ***Figure 8.10d***. The S 2p core level can be decoupled into two main peaks located at 161.7 and 162.8 eV as well as one shake-up satellite centered at 167.2 eV. The fitted peak at 163.8 corresponds to metal-sulfur bonds while the one at 162.7 eV can be attributed to sulfur ions (S^{2-}) at low coordination edges on the surface.[31]

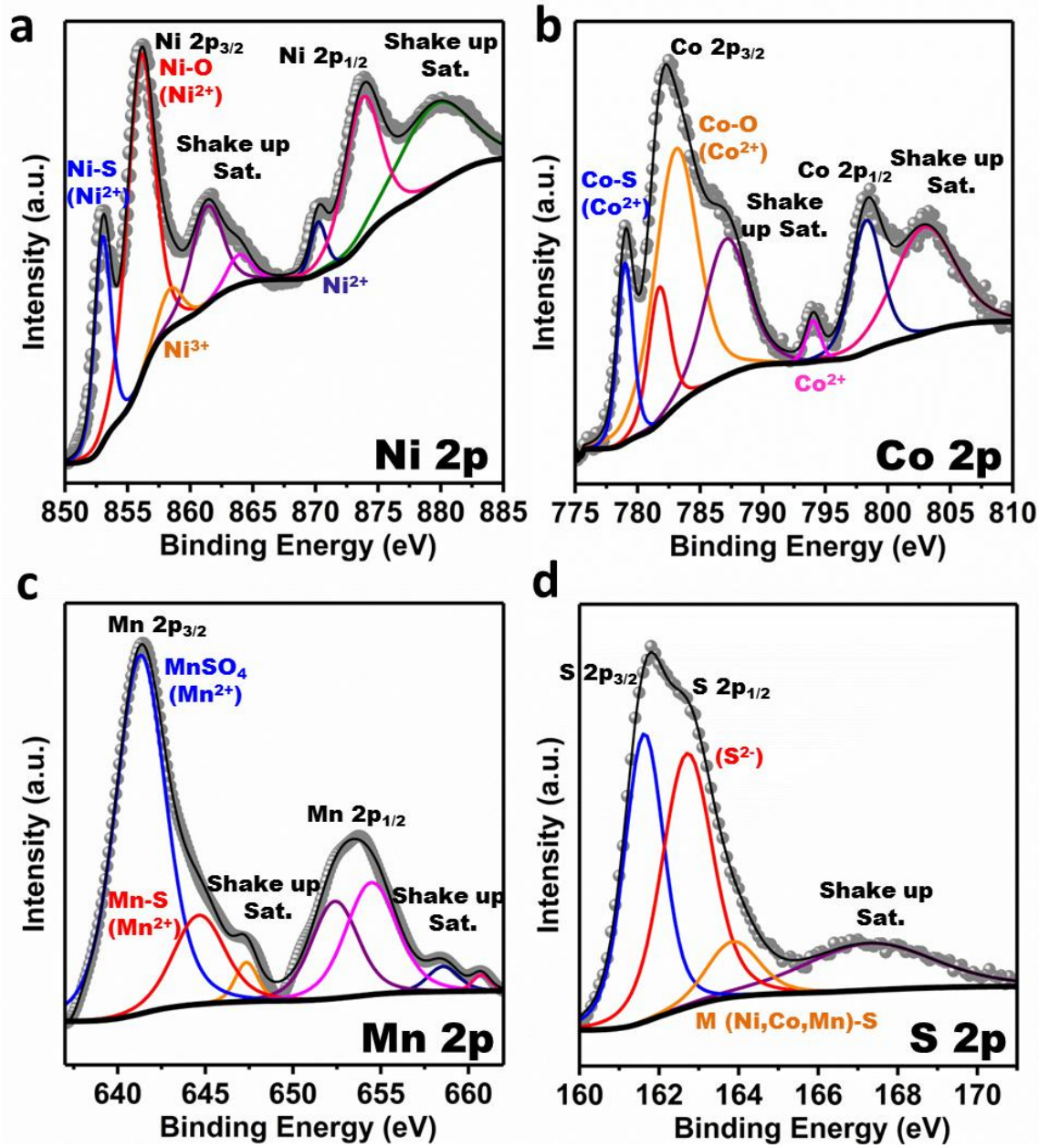

Figure 8.10 High-resolution XPS analysis of the $NiCoMnS_2$ needles: (a) Ni 2p, (b) Co 2p, (c) Mn 2p and (d) S 2p core levels

8.2.2 Electrochemical Evaluation of the samples in half-cells

With the idea of demonstrating the potential application of the as-synthesized samples as positive electrode materials for hybrid electrochemical energy storage devices, CV, GCD and EIS measurements were conducted in 3 electrode electrochemical cells. ***Figure 8.11a*** depicts the CV

curves of $NiCoMnS_2$ nano-needle and $(Ni_{1-(x+y)}Mn_xCo_y)OH_2$ urchin-like electrodes at a scan rate of 5 $mV{\cdot}s^{-1}$. For the sake of comparison, $Ni_{1-(x+y)}Mn_xCo_y)OH_2$ were also tested under identical conditions.

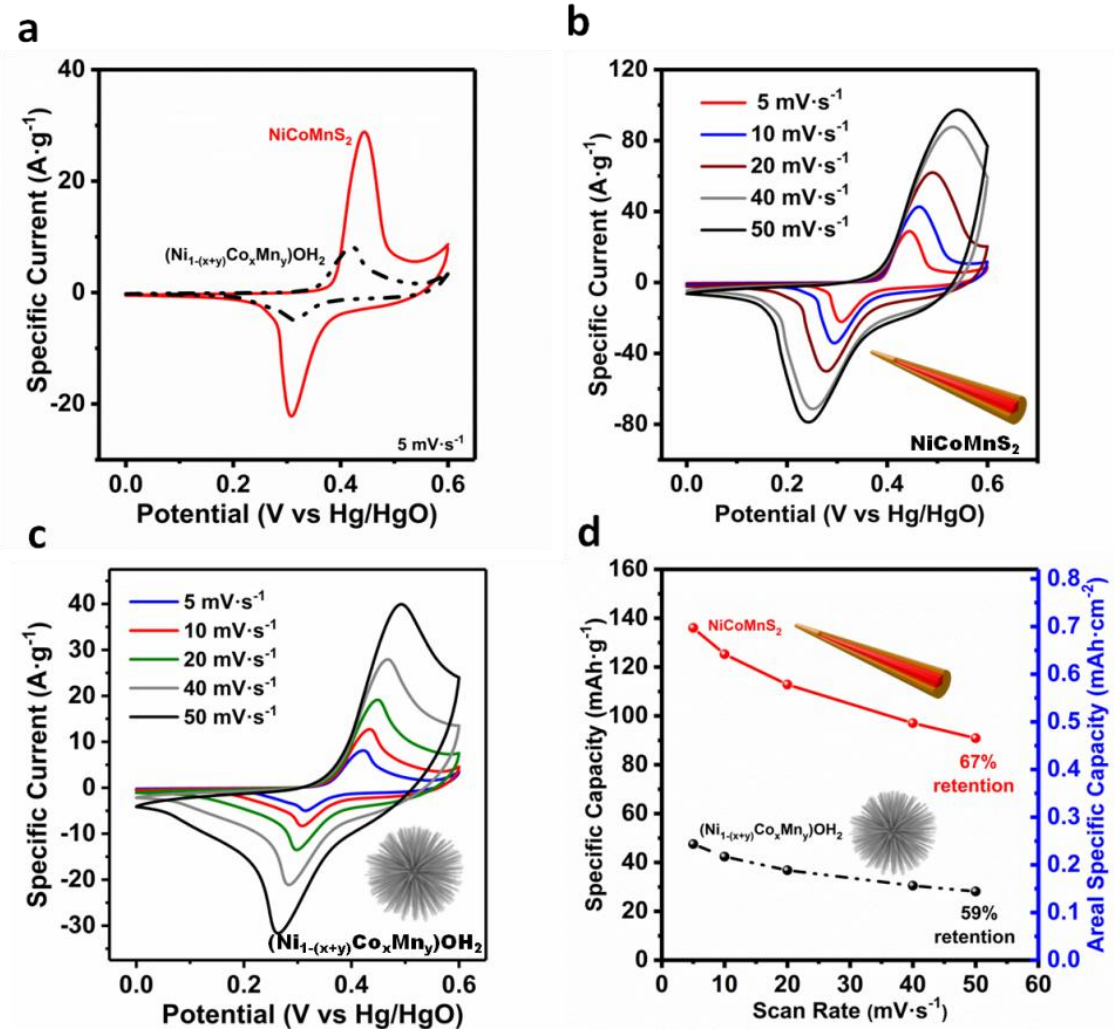

Figure 8.11 (a) CV curves of $NiCoMnS_2$ nano-needles and $(Ni_{1-(x+y)}Mn_xCo_y)OH_2$ urchin-like at a scan rate of 5 $mV{\cdot}s^{-1}$ (b) CV curves of the $NiCoMnS_2$ nano-needle at different scan rates (c) CV curves of the $(Ni_{1-(x+y)}Co_xMn_y)OH_2$ sample at various scan rates (d) Rate capability of the samples at various scan rates

While both samples revealed a clear battery-type behavior with well-defined redox peaks, the sulfide exhibited much more pronounced signals evidencing that it provides much larger specific capacity, probably due to its unique morphology and structural phase. Moreover, upon increasing the scan rate in CV from 5 $mV{\cdot}s^{-1}$ to 50 $mV{\cdot}s^{-1}$, the well maintained curve shapes, as shown in ***Figure 8.11b,c*** suggests high rate capability and improved mass transport of the electrodes.[32] Accordingly, ***Figure 8.11d*** shows that the $NiCoMnS_2$ electrode exhibited a high specific capacity of

136 mAh·g^{-1} (0.7 mAh·cm^{-2}) at 5 mV·s^{-1} with a 67% capacity retention (91 mAh·g^{-1}) when the scan rate increased tenfold, demonstrating excellent rate capability of $NiCoMnS_2$, which is remarkable for such a high mass loaded electrode (~5 mg·cm^{-2}). On the other hand, $(Ni_{1-(x+y)}Mn_xCo_y)OH_2$ sample showed lower capacities in all the examined scan rates with a maximum capacity of 48 mAh·g^{-1} at 5 mV·s^{-1} (almost three times less than that of sulfide).

Kinetic parameters were further gained from CV curves (***Figure 8.11b***) to shed light on charge storage phenomena in $NiCoMnS_2$ nano-needles. By plotting log (anodic-cathodic peak current) vs log (scan rate) for $NiCoMnS_2$ electrode (***Figure 8.12a***), a "b-value" of 0.5356 and 0.5609 for cathodic and anodic peak were obtained, respectively, indicating that semi-infinite linear diffusion mainly governs the reaction in $NiCoMnS_2$, according to [Eq. 3.11] in experimental.

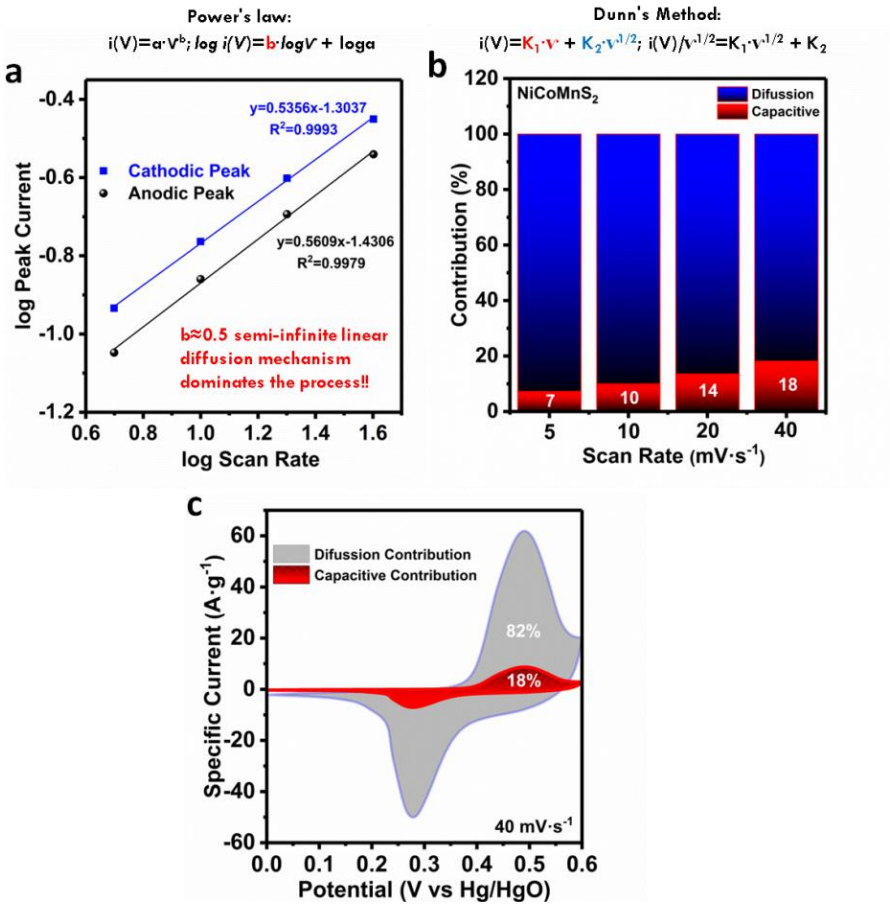

Figure 8.12 (a) Variation between log(i) vs. log (scan rate) for Power's law from the CV curves of $NiCoMnS_2$, (b) contribution percentages for diffusion-limited process and capacitive process for scan rates 5 to 40 mV·s^{-1} in $NiCoMnS_2$ electrode, (c) capacitive and diffusion-controlled contribution to charge storage at 40 mV·s^{-1}

On the other hand, by calculating both k_1 and k_2 constants according to Dunn´s method, [Eq. 3.12] in experimental, we could find current contributions from capacitance and diffusion (***Figure 8.12b***), revealing the dominance of diffusion-controlled reactions. With more careful look one can readily notice that the capacitive contribution is enhanced with increased scan rate, resulting in a maximum value of 18% at 40 $mV{\cdot}s^{-1}$. Being more representative, in ***Figure 8.12c*** one can appreciate the overall visualization of capacitive and diffusion contributions at 40 $mV{\cdot}s^{-1}$ for $NiCoMnS_2$ nano-needles.[33]

In good agreement with CV analysis, GCD profiles performed in 3-electrode electrochemical cells showed pronounced potential plateaus between 0.3 and 0.4 V corroborating the faradaic origin of the charge storage phenomenon ***(see Figure 8.13)***. Moreover, the nearly symmetric charge and discharge curves in ***Figure 8.13*** imply excellent reversibility and coulombic efficiency in both materials. Also in good agreement with CV analysis, charge-discharge profile of $NiCoMnS_2$ nano-needle electrode showed significant longer discharge time in comparison with that of the $(Ni_{1-(x+y)}Mn_xCo_y)OH_2$ urchin-like electrode. Accordingly, at a current density of 1 $A{\cdot}g^{-1}$ a higher specific capacity of 138 $mAh{\cdot}g^{-1}$ (0.71 $mAh{\cdot}cm^{-2}$) was obtained for the $NiCoMnS_2$ nano-needles against 36 $mAh{\cdot}g^{-1}$ (0.18 $mAh{\cdot}cm^{-2}$) for $(Ni_{1-(x+y)}Mn_xCo_y)OH_2$.

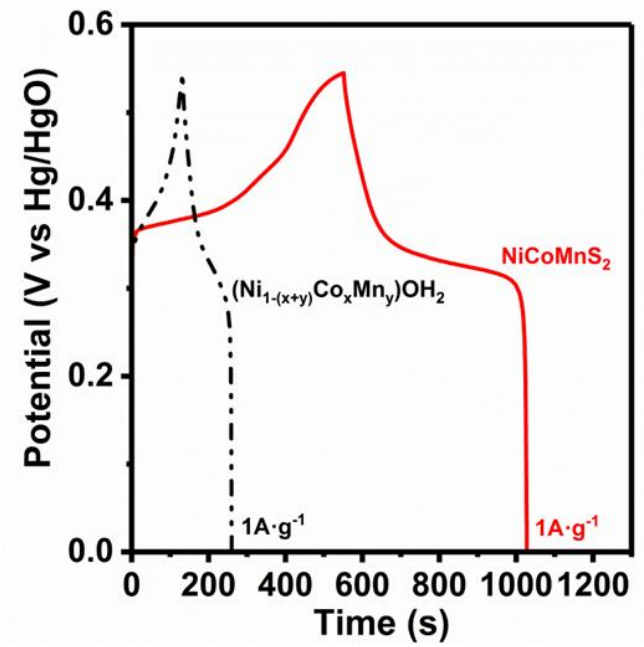

Figure 8.13 Galvanostatic charge-discharge profiles (GCDL) of the samples at a specific current of 1 $A{\cdot}g^{-1}$

Table 8.1 compares the energy storage performance of our $NiCoMnS_2$ nano-needle with respect to that of previously reported similar works in literature. It can be seen that the $NiCoMnS_2$ nano-needles displayed superior or comparable performance (e.g. in terms of specific capacity) even though employed higher mass loaded electrodes. This suggests $NiCoMnS_2$ nano-needles as high performance positive electrode materials for practical uses.

Table 8.1 Comparison of the electrochemical properties of the $NiCoMnS_2$ with some previous corresponding reports of mixed metal oxides or sulfides

Sample	Electrolyte	Synthesis Method	Specific Capacity ($mA.h.g^{-1}$)	Areal Capacity ($mA.h.cm^{-2}$)	Potential Window (V)	Mass Loading ($mg.cm^{-2}$)	Ref.
$NiCoMnS_2$ Nanoneedles	**3M KOH**	**Hydrothermal**	**138 @ 1 $A{\cdot}g^{-1}$**	**0.72**	**0.6**	**5.2**	**This work**
$NiCoMnO_4$ Nanowire	6M KOH	Hydrothermal	88 @ 1 $A{\cdot}g^{-1}$	0.16	0.5	1.8	[34]
$NiCo_2S_4$-rGO	6M KOH	Hydrothermal + Freeze-dried	137 @ 1 $A{\cdot}g^{-1}$	-	0.45	-	[35]
$NiCo_2S_4$ Nanosheets	3M KOH	Hydrothermal	103 @ 1 $A{\cdot}g^{-1}$	0.103	0.5	1	[9]
$NiCo_2S_4$ Nanoparticles	6M KOH	Hydrothermal	75 @ 1 $A{\cdot}g^{-1}$	0.37	0.5	5	[36]
$NiCo_2S_4$ ball-in-ball hollow spheres	6M KOH	Hydrothermal	129 @ 1 $A{\cdot}g^{-1}$	0.64	0.45	5	[5]
NiCoMnS Nanosheets	2M KOH	Cathodic Electrodeposition	286 @ 1 $A{\cdot}g^{-1}$	0.23	0.4	0.8	[37]

Excellent electrochemical performance of $NiCoMnS_2$ sample could be mainly ascribed to their unique morphology, comprising vertically oriented 1D nano-needle directly grown on to Ni foam (NF). This facilitates reversible and fast redox reactions in a large number of accessible electroactive sites and provides shorter ion transport pathways while enhancing electrode-electrolyte contact.[38]

To further investigate the electrochemical performance of the as-synthesized samples, electrochemical impedance spectroscopy was conducted. It can be observed from the Nyquist Plots in ***Figure 8.14a*** that overall impedance of $NiCoMnS_2$ sample is much smaller than that of $(Ni_{1-(x+y)}Mn_xCo_y)OH_2$. Moreover, uncompensated resistance (R_s) of the sulfide sample; calculated by the intersection of the curve with the X-axis in the Nyquist Plot, is clearly lower than hydroxide sample (***Figure 8.14b***) which demonstrates its better electrical conductivity.

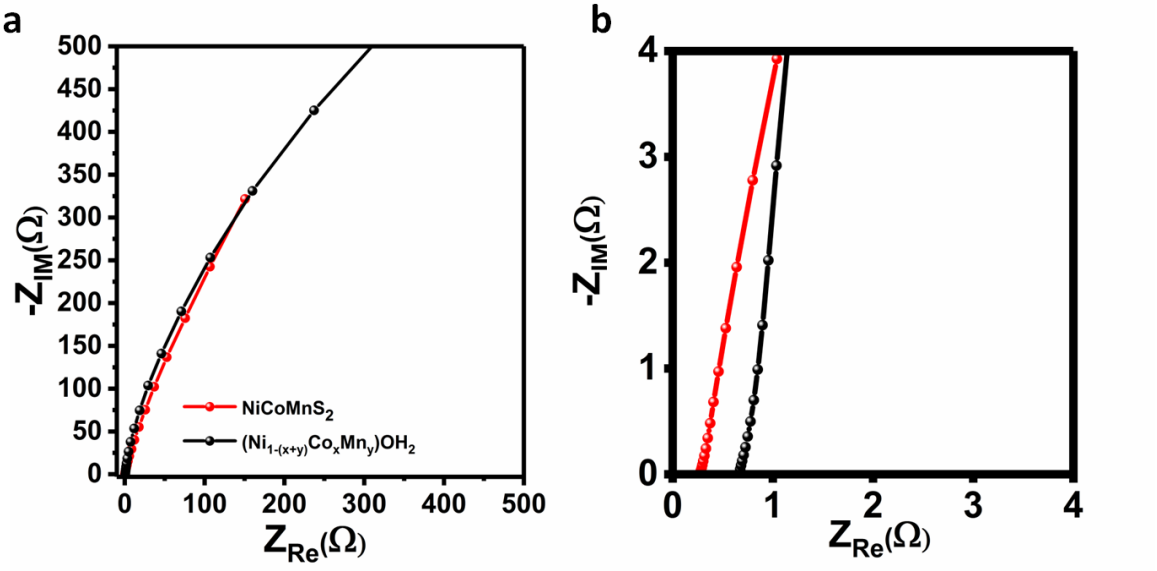

Figure 8.14 (a) Nyquist plot of the as-prepared $NiCoMnS_2$ and $(Ni_{1-(x+y)}Co_xMn_y)OH_2$ electrode, (b) zoom in the ESR of the Nyquist Plot

One of the key parameters for electrode materials in any energy storage system is long-term cycling stability. Accordingly, $NiCoMnS_2$ needle-like samples were evaluated under continuous CV cycles at 20 $mV \cdot s^{-1}$, as shown in ***Figure 8.15.***

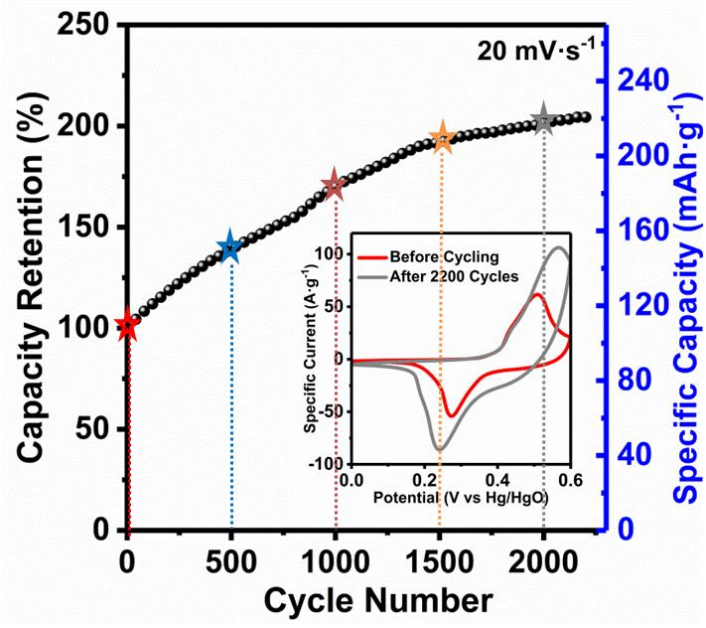

Figure 8.15 (a) Cycling performance of the $NiCoMnS_2$ in three-electrode configuration at 20 $mV \cdot s^{-1}$. Inset shows the CV signals before and after 2200 cycles

Interestingly, it was identified that specific capacity of $NiCoMnS_2$ nano-needle electrodes increases over the first 2000 cycles, reaching an almost steady value of 204 $mAh \cdot g^{-1}$, almost double of the initial capacity (~110 $mAh \cdot g^{-1}$). Inset of the ***Figure 8.15*** shows the CV curves before and after cycling, revealing significant enhanced peak currents and integrated area under the curve, justifying the aforementioned observed increase in the stored charge. This appealing performance might be attributed to the electro-activation of the electrode-electrolyte interface and significant increase in accessible active sites for the electrolyte. Although similar behavior has been observed in previous reports and capacity increase attributed to material activation,[39–44] there is no detailed study to illuminate the nature of such electro-activation, specifically in mixed metal sulfides (MMSs).

8.2.3 Elucidation of activation process by Ex-Situ/Operando Studies

In order to shed certain light on the activation phenomenon and the energy storage mechanism in MMSs, ex-situ XRD and Raman measurements were conducted at different states of charge, as shown ***Figure 8.16.*** In ***Figure 8.16b***, no significant change was realized in XRD pattern of heazlewoodite phase upon applying various potential pulses. On the contrary, Raman spectra (***Figure 8.16c***) of the same electrode at different states of charge unveiled the appearance of a broad band around 550 cm^{-1} in the charged state when the faradaic reaction takes place, suggesting the formation of M-OH species.[45,46]

The absence of diffraction peaks corresponding to the hydroxide species in XRD patterns (***Figure 8.16b***) further suggests the amorphous character of the formed hydroxide layer. It can be also appreciated in ***Figure 8.16c*** that the appeared broad band later split in two different peaks when the electrode was cycled up to 2nd cycle, while the bands related to heazlewoodite phase were depressed.

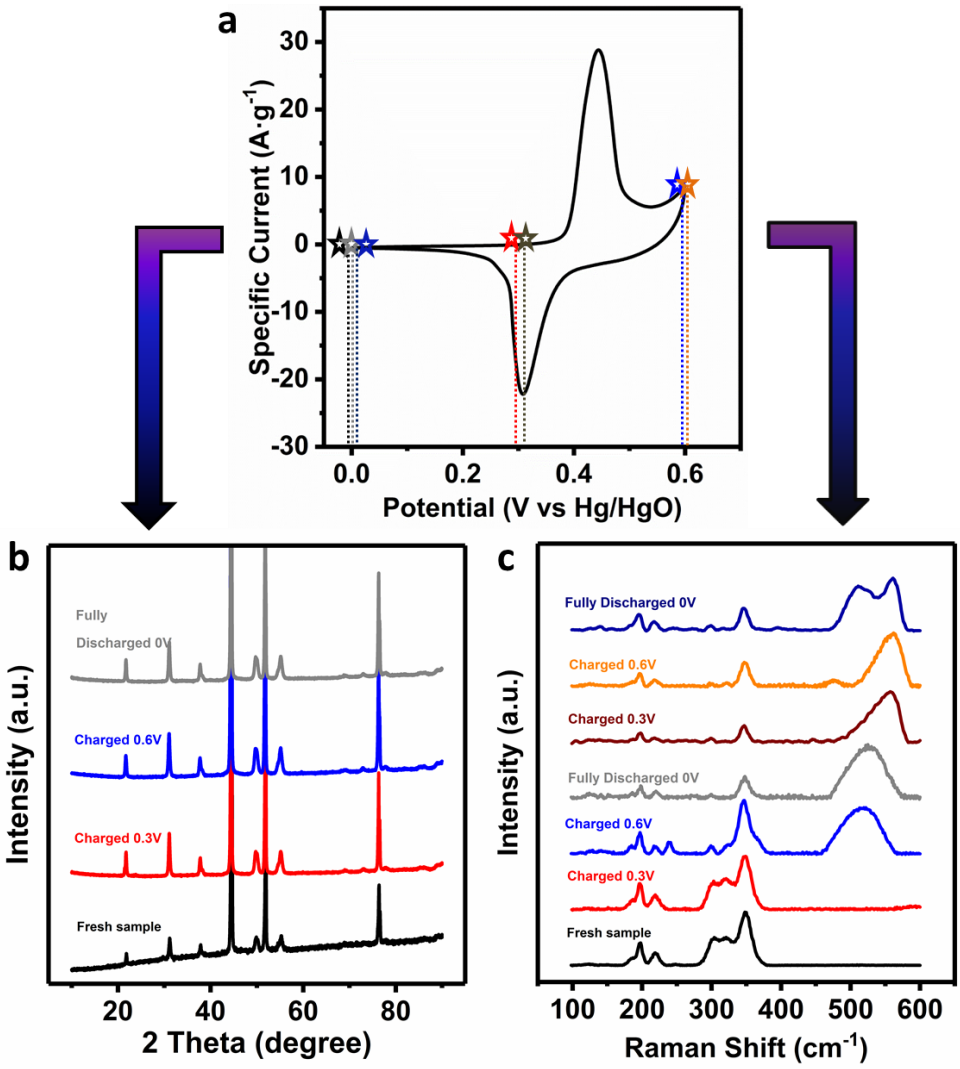

Figure 8.16 (a) CV curve of $NiCoMnS_2$ with various ex-situ points marked at different states of charge (b) XRD of the $NiCoMnS_2$ sample at different states of charge (c) Raman spectra of the $NiCoMnS_2$ sample at different states of charge

In addition, ex-situ XRD and Raman measurements were also carried out at different cycling states, as it is represented in ***Figure 8.17***. After 2000 cycles, the Raman sulfide bands are nearly disappeared (***Figure 8.17a***) while the $NiCoMnS_2$ characteristic diffraction peaks could be readily distinguished even after long cycling, although with lower intensity and higher peak broadness (***Figure 8.17b***). This is possibly attributed to a decrease in the crystallinity of the sulfide as well as the formation and growth of the amorphous hydroxide layer on top of the sulfide.

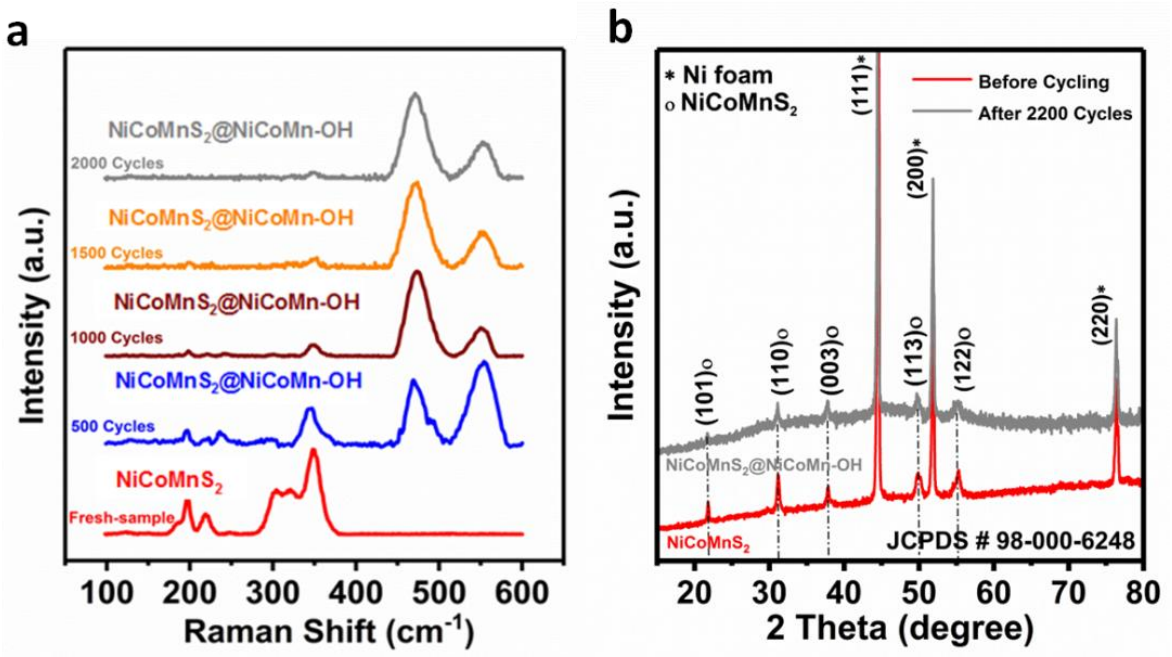

Figure 8.17 (a) Raman spectra of the $NiCoMnS_2$ electrode and formation of $NiCoMnS_2$@NiCoMn-OH at different cycle numbers. (c) XRD patterns before and after long cycling

Moreover, it could be seen in ***Figure 8.17a*** that two clear peaks appeared after 500 cycles centered at 472 and 555 cm^{-1}, which may be correlated to Co-O vibrations and to Ni-O and/or Mn-O species, respectively,[11,47,48] quite similar to the previously commented splitting of the hydroxide peak into two bands in ***Figure 8.16c***.

In order to track more accurately the possible chemical changes in $NiCoMnS_2$ nano-needles during electrochemical reaction, operando Raman spectroscopy was carried out in a home-made three-electrode cell (***Figure 8.18a***). ***Figure 8.18b*** shows the operando Raman spectra of $NiCoMnS_2$ sample collected at different applied potentials during CV cycles (oxidation-reduction) with a scan rate of 2 $mV \cdot s^{-1}$. As it is observed and in agreement with observed ex-situ results, above 0.45 V during the first charge (once the faradaic reaction takes place), the broad band corresponding to the amorphous hydroxide layer is appeared. Subsequently, although the wide hydroxide band experiences changes (e.g. splitting and peak ratio changes) but it does not completely disappear upon discharge, suggesting quasi-reversibility of the sulfide-hydroxide conversion. This quasi-reversible conversion can be further identified by reduced and increased intensity of sulfide peaks, during oxidation and reduction processes, respectively. However, it should be noticed that sulfide

bands decreased in general over the whole cycling, which is in concordance with the ex-situ Raman after long cycling in ***Figure 8.17a***.

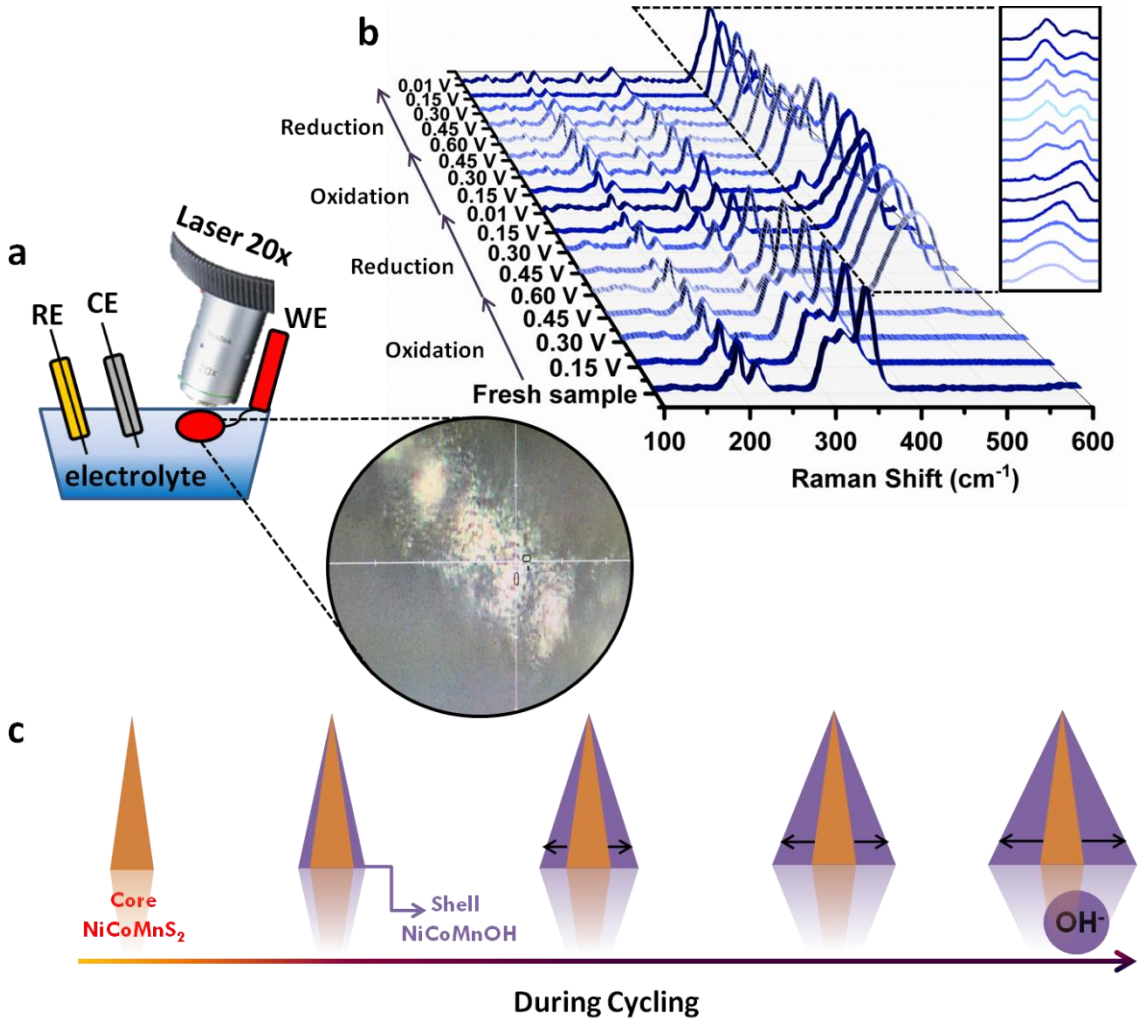

Figure 8.18 (a) Schematic representations of operando Raman setup along with the acquired optical image (b) Operando Raman spectra of the $NiCoMnS_2$ electrode collected during oxidation and reduction in two consecutive cycles (c) Schematic illustration of the formation of $NiCoMnS_2$@NiCoMn-OH hierarchical core-shell structure in the course of cycling

In spite of the fact that the reversible potentials of the $NiCoMnS_2$ are difficult to be determined, it is likely that $NiCoMnS_2$ is first oxidized to $NiCoMnSOH^-$ which later can be quasi-reversibly converted to mixed sulfide again, resulting in re-rising of the heazlewoodite Raman bands during discharge. Afterwards, the already mentioned splitting of the sulfo-hydroxide band into two peaks may be explained to formation of single metal hydroxide phases due to preferential phase conversion rates. This single metal hydroxides are demonstrated to be more stable than their

sulfide counterparts under alkaline conditions justifying the overall intensity reduction of the mixed metal sulfide bands over consecutive cycling.[49,27] ***Figure 8.18c*** depicts a schematic illustration of the hierarchical core-shell formation process ($NiCoMnS_2$@NiCoMn-OH) during cycling. All the obtained results from ex-situ and operando characterization, demonstrates the formation and growth of amorphous (M–OH; M=Ni, Co, Mn) layer (shell) on the surface of the $NiCoMnS_2$ (core), which is likely responsible for electrochemical signal activation observed during cycling in ***Figure 8.15***.

To further investigate structural and morphological evolution upon cycling and evidence possible formation of the already mentioned core-shell structure, TEM measurements were conducted coupled with elemental areal/line mapping on fresh electrodes as well as the one cycled for 2200 consecutive charge-discharge. ***Figure 8.19a*** shows a dark-field image of an isolated $NiCoMnS_2$ nano-needle before cycling with its corresponding STEM elemental mapping of sulfur (***Figure 8.19b***) and oxygen (***Figure 8.19c***). As it is seen, the nano-needle structure is mainly comprised of mixed metal sulfide while certain amount of oxygen signal could be collected at the edges, which likely originated from possible long acquisition time and sample destruction with the electron beam. This can be clearly observed in line mapping curve shown in ***Figure 8.19d***. On the other hand, a dark-field image of $NiCoMnS_2$ nano-needle after cycling (***Figure 8.19e***) clearly showed that the nano-needle surface is not smooth after cycling but it hosts tiny nano-sheets surrounding the metal sulfide core. As proved in the ***Figure 8.19f-h***, the core is mainly comprised of mixed metal sulfide while the thick shell bears a significant concentration of oxygen which is in agreement with the hypothesis of formation and growth of the hydroxide shell on top of the mixed metal sulfide. This structural change can be clearly observed in the line mapping shown in ***Figure 8.19h*** which in comparison with the one before cycling (***Figure 8.19d***) reveals higher concentration of oxygen at the shell. ***Figure 8.19i-j*** depicts the STEM elemental mapping of transition metals (Ni, Co and Mn) for samples before and after cycling showing their homogeneous distribution all along the nano-needles.

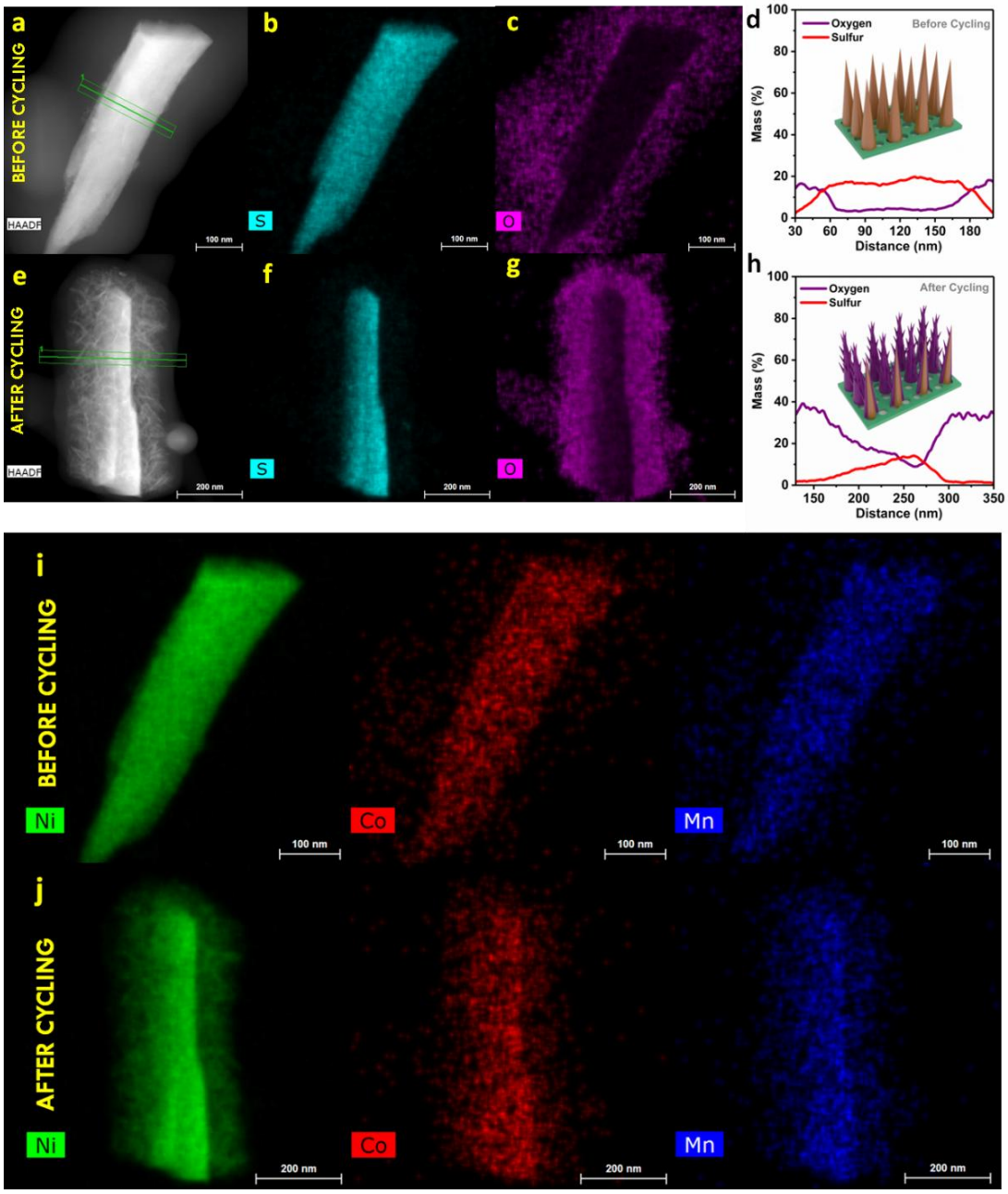

Figure 8.19 (a) Dark-field TEM image of a single $NiCoMnS_2$ nano-needle before cycling and (b,c) its corresponding STEM elemental mappings for S and O. (d) Elemental line scans across the diameter of $NiCoMnS_2$ nanoneedle before cycling. (e) Dark-field image of a $NiCoMnS_2$ nano-needle after cycling and (f,g) its corresponding STEM elemental mappings; (h) Elemental line scans across the $NiCoMnS_2$ nano-needle after cycling. The inset shows a schematic representation of the core–shell structure formation (i) STEM elemental maps of Ni, Co and Mn before cycling, (j) STEM elemental maps of Ni, Co and Mn after cycling

The formation of tiny nano-sheets of NiCoMn-OH around the sulfide core can easily justify the enhancement in capacity during cycling through enhanced accessible surface to the electrolyte and decreased ion diffusion path as seen schematically illustrated in ***Figure 8.20***. As it is schematically represented in ***Figure 8.20***, plenty of OH^- (balls represented in red and white) are surrounding the core-shell structure looking for the different ion transfer paths in the course of the electrochemical reaction on $NiCoMnS_2$.

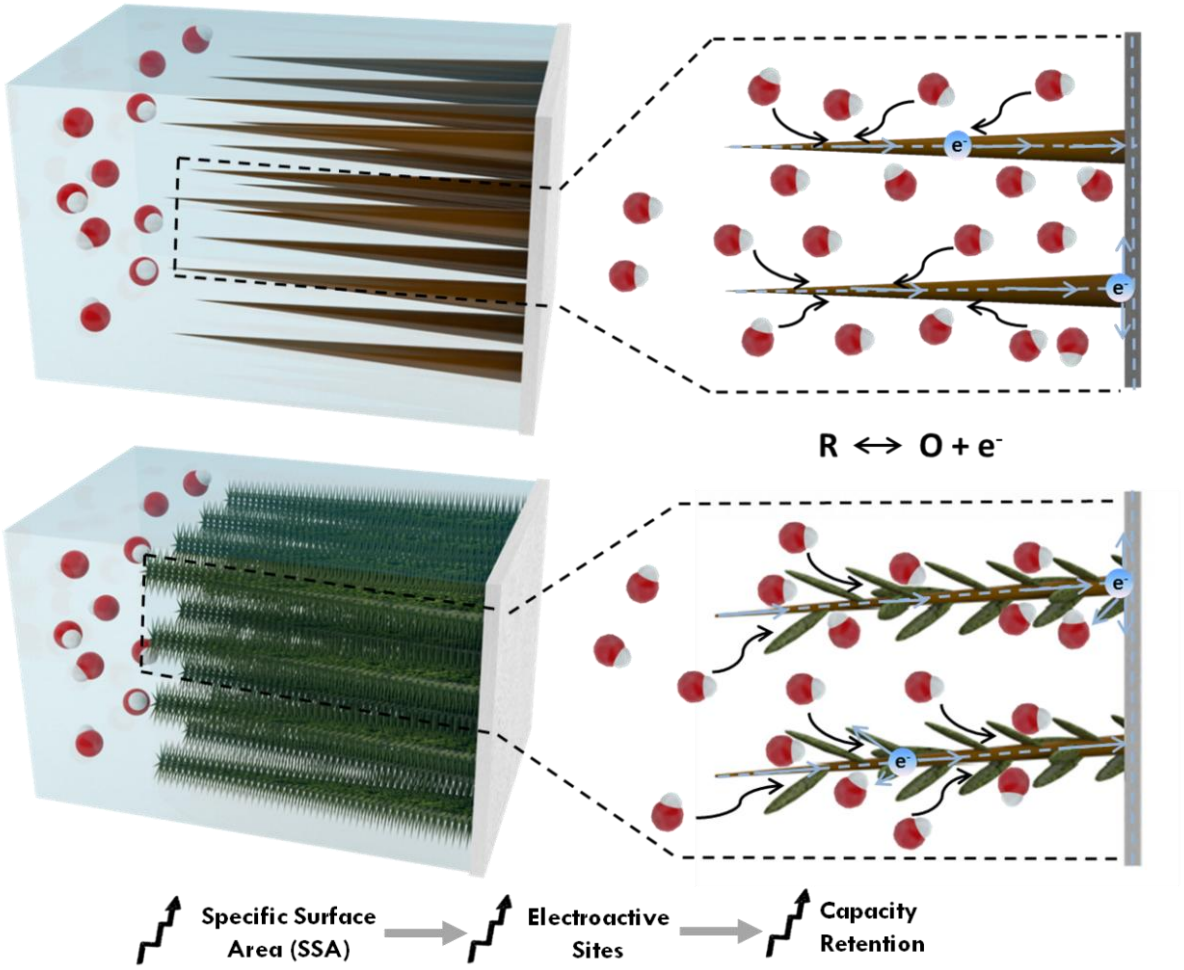

Figure 8.20 Schematic illustration of the ion and electron transfer paths in the course of electrochemical reaction on $NiCoMnS_2$ (upper panel) and the formed core-shell $NiCoMnS_2$@NiCoMn-OH (bottom panel)

In consequence, based on the obtained results (e.g. XPS and operando Raman) described in this work, the following charge storage mechanism can be proposed for heazlewoodite $NiCoMnS_2$ faradaic reactions:

$(Ni_{1.57}Co_{0.79}Mn_{0.64})S_{2(heazlewoodyte)}+OH^- \leftrightarrow 2(Ni_{1.57}Co_{0.79}Mn_{0.64})SOH^- + e^-$ [Eq. 8.1]

$(Ni_{1.57}Co_{0.79}Mn_{0.64})SOH^- \leftrightarrow 1.57\ NiSOH^- + 0.79\ CoSOH^- + 0.64\ MnSOH^-$ [Eq. 8.2]

$CoSOH + OH^- \leftrightarrow CoSO + H_2O + e^-$ [Eq. 8.3]

$MnSOH + OH^- \leftrightarrow MnSO + H_2O + e^-$ [Eq. 8.4]

The charge storage in heazlewoodyte phase is likely governed by a two-step reaction, where firstly conversion of $(Ni_{1.57}Co_{0.79}Mn_{0.64})S_{2(heazlewoodyte)}$ occurs and sulfo-hydroxide species $NiSOH^-$,$CoSOH^-$ and $MnSOH^-$ are formed. In the second step, transformation of $CoSOH^-$ and $MnSOH^-$ into CoSO and MnSO, respectively are involved during charge and discharge cycles, as we were able to appreciate in the intensity variation of the OH^- peaks in Raman operando ***Figure 8.18b.***

8.2.4 rGO//$NiCoMnS_2$ Hybrid Energy Storage Device

Considering $NiCoMnS_2$ electrodes for practical application, the development of hybrid energy storage devices as we previously addressed in introduction chapter, is an ideal route to increase the energy and power density of common SCs and batteries, respectively. Reduced graphene oxide (rGO) was prepared by our previously reported method and it was employed as negative electrode material.[50] This hybrid device (***Figure 8.21a***) benefits from a high redox-capacity $NiCoMnS_2$ nano-needle electrode and a high power carbon-based electrode (rGO), extending the potential window to the sum of positive and negative electrodes (1.6 V) and ensuring high performance of the final device in alkaline media (3M KOH). The mass loading of the positive and negative electrodes in the hybrid device was adjusted employing the charge balance theory as usual $(m^-/m^+) = 3.77$***,*** according to [Eq. 3.13]. ***Figure 8.21b*** displays the CV curves of the $NiCoMnS_2$ nano-needle and rGO electrodes at 5 $mV{\cdot}s^{-1}$ in three electrode configuration. As can be clearly seen, the CV curve is nearly rectangular in rGO electrode, revealing the EDLC charge storage contribution, which is typical in carbonaceous materials. ***Figure 8.21c*** shows the CV curves of the rGO//$NiCoMnS_2$ hybrid device at different scan rates, demonstrating insignificant redox peak shifts from 5 to 100 $mV{\cdot}s^{-1}$ scan rates, revealing the high rate capability and reversibility of the hybrid device. Specific capacities of the full device were calculated based on CV curves and were plotted

in ***Figure 8.21d***, showing that hybrid device provided a high capacity of 41 mAh·g^{-1} (0.34 mAh·cm^{-2}) at 5 mV·s^{-1} scan rate and still retained 54% of initial capacity at high scan rate of 100 mV·s^{-1}.

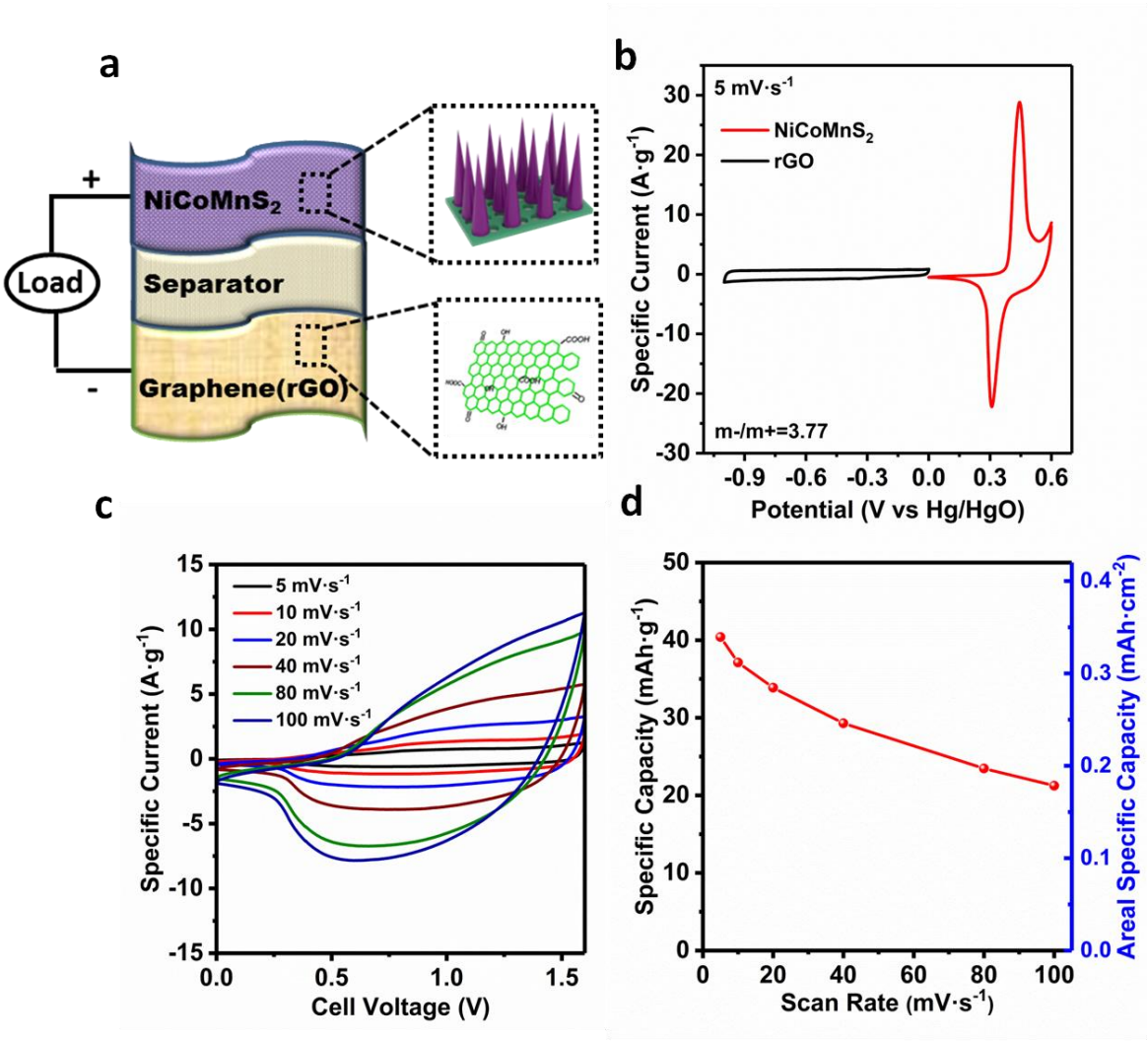

Figure 8.21 (a) Scheme Hybrid Device (b) CV curves of the negative rGO and positive $NiCoMnS_2$ in three-electrode configuration (c) CV curves of the $NiCoMnS_2$//rGO hybrid device at different scan rates (d) Rate capability of the rGO NSs//$NiCoMnS_2$ hybrid device at different scan rates

GCD experiments were conducted at various discharge current densities ranging from 0.5 to 20 A·g^{-1}, as shown in ***Figure 8.22a.*** The nearly symmetrical shapes of the charge-discharge profiles suggest an excellent rate capability and a very low iR drops revealing low internal resistance of the device. As shown in ***Figure 8.22b***, our device exhibits a specific capacity of 44 mAh·g^{-1}(0.36 mAh·cm^{-2}) at minimum current density of 0.5 A·g^{-1} with a 56% capacity retention at an ultrahigh current density of 20 A·g^{-1}, confirming its excellent rate capability behavior.

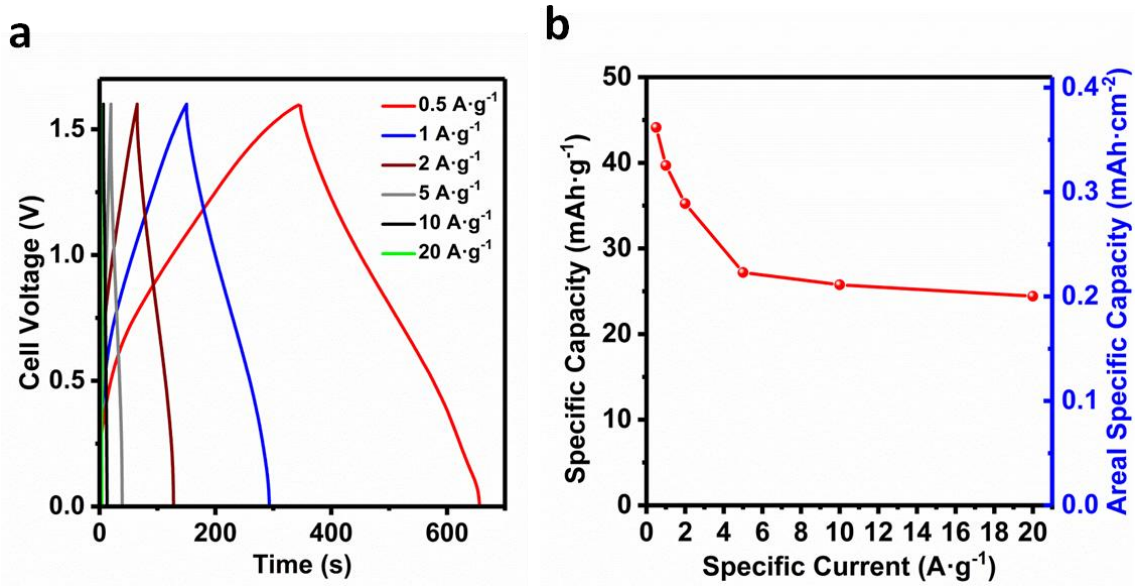

Figure 8.22 (a) GCD profiles of the $NiCoMnS_2$//rGO hybrid device at different specific currents (b) Rate capability of the $NiCoMnS_2$//rGO hybrid device at different current densities

The electrochemical response of individual electrodes in the full cell was monitored via a Hg/HgO reference electrode placed in a T-shape Swagelok® cell at discharge current density of 0.25 $A \cdot g^{-1}$ to make sure that the charge of electrodes are well balanced by adjusting the mass of electrodes; the signals for positive and negative electrodes are shown in ***Figure 8.23.***

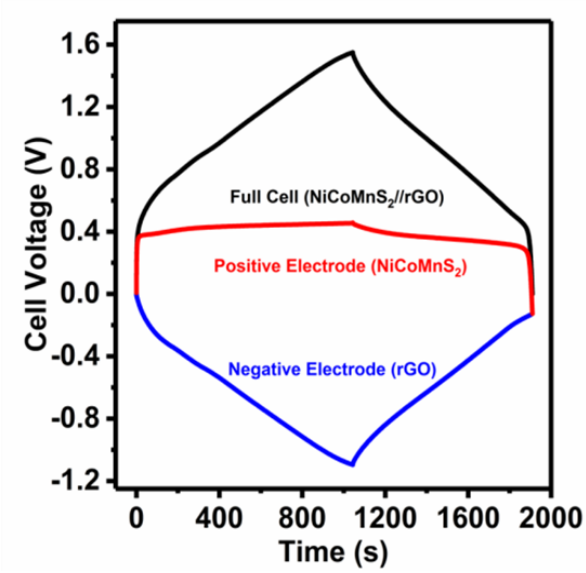

Figure 8.23 Behavior of individual electrodes in the full cell monitored via a Hg/HgO reference electrode at a discharge current density of 0.25 $A \cdot g^{-1}$

As can be recognized, each electrode behaved in the same way as it performed in the three-electrode configuration. This behavior corroborates that mass of electrodes are well balanced with each electrode performing in its corresponding potential region. Clearly, the overall profile of the full cell (black line) is a combination of the two charge storage mechanism.

In order to present the general performance of the $NiCoMnS_2$//rGO hybrid energy storage device, its Ragone plot is illustrated in ***Figure 8.24a***.

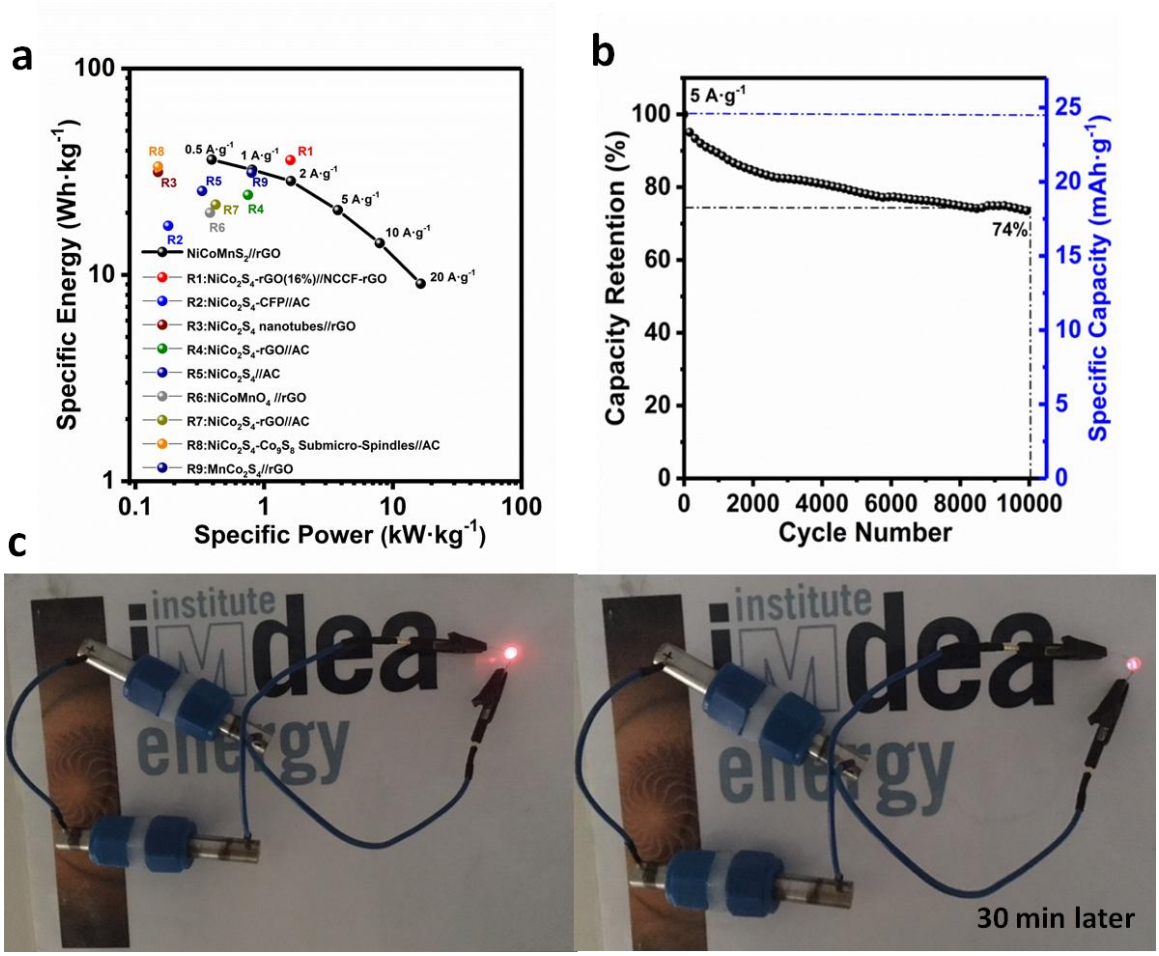

Figure 8.24 (a) Ragone plot of the hybrid energy storage device at various specific currents (b) Cycling performance of the $NiCoMnS_2$//rGO hybrid device at a specific current of 5 $A{\cdot}g^{-1}$ after 10,000 cycles (c) Photographs of red LED powered on by 2 cells in series for a duration more than 30 min

As shown, a high energy density of 36.2 $Wh{\cdot}Kg^{-1}$ at a power density of 0.39 $kW{\cdot}Kg^{-1}$ was calculated at 0.5 $A{\cdot}g^{-1}$, according to [Eq. 3.16] in experimental. Interestingly, by increasing the current load up to 20 $A.g^{-1}$, a very high power of 16.5 $kW{\cdot}kg^{-1}$ is achieved still maintaining an acceptable energy

density of 9.1 $Wh \cdot kg^{-1}$. As noticed, these results showed superior or comparable performance in comparison with previous sulfide-based hybrid devices reported in literature, such as $NiCo_2S_4$-rGO(16%)//NCCF-rGO[35] (36 $Wh \cdot kg^{-1}$ at 1.6 $kW \cdot kg^{-1}$), $NiCo_2S_4$/CFP//AC[51] (17.3 $Wh \cdot kg^{-1}$ at 0.18 $kW \cdot kg^{-1}$), $NiCo_2S_4$ Nanotubes//rGO[52] (31.5 $Wh \cdot kg^{-1}$ at 0.16 $kW \cdot kg^{-1}$) , $NiCo_2S_4$/rGO//AC[53] (24.4 $Wh \cdot kg^{-1}$ at 0.75 $kW \cdot kg^{-1}$), $NiCo_2S_4$//AC[9] (25.5 $Wh \cdot kg^{-1}$ at 0.33 $kW \cdot kg^{-1}$), $NCMO_4$//rGO[54] (20 $Wh \cdot kg^{-1}$ at 0.38 $kW \cdot kg^{-1}$), $NiCo_2S_4$@rGO//AC [55] (21.9 $Wh \cdot kg^{-1}$ at 0.42 $kW \cdot kg^{-1}$), $NiCo_2S_4/Co_9S_8$ Submicro-Spindles//AC [56] (33.5 $Wh \cdot kg^{-1}$ at 0.15 $kW \cdot kg^{-1}$), $MnCo_2S_4$//rGO [57] (31.3 $Wh \cdot kg^{-1}$ at 0.8 $kW \cdot kg^{-1}$). More importantly, among the energy storage devices reported, present one achieved a very high-power density without large energy depletion, framing the device into a novel faradaic-based high power system. Apart from energy and power, a long cycling stability is an important factor also for the practical application of an energy storage device. As shown in ***Figure 8.24b***, cycling stability of the full cell was evaluated by repeated charge-discharge at 5 $A \cdot g^{-1}$ over 10,000 cycles. Since continuous cycles affect the composition, morphology and internal resistance of the cell, a decreased in the cycling stability was observed to 74% with a long cycling of 10k cycles, demonstrating the excellent cycling stability of the device. To demonstrate the viability of our $NiCoMnS_2$//rGO Faradaic-based high power system, two devices were connected in series lighting up a red LED (20 mA) for almost 30 min, as shown in ***Figure 8.24c***.

8.3 Conclusions

In summary, in the present chapter $NiCoMnS_2$ nano-needles were synthesized for the first time and their application as positive electrode in high-performance hybrid energy storage devices was explored. The mixed metal sulfide sample exhibited superior electrochemical performance to its hydroxide analogue, which can be associated to their differences in morphology and crystal structure. A detailed structural and morphological evolution of $NiCoMnS_2$ faradaic electrode upon cycling was examined systematically employing various ex-situ techniques (XRD, Raman and STEM) and operando Raman spectroscopy, resulting in an increased specific surface area, electroactive sites and consequently capacity upon forming the core-shell $NiCoMnS_2$@NiCoMn-OH. Based on the obtained results (e.g. XPS and operando Raman), charge storage mechanism of mixed metal sulfides in alkaline media was proposed. Furthermore, $NiCoMnS_2$ showed excellent performance as a positive electrode when assembled in a hybrid energy storage device with rGO as a negative electrode, exhibiting a high energy density of 36.2 $Wh \cdot Kg^{-1}$ and a maximum power density of 16.5 $kW \cdot kg^{-1}$, with excellent cycling stability after 10k consecutive cycles. Therefore, the present work not only sketches the possible hybridization of SCs and Batteries in an electrochemical device employing mixed metal sulfides as positive electrodes but also provides some insight for a better understanding of the electro-activation process and the charge storage mechanism of these materials in alkaline media.

8.4 References

1 P. Kulkarni, N. Sanna Kotrappanavar, G. R. Balakrishna, D. H. Nagaraju and M. V. V. Reddy, *J. Mater. Chem. A*, 2017, **5**, 22040–22094.

2 X. Y. Yu and X. W. Lou, *Adv. Energy Mater.*, 2017, **8**, 1701592–1701629.

3 H. Chen, J. Jiang, L. Zhang, H. Wan, T. Qi and D. Xia, *Nanoscale*, 2013, **5**, 8879–8883.

4 Y. Xu, X. Gao, W. Chu, Q. Li, T. Li, C. Liang and Z. Lin, *J. Mater. Chem. A*, 2016, **4**, 10248–10253.

5 L. Shen, L. Yu, H. Bin Wu, X. Y. Yu, X. Zhang and X. W. Lou, *Nat. Commun.*, 2015, **6**, 6694–6702.

6 Y. Wen, S. Peng, Z. Wang, J. Hao, T. Qin, S. Lu, J. Zhang, D. He, X. Fan and G. Cao, *J. Mater. Chem. A*, 2017, **5**, 7144–7152.

7 S. E. Moosavifard, S. Fani and M. Rahmanian, *Chem. Commun.*, 2016, **52**, 4517–4520.

8 A. M. Elshahawy, X. Li, H. Zhang, Y. Hu, K. H. Ho, C. Guan and J. Wang, *J. Mater. Chem. A*, 2017, **5**, 7494–7506.

9 Z. Wu, X. Pu, X. Ji, M. Jing, Q. Chen and F. Jiao, *Electrochim. Acta*, 2015, **174**, 238–245.

10 X. Li, Q. Li, Y. Wu, M. Rui and H. Zeng, *Appl. Mater. Interfaces*, 2015, **7**, 19316–19323.

11 S. Sahoo and C. S. Rout, *Electrochim. Acta*, 2016, **220**, 57–66.

12 Z. Zhang, Z. Huang, L. Ren, Y. Shen and X. Qi, *Electrochim. Acta*, 2014, **149**, 316–323.

13 H. Huo, Y. Zhao and C. Xu, *J. Mater. Chem. A*, 2014, **2**, 15111–15117.

14 Y. Chang, Y. W. Sui, J. Q. Qi, L. Y. Jiang, Y. Z. He, F. X. Wei and Q. K. Meng, *Mater. Lett.*, 2016, **176**, 274–277.

15 A. Canbin, O. Xin, W. Chen and W. Xiaoxu, *Electrochim. Acta*, 2015, **174**, 297–301.

16 Z. Li, X. Li, L. Xiang, X. Xie, X. Li, D.-R. Xiao, J. Shen, W. Lu, L. Lu and S. Liu, *J. Mater. Chem. A*, 2016, **4**, 18335–18341.

17 N. R. Chodankar, D. P. Dubal, Y. Kwon and D.-H. Kim, *NPG Asia Mater.*, 2017, **9**, 419–429.

18 J. Liao, P. Zou, S. Su, A. Nairan, Y. Wang, D. Wu, C. P. Wong, F. Kang and C. Yang, *J. Mater. Chem. A*, 2018, **6**, 15284–15293.

19 B. Yang, L. Yu, H. Yan, Y. Sun, Q. Liu, J. Liu, D. Song, S. Hu, Y. Yuan, L. Liu and J. Wang, *J. Mater. Chem. A*, 2015, **3**, 13308–13316.

20 J. M. Falkowski, N. M. Concannon, B. Yan and Y. Surendranath, *J. Am. Chem. Soc.*, 2015, **137**, 7978–7981.

21 J. T. Zhang, S. Liu, G. L. Pan, G. R. Li and X. P. Gao, *J. Mater. Chem. A*, 2014, **2**, 1524–1529.

22 N. Feng, D. Hu, P. Wang, X. Sun, X. Li and D. He, *Phys. Chem. Chem. Phys.*, 2013, **15**, 9924–9930.

23 Z. Zhang, X. Liu, X. Qi, Z. Huang, L. Ren and J. Zhong, *RSC Adv.*, 2014, **4**, 37278–37283.

24 Z. Cheng, H. Abernathy and M. Liu, *J. Phys. Chem. C Lett.*, 2007, **111**, 17997–18000.

25 C. Zhao, Z. Zhang, Q. Wang, S. Min and X. Qian, *RSC Adv.*, 2015, **5**, 63528–63536.

26 W. G. Fateley, N. T. McDevitt and F. F. Bentley, *Appl. Spectrosc.*, 2007, **25**, 155–173.

27 H. D. Lutz, H. Möller and M. Schmidt, *J. Mol. Struct.*, 1994, **328**, 121–132.

28 L. Xie, Z. Hu, C. Lv, G. Sun, J. Wang, Y. Li, H. He, J. Weng and K. Li, *Electrochim. Acta*, 2012, **78**, 205–211.

29 K. O. Oyedotun, M. J. Madito, D. Y. Momodu, A. A. Mirghni, T. M. Masikhwa and N. Manyala, *Chem. Eng. J.*, 2018, **335**, 416–433.

30 M. C. Biesinger, B. P. Payne, L. W. M. Lau, A. Gerson and R. S. C. Smart, *Surf. Interface Anal.*, 2009, **41**, 324–332.

31 X. Han, X. Wu, C. Zhong, Y. Deng, N. Zhao and W. Hu, *Nano Energy*, 2017, **31**, 541–550.

32 S. E. Moosavifard, M. F. El-Kady, M. S. Rahmanifar, R. B. Kaner and M. F. Mousavi, *ACS Appl. Mater. Interfaces*, 2015, **7**, 4851–4860.

33 C. Chen, Y. Wen, X. Ji, M. Yan, L. Mai, P. Hu, B. Shan, X. Hu and Y. Huang, *Nat. Commun.*, 2015, **6**, 6929–6937.

34 L. Li, Y. Zhang, F. Shi, Y. Zhang, J. Zhang, C. Gu, X. Wang and J. Tu, *ACS Appl. Mater. Interfaces*, 2014, **6**, 18040–18047.

35 Y. Fan, Y. Liu and X. Liu, *Electrochim. Acta*, 2017, **249**, 1–8.

36 Y. Gao, Q. Lin, G. Zhong, Y. Fu and X. Ma, *J. Alloys Compd.*, 2017, **704**, 70–78.

37 S. Sahoo, R. Mondal, D. J. Late and C. S. Rout, *Microporous Mesoporous Mater.*, 2017, **244**, 101–108.

38 K. P. Annamalai, L. Liu and Y. Tao, *J. Mater. Chem. A*, 2017, **5**, 9991–9997.

39 A. Pendashteh, J. Palma, M. Anderson and R. Marcilla, *J. Mater. Chem. A*, 2015, **3**, 16849–16859.

40 S. K. Meher and G. R. Rao, *J. Phys. Chem. C*, 2011, **115**, 15646–15654.

41 X. Liu, S. Shi, Q. Xiong, L. Li, Y. Zhang, H. Tang, C. Gu, X. Wang and J. Tu, *ACS Appl. Mater. Interfaces*, 2013, **5**, 8790–8795.

42 R. Dhanabal, A. Chithambararaj, S. Velmathi and A. C. Bose, *ACS Sustain. Chem. Eng.*, 2017, **5**, 4757–4770.

43 Y. Zhu, X. Ji, R. Yin, Z. Hu and X. Qiu, *RSC Adv.*, 2017, **7**, 11123–11128.

44 M. A. Bissett, I. A. Kinloch and R. A. W. Dryfe, *Acc. Chem. Res.*, 2015, **7**, 17388–17398.

45 X. Zou, X. Zou, Q. Sun, Y. Zhang, G. D. Li, Y. Liu, Y. Wu and L. Yang, *Sci. Rep.*, 2018, **8**, 4478–4487.

46 L. Chang, K. Wang, L. A. Huang, Z. He, S. Zhu, M. Chen, H. Shao and J. Wang, *J. Mater. Chem. A*, 2017, **5**, 20892–20902.

47 R. Kostecki and F. Mclarnont, *J. Electrochem. Soc.*, 1997, **144**, 485–493.

48 J. M. Gonçalves, R. R. Guimarães, C. V. Nunes, A. Duarte, B. B. N. S. Brandão, H. E. Toma and K. Araki, *RSC Adv.*, 2016, **6**, 102504–102512.

49 S. R. Shieh and T. S. Duffy, *Phys. Rev. B - Condens. Matter Mater. Phys.*, 2002, **66**, 134301–134309.

50 A. Pendashteh, J. Palma, M. Anderson and R. Marcilla, *RSC Adv.*, 2016, **6**, 28970–28980.

51 X. Xiong, G. Waller, D. Ding, D. Chen, B. Rainwater, B. Zhao, Z. Wang and M. Liu, *Nano Energy*, 2015, **16**, 71–80.

52 H. Chen, J. Jiang, L. Zhang, D. Xia, Y. Zhao, D. Guo, T. Qi and H. Wan, *J. Power Sources*, 2014, **254**, 249–257.

53 Z. Li, X. Ji, J. Han, Y. Hu and R. Guo, *J. Colloid Interface Sci.*, 2016, **477**, 46–53.

54 A. Pendashteh, J. Palma, M. Anderson and R. Marcilla, *RSC Adv.*, 2016, **6**, 28970–28980.

55 F. Wang, G. Li, Q. Zhou, J. Zheng, C. Yang and Q. Wang, *Appl. Surf. Sci.*, 2017, **425**, 180–187.

56 L. Hou, Y. Shi, S. Zhu, M. Rehan, G. Pang, X. Zhang and C. Yuan, *J. Mater. Chem. A*, 2016, **5**, 133–144.

57 S. Liu and S. C. Jun, *J. Power Sources*, 2017, **342**, 629–637.

CHAPTER 9

Anchored $NiCoMnS_4$ Nanoparticles on N-doped rGO: A Bifunctional Electrocatalysts for Rechargeable Zn-Air Batteries

9.1 Research Background

Among all existing and emerging green energy storage/conversion technologies, those consuming atmospheric oxygen (e.g. metal-air batteries) are of great importance due to the fact that one half of the battery is simply air. As it was previously highlighted in Chapter 7, the bottleneck in advancing these technologies is the development of efficient bifunctional electrocatalysts to increase the speed of intrinsically sluggish oxygen reduction (ORR) and evolution (OER) reactions. As mentioned in Chapter 7, different types of materials have been investigated as oxygen electrocatalysts including non-precious metal compounds[1] and different carbonaceous materials.[2]

It has been already demonstrated in previous chapters that combination of rGO or nitrogen doped rGO with metal oxides in a hybrid material enriches their electrochemical performance as compared to pure oxides.[3,4] Accordingly, as described in Chapter 7, N-rGO/Co_3O_4 hybrids were optimized for electrocatalysis application, sketching the advantages of hybridizing a metal oxide with N-doped rGO for reversible oxygen reduction and evolution. On the other hand, the existence of multi-valence transition metals can also enhance the electrocatalytic activity through providing donor-acceptor chemisorption sites for reversible adsorption of the oxygen molecule.[5] Particularly, ternary cobalt oxides have been demonstrated as promising materials for energy applications due to their low Co content and rich electrochemistry. In fact, our group have been one of the pioneers in evaluating ternary nickel cobalt manganese oxides ($NiCoMnO_x$) as electrode materials for hybrid energy storage devices[4] and as highly efficient bifunctional electrocatalysts for oxygen[6], suggesting superior performance of the mixed metal chemistry.

Recently, mixed metal chalcogenides has attracted considerable attention for energy applications due to their interesting and enhanced electronic and electrocatalytic properties as compared to their oxide analogues.[7] Among different chalcogenides, cobalt sulfides are of specific interest as their catalytic activity is predicted to be similar to Pt surfaces.[8] However, in practice, their catalytic performance lags far behind Pt and evidencing that further investigation is needed. Although binary metal sulfides (e.g. $NiCo_2S_4$) have been extensively studied as anode materials in Li-ion or Na-ion batteries,[9,10] as electrode materials for hybrid supercapacitors[11,12] and as electrocatalyst materials for water splitting,[7] there are only a few reports evaluating these sulfides as bifunctional oxygen electrocatalyst for metal-air batteries.[13,14] Additionally, to the best of our knowledge there

is no report on electrochemical characterization of ternary metal sulfides as bifunctional oxygen electrocatalyst for metal-air batteries.

In the present Chapter, we will report the synthesis of spinel ternary mixed metal sulfide ($NiCoMnS_4$) anchored on nitrogen-doped reduced graphene (N-rGO) oxide as highly efficient bifunctional electrocatalysts for ORR and OER. Moreover, the $NiCoMnS_4$/N-rGO hybrid will be used as air-cathode for rechargeable Zn-air batteries.

9.2 Results and discussion

9.2.1 Synthesis and Physico-Chemical Characterization of $NiCoMnS_4$/N-rGO

As detailed in Chapter 3, $NiCoMnS_4$/N-rGO hybrids were synthesized via a facile hydrothermal method, illustrated in ***Figure 9.1***. For a fair comparison, pure $NiCoMnS_4$ and N-rGO samples were prepared using a similar approach by excluding GO and M $(CH_3CO_2)_2$ precursors, respectively.

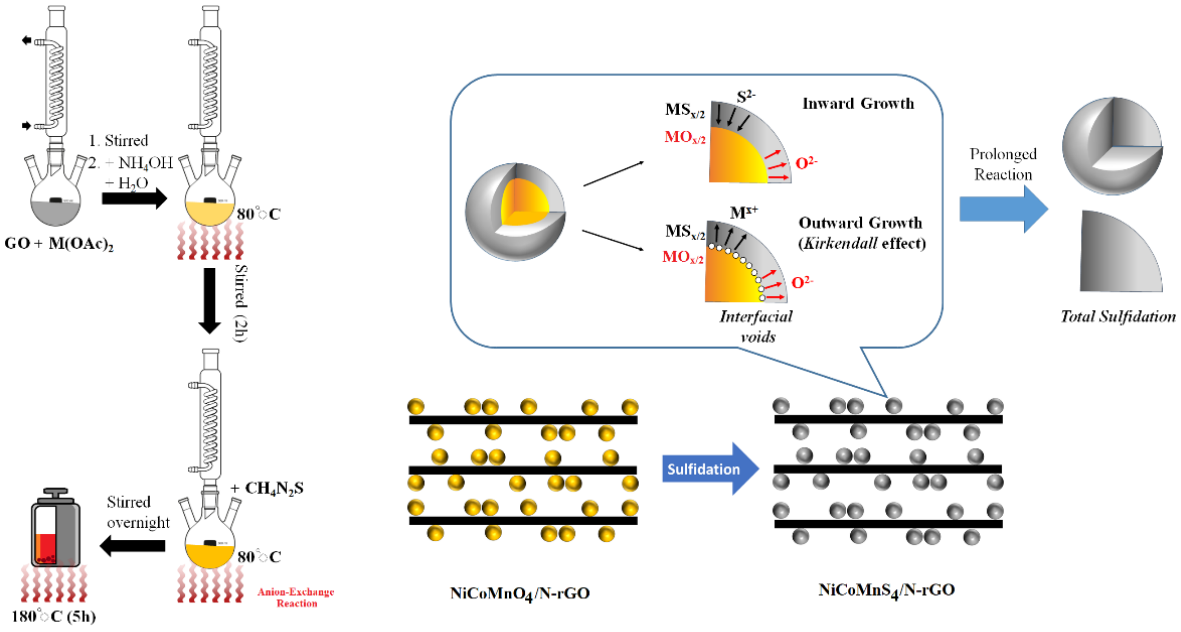

Figure 9.1 Schematic illustration of the synthesis procedure for $NiCoMnS_4$/N-rGO hybrid materials

In the course of synthesis, the negatively charged surface of graphene oxide nanoflakes governs the uniform distribution and anchors the mixed metal cations onto the graphitic network. Later, nucleation of mixed metal hydroxide particles is triggered by addition of ammonia which can be

further converted to metal oxides by aging at 80°C. Lastly, sulfidation proceeds through anion exchange according to the following reactions:[15]

$$M(OH)_2 + (NH_2)_2CS \rightarrow MS + H_2NCN + 2H_2O \quad [Eq. 9.1]$$

$$(NH_2)_2CS + 2H_2O \rightarrow 2NH_3 + CO_2 + H_2S \quad [Eq. 9.2]$$

$$MO + H_2S \rightarrow MS + H_2O \quad [Eq. 9.3]$$

Sulfidation can occur either through an inward or outward growth (depicted in ***Figure 9.1***). In an inward mechanism, sulfur diffuses through metal sulfide layer on the surface while the oxygen atoms are expelled, forming water molecules associated with protons. In the outward route known as Kirkendall growth, both metal cations and O^{2-} diffuse through the metal sulfide layer, resulting in sulfide growth and H_2O molecule release. Relative diffusive migrations stimulate formation of voids in the interface of metal sulfide and metal oxide.[16] Presence of multivalence cations and consequently sulfur vacancies can favor the inward mechanism.[17] On the other hand, prolonged hydrothermal reaction can result in complete sulfidation of metal oxide/hydroxide and a collapsing of the interfacial voids. ***Figure 9.2a*** displays powder X-ray diffraction patterns of $NiCoMnS_4$ and hybrid $NiCoMnS_4$/N-rGO samples.

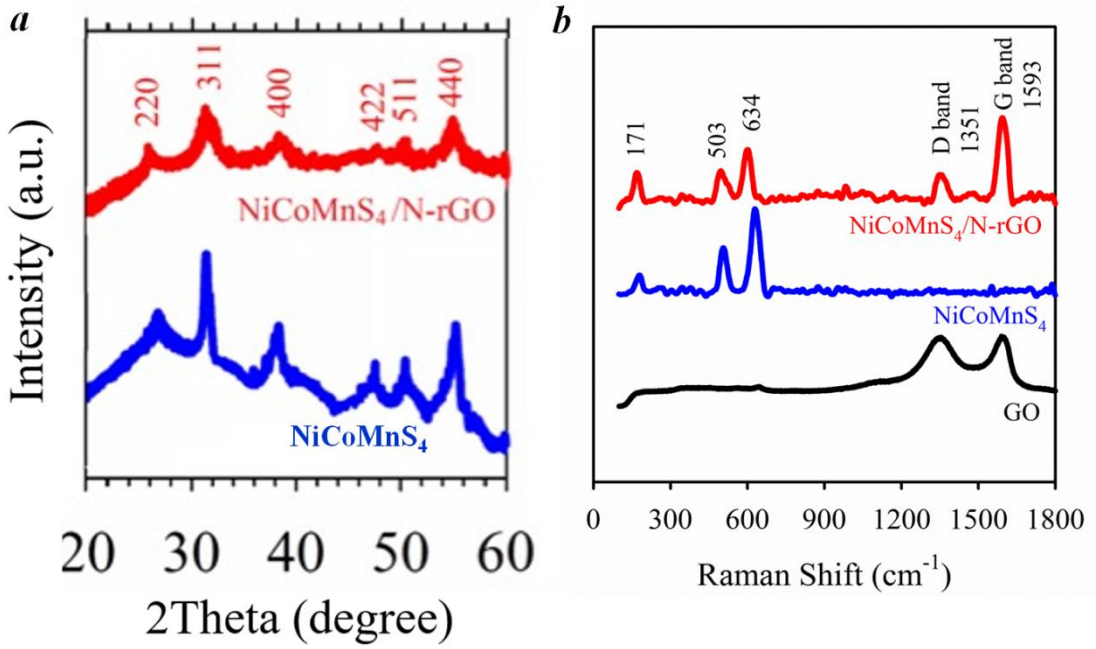

Figure 9.2 (a) XRD pattern of $NiCoMnS_4$ and $NiCoMnS_4$/N-rGO hybrid species (b) Raman spectra of the samples including GO, $NiCoMnS_4$, and $NiCoMnS_4$/N-rGO hybrid

As shown, eight diffraction peaks can be observed in both XRD patterns, ascribed to cubic system with a space group of *Fd-3m*, well in accordance with *JCPDS* card no. 20-0782. Moreover, hybrid sample presents broader peaks and lower intensity, suggesting that the sample is comprised of fine nanocrystals. No other peaks can be found indicating the purity of the as-synthesized samples. Furthermore, the absence of a clear peak in 2θ range of 22 to 28° in the hybrid, typically seen for graphitic diffraction of [002] plane (JCPDS No. 41-1487),[18] can be associated to the enlarged interlayer distance and small graphitic domains in reduced GO. Further evidence of successful GO reduction during synthesis of the hybrid sample to rGO has been provided through Raman spectroscopy (***Figure 9.2b***), where I_D/I_G ratio in the $NiCoMnS_4$/N-rGO sample (I_D/I_G = 0.32) significantly decreased in comparison with that of the GO (I_D/I_G = 0.89).[6] As revealed by Raman results in hybrid and pure $NiCoMnS_4$ sample, three clear peaks can be seen in the range of 100 to 650 cm^{-1}, originating from vibrational mode of metal–S bonds.[19] The presence of similar peaks in the $NiCoMnS_4$/N-rGO hybrid compared to the pure $NiCoMnS_4$ in addition with the D (1351 cm^{-1}) and G (1593 cm^{-1}) bands, corresponding to graphene compound, suggest that the bulk structure of the two components remained intact during the hybridization.

The formation of ternary metal sulfide nanocrystals on N-rGO layers was further probed employing high-resolution transmission electron microscopy (HR-TEM). As observed in ***Figure 9.3a***, N-rGO layers are heavily and uniformly covered by nanocrystals, ranging from 5 to 20 nm in size (marked with red dashed circles). It can be observed that the nanoparticles are slightly denser (or darker) than graphene layers, revealing that the particles are thin as well. As seen in ***Figure 9.3b***, lattice fringes with inter-planar distance of 1.97 and 3.32 Å can be readily distinguished in $NiCoMnS_4$ particles, corresponding to [220] and [111] crystal planes, respectively. These further reveal that cubic $NiCoMnS_4$ is the dominant phase of the mixed metal sulfide nanoparticles. Moreover, HAADF-STEM micrograph (***Figure 9.3c***) and its corresponding EDX mapping images (***Figure 9.3d-i***) disclosed the homogenous distribution of metal cations, and sulfur on carbon network. In addition, mapping of nitrogen (***Figure 9.3e***) shows that the carbon matrix is thoroughly and uniformly doped with N. This is of great importance in electrocatalysis, as nitrogen doping can generate highly active sites for oxygen adsorption.[20] Interestingly, significant porosity could not be distinguished within the nanoparticle domains magnified in ***Figure 9.3b*** suggesting that sulfidation must have proceeded through the inward mechanism. This is in agreement with

previous reports suggesting that the inward path is dominant in the presence of multivalence cations.[17]

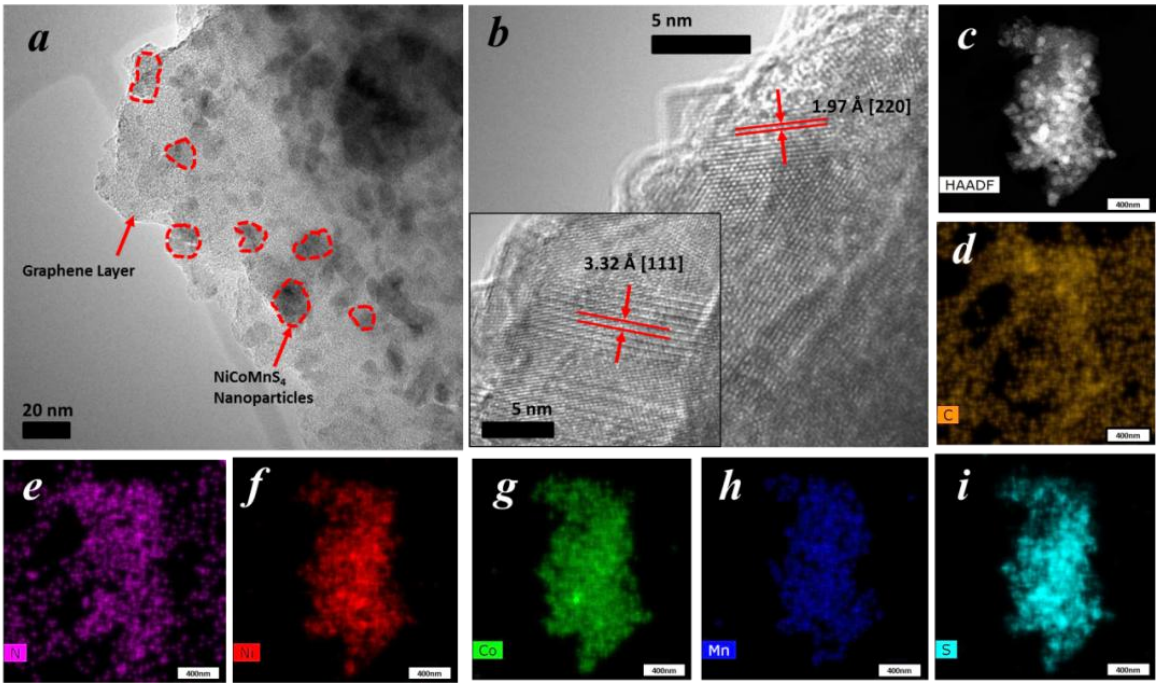

Figure 9.3 (a) TEM micrograph of the $NiCoMnS_4$/N-rGO hybrid showing anchored crystalline sulfide nanoparticles on thin rGO layers, and (b) corresponding HR-TEM image. (c) Wide HAADF-STEM micrograph of the $NiCoMnS_4$/N-rGO hybrid. (d-i) EDX mapping for different elements

Moreover, HR-TEM (***Figure 9.4***) shows that nanoparticles present undefined boundaries suggesting that the surface of the nanocrystals is comprised of a thin amorphous hydrated layer.

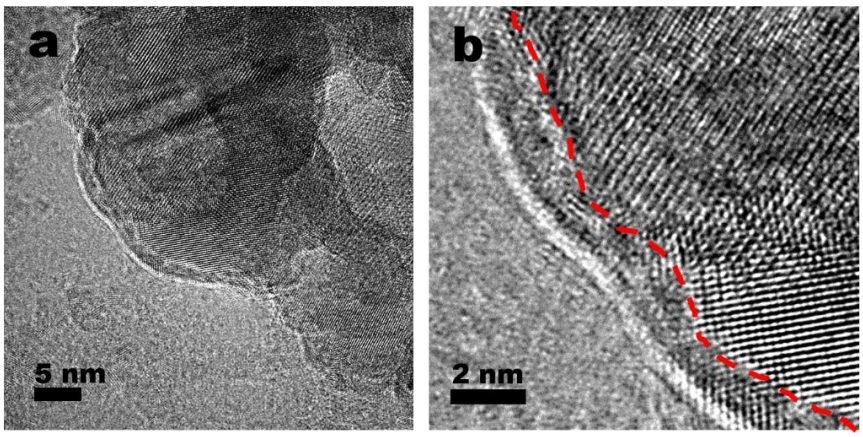

Figure 9.4 HR-TEM micrographs of the $NiCoMnS_4$/N-rGO hybrid showing the crystalline sulfide nanoparticles and the thin amorphous surface layer

X-ray photoelectron spectroscopy (XPS) was further performed to characterize the surface chemical composition, elemental valence states, and nitrogen doping in the $NiCoMnS_4$/N-rGO hybrid. XPS survey spectra for pure sulfide and the hybrid can be seen in ***Figure 9.5a***, indicating the presence of Ni, Co, Mn, S, O and C elements on the surface of samples. Interestingly, the high-resolution O 1s in pure sulfide and hybrid material displayed in ***Figure 9.5b-c***, respectively discloses the absence of any signal in a binding energy of 530 eV, normally seen for lattice oxygen in metal oxides. On contrary, a sharp and intense peak can be realized in a binding energy around 532.1 eV for both pure sulfide and the hybrid sample, which is attributed to metal atoms bound to hydroxyl groups. These results strongly suggest that surface of the synthesized metal sulfide is terminated by M–OH bonds (M = Ni, Co, or Mn).[21,22] The presence of M-O bonds in the distinct metal core levels can be attributed to the possible formation of a very thin hydroxide layer on the surface of metal sulfide in lattice termination edges which may have been developed due to the basic nature of the chemical bath. It should be also mentioned that signal related to the oxide or hydroxide components was not detected either in XRD (***Figure 9.2a***) or Raman (***Figure 9.2b***), suggesting ultrathin and amorphous character of the outer hydroxide layer. This is in good agreement with the observed amorphous surface of the nanocrystals in HR-TEM images depicted in ***Figure 9.4***.

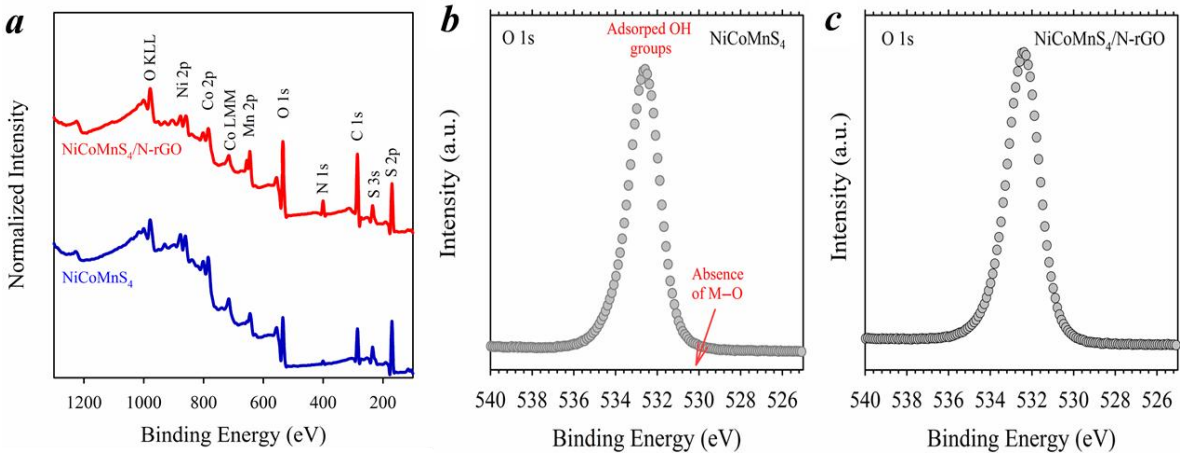

Figure 9.5 (a) XPS survey spectra for $NiCoMnS_4$ and $NiCoMnS_4$/N-rGO hybrid samples. Typical high-resolution O 1s core level for (b) $NiCoMnS_4$ and (c) $NiCoMnS_4$/N-rGO samples

Moreover, the appearance of a new peak in ***Figure 9.5a*** at binding energies close to 400 eV belong to N1s in the hybrid sample further confirms the N-doping of rGO. Based on the area under N 1*s*,

nitrogen content on the surface of $NiCoMnS_4$/N-rGO sample was estimated to be 5.49% (comparable with 6.45% nitrogen according to EDX). The Ni 2p high-resolution spectrum of $NiCoMnS_4$/N-rGO (***Figure 9.6a***) displays three clear peaks in $2p_{3/2}$ region which have been fit into five components associated to Ni^{2+} and Ni^{3+} species and their corresponding shake-up satellite peaks.[23] In the high-resolution spectrum of the Co 2p core level (***Figure 9.6b***), two clear spin-orbit doublets of $2p_{3/2}$ and $2p_{1/2}$ can be readily identified at 782.2 and 797.9 eV, respectively. Analyzing the $2p_{3/2}$ envelope reveals that Co^{2+} is the dominant species on the surface of sample.

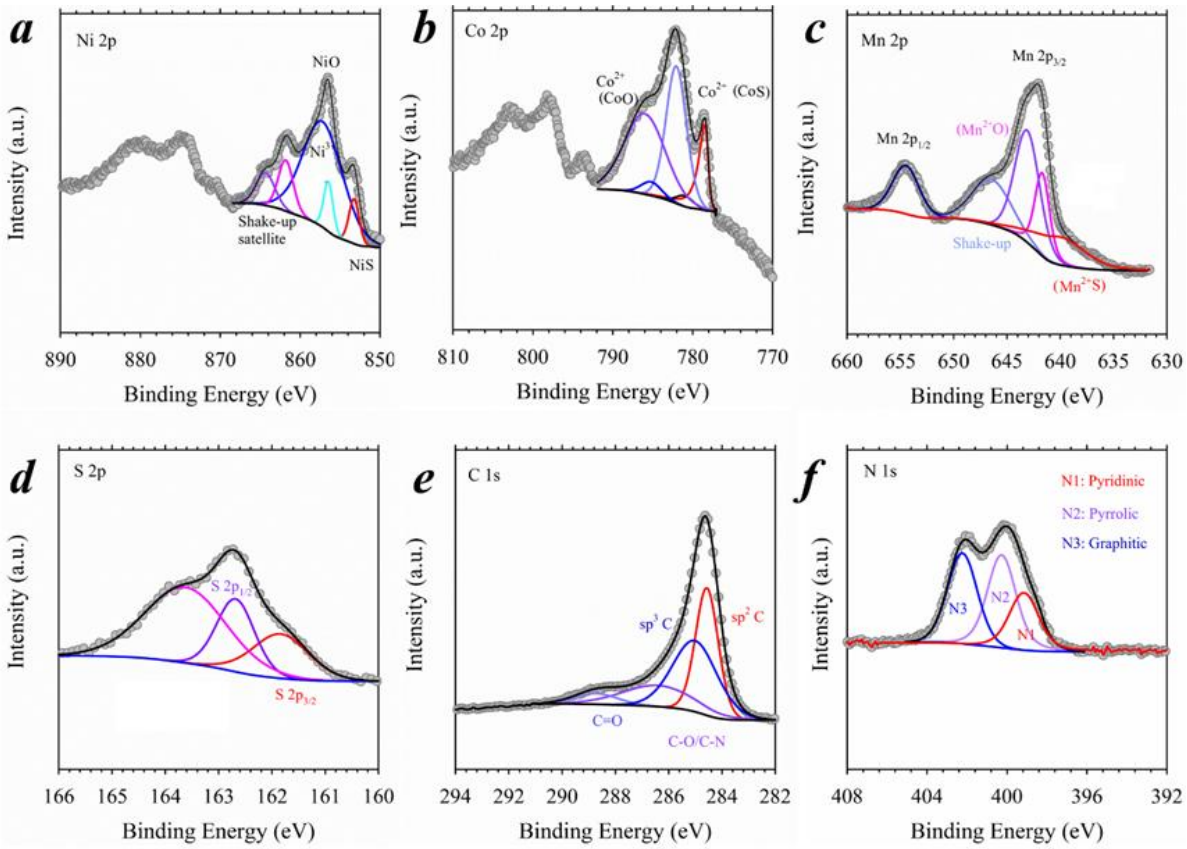

Figure 9.6 XPS surface analysis of $NiCoMnS_4$/N-rGO hybrid: high-resolution of (*a*) Ni 2p, (*b*) Co 2p, (*c*) Mn 2p, (*d*) S 2p, (*e*) C 1s, and (*f*) N 1s envelops

Moreover, ***Figure 9.6c*** depicts the Mn 2p region, consisting of $2p_{3/2}$ centered at 641.9 eV and $2p_{1/2}$ at 654.7 eV. The appearance of an intense peak in the S 2p region (***Figure 9.6d***) suggests the existence of metal sulfide on the surface. The binding energies at 162.7 eV and 161.8 correspond to S $2p_{1/2}$ and S $2p_{3/2}$, respectively, which is in good agreement with literature.[13] ***Figure 9.6e***

depicts the XPS core level of C 1*s*, originating from the rGO content in the hybrid sample. As can be observed, an intense, asymmetric peak appears at 284.6 eV which was later fit to four characteristic components: 284.8 eV (sp^2-hybridized C), 285.1 eV (sp^3 carbon), 286.4 eV (oxygen-containing groups or nitrogen bonded to C), and 288.7 eV (carbonyl or carboxyl C).[2] Moreover, the detailed fitting analysis of Mn $2p_{3/2}$ region together with the clear splitting of 6.0 eV in Mn 3*s* core level (shown in ***Figure 9.7***) reveal Mn^{2+} species are dominant on surface of the sample.[24,25]

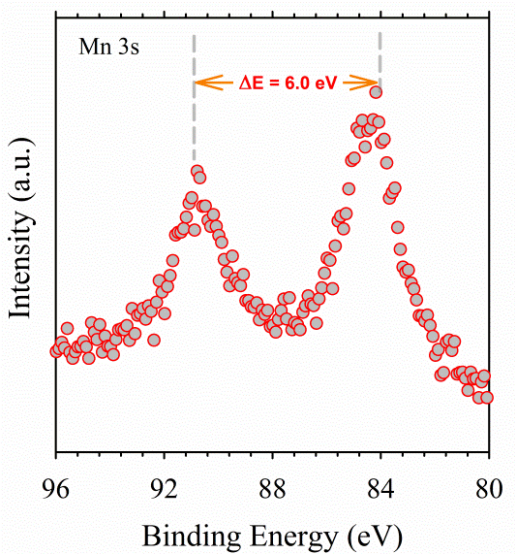

Figure 9.7 High-resolution Mn 3s core level for $NiCoMnS_4$/N-rGO hybrid sample

The presence of the N1s peak *(**Figure 9.6f**)* reveals the successful doping of nitrogen atoms into the carbon framework. The high-resolution XPS spectrum of N1s could be fit into three main components including pyridinic nitrogen (398.5 eV), pyrrolic nitrogen (400.0 eV), and graphitic nitrogen (402.2 eV).[26] Note that the presence of nitrogen in carbon network, particularly pyridinic and graphitic types are of great importance as they can facilitate oxygen adsorption and hydroperoxide decomposition.[20,27] As observed in ***Figure 9.8***, the overall XPS signals for pure sulfide are similar to that obtained for the $NiCoMnS_4$/N-rGO hybrid sample, demonstrating the similar chemical composition of the sulfide nanoparticles in both samples.

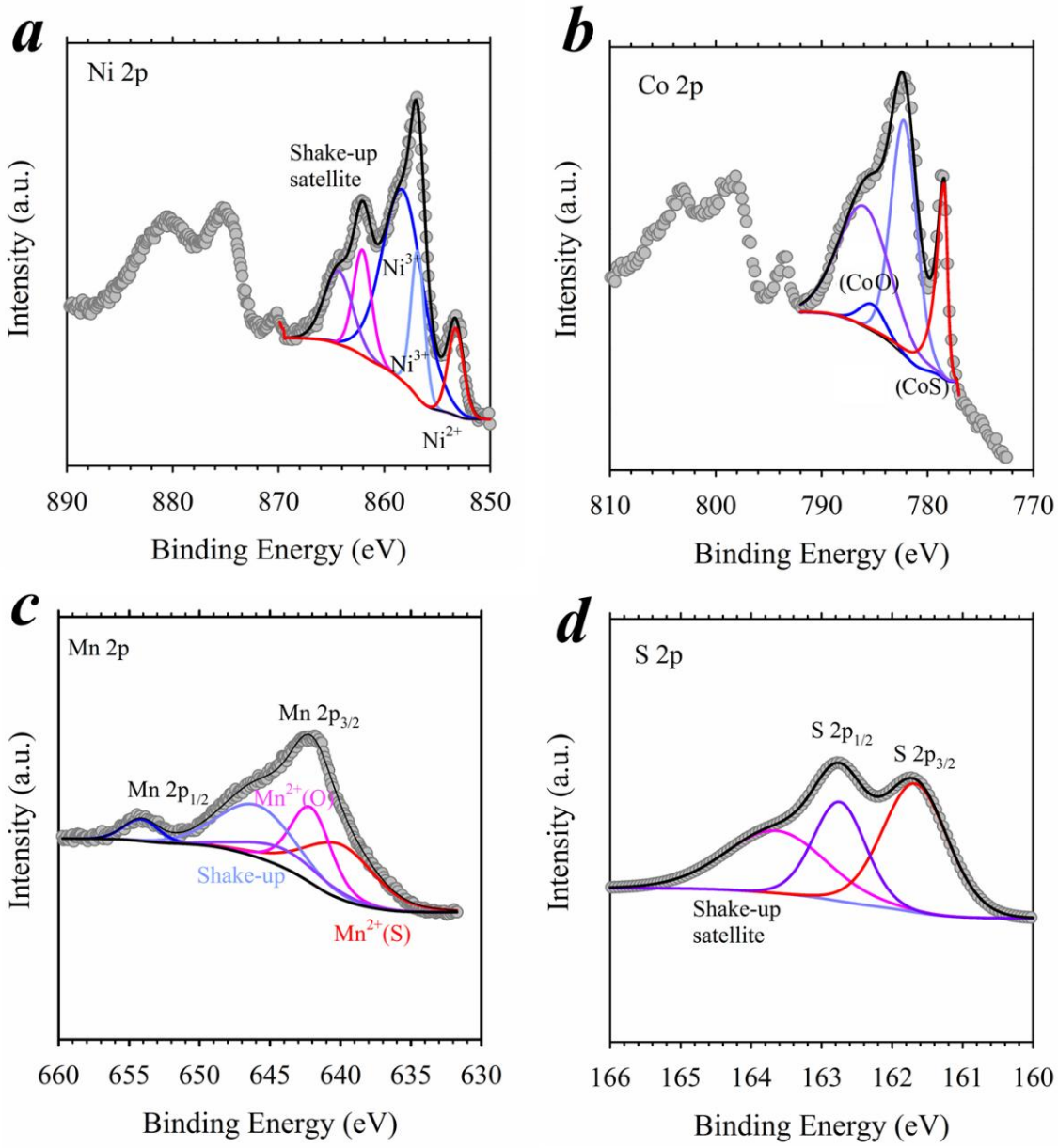

Figure 9.8 XPS surface analysis of $NiCoMnS_4$ sample: high-resolution of (a) Ni 2p, (b) Co 2p, (c) Mn 2p, and (d) S 2p envelops

9.2.2 Electrocatalytic performance of $NiCoMnS_4$/N-rGO

Different hybrid materials were synthesized varying the actual sulfide to carbon ratio; this ratio was corroborated through thermal gravimetric analysis (***Figure 9.9***).

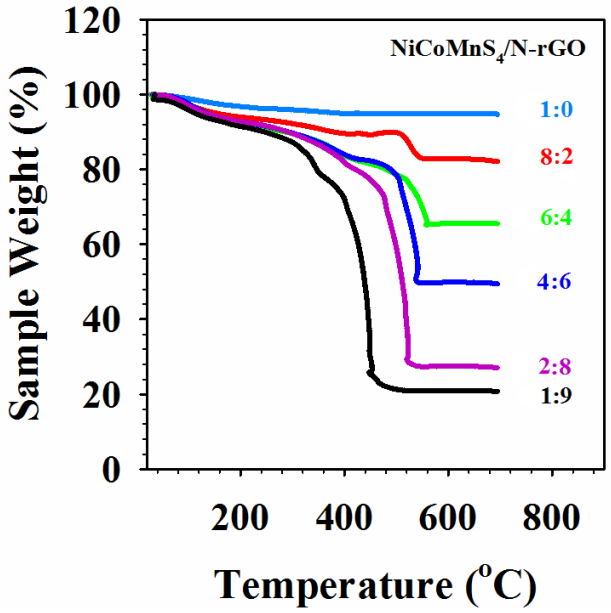

Figure 9.9 TGA analysis of the $NiCoMnS_4$/N-rGO hybrids with different component ratios and a heating rate of 10°C·min^{-1} under air flow

The prepared catalysts were drop casted on GCE (see Experimental chapter) and their electrocatalytic activity was tested in O_2-saturated 0.1M KOH solution. ***Figure 9.10*** displays the LSV curves of different samples recorded at 1500 rpm with a scan rate of 20 mV·s^{-1}.

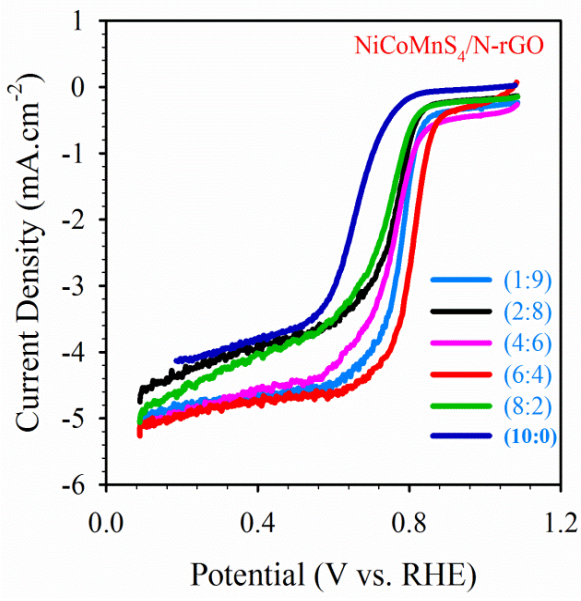

Figure 9.10 LSV curves for $NiCoMnS_4$/N-rGO hybrids with different component ratios at 1500 rpm in O_2-saturaed 0.1 M KOH solution with a scan rate of 20 mV·s^{-1}

As observed, all hybrid samples at different ratios ((1:9), (2:8), (4:6), (6:4), (8:2)) outperformed pure $NiCoMnS_4$ (10:0) in terms of onset potential and limiting current. Moreover, although the limiting current in the minimum content of metal sulfide (1:9) is high, the onset potential is moderate (~0.88 V). Among the prepared five $NiCoMnS_4$/N-rGO hybrids, the sample with 60% of the metal sulfide (6:4) presents the best performance including the more positive onset potential and the largest limiting current. On the other hand, linearity and similar slopes of Koutecky-Levich plots in ***Figure 9.11*** display first-order reaction kinetics with respect to the dissolved oxygen over a broad range of potential. Accordingly, the number of transferred electrons was calculated for the different sample ratios (***Figure 9.11***), revealing an increase by increasing the sulfide content up to a (6:4) composition, reaching a value of 3.96.

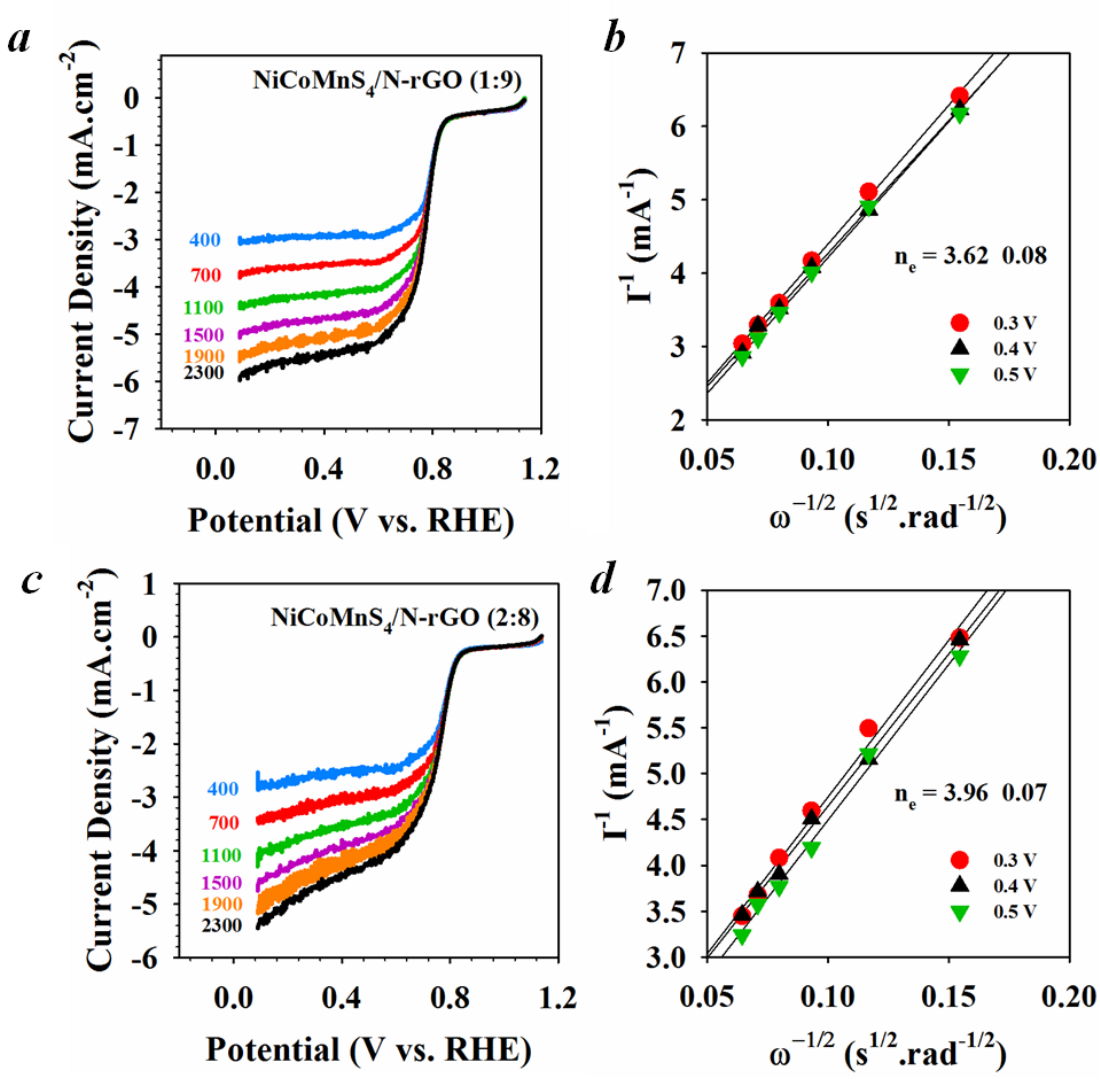

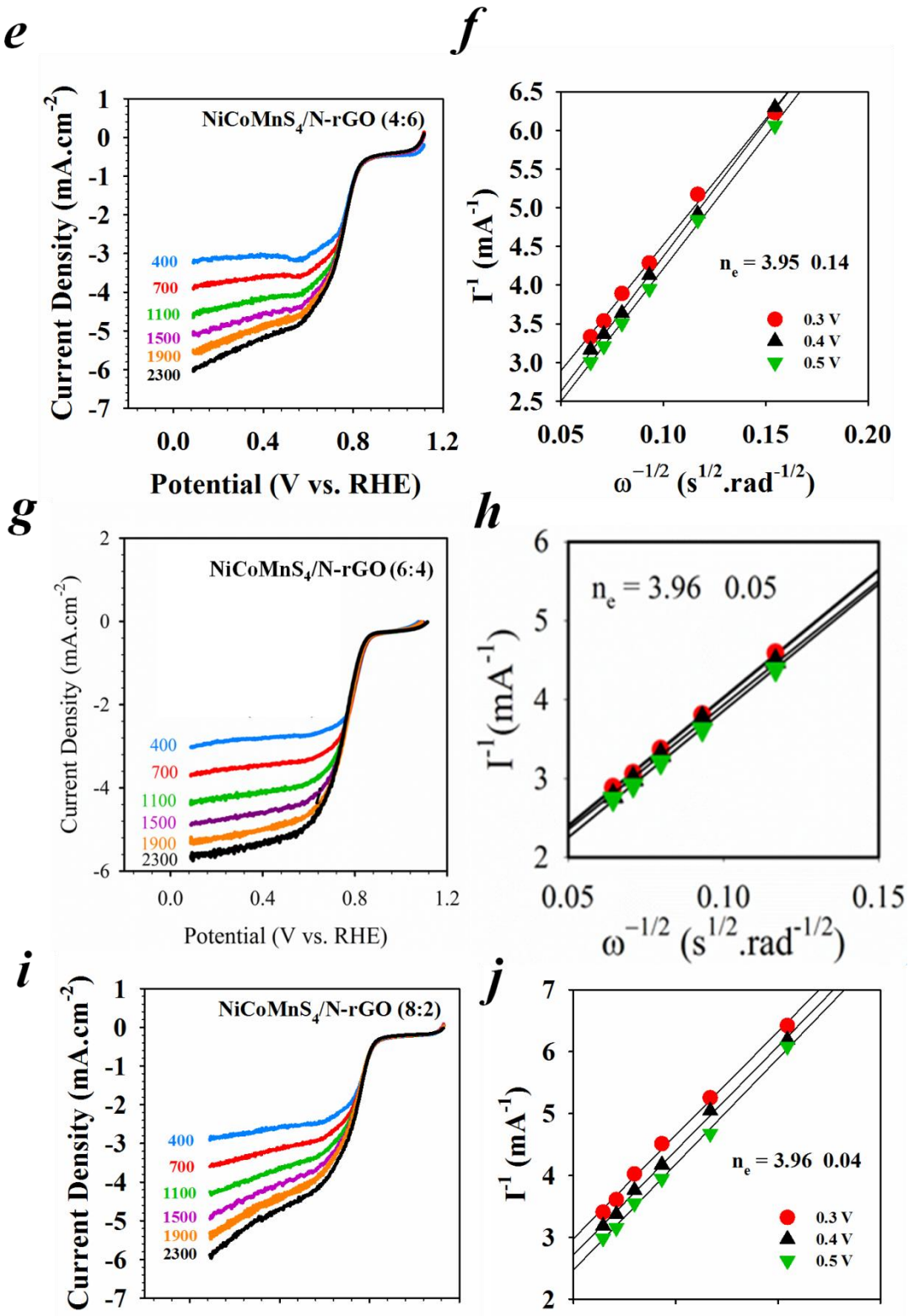

Figure 9.11 (*a, c, e, g, i*) LSV curves of $NiCoMnS_4$/N-rGO hybrids with different component ratios at various rotation rates with a scan rate of 20 $mV \cdot s^{-1}$ and (*b, d, f, h, j*) their corresponding Koutechy-Levich plots

The improved electrocatalytic performance in the (6:4) composition is possibly related to the synergism arisen from hybridization of metal sulfide nanoparticles with nitrogen-doped thin graphene layers. The number of transferred electrons when $NiCoMnS_4$/N-rGO hybrid catalyzes the ORR was calculated to be as high as 3.96, close to that of the state-of-the-art Pt/C 20% catalyst (3.99). Accordingly, the $NiCoMnS_4$/N-rGO hybrid with a (6:4) composition was chosen as the optimized sample and hereafter, in next sections we refer to results from the $NiCoMnS_4$/N-rGO hybrid denoted as the (6:4) composition unless stated otherwise.

Figure 9.12a depicts CV of the optimized $NiCoMnS_4$/N-rGO sample. The blue dashed-line curve shows control experiment in Ar-saturated solution, suggesting the lack of a perceptible cathodic peak in the absence of O_2. On the contrary, the appearance of an intense redox peak at 0.76 V in O_2-saturated solution suggests that the $NiCoMnS_4$/N-rGO hybrid is catalyzing the oxygen reduction reaction.

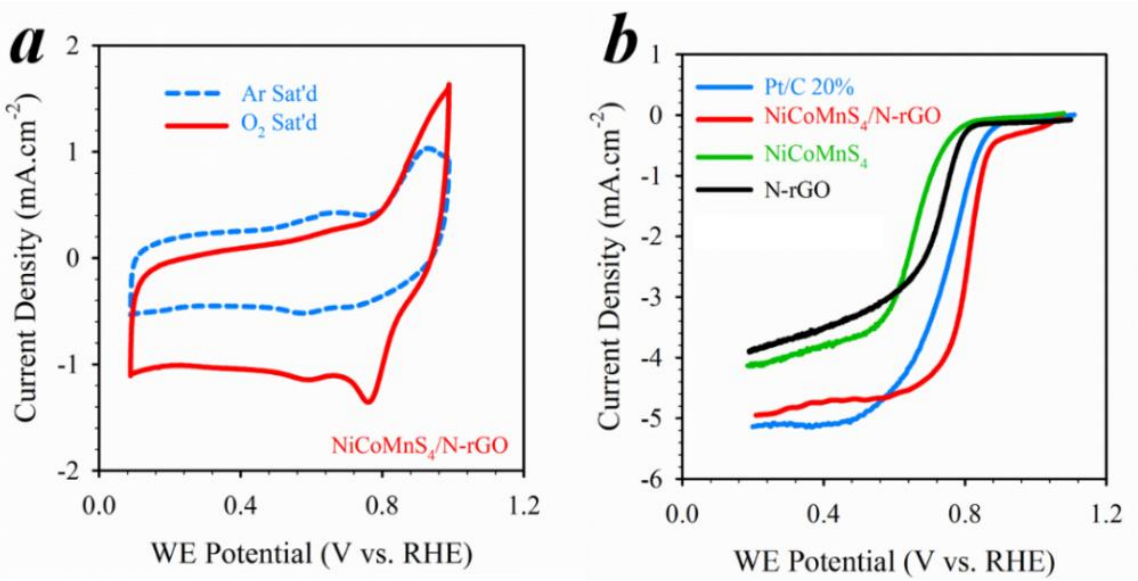

Figure 9.12 (a) CV curves of $NiCoMnS_4$/N-rGO catalyst with a scan rate of 20 $mV \cdot s^{-1}$; solid line represents the measurement in O_2 and dashed line in Ar. (b) Linear sweep voltammograms of different samples recorded at 1500 rpm in the presence of O_2

Figure 9.12b shows the LSV curves of various catalysts including Pt/C 20% as the state-of-the-art catalyst and the pure individual components of the hybrid material. The extracted parameters from LSV in ***Figure 9.12b*** are summarized in ***Table 9.1***. As can be seen, the pure mixed metal sulfide $NiCoMnS_4$ and the N-rGO exhibited mediocre ORR catalytic activity with ORR onset

potentials of 0.81 V and 0.86V, respectively and small limiting currents (J_{Levich}) in comparison with the hybrid $NiCoMnS_4$/N-rGO (6:4) and the commercial Pt/C 20%.

Table 9.1 Electrochemical parameters extracted from LSV curves in Figure 9.13*b*. Comparison of electrocatalytic performance of the as-synthesized samples and the Pt/C 20% benchmark

Sample	E_{onset} (V vs. RHE)	$E_{1/2}$ (V vs. RHE)	J_{Levich} (mA·cm^{-2})
$NiCoMnS_4$	0.81	0.68	4.13
N-rGO	0.86	0.72	3.89
$NiCoMnS_4$/N-rGO	0.94	0.81	4.98
Pt/C 20%	0.96	0.75	5.15

As clearly seen, the optimized $NiCoMnS_4$/N-rGO hybrid sample (6:4) outperformed the individual examined catalysts and showed comparable performance with respect to Pt/C 20% benchmark catalyst. Particularly, the hybrid sample exhibited a significant increased limiting current (J_{Levich}) over that of the mixed sulfide compound (~21% higher) and N-rGO (~27% higher) and comparable to the one collected from the Pt/C 20% catalyst, clearly unveiling that the electronic coupling of $NiCoMnS_4$ nanoparticles with N-rGO nanosheets enhanced the electrocatalytic activity of the pure individual components. Interestingly, the $NiCoMnS_4$/N-rGO hybrid displayed a much smaller mixed kinetic-diffusion control region resulting in significantly more positive half-wave potential ($E_{1/2}$) than the rest of the samples (0.81 V against 0.75 V for Pt/C 20%). In the hybrid sample, the oxygen containing groups on graphene oxide serves as a nucleation sites for the homogeneous formation and distribution of small metal nuclei, later converting to fine crystalline particles on nitrogen-doped graphene layers during the hydrothermal reaction, as noted from XRD and TEM results above. This provides innumerable active sites in $NiCoMnS_4$/N-rGO for ORR and further enhances the catalytic activity by synergism in the hybrid material.

The ORR mechanism in the case of reference samples ($NiCoMnS_4$, N-rGO, $NiCoMnO_4$, Pt/C 20%) were further discerned by collecting LSVs in O_2-saturated solutions at various rotation velocities and represented in ***Figure 9.13***. As seen, pure N-rGO and $NiCoMnS_4$ samples shown smaller number of transferred electrons (3.71 and 2.44, respectively) reinforcing the previous results that the $NiCoMnS_4$/N-rGO hybrid is superior to its corresponding pure components.

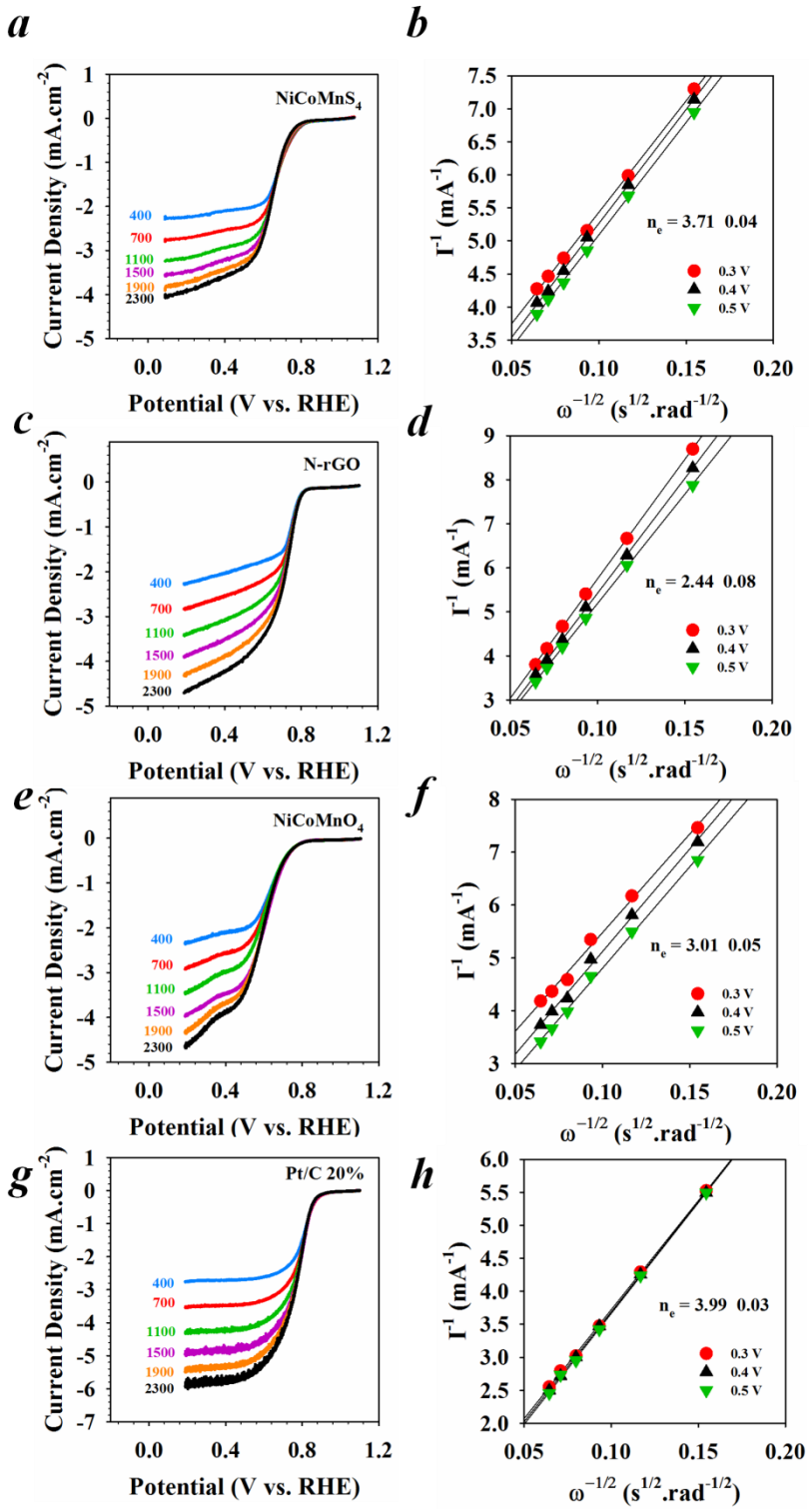

Figure 9.13 (*a, c, e, g*) LSV curves of $NiCoMnS_4$, N-rGO, $NiCoMnO_4$ and commercial Pt/C 20% catalysts at various rotation rates in O_2-saturaed 0.1 M KOH solution with a scan rate of 20 $mV \cdot s^{-1}$ and (*b, d, f, h*) their corresponding Koutechy-Levich plots at different potentials

Moreover, $NiCoMnS_4$/N-rGO catalyzes the oxygen reduction through a 4e pathway as we observed in the schematic illustration of $NiCoMnS_4$/N-rGO (***Figure 9.14).***

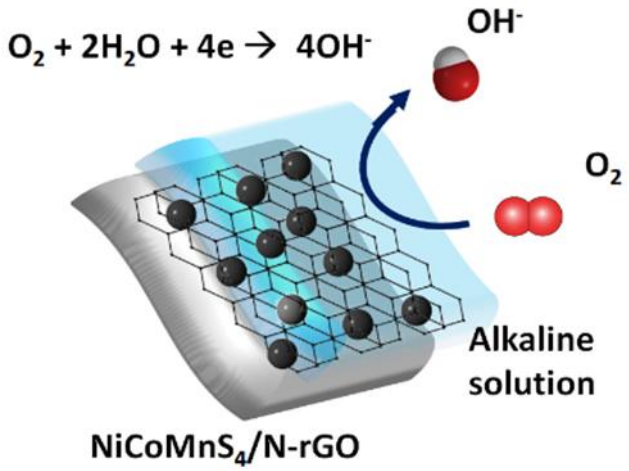

Figure 9.14 Schematic illustration of electrocatalytic activity of $NiCoMnS_4$/N-rGO hybrid through a 4e pathway

Rotating ring-disk electrode (RRDE) experiments were also conducted to demonstrate the superior ORR mechanism occurring with this optimized $NiCoMnS_4$/N-rGO hybrid. When oxygen is reduced, an unwanted and harmful by-product, hydrogen peroxide, may be produced. Hydrogen peroxide can damage the internal components of a metal-air battery, so oxygen-reduction electrocatalysts are engineered in such a way as to limit the amount of peroxide formed. Therefore, RRDE experiments can be used to probe the peroxide generating tendencies of a certain electrocatalyst. The number of electrons transferred and percentage of peroxide formation were calculated according to [Eq 3.6] and [Eq 3.7], respectively in which the ring and the disk currents detected in ***Figure 9.15a*** are involved. ***Figure 9.15a*** shows disk and ring currents for the $NiCoMnS_4$/N-rGO hybrid and commercial Pt/C 20%, revealing excellent performance of the $NiCoMnS_4$/N-rGO hybrid as an ORR electrocatalyst, pretty similar to the state-of-the-art Pt/C 20% catalyst. These results strongly suggest that the reaction proceeds mainly from a 4e pathway and hence very small amount of HO_2^- is formed as a by-product. The number of transferred electrons per O_2 molecule and the O_2^{2-} yield over a wide potential range of 0.85 to 0.15 V is shown in ***Figure 9.15b***. As observed, the HO_2^- percentage did not exceed 6% over this entire potential range and an average number of electrons of 3.92 ± 0.04 was obtained. This value is in good agreement with the calculated number of transferred electrons from RDE measurements (3.96 ± 0.05). These results

further demonstrate that $NiCoMnS_4$/N-rGO hybrid catalyzes the ORR mainly through a 4e pathway, producing hydroxyl groups, as illustrated in ***Figure 9.14.***

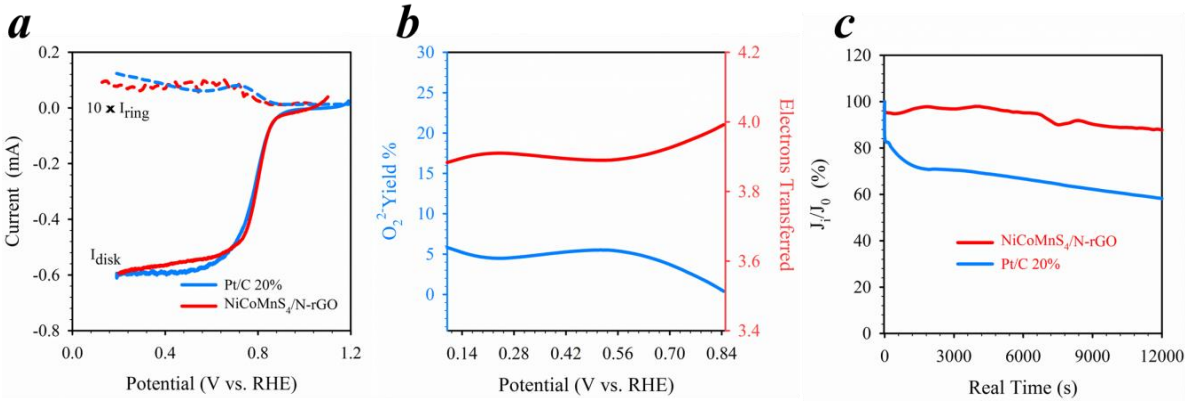

Figure 9.15 (*a*) RRDE LSV profiles at 1500 rpm with a scan rate of 20 $mV{\cdot}s^{-1}$, and (b) corresponding percentage of peroxide and number of transferred electrons with $NiCoMnS_4$/N-rGO hybrid material at various potentials. (c) Durability of ORR catalytic activity for $NiCoMnS_4$/N-rGO and carbon supported Pt (Pt/C 20%)

Apart from the high catalytic activity, $NiCoMnS_4$/N-rGO also exhibits considerable catalytic durability. This aspect is of particular interest as the excellent demonstrated catalytic activity of Pt-based electrocatalysts commonly declines over long period of use.[28] The chronoamperometric measurement (0.65 V vs. RHE over 500 mV of overpotential) maintains ORR current (J/J_o) close to 90% of the initial value after a continuous polarization period of 12000 s, which obviously outperforms that the commercial Pt-based catalyst (58% of the initial value) (***Figure 9.15c***), proving the superior long-term ORR catalytic performance of our $NiCoMnS_4$/N-rGO in comparison with the Pt catalyst under the same conditions.

The reverse reaction, OER is also of great relevance in rechargeable metal-air battery technology. In order to demonstrate the electrocatalytic activity of $NiCoMnS_4$/N-rGO hybrid towards the OER, the electrodes were anodically swept in a 0.1 M KOH solution (***Figure 9.16a***). Commercial Pt/C 20% and precious RuO_2 (more appropriate for OER) mixed with Vulcan Carbon (2.5:1) were also evaluated for comparison. In the case of $NiCoMnS_4$/N-rGO hybrid, a small anodic peak appeared at ~1.36 V which can be attributed to the conversion of cobalt and/or manganese oxidation states as previously reported for similar spinel compounds.[6] Subsequently, the evolution of oxygen appear with an OER onset potential of ~1.52 V, which is by far better than Pt supported on carbon (~1.63

V) and is comparable with that of the state-of-the-art RuO_2 OER catalyst (~1.48 V). In addition, the overpotential for reaching 10 $mA{\cdot}cm^{-2}$ is only ~18 *m*V higher in our $NiCoMnS_4$/N-rGO hybrid (1.64 V) than that of a RuO_2-VC catalyst (1.62 V vs. RHE). As can be seen, at higher overpotentials the current of $NiCoMnS_4$/N-rGO hybrid surpass that of RuO_2. Moreover, the superlative OER catalytic activity of this $NiCoMnS_4$/N-rGO hybrid was further proved from its small Tafel slope (***Figure 9.16b***) according to [Eq 3.5]. In order to examine the electrocatalytic activity stability of our $NiCoMnS_4$/N-rGO hybrid during OER (charge) and ORR (discharge), chronoamperometric experiments were conducted. ***Figure 9.16c*** shows that the hybrid air electrode could incredibly retain the anodic and cathodic currents; performing as a highly active and durable bifunctional electrocatalyst for air electrodes.

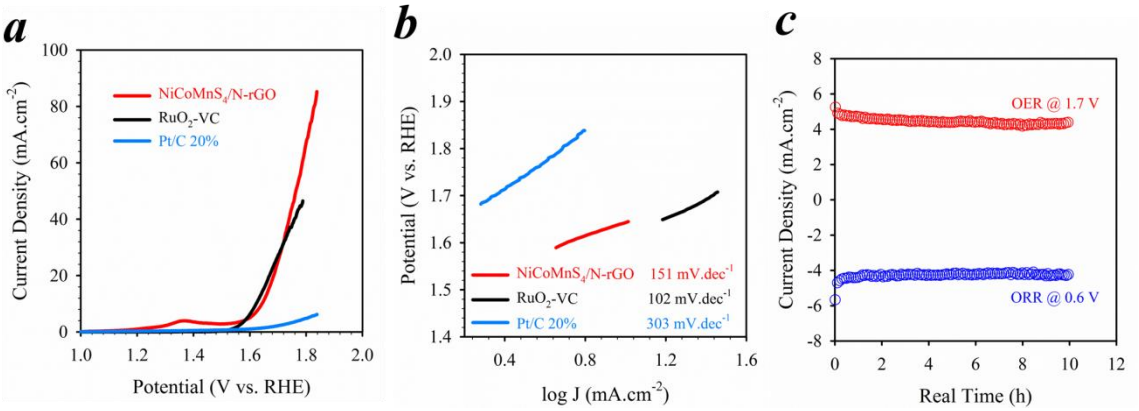

Figure 9.16 (a) Evaluation of OER catalytic activity of $NiCoMnS_4$/N-rGO, commercial Pt/C 20%, and RuO_2 mixed with Vulcan Carbon through LSV curves at 20 $mV{\cdot}s^{-1}$ and (b) corresponding Tafel plots. (c) Chronoamperometric ORR and OER catalytic responses of $NiCoMnS_4$/N-rGO air electrode. Note: 0.1 M KOH used as electrolyte and voltammograms were collected at 20 $mV{\cdot}s^{-1}$

All these results reveal excellent OER catalytic properties of the $NiCoMnS_4$/N-rGO hybrid which likely can be attributed to a superior distribution of fine $NiCoMnS_4$ nanoparticles on thin N-rGO layers (as noted above from TEM images in ***Figure 9.3***) that provide plenty of catalytically active sites and suppresses the activation energy for the evolution of O_2. Additionally, graphene layers act as a highly conductive support, resulting in enhanced electric conductivity of the final hybrid material. On the other hand, doped nitrogen atoms in graphene matrix not only provide excellent sites for anchoring the spinel sulfide nanoparticles, but they also induce active sites to facilitate the cleavage of O-H bonds in the water molecule and the formation of O-O bonds in the O_2

molecule.[29] Considering all these aspects, the catalytic activity of the $NiCoMnS_4$/N-rGO hybrid towards OER is enhanced. To put all these results into a context, ***Table 9.2*** show the bifunctional electrocatalytic activity of $NiCoMnS_4$/N-rGO hybrid compared with recently reported metal sulfide catalysts.

Table 9.2 Comparison of ORR/OER electrocatalytic activity of $NiCoMnS_4$/N-rGO hybrid catalyst with some recently reported mixed metal catalysts

Sample	E_{onset}^{ORR} (V)	$E_{1/2}$ (V)	n_e	E_{onset}^{OER} (V)	$E_{j=10}$ (V)	ΔE (V)	Ref.
$NiCoMnS_4$/N-rGO	0.94	0.82	3.96	1.52	1.64	0.82	**This work**
$NiCoMnO_4$/N-rGO	0.92	-	3.92	1.50	-	-	[6]
$CuCo_2S_4$ NSs	0.90	0.74	3.82	1.50	1.57	0.83	[30]
$NiCo_2S_4$-rGO	0.88	0.73	3.78	-	-	-	[31]
$NiCo_2S_4$@N/S-rGO	0.88	-	3.70	-	-	0.94	[32]
$NiCo_2S_4$/N-CNT	0.93	0.80	3.82	-	-	0.80	[13]
NiCo/PFC aerogels	0.92	0.79	3.89	-	-	0.86	[33]

As seen, $NiCoMnS_4$/N-rGO hybrid displayed superior or comparable catalytic performance both with respect to the ORR and OER in comparison with reported mixed metal catalysts. As we explained in Chapter 8 of the present thesis, a small Δ*E* value ($\Delta E = E_{j=10} - E_{1/2}$) commonly indicate a higher bifunctional catalytic activity. Accordingly, $NiCoMnS_4$/N-rGO presents a Δ*E* value of 0.82 V which is amongst smallest values reported for similar catalysts. This further supports the promise of this NiCoMnS4/N-rGO hybrid as an efficient bifunctional oxygen electrocatalyst capable of serving as an excellent non-precious catalyst with excellent performance durability.

9.2.3 Rechargeable Zn-Air Battery

To elucidate the practical applicability of our $NiCoMnS_4$/N-rGO hybrid as air-cathode, rechargeable Zn-air batteries were assembled. Air cathodes were fabricated by drop-casting of the catalyst ink on commercial gas diffusion layer (GDL). The prepared cathode was mounted together with a Zn foil (anode) in a 3D-printed cell with a perforated cathode side (see ***Figure 9.17c***). The cell was filled with 6M KOH and 0.02M $ZnSO_4$ solution as the electrolyte. ***Figure 9.17a*** shows the galvanodynamic discharge profile as well as its corresponding power density curve of the battery that exhibited an open circuit voltage of 1.41 V (see ***Figure 9.17c***). The power density acquired from the Zn-air battery assembled was 56 $mW \cdot cm^{-2}$ at 79 $mA \cdot cm^{-2}$. Moreover, when discharged at

constant current density of 5 mA·cm^{-2} (***Figure* 9.17b**), a stable voltage plateau of ~1.15 V could be achieved with a high specific capacity of 834 mAh·g^{-1}, corresponding to a high energy density of 959 Wh·kg$_{Zn}^{-1}$ that is around 88% of the theoretical energy density (1086 Wh·kg^{-1}).

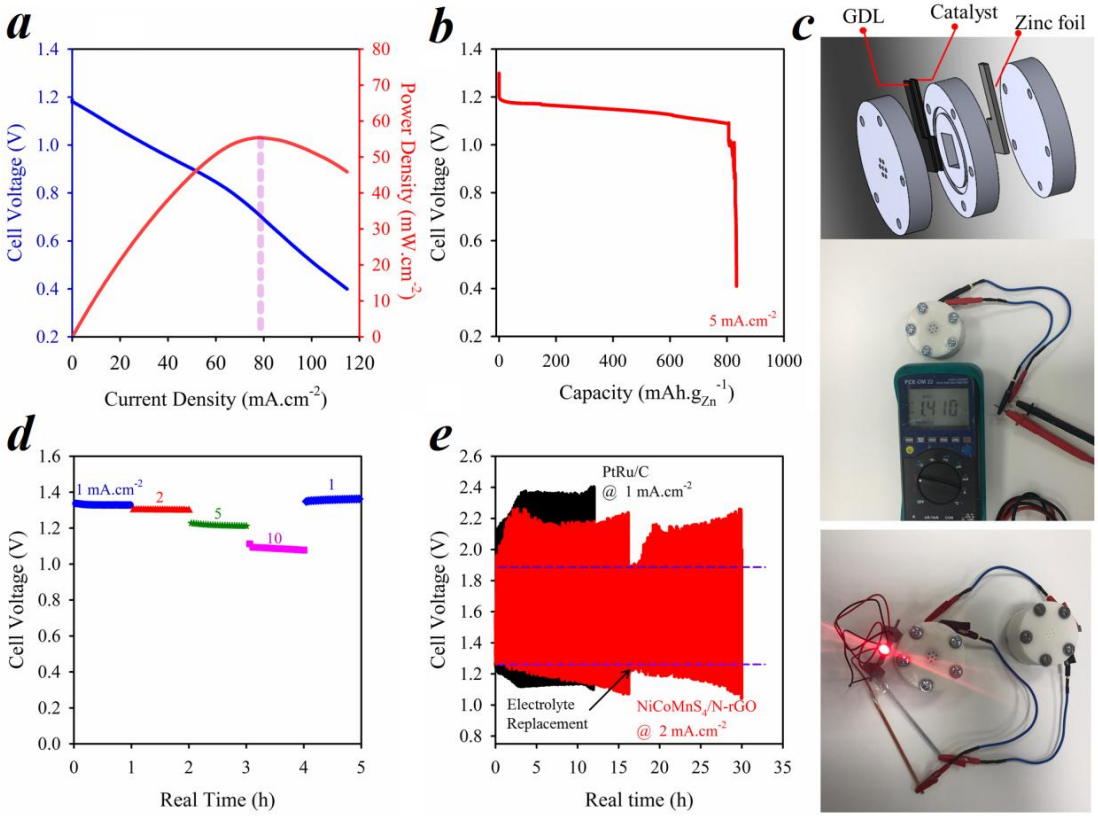

Figure 9.17 (*a*) Galvanodynamic discharge profile and power density curve of $NiCoMnS_4$/N-rGO air cathodes. (*b*) Discharge curve of Zn-air batteries with $NiCoMnS_4$/N-rGO hybrid as oxygen electrode catalysts at 5 mA·cm^{-2}. (*c*) Schematic illustration of 3D-printed Zn-air cell and images of a cell showing an OCP = 1.41 V and red LED powered by 2 series-connected Zn-air batteries. (*d*) Discharge profiles of the Zn-air battery based on $NiCoMnS_4$/N-rGO oxygen catalyst electrode at various current densities. (*e*) Charge-discharge profiles of Zn-air batteries with $NiCoMnS_4$/N-rGO and PtRu/C oxygen catalysts at 2 and 1 mA·cm^{-2}, respectively (each cycle takes 600 s)

As observed in ***Figure* 9.17d**, the battery could provide fairly stable plateaus under different current loads maintaining high discharge voltage even at high currents (e.g. 1.12 V at 10 mA·cm^{-2}), verifying the excellent catalytic activity of the hybrid towards ORR. Additionally, the charge-discharge profiles of Zn-air batteries with $NiCoMnS_4$/N-rGO and PtRu/C oxygen catalyst electrodes are compared in ***Figure* 9.17e**. A small round-trip voltage difference of 0.69 V was seen for the

battery loaded with the hybrid which is around 24% lower than the one obtained with PtRu/C air cathode (round-trip voltage difference of 0.86 V). It is also observed that the round-trip voltage of $NiCoMnS_4$/N-rGO hybrid gradually increased reaching a value of 1.06 V after 12h, by far smaller value than the one obtained for PtRu/C electrode (~1.34 V). These results clearly unveil the superior bifunctional catalytic activity of the hybrid with respect to the commercial PtRu/C air cathode. Moreover, it can be seen for $NiCoMnS_4$/N-rGO hybrid the voltage efficiency has been completely recovered after changing the electrolyte after 17h, suggesting that the performance fade is likely originated from electrolyte loss over cycling. All of these observations further demonstrate high ORR/OER bifunctional activity and excellent catalytic durability of $NiCoMnS_4$/N-rGO as air-cathode for metal-air batteries.

9.3 Conclusions

In this Chapter, ternary mixed metal sulfide nanoparticles, $NiCoMnS_4$ NPs, were anchored on nitrogen-doped reduced graphene oxide nanosheets ($NiCoMnS_4$/N-rGO) for the first time and their electrochemical signature as oxygen bifunctional electrocatalysts was demonstrated via RDE and RRDE measurements. Through hybridization and component ratio optimization with nitrogen-doped reduced graphene oxide, a highly efficient bifunctional catalyst with a small ΔE = 0.82 V and excellent activity and durability was developed. Moreover, the $NiCoMnS_4$/N-rGO hybrid exhibited superb performance as an air cathode when assembled in a rechargeable Zn-air battery, resulting in a high capacity of 834 $mAh \cdot g^{-1}$ and high energy density of 959 $Wh \cdot kg_{Zn}^{-1}$. In addition, an improved cycling stability as compared to the state-of-the-art PtRu/C 20%-loaded air cathode has also been demonstrated. This work suggests a facile synthetic route to produce $NiCoMnS_4$/N-rGO hybrid that is easy to use and may allow this hybrid to be utilized as a highly efficient oxygen bifunctional electrocatalyst for energy storage applications.

ELSEVIER

Energy Storage Materials

Available online 19 April 2019

In Press, Corrected Proof

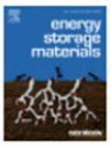

Anchored $NiCoMnS_4$ nanoparticles on N-doped rGO: High-performance bifunctional electrocatalysts for rechargeable Zn-Air batteries

Afshin Pendashteh [a, b], Jaime S. Sanchez [a], Jesus Palma [a], Marc Anderson [a, c], Rebeca Marcilla [a]

Show more

https://doi.org/10.1016/j.ensm.2019.04.018

Get rights and content

Abstract

The vast commercialization of advanced energy storage/conversion technologies like rechargeable metal–air batteries and regenerative fuel cells is greatly tied to the development of efficient catalysts capable of proceeding the pertinent electrochemical processes like oxygen reduction reaction (ORR) and oxygen evolution reaction (OER). Hence, exploiting an ideal bifunctional catalyst, e.g. the one includes dual active sites for both reactions, is of high interest and importance. Herein, a novel nonprecious-metal bifunctional catalyst based on a quaternary mixed metal sulfide synergized with nitrogen-doped reduced graphene oxide ($NiCoMnS_4$/N-rGO) is synthesized through a simple anion-exchange route. The unique composition and synergism arising from uniformly anchoring the metal sulfide nanoparticles on N-rGO endow the as-prepared catalyst with remarkable electrocatalytic activity and durability towards ORR and OER. Importantly, the excellent electrocatalytic performance of $NiCoMnS_4$/N-rGO hybrid was demonstrated in rechargeable Zn-air batteries (ZABs) as a real application. Accordingly, rechargeable ZABs assembled by $NiCoMnS_4$/N-rGO hybrid-based air cathodes exhibit high capacity, energy density and excellent rate capability as well as favorable cycling stability. The outstanding performance of this $NiCoMnS_4$/N-rGO hybrid together with the simplicity of synthetic method, make this hybrid promising as a highly efficient air-cathode catalyst for energy-related applications including high-performance rechargeable ZABs.

Keywords

Mixed metal sulfide; $NiCoMnS_4$; Electrocatalysis; Bifunctional catalyst; Rechargeable Zn-Air battery

9.4 References

1 Y. Liang, Y. Li, H. Wang, J. Zhou, J. Wang, T. Regier and H. Dai, *Nat. Mater.*, 2011, **10**, 780–786.

2 A. Pendashteh, J. J. Vilatela, M. Anderson, J. Palma and R. Marcilla, *ACS Appl. Energy Mater.*, 2018, **1**, 2434–2439.

3 Y. Xie, X. W. Lou, C. Yuan, H. Bin Wu, Y. Xie, X. Wen and D. Lou, *Angew. Chem. Int.*, 2014, **53**, 1488–1504.

4 A. Pendashteh, J. Palma, M. Anderson and R. Marcilla, *RSC Adv.*, 2016, **6**, 28970–28980.

5 F. Cheng, J. Shen, B. Peng, Y. Pan, Z. Tao and J. Chen, *Nat. Chem.*, 2010, **3**, 79–84.

6 A. Pendashteh, J. Palma, M. Anderson and R. Marcilla, *Appl. Catal. B Environ.*, 2017, **201**, 241–252.

7 Y. Zhang, Q. Zhou, J. Zhu, Q. Yan, S. X. Dou and W. Sun, *Adv. Funct. Mater.*, 2017, **27**, 1702317–1702351.

8 R. A. Sidik and A. B. Anderson, *J. Phys. Chem. B*, 2006, **110**, 936–941.

9 S. H. Choi and Y. C. Kang, *Nanoscale*, 2015, **7**, 6230–6237.

10 D. Yuan, G. Huang, D. Yin, X. Wang, C. Wang and L. Wang, *ACS Appl. Mater. Interfaces*, 2017, **9**, 18178–18186.

11 H. Chen, J. Jiang, L. Zhang, H. Wan, T. Qi and D. Xia, *Nanoscale*, 2013, **5**, 8879–8883.

12 L. Shen, L. Yu, H. Bin Wu, X.-Y. Yu, X. Zhang and X. W. (David) Lou, *Nat. Commun.*, 2015, **6**, 6694–6702.

13 X. Han, X. Wu, C. Zhong, Y. Deng, N. Zhao and W. Hu, *Nano Energy*, 2017, **31**, 541–550.

14 K. Feng, A. Yu, J. Zhang, Z. Chen, W. Liu, M. Li, Z. Bai, G. Jiang, Y. Ding, L. Yang and T. Yu, *Adv. Funct. Mater.*, 2018, **28**, 1706675–1706686.

15 J. A. García-Valenzuela, *Comments Inorg. Chem.*, 2017, **37**, 99–115.

16 X. M. Shuai and W. Z. Shen, *J. Phys. Chem. C*, 2011, **115**, 6415–6422.

17 I. Bezverkhyy, J. Skrzypski, O. Safonova and J. P. Bellat, *J. Phys. Chem. C*, 2012, **116**, 14423–14430.

18 C. Cai, J. Tang, X. Ma, P. Yuan and Y. Fu, *Adv. Energy Mater.*, 2016, **6**, 1600813–1600824.

19 P. Li, C. Xia, A. N. Gandi, H. N. Alshareef and U. Schwingenschlögl, *Chem. Mater.*, 2015, **27**, 6482–6485.

20 S. Maldonado and K. J. Stevenson, *J. Phys. Chem. B*, 2005, **109**, 4707–4716.

21 Y. Wen, S. Peng, Z. Wang, J. Hao, T. Qin, S. Lu, J. Zhang, D. He, X. Fan and G. Cao, *J. Mater. Chem. A*, 2017, **5**, 7144–7152.

22 Y. Xue, Z. Zuo, Y. Li, H. Liu and Y. Li, *Small*, 2017, **13**, 1700936–1700946.

23 M. C. Biesinger, B. P. Payne, L. W. M. Lau, A. Gerson and R. S. C. Smart, *Surf. Interface Anal.*, 2009, **41**, 324–332.

24 L. W. M. Lau, A. R. Gerson, B. P. Payne, R. S. C. Smart, M. C. Biesinger and A. P. Grosvenor, *Appl. Surf. Sci.*, 2010, **257**, 2717–2730.

25 V. Di Castro and G. Polzonetti, *J. Electron Spectros. Relat. Phenomena*, 1989, **48**, 117–123.

26 N. López-Salas, M. C. Gutiérrez, C. O. Ania, M. A. Muñoz-Márquez, M. Luisa Ferrer and F. Del Monte, *J. Mater. Chem. A*, 2016, **4**, 478–488.

27 J. D. Wiggins-Camacho and K. J. Stevenson, *J. Phys. Chem. C*, 2011, **115**, 20002–20010.

28 M. Shao, Q. Chang, J.-P. Dodelet and R. Chenitz, *Chem. Rev.*, 2016, **116**, 3594–3657.

29 C. Hu and L. Dai, *Angew. Chemie - Int. Ed.*, 2016, **55**, 11736–11758.

30 S. Zhao, Y. Wang, Q. Zhang, Y. Li, L. Gu, Z. Dai, S. Liu, Y. Q. Lan, M. Han and J. Bao, *Inorg. Chem. Front.*, 2016, **3**, 1501–1509.

31 A. Shen, J. Wu, S. Dou, X. Wang, C. Ouyang, S. Wang and Z. Ma, *J. Mater. Chem. A*, 2014, **2**, 20990–20995.

32 Q. Liu, J. Lin and J. Zhang, *Appl. Mater. Interfaces*, 2013, **5**, 5002–5008.

33 G. Fu, Y. Chen, Z. Cui, Y. Li, W. Zhou, S. Xin, Y. Tang and J. B. Goodenough, *Nano Lett.*, 2016, **16**, 6516–6522.

CHAPTER 10

Overall Conclusions and Future Perspectives

10.1 Overall Conclusions

In the present *PhD Thesis*, synthesis and physicochemical characterization of graphene-based hybrid materials with nanostructured transition metal oxides/sulfides have been carried out with the aim to tune the material properties for energy storage applications. To this end, the relationship between the structural and compositional properties such as particle sizes, specific surface area, morphological aspects, the coexistence of multivalent metal ions, substitution of transition metal cations and crystalline phase on electrochemical properties of the metal compounds were probed for the subjected samples. In addition, the hybridization of the prepared samples with graphene-based materials (e.g. reduced graphene oxide (rGO) and their doped derivatives such as N-doped rGO) was evaluated, tracking the effect of hybridization parameters like component ratio and doping on electrochemical behavior and therefore energy storage performance of the hybrid samples.

As seen in the course of the thesis, the studied samples were evaluated either as electrode materials (negative or positive) for aqueous-based energy storage devices or as heterogeneous electrocatalysts for oxygen reactions (e.g. ORR and OER) in rechargeable metal-air battery application. In each case, the high-performance of the systematically designed/optimized samples was demonstrated through various electrochemical measurements and assembly of full-devices for real application realization.

Although the main conclusions obtained for each type of material investigated have been summarized at the end of each chapter, herein in this final chapter we want to make a performance comparison of the results obtained for every single material in their corresponding application.

The most relevant **overall conclusions** of the present PhD thesis are gathered below:

- Graphene derivatives such as GO or rGO are excellent substrates for anchoring transition metal compounds with the aim to improve both the electrical conductivity and the textural properties of the samples which indeed have great influence on electrochemical signature of the final products. Enriched textural properties such as increased specific surface area and open interconnected pores facilitate the

electrolyte ion movements and result in shortened diffusion path. Such enhanced active surface and improved ion mobility in combination with enhanced electrical conductivity due to presence of carbon network led to boost the electrochemical performance of the studied metal oxides/sulfides.

- Electrostatic coagulation and hydrothermal methods have been demonstrated as facile and easy-to-tune methods for hybridization of metal compounds with graphene derivatives depending on having already prepared metal compound nanoparticles (e.g. commercial samples or previously optimized samples) or carrying out the synthesis and hybridization in one single pot, respectively.
- The presence of multi-valence transition metal ions in the metal compounds (e.g. oxides or sulfides) demonstrated to achieve superior electrochemical performance (both as electrode materials for energy storage devices or as electrocatalysts for oxygen reduction/evolution reactions) due to enriched redox-reactions, electrical conductivity and possible synergistic effects as compared to single metal compounds.
- It has been demonstrated that structural changes (such as phase of the oxide) can significantly influence the electrochemical behavior and consequently the storage performance of the sample. For instance, it has been shown that the rock-salt structure in NiCoMn ternary metal oxide provides a superior performance in comparison with the spinel one.
- Hybridization of capacitor-type (e.g. graphene-related species) and battery-type (metal oxides or sulfides) materials in a single electrode demonstrated to provide enhanced electrochemical properties and boosted energy storage performance than their corresponding single components; and even higher than simply summation of their storage features (e.g. specific capacity) due to arisen synergistic effects upon microscale-hybridization.
- Charge storage mechanism of mixed metal sulfide ($NiCoMnS_2$) in alkaline media was unveiled through ex-situ and operando measurements.
- Hybridization of Nitrogen-doped reduced graphene oxide and battery-type (metal oxides or sulfides) materials employed as air-cathodes for rechargeable Zn-air batteries, have demonstrated to provide efficient bifunctional electrocatalyst performance and excellent durability.

More specifically, ***Table 10.1*** provides an overall comparison of the electrochemical properties exhibited by the different graphene-based hybrids synthesized and tested as electrode materials in aqueous-based energy storage devices.

Table 10.1 Comparison of the electrochemical properties of the different graphene-based hybrids synthesized in the present *PhD Thesis* in a 3-electrode configuration

Sample	Electrolyte	Voltage window	Synthesis method	Specific Capacity ($mAh \cdot g^{-1}$)	Discharge Regime	Mass loading ($mg \cdot cm^{-2}$)	Areal Capacity ($mAh \cdot cm^{-2}$)
Fe_3O_4-rGO [60-40] **(Chapter 4)**	3M KOH	-1.2/-0.3 (Negative Electrode)	Electrostatic Coagulation	112	1 $A \cdot g^{-1}$	8.4	0.937
$NiMnO_3$-rGO Nanosheets **(Chapter 5)**	3M KOH	0/0.6 (Positive electrode)	Hydrothermal	62	1 $A \cdot g^{-1}$	3-6	0.31
NCMO_rGO Nanosheets **(Chapter 6)**	3M KOH	0/0.6 (Positive electrode)	Hydrothermal	115	1 $A \cdot g^{-1}$	6-8	0.784
$NiCoMnS_2$ Nanoneedles **(Chapter 8)**	3M KOH	0/0.6 (Positive electrode)	Hydrothermal	138	1 $A \cdot g^{-1}$	5.2	0.72

Based on ***Table 10.1***, the following conclusions related to the electrochemical performance of investigated materials can be summarized:

- As shown, $NiCoMnS_2$ nanoneedles displayed superior performance (e.g. in terms of specific capacity) as positive electrode material, mainly ascribed to their unique morphology, comprising vertically oriented 1D nano-needle directly grown on to Ni foam (NF).
- On the other hand, Fe_3O_4-rGO synthesized by a simple electrocoagulation method and using commercial available Fe_3O_4 shows a high specific capacity (112 $mAh \cdot g^{-1}$) in negative potentials. This is the only hybrid material that exhibited redox activity at negative potentials and therefore the only one suitable to be used as anode in this potential range. It is important to mention that, all the electrodes prepared and tested in this PhD had moderate-high mass loadings making them appropriate for practical devices.

Novel graphene-based hybrids with metal compounds were also employed as bifunctional electrocatalyst materials for Zn-Air Batteries. ***Table 10.2*** provides an overall comparison of the ORR/OER electrocatalytic activity between the different graphene-based hybrids synthesized in the present *PhD Thesis.*

Table 10.2 Comparison of ORR/OER electrocatalytic activity of graphene-based hybrid catalyst synthesized in the present *PhD Thesis*

Sample	E_{onset}^{ORR}(V)	$E_{1/2}$ (V)	n_e	E_{onset}^{OER} (V)	$E_{j=10}$ (V)	ΔE (V)
N-rGO/Co_3O_4 Nanorods **(Chapter 7)**	0.91	0.80	3.96	1.42	1.58	0.78
$NiCoMnS_4$/N-rGO **(Chapter 9)**	0.94	0.82	3.96	1.52	1.64	0.82

- In both type of samples, it has been demostrated that N-doping enhances the electrocatalytic activity of the hybrid samples likely through enhanced electrical conductivity and better distribution of the metal compound nanoparticles on the graphene network.
- The importance of an optimized cation valence ratio has been sketched by preparing cobalt oxides with different Co^{2+}/Co^{3+} species, modifying the temperature of the calcination step. The Co^{3+} is considered to be highly active for oxygen electrocatalytic activity. Therefore, Co_3O_4 Nanorods with the highest Co^{3+}/Co^{2+} ratio are desirable for electrocatalyst applications.
- The synthesized bifunctional hybrid nanocatalysts (N-rGO/Co_3O_4 and $NiCoMnS_4$/N-rGO) surpassed the electrocatalytic performance of noble-metal benchmarks (PtRuC 20%), demonstrating exceptional properties as air-cathodes in Zn-Air Batteries.
- As seen in ***Table 10.2***, N-rGO/Co_3O_4 Nanorods hybrid displayed superior catalytic performance with respect to the ORR and OER in comparison with $NiCoMnS_4$/N-rGO. A small Δ*E* value ($\Delta E = E_{j=10} - E_{1/2}$) (0.78 against 0.82) indicate a higher bifunctional catalytic activity.

In summary, this *doctoral thesis* not only provides several novel graphene-based hybrid samples as high-performance electrode materials or electrocatalysts for energy applications but also exercises the effect of structural or compositional features on electrochemical response of transition metal

compounds. The evolution of the samples in the course of reactions were also evidenced which can shed light on better understanding of the reactions of these family of materials. This information can pave the path for developing and optimizing more efficient energy-related materials.

10.2 Future works and Perspectives

Despite all achievements in this *PhD Thesis*, yet some challenges remained to increase specific capacities of the materials and real specific energy density of energy storage devices without deteriorates its power density and safety, along the diagonal of the Ragone plot. On the other hand, nano-structural engineering of novel graphene-based hybrid materials further improves the activity and durability of bi-functional catalysts based on the knowledge gained from the above studies. In this regards, a number of directions can be identified that require further improvements in the future:

- It will be necessary to investigate the effect of raw graphite materials on the quality of resulting graphene derivatives, such as GO or rGO synthesized by Chemical Methods. For example number of defects on the layers or number of functional groups on the edges or in the basal plane can be affected by the purity or quality of the initial graphite employed.
- To study in greater deep the influence of different metal cations in the hybrid structure via employing in situ/operando XPS, XRD or Raman spectroscopy coupled with electrochemical techniques; as we proceed in Chapter 8, need to gain even more insight in order to track the charge storage mechanisms of the different hybrid materials
- Morphology-wise, other synthesis techniques can be developed based on high throughput methods such as CVD (Chemical Vapor Deposition) or ALD (Atomic Layer Deposition) in order to fabricate hybrid materials with controlled oxide/sulfide thickness as a competitive cost. Here, the commercialization is probably the biggest issue. Cost and production consistency are of equal importance. So far, none of synthesis techniques has shown sufficient commercialization potential but it is expected a reduction in the overall cost in the near future.

- In the field of electro-catalysis, more rigorous and systematic analysis of degradation pathways coupled with post-durability characterizations or in-situ studies has to be conducted to understand the degradation mechanisms and come up with appropriate mitigation strategies to prevent performance fading.

Despite of many attempts that have been made to standardize the evaluation methods of electrochemical energy storage systems, there is still a lack of clear rules for evaluating the performance of these devices in a fair and systematic way. We believe that there are still huge challenges in the employment of appropriate metrics and the development of a common protocol for accurate assessment of electrochemical energy storage systems. All of these standards will help in reaching a point where we can all speak the same language in energy storage community.

CAPÍTULO 10

Conclusiones Generales y Perspectivas Futuras

10.1 Conclusiones Generales

En la presente *Tesis doctoral*, se ha estudiado en profundidad la síntesis y caracterización físico-química de materiales híbridos en base grafeno con óxidos/sulfuros de metales de transición nanoestructurados, con el objetivo principal de encontrar las propiedades óptimas de la hibridación resultante para su empleo en aplicaciones de almacenamiento de energía. Para tal finalidad, se ha evaluado la relación entre las propiedades estructurales y de composición, tales como tamaño de partícula, área superficial específica, aspectos morfológicos, coexistencia de iones metálicos multivalentes, sustitución de cationes de metales de transición y distinta fase cristalina estudiando su efecto en las propiedades electroquímicas de los compuestos metálicos sintetizados. Además, se ha evaluado la hibridación de dichos compuestos metálicos con materiales en base grafeno (p. Ej., Óxido de grafeno reducido (rGO) y sus derivados como el rGO dopado con N), evaluando el efecto de los distintos parámetros de hibridación como la proporción de componentes en el híbrido (ratio), el dopaje con nitrógeno en el comportamiento electroquímico, y su posterior rendimiento final en dispositivos de almacenamiento de energía.

Como se ha podido observar en el transcurso de la presente *Tesis doctoral*, los materiales sintetizados se evaluaron como materiales de electrodo (negativos o positivos) para su empleo en dispositivos de almacenamiento de energía acuosos, o como electrocatalizadores heterogéneos para las reacciones de oxígeno (ORR y OER) y su aplicación en baterías recargables de metal-aire. En cada caso, el alto rendimiento mostrado por las muestras sintetizadas/optimizadas se demostró a través de diversos ensayos electroquímicos con su posterior aplicación en dispositivos de almacenamiento, para así demostrar su aplicación real.

Aunque las principales conclusiones extraídas en cada tipo de material sintetizado han sido detalladas al final de cada uno de los capítulos a lo largo del documento de tesis, este capítulo final pretende a su vez realizar una comparación entre los resultados obtenidos con los distintos materiales sintetizados dependiendo de la aplicación final.

A continuación se recogen las **conclusiones generales** más relevantes de la presente tesis doctoral:

- Los materiales derivados del grafeno (GO o rGO) son excelentes sustratos para anclar compuestos de metales de transición, buscando como objetivo mejorar tanto la conductividad eléctrica como las propiedades texturales de los compuestos metálicos sintetizados, por consiguiente estas mejoras traen una gran influencia en la respuesta electroquímica de los productos finales. Dicha respuesta en las propiedades texturales, como el aumento de superficie específica y la presencia de poros abiertos interconectados, facilitan el movimiento de los iones del electrólito en cuestión, dando como resultado un camino más corto para su difusión. Estas mejoras están relacionadas con la presencia de una red de carbono que permite aumentar el rendimiento electroquímico de los óxidos/sulfuros metálicos estudiados.
- Los métodos de coagulación electrostática e hidrotermal han demostrado ser métodos de síntesis relativamente sencillos y fáciles de ejecutar para sintetizar los materiales híbridos en cuestión (metales de transición con derivados de grafeno), dependiendo en algunos casos de haber preparado con anterioridad nanopartículas de compuestos metálicos (por ejemplo, muestras comerciales o muestras previamente optimizadas) como en los casos de la coagulación electrostática o de llevar a cabo la síntesis e hibridación en un solo paso de síntesis, como en los casos hidrotermales.
- La presencia de iones multivalencia de distintos metales de transición en los compuestos metálicos (por ejemplo óxidos o sulfuros mixtos) demostró lograr un rendimiento electroquímico superior (como materiales de electrodos para dispositivos de almacenamiento de energía o como electrocatalizadores para reacciones de reducción/evolución de oxígeno) debido al mejor comportamiento redox, una mejora en la conductividad eléctrica y posibles efectos sinérgicos en comparación con compuestos metálicos simples.
- A su vez, se ha demostrado que los cambios estructurales (como la fase del óxido) pueden influir significativamente en el comportamiento electroquímico y, en consecuencia, en el rendimiento electroquímico de la muestra. Por ejemplo, se ha demostrado que la estructura “rocksalt” en un óxido de metal ternario de NiCoMn proporciona un rendimiento superior en comparación con la estructura espinela.
- La hibridación de materiales capacitivos (por ejemplo, especies relacionadas con el grafeno) y de tipo batería (óxidos o sulfuros de metal) en un solo electrodo ha

demostrado proporcionar propiedades electroquímicas mejoradas y una mejor respuesta electroquímica que sus componentes individuales correspondientes. Incluso en algunos casos, esta respuesta es más alta que la simple suma de sus propiedades de almacenamiento por separado (por ejemplo, al calcular la capacidad específica) debido a los efectos sinérgicos surgidos en la hibridación sintetizada.

- El mecanismo de almacenamiento de carga de un sulfuro de metal mixto ($NiCoMnS_2$) en medios alcalino se ha deducido a través de mediciones ex situ y operando.
- La hibridación del óxido de grafeno reducido dopado con nitrógeno y los materiales tipo batería (óxidos o sulfuros de metal) empleados como cátodos de aire para baterías recargables de Zn-aire, demostraron proporcionar un rendimiento eficiente como electrocatalizadores bifuncionales y una excelente durabilidad.

De una manera más específica, la ***Tabla 10.1*** proporciona una comparación general de las propiedades electroquímicas demostradas por los distintos materiales híbridos en base grafeno sintetizados y testeados como materiales de electrodo en dispositivos de almacenamiento de energía acuosos.

Tabla 10.1 Comparación de las propiedades electroquímicas de los diferentes híbridos basados en grafeno sintetizados en la presente tesis doctoral en una configuración de 3 electrodos

Material	Electrolito	Ventana de Potencial	Método de Sintesis	Capacidad específica ($mAh \cdot g^{-1}$)	Régimen de descarga	Carga másica electrodos ($mg \cdot cm^{-2}$)	Capacidad areal ($mAh \cdot cm^{-2}$)
Fe_3O_4-rGO [60-40] **(Capítulo 4)**	3M KOH	-1.2/-0.3 (Negative Electrode)	Coagulación Electrostática	112	1 $A \cdot g^{-1}$	8.4	0.937
$NiMnO_3$-rGO Nanoláminas **(Capítulo 5)**	3M KOH	0/0.6 (Positive electrode)	Hidrotermal	62	1 $A \cdot g^{-1}$	3-6	0.31
NCMO_rGO Nanoláminas **(Capítulo 6)**	3M KOH	0/0.6 (Positive electrode)	Hidrotermal	115	1 $A \cdot g^{-1}$	6-8	0.784
$NiCoMnS_2$ Nanoagujas **(Capítulo 8)**	3M KOH	0/0.6 (Positive electrode)	Hidrotermal	138	1 $A \cdot g^{-1}$	5.2	0.72

Basándose en la ***Tabla 10.1***, se pueden deducir las siguientes conclusiones relacionadas con el rendimiento electroquímico de los materiales investigados:

- Como se puede observar, las nanoagujas de $NiCoMnS_2$ mostraron un rendimiento superior (por ejemplo, en términos de capacidad específica) como material de electrodo positivo, principalmente atribuido a su morfología única, que comprende una nano-aguja 1D orientada verticalmente sobre espuma de Ni (NF).
- Por otro lado, el Fe_3O_4-rGO sintetizado por un método simple de coagulación electrostática; empleando un Fe_3O_4 comercial, muestra una alta capacidad específica (112 $mAh \cdot g^{-1}$) en potenciales negativos. Este es el único material híbrido que exhibe su actividad redox en potenciales negativos y, por lo tanto, el único adecuado para ser utilizado como ánodo en este rango de potencial. Es importante mencionar que todos los electrodos preparados y testeados en este PhD tenían cargas másicas elevadas, lo que los hace apropiados para dispositivos prácticos a nivel comercial.

También se emplearon materiales híbridos en base grafeno con compuestos metálicos como materiales de electrocatalizadores bifuncionales para baterías Zn-aire. La ***Tabla 10.2*** proporciona una comparación global de la actividad electrocatalítica ORR/OER entre los diferentes híbridos basados en grafeno sintetizados en la presente *Tesis doctoral*.

Tabla 10.2 Comparación de la actividad electrocatalítica ORR/OER de los distintos catalizador híbridos basados en grafeno sintetizados en la presente tesis doctoral

Material	E_{onset}^{ORR}(V)	$E_{1/2}$ (V)	n_e	E_{onset}^{OER} (V)	$E_{j=10}$ (V)	ΔE (V)
N-rGO/Co_3O_4 Nanorods **(Capítulo 7)**	0.91	0.80	3.96	1.42	1.58	0.78
$NiCoMnS_4$/N-rGO **(Capítulo 9)**	0.94	0.82	3.96	1.52	1.64	0.82

- En ambos materiales, se ha demostrado que el dopaje con nitrogeno mejora la actividad electrocatalítica de las muestras híbridas probablemente a través de una conductividad eléctrica mejorada y una mejor distribución de las nanopartículas de compuestos metálicos en la red de grafeno.
- La importancia de optimizar la relación de valencia catiónica, se ha evaluado mediante la preparación de óxidos de cobalto con diferentes especies de Co^{2+}/Co^{3+} a diferentes temperaturas de calcinación. El Co^{3+} se considera altamente activo para la electrocatálisis del oxígeno. Por lo tanto, los nanorods de Co_3O_4 con la relación más alta de Co^{3+}/Co^{2+} son los óxidos deseables para su aplicación como materiales en electrocatalizadores.
- Los nanocatalizadores híbridos bifuncionales sintetizados (N-rGO/Co_3O_4 y $NiCoMnS_4$/ N-rGO) superaron el rendimiento electrocatalítico de los materiales referencia; metales nobles como por ejemplo PtRuC 20%, demostrando propiedades excepcionales como cátodos de aire en baterías de Zn-Aire.
- Como se puede observar en la ***Tabla 10.2***, el material híbrido N-rGO/Co_3O_4 ha mostrado un rendimiento catalítico superior (ORR y OER) en comparación con $NiCoMnS_4$/N-rGO. Un valor pequeño de ΔE ($\Delta E = E_{j=10} - E_{1/2}$) (0.78 contra 0.82) nos indica una actividad catalítica bifuncional más alta.

En resumen, la presente tesis doctoral no solo detalla la síntesis de nuevos materiales híbridos basados en grafeno y su empleo como materiales de electrodo de alto rendimiento o electrocatalizadores para aplicaciones energéticas, sino que también demuestra el efecto de las características estructurales o de composición en la respuesta electroquímica de distintos compuestos de metales de transición. También se ha evidenciado la evolución de las muestras en el curso de las reacciones, permitiendo una mejor comprensión de las reacciones de esta familia de materiales. Toda esta información recogida en el documento de tesis, puede servir como referencia para desarrollar y optimizar materiales más eficientes para las distintas aplicaciones en el mundo del almacenamiento de energía.

10.2 Perspectivas Futuras

A pesar de los avances demostrados en la presente tesis, aún quedan multitud de desafíos para aumentar las propiedades de almacenamiento de los materiales en base grafeno, así como la densidad de energía específica de los dispositivos de almacenamiento estudiados sin reducir su densidad de potencia y seguridad, tratando de avanzar a lo largo de la diagonal del gráfico de Ragone. Por otro lado, la ingeniería nanoestructural de nuevos materiales híbridos basados en grafeno mejora aún más la actividad y la durabilidad de los catalizadores bifuncionales como se ha podido demostrar en base al conocimiento adquirido durante la presente tesis. En este sentido, se pueden identificar varios caminos que pueden dirigirnos hacia mejoras adicionales futuras:

- Será necesario investigar el efecto de la calidad del grafito inicial en la síntesis y en las propiedades de los distintos derivados de grafeno resultantes, como GO o rGO sintetizados por métodos químicos. Por ejemplo, el número de defectos en las capas o el número de grupos funcionales en los bordes o en el plano basal pueden verse afectados por la pureza o calidad del grafito inicial empleado.
- Estudiar en mayor profundidad la influencia de diferentes cationes metálicos en la estructura híbrida mediante el empleo de espectroscopia XPS, XRD o Raman in situ/ operando junto con técnicas electroquímicas; como tratamos de realizar en el Capítulo 8, se necesita obtener aún más información para deducir con mayor exactitud los mecanismos de almacenamiento de carga de los diferentes materiales híbridos.

- Desde el punto de vista de la morfología de las muestras, se pueden desarrollar otras técnicas de síntesis basadas en métodos de alto rendimiento como CVD (Deposición Química de Vapor) o ALD (Deposición Atómica de Capas) para fabricar materiales híbridos con un espesor controlado del óxido/sulfuro en cuestión a un coste reducido. Aquí, el coste es probablemente el mayor problema. Coste, calidad y producción son aspectos de igual importancia en un método de síntesis. Sin embargo, hasta la fecha, ninguna de las técnicas de síntesis arriba mencionadas ha demostrado un potencial de comercialización suficiente, esperando una reducción en el costo general en un futuro cercano.
- En el campo de la electrocatálisis, se debe realizar un análisis más riguroso y sistemático de las vías de degradación del electrocatalizador, junto con estudios de caracterización físico-química relacionados con la durabilidad del catalizador o estudios in situ para comprender los mecanismos de degradación e idear estrategias de mitigación adecuadas para evitar el deterioro del rendimiento.

A pesar de los muchos intentos que se han llevado a cabo para estandarizar los métodos de evaluación de los sistemas de almacenamiento de energía electroquímicos, aún a día de hoy faltan reglas claras para evaluar el rendimiento de estos dispositivos de una manera justa y sistemática. Creemos que todavía existen grandes desafíos en el empleo de métricas apropiadas y el desarrollo de un protocolo común para la evaluación precisa de los sistemas de almacenamiento de energía electroquímicos. Todos estos estándares que actualmente se persiguen, ayudarán a alcanzar un punto en el que todos podamos evaluar y comparar nuestros dispositivos de almacenamiento de energía de una manera más efectiva y rigurosa.

APPENDIX A

Scientific Contributions

The work presented in this doctoral thesis has given rise to several publications in peer-reviewed international scientific journals and oral/poster contributions in national and international conferences. Additionally, an international secondment period was enjoyed.

- ## Peer-Reviewed Publications

1. **J. S. Sanchez**, A. Pendashteh*, J. Palma, M. Anderson, R. Marcilla*, Anchored Fe_3O_4 Nanoparticles on rGO Nanosheets as High-Power Negative Electrodes for Aqueous Batteries, ***ChemElectroChem,*** 2017, 4, 1295–1305. doi: 10.1002/celc.201700048, *IF = 4.446*

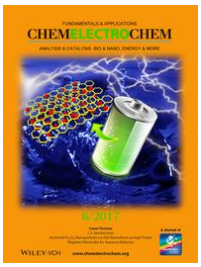

2. **J. S. Sanchez**, A. Pendashteh*, J. Palma, M. Anderson, R. Marcilla*, Synthesis and application of $NiMnO_3$-rGO Nanocomposites as Electrode Materials for Hybrid Energy Storage Devices, ***Applied Surface Science***, 2018, 460, 74-83. doi: 10.1016/j.apsusc.2018.02.165 , (Impact Factor *IF = 4.439)*

3. **J. S. Sanchez**, A. Pendashteh*, J. Palma, M. Anderson, R. Marcilla*, Porous NiCoMn Ternary Metal Oxide/Graphene Nanocomposites for High Performance Hybrid Energy Storage Devices, ***Electrochimica Acta***, 2018, 279, 44-56. doi: 10.1016/j.electacta.2018.05.072, (Impact Factor *IF = 5.116)*

4. A. Pendashteh*, **J. S. Sanchez** J. Palma, M. Anderson, R. Marcilla, Anchored $NiCoMnS_4$ Nanoparticles on N-doped rGO: High-performance Bifunctional Electrocatalysts for Rechargeable Zn-Air batteries, ***Energy Storage Materials***, 2019, In press. doi: 10.1016/j.ensm.2019.04.018

5. **J. S. Sanchez,** R. Maça, A. Pendashteh*, V. Etacheri, M. Castillo Rodríguez, J. Palma, M. Anderson, R. Marcilla, Hierarchical Co_3O_4 Nanorods Anchored on Nitrogen Doped Reduced Graphene Oxide: A Highly Efficient Bifunctional Electrocatalyst for Rechargeable Zn-Air Batteries, ***Journal of Power Sources*** (under review).*I.F=6.9*

6. **J. S. Sanchez**, A. Pendashteh*, J. Palma, M. Anderson, R. Marcilla, Understanding Charge Storage Mechanism of Mixed Metal Sulfides in Alkaline Media: $NiCoMnS_2$ Nano-needles

Forming Core-Shell Structures for Hybrid Energy Storage, ***Journal of Material Chemistry A*** (under review). *I.F.=9.9*

- **Oral Presentations in Conferences and Meetings**

  - **J.S. Sanchez**, A. Pendashteh, J. Palma, M. Anderson, R. Marcilla, Graphene-Based Materials for Hybrid Energy Storage, **Internal Seminar IMDEA Energy**, June, 2016, Madrid, Imdea Energy Institute

  - **J.S. Sanchez**, A. Pendashteh, J. Palma, M. Anderson, R. Marcilla, Graphene-Based Nanocomposites: Hybrid Materials to Push-up Energy Storage Performance, **5*th*** ***Annual Workshop of Young Researchers***, December, 2016, Madrid, IMDEA Energy Institute

  - **J.S. Sanchez**, A. Pendashteh, J. Palma, M. Anderson, R. Marcilla, 2D Porous $NiCoMnO_4$-Graphene Nanocomposites for High-Performance Hybrid Energy Storage Devices, ***E-MRS Spring Meeting***, May 22 – 26, 2017, Strasbourg, France.

  - **J.S. Sanchez**, A. Pendashteh, J. Palma, M. Anderson, R. Marcilla, Hybrid Energy Storage: The Merging of Battery and Supercapacitor Technologies, **6*th*** ***Annual Workshop of Young Researchers***, December, 2017, Madrid, Imdea Energy Institute.

  - **J.S. Sanchez**, A. Pendashteh, J. Palma, M. Anderson, R. Marcilla, 2D Porous NiCoMn Ternary Metal Oxide/Graphene Nanocomposites for Energy Storage Application, ***Power Our Future (POF)***, July, 2017, Vitoria, Spain.

  - **J.S. Sanchez**, A. Pendashteh, J. Palma, M. Anderson, R. Marcilla, Graphene-Based Materials for Energy Storage Devices, ***Research Plan Defense***, July 5th, 2017, Vitoria, Spain.

- **J.S. Sanchez**, A. Pendashteh, J. Palma, M. Anderson, R. Marcilla, Understanding Charge Storage Mechanism of Mixed Metal Sulfides in Alkaline Media: $NiCoMnS_2$ Nano-needles Case Study, ***E-MRS Fall Meeting***, September, 2018, Warsaw, Poland.

• Poster Presentations in Conferences and Meetings

- **J.S. Sanchez**, A. Pendashteh, J. Palma, M. Anderson, R. Marcilla, Boosting Energy Storage Performance of Commercial Fe_3O_4 Nanoparticles by Facile Anchoring on rGO Nanosheets , **4th *Annual Workshop of Young Researchers***, December, 2015, Madrid, Imdea Energy Institute

- **J. S. Sanchez**, A. Pendashteh, J. Palma, M. Anderson, R. Marcilla, Boosting energy storage performance of commercial Fe_3O_4 Nanoparticles by Facile Anchoring on rGO Nanosheets, ***Graphene 2016***, April, 2016, Genoa, Italy.

- **J.S. Sanchez**, A. Pendashteh, J. Palma, M. Anderson, R. Marcilla, 2D Porous $NiCoMnO_4$-Graphene Nanocomposites for High Performance Hybrid Energy Storage Device, **5th *Annual Workshop of Young Researchers***, December, 2016, Madrid, IMDEA Energy Institute

- **J.S. Sanchez**, A. Pendashteh, J. Palma, M. Anderson, R. Marcilla, Synthesis and Application of $NiMnO_3$-rGO nanocomposites as electrode materials for Hybrid Energy Storage Devices , **6th *Annual Workshop of Young Researchers***, December, 2017, Madrid, Imdea Energy Institute.

• International Secondment Period

The research stay was framed within a potential collaboration with the Inorganic Chemistry department and its group of electronic structure in the research institute "Fritz-Haber-Institut der Max-Planck-Gesellschaft" (FHI-MPI) (Berlin-Dhalem) under the supervision of Dr. Axel Knop-Gericke (September-December 2018).

The main purpose of the short stay was to deepen through In-situ or Operando characterization techniques in the reaction mechanism that governs the faradaic processes in alkaline environment of transition metals mixed sulfides (Ni, Co, Mn) and their hybrids with graphene. The idea was to combine spectroscopy techniques (mainly X-ray spectroscopy, XPS and XAS) with electrochemical characterization techniques in order to evaluate what type of changes are observed in the oxidation state of the metal cations participants in the electrochemical reaction. For this purpose, we employed the electrochemical cells designed and provided by the hosting center, adapted for use in the Berliner Elektronenspeicherring-Gesellschaft für Synchrotronstrahlung (BESSY), a third-generation synchrotron radiation center. This work gave the expertise and scientific knowledge necessary to include Raman Operando experiments in a scientific contribution entitled *Understanding Charge Storage Mechanism of Mixed Metal Sulfides in Alkaline Media: NiCoMnS_2 Nano-needles forming core-shell structures for Hybrid Energy St*orage under review in Journal of Material Chemistry A which main results are gathered in Chapter 8 of the present Thesis.

APPENDIX B

List of Figures, Tables and Acronyms

In the following Appendix, the list of Figures, list of Tables and a list of the Acronyms employed in the present thesis are gathered:

List of Figures

CHAPTER 1: INTRODUCTION AND LITERATURE OVERVIEW

CHAPTER 3: EXPERIMENTAL

CHAPTER 4: ANCHORED Fe_3O_4 NPs ON rGO NSs AS HIGH POWER NEGATIVES ELECTRODES FOR AQUEOUS BATTERIES

CHAPTER 5: $NiMnO_3$-rGO AS POSITIVE ELECTRODE MATERIALS FOR HYBRID ENERGY STORAGE DEVICES

CHAPTER 6: POROUS NiCoMn TERNARY METAL OXIDE/GRAPHENE AS POSITIVE ELECTRODE MATERIALS FOR HYBRID ENERGY STORAGE DEVICES

CHAPTER 8: MIXED METAL SULFIDES NANO-NEEDLES FORMING CORE-SHELL STRUCTURES FOR HYBRID ENERGY STORAGE

CHAPTER 9: ANCHORED NiCoMnS4 NANOPARTICLES ON N-DOPED rGO: A BIFUNCTIONAL ELECTROCATALYST FOR RECHARGEABLE ZN-AIR BATTERIES

List of Tables

CHAPTER 1: INTRODUCTION AND LITERATURE OVERVIEW

CHAPTER 3: EXPERIMENTAL

CHAPTER 4: ANCHORED Fe_3O_4 NPs ON rGO NSs AS HIGH POWER NEGATIVES ELECTRODES FOR AQUEOUS BATTERIES

CHAPTER 5: $NiMnO_3$-rGO AS POSITIVE ELECTRODE MATERIALS FOR HYBRID ENERGY STORAGE DEVICES

CHAPTER 6: POROUS NiCoMn TERNARY METAL OXIDE/GRAPHENE AS POSITIVE ELECTRODE MATERIALS FOR HYBRID ENERGY STORAGE DEVICES

CHAPTER 7: Co_3O_4 NANORODS ANCHORED ON N-rGO: AN EFFICIENT BIFUNCTIONAL ELECTROCATALYST FOR RECHARGEABLE ZN-AIR BATTERIES

CHAPTER 8: MIXED METAL SULFIDES NANO-NEEDLES FORMING CORE-SHELL STRUCTURES FOR HYBRID ENERGY STORAGE

CHAPTER 9: ANCHORED NiCoMnS4 NANOPARTICLES ON N-DOPED rGO: A BIFUNCTIONAL ELECTROCATALYST FOR RECHARGEABLE ZN-AIR BATTERIES

CHAPTER 10: OVERALL CONCLUSIONS AND PERSPECTIVES

Acronyms

EV	Electric Vehicles
TWh	TeraWatt hour
PV	Photovoltaics
ESTs	Energy Storage Technologies
SCs	Supercapacitors
Ni-MH	Nickel-Metal Hydride
ORR	Oxygen Reduction Reaction
OER	Oxygen Evolution Reaction
US	United States of America
CNTs	Carbon Nanotubes
rGO	reduced Graphene Oxide
ECs	Electrochemical Capacitors
EDLCs	Electrochemical Double-Layer Capacitors
PSCs	Pseudo-Capacitors
AC	Activated Carbon
$\mathcal{E}_r$	Relative permittivity
$\mathcal{E}_O$	Dielectric Constant of Vacuum
A	Specific Surface Area
d	Effective thickness of the EDL
$C_{electrode}$	Capacitance of a single electrode
C	Capacitance of the device
V	Operation Voltage Window
ESR	Equivalent Series Resistance
GO	Graphene Oxide
N-rGO	N-doped reduced Graphene Oxide
UPD	Under-Potential Deposition
PANI	Polyaniline
PPy	Polypyrrole
CV	Cyclic Voltammetry

GCD	Galvanostatic Charge-Discharge
ΔQ	Differential charge stored
ΔV	Width of the voltage window
TMOs	Transition Metal Oxides
MTMOs	Mixed Transition Metal Oxides
MSs	Metal Sulfides
MMSs	Mixed Metal Sulfides
CVD	Chemical Vapor Deposition
GIC	Graphite Intercalation Compound
MWCNTs	Multi-Wall Carbon Nanotubes
PGO	Pyrolytic Graphene Oxide
HPGO	Hydrogen-reduced Pyrolytic Graphene Oxide
MOFs	Metal Organic Frameworks
LDH	Layer Double Hydroxide
DMF	Dimethylformamide
TAA	Thioacetamide
RT	Room Temperature
NRs	Nanorods
NSs	Nanosheets
NPs	Nanoparticles
NCMO	Nickel-Cobalt-Manganese Oxide
NF	Ni foam
SEM	Scanning Electron Microscope
TEM	Transmission Electron Microscope
HR-TEM	High-Resolution Transmission Electron Microscopy
HAADF-STEM	High-angle annular dark-field scanning transmission electron microscopy
EDS or EDX	Energy dispersive X-ray spectroscopy
TGA	Thermogravimetric Analysis
FT-IR	Fourier Transform Infrared Spectroscopy
XPS	X-ray photoelectron spectroscopy
ESCA	Electron spectroscopy for chemical analysis
XRD	X-ray diffraction

λ	wavelength of the X-rays
BET	Brunauer, Emmett and Teller
N_A	Avogadro´s number
n_m^a	monolayer capacity
BJH	Barrett-Joyner-Halenda
RE	Reference Electrode
CE	Counter Electrode
WE	Working Electrode
PTFE	Polytetrafluoroethylene
RDE	Rotating Disk Electrode
RRDE	Rotating Ring Disk Electrode
VC	Vulcan carbon
NMP	N-Methyl-2-pyrrolidone
GCE	Glassy Carbon Electrode
SCE	Saturated Calomel Electrode
J	Experimental current density
J_K	kinetic-limiting current density
J_L	diffusion-limiting current density
ω	angular velocity
F	Faraday constant
C_{O_2}	Bulk concentration of O_2
D_{O_2}	Diffusion coefficient of O_2
v	kinematic viscosity of the electrolyte
n	Number of electrons
I_D	Disk current
I_r	Ring current
N	Current collection efficiency
LSV	Linear sweep voltammetry
EIS	Electrochemical Impedance Spectroscopy
Q	Specific capacity
I	Current
m	mass of active material

dt	time differential
C_{am}	Specific capacitance of the capacitor-type electrodes
s	scan rate
Z	impedance
f	frequency
$-Z_{im}$	imaginary part of the impedance
Z_{re}	real part of the impedance
m^+	mass of the positive
m^-	mass of the negative electrode
Q^+	specific capacity/capacitance of positive electrode
Q^-	specific capacity/capacitance of negative electrode
ΔV^+	working potential window of positive electrode
ΔV^-	working potential window of negative electrode
GDL	Gas Diffusion Layer
Z_p	Zeta-potential
ΔEp	peak separation
R_s	uncompensated resistance
R_{ct}	faradaic charge transfer resistance
W	Warburg impedance
CPE	Constant Phase Element